AD_____

Award Number: DAMD17-03-1-0132

TITLE: Real-Time Dosimetry and Optimization of Prostate Photodynamic Therapy

PRINCIPAL INVESTIGATOR: Timothy C. Zhu

CONTRACTING ORGANIZATION: University of Pennsylvania
Philadelphia, PA 19104

REPORT DATE: September 2006

TYPE OF REPORT: Final

PREPARED FOR: U.S. Army Medical Research and Materiel Command
Fort Detrick, Maryland 21702-5012

REPORT DOCUMENTATION PAGE

Form Approved
OMB No. 0704-0188

1. REPORT DATE	2. REPORT TYPE	3. DATES COVERED
01-09-2006	Final	1 May 2003 – 31 Aug 2006

4. TITLE AND SUBTITLE

Real-Time Dosimetry and Optimization of Prostate Photodynamic Therapy

5a. CONTRACT NUMBER

5b. GRANT NUMBER
DAMD17-03-1-0132

5c. PROGRAM ELEMENT NUMBER

6. AUTHOR(S)

Timothy C. Zhu

5d. PROJECT NUMBER

5e. TASK NUMBER

5f. WORK UNIT NUMBER

7. PERFORMING ORGANIZATION NAME(S) AND ADDRESS(ES)

University of Pennsylvania
Philadelphia, PA 19104

8. PERFORMING ORGANIZATION REPORT NUMBER

9. SPONSORING / MONITORING AGENCY NAME(S) AND ADDRESS(ES)
U.S. Army Medical Research and Materiel Command
Fort Detrick, Maryland 21702-5012

10. SPONSOR/MONITOR'S ACRONYM(S)

11. SPONSOR/MONITOR'S REPORT NUMBER(S)

12. DISTRIBUTION / AVAILABILITY STATEMENT
Approved for Public Release; Distribution Unlimited

13. SUPPLEMENTARY NOTES
Original contains colored plates: ALL DTIC reproductions will be in black and white.

14. ABSTRACT

We have completed all specific aims of the project. We have developed motorized probe and associate software to characterization of optical properties in vivo in human prostate (specific aim 1). We have shown that the effective attenuation coefficient μeff varied between 0.91–6.7 cm-1 (mean 2.9 ± 0.8 cm-1), corresponding to an optical penetration depth (δ = 1/μeff) of 0.2–1.1 cm (mean 0.4 ± 0.1 cm). We have made comparison of light fluence rate between calculation and measurement (specific aim 2) in 14 patients and have shown an agreement of 30%. We have developed the motorized probe and associate software to measure the distribution of optical properties, drug concentration, and StO2 interstitially using both absorption and fluorescence techniques (specific aim 3) and have verified the agreement between the two methods for determination of photosensitizer. We developed software to automatically optimize the light source weights, lengths, strengths in near real-time to improve the light fluence rate distribution in prostate and spare dose to critical structures (specific aim 4). In addition, we have developed a 12-channel beamsplitter for light delivery with motorized attenuators.

15. SUBJECT TERMS
Prostate Phytodynamic Therapy, Optical properties, Photosensitizer, PDT dose

16. SECURITY CLASSIFICATION OF:				18. NUMBER OF PAGES	19a. NAME OF RESPONSIBLE PERSON
					USAMRMC
a. REPORT	b. ABSTRACT	c. THIS PAGE			19b. TELEPHONE NUMBER *(include area code)*
U	U	U	UU	119	

Standard Form 298 (Rev. 8-98)
Prescribed by ANSI Std. Z39.18

Table of Contents

INTRODUCTION

This report summarizes the works done for the entire 3 year grant, between May 1, 2002 and August 31, 2006.

1. Scope of work

The scope of the work includes software and instrument development outline below.

Task 1. To develop instruments to measure the optical properties (1 – 6 months)
- a. Construct a motorized detector probe (1 – 3 months).
- b. Verify the feasibility software of the detector probe in phantom (4 – 6 months).
- c. Develop a 16-channel *in-vivo* light dosimetry system capable of interfacing with the motorized detector probe (1 – 6 months).

Task 2. To develop software for light dose calculation and optimization, and accumulate clinical data (6 – 18 months)
- a. Develop a kernel based dose calculation algorithm and compare with optical phantom measurements (6 – 12 months).
- b. Verify the accuracy of the calculation of light dosimetry in patients (6 – 24 months).
- c. Develop the software to optimize the weights of PDT light sources (1 – 18 months).
- d. Improve *in situ* fluorescence measurements of photosensitizer (1 – 18 months).

Task 3. To develop instruments and software for integrated real-time in-vivo light monitoring and optimized light delivery (18 – 36 months)
- a. Develop an 8-way beamsplitter system for light delivery (18 – 24 months).
- b. Interface the *in-vivo* light dosimetry system with the calculation engine (18 – 24 months).
- c. Interface the fluorescence and absorption measurement to determine drug concentration and tissue oxygenation with the PDT dose calculation engine (18 – 24 months).
- d. Refine the integrated system for real-time light monitoring and optimization in patients (24 – 36 months).

For the scientific research, the scientific objectives are outlined below as specific aims:

1: Characterize the optical properties (scattering and absorption coefficients) of the prostate gland *in vivo*:
2: Add the ability to calculate light fluence rate within the prostate volume during PDT to the current light dosimetry system that measures light fluence at selected points:
3: Measure photosensitizer (MLu) drug concentration and tissue oxygenation measured with optical fluorescence and absorption spectra and incorporate these values in a determination of PDT dose:
4: Develop optimization methods for placement of the light source to achieve uniform PDT dose in the prostate gland:

2. Summary of accomplishment

For the instrument and software development works, we have completed Tasks 1 - 3. For the scientific research, we have completed specific aims 1 - 4.

BODY

1. Characterize the distribution of optical properties (scattering and absorption coefficients) of the prostate gland *in vivo*

Following the successful completion of the characterization of optical properties in 12 patients in the first year, we have published the results (for 14 patients) in a peer-reviewed journal (Ref. 1). We have improved the motorized detector probe to characterize the optical properties at different depths in a catheter (see Section A below). This new design along with improved software (Section B) allows us to measure the ***distribution*** of optical properties in prostate (Ref. 2). We have now characterized the accuracy of determining the optical properties using the instrument (Ref. 3).

A. Motorized detector probe

The motorized detector probe system has been expanded from the single-channel, single-motor device reported last year to a two-motor system capable of controlling up to 5 detectors simultaneously. This device allows one light source and up to four detectors to be used to make optical property measurements in four regions of a single prostate quadrant at the same time. The device is shown in figure 1. An additional enhancement of the device is the addition of plastic extensions onto the catheters used for detection. These extensions are held by a clamp mounted on the front of the motor assembly, and allow the optical fibers to be translated along curved paths without binding or interference, greatly improving the accuracy of positioning.

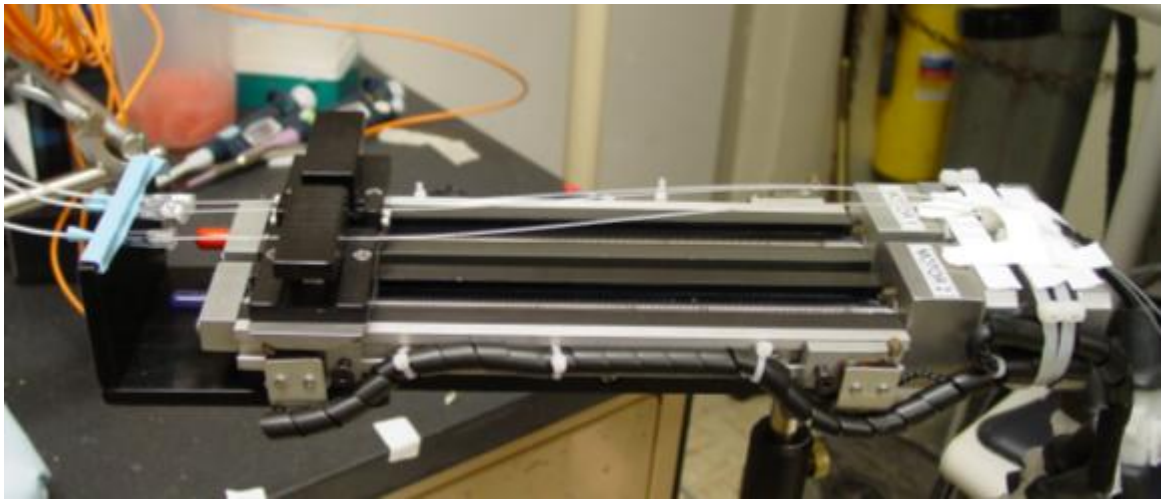

Figure 1: Photograph of the multichannel step motor assembly used to move multiple detectors and a single source simultaneously.

B. Software

The introduction of the two-motor positioning system has been accompanied by an enhancement in our dosimetry software, allowing us to use the motorized positioner to characterize the fluence rate distribution during treatment. Previously, the maximum value in each quadrant (to which the prescription is specified) was found by manual positioning of the fiber. In the new system, the detection fiber in the quadrant being treated is controlled by the motorized positioner. The detector is scanned along its catheter under computer control without interruption of dosimetry measurements. The resulting fluence rate profile is stored for future analysis, and the motor automatically moves the detector to the position of maximum fluence rate. This not only greatly improves the accuracy and speed with which the point of maximum fluence rate can be found, but also gives a quantitative measure of the fluence rate profile within the quadrant. Because this measurement requires only one of the two motors, the other can be used to make profile measurements in adjacent quadrants. This allows characterization of the diffusion of light from one quadrant into another and also ensures that the dosimetric measurements will accurately reflect the total dose given to each quadrant, including contributions from adjacent quadrants.

C. Instrument accuracy

The instrument accuracy has been characterized in optical phantom. We find that μ_a and μ_s' can be determined by this method with a standard (maximum) deviation of 8% (15%) and 18% (32%) for μ_a and μ_s', respectively (see Abstract and Fig 9 of Appendix 3, Ref.3).

D. Summary of in-vivo measurements

Measurements were made in all four quadrants of the prostate using a motorized probe. μ_a and μ_s' varied between 0.07-1.62 cm^{-1} (mean 0.37±0.24 cm^{-1}) and 1.1-44 cm^{-1} (mean 14±11 cm^{-1}), respectively. μ_{eff} varied between 0.91-6.7 cm^{-1} (mean 2.9±0.7 cm^{-1}), corresponding to an optical penetration depth ($\delta = 1/\mu_{eff}$) of 0.1-1.1 cm (mean 0.4±0.1 cm) (see Table 1). Our preliminary study showed significant inter- and intra- prostatic differences in the optical properties, indicating a need for obtaining patient-specific optical properties. The optical penetration depth varied by a factor of 2.5 among patients (Ref. 2) and at least as much within a prostate.

Table 1: Summary of optical properties before and after PDT in human prostates. The values in the parentheses are the standard deviation (s.d.) of the mean values measured from different locations of the same prostate.

Patient	Before PDT				After PDT			
number	μ_a (cm^{-1})	μ_s' (cm^{-1})	δ (cm)	ϕ/S (cm^{-2})	μ_a (cm^{-1})	μ_s' (cm^{-1})	δ (cm)	ϕ/S (cm^{-2})
2	0.09	29.8	0.34	3.34	0.09	43.7	0.29	3.78
3	0.15	22.0	0.31	2.15	0.07	33.4	0.37	4.07
4	0.43 (0.28)	7.69 (4.76)	0.41 (0.14)	0.97 (0.81)	0.51	1.67	0.63	0.36
5	0.21	11.8	0.37	1.44	0.13	7.18	0.60	1.48
6	0.27 (0.27)	10.5 (11.2)	0.50 (0.05)	1.74 (1.78)	0.19 (0.20)	18.9 (18.4)	0.45 (0.06)	3.18 (3.32)
7	—	—	—	—	0.30 (0.08)	23.7 (13.9)	0.24 (0.11)	1.09 (0.40)
9	0.53 (0.36)	6.61 (4.51)	0.41 (0.09)	0.77 (0.42)	0.64 (0.25)	7.00 (5.59)	0.33 (0.10)	0.54 (0.23)
10	0.63 (0.32)	4.62 (2.87)	0.42 (0.10)	0.56 (0.29)	0.19 (0.05)	9.27 (4.47)	0.54 (0.31)	1.33 (0.64)
11	0.67 (0.17)	6.39 (3.18)	0.32 (0.10)	0.51 (0.18)	0.83 (0.45)	5.45 (3.89)	0.38 (0.16)	0.47 (0.30)
12	0.71 (0.43)	8.99 (6.51)	0.32 (0.12)	0.61 (0.35)	0.30 (0.06)	20.2 (4.8)	0.28 (0.08)	0.98 (0.05)
13	0.27 (0.14)	18.5 (11.6)	0.30 (0.07)	1.46 (0.72)	0.26 (0.09)	17.0 (8.8)	0.31 (0.07)	1.42 (0.56)
14	0.72 (0.11)	3.37 (1.37)	0.39 (0.11)	0.40 (0.01)	—	—	—	—

E. 3D distribution of optical properties

If sufficient measurements were made in a prostate, it is possible to make a 3D map. This is done for patient #15 for absorption (Fig. 2a) and reduced scattering coefficients (Fig. 2b). The absorption coefficient varied between 0.06 – 1 cm^{-1} and the reduced scattering coefficient varied between 6–49 cm^{-1}. The spatial distribution of μ_a and μ_s' were also calculated via a 2D continuous wave Diffuse Optical Tomography model (Fig. 2c and Fig. 2d). A dual mesh scheme was used to calculate the distribution of μ_a and μ_s' on this particular slice (z=0.5cm). 918 elements with 484 nodes were used in the forward model to simulate the fluence distribution while a coarser mesh (10 by 10) with 14 measurements of absolute

fluence rate were used in the inverse model to calculate μ_a and μ_s'. Significant heterogeneity for absorption and scattering properties were observed in images obtained by both point-by-point method and DOT method. Compared these two methods, discrepancy in the absorption coefficient is relatively low (root-mean-square difference = 28%) compared to the discrepancy in the scattering coefficient (rms difference = 79%), which might due to the absorption-scattering crosstalk in DOT reconstruction. These preliminary results indicate that diffuse optical tomography method can be implemented for the interstitial geometry and recover the optical properties of the prostate tissue.

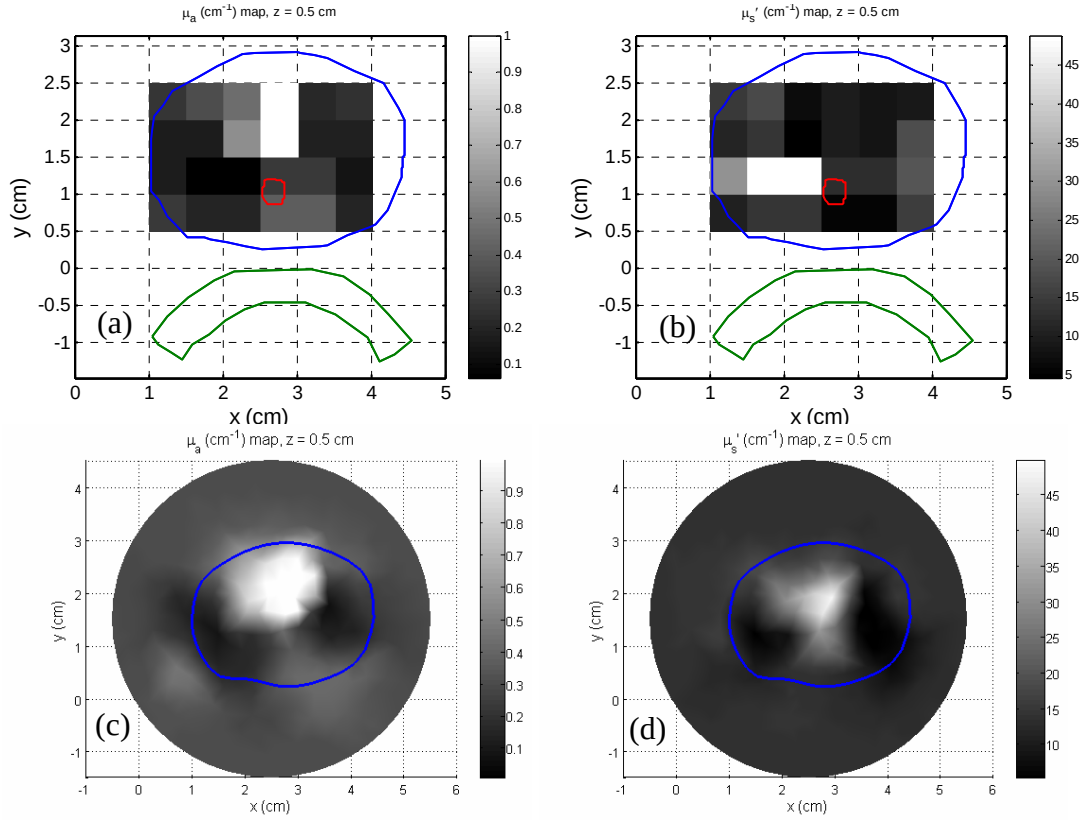

Figure 2: Preliminary result of in-vivo 3D map of absorption coefficient ((a) and (c)) and reduced scattering coefficients ((b) and (d)) for patient #15. (a) and (b) were measured using point-by-point method; (c) and (d) were calculated using diffuse optical tomography.

2. Development of dosimetry system for interstitial light fluence rate measurement in prostate gland *in vivo*

We have developed a 16-channel in-vivo dosimetry system (see Figs. 3 and 4). The instrument consists of the following major components: (1) isotropic detectors, (2) photodiodes, (3) preamplifiers, (4) A/D (analog-to-digital) converters, and (5) PC control software. The gain of the preamplifier can be adjusted by between 1 and 8 in increment of 2 by the software. It also contains a Windows-based graphics user interface (GUI) for displaying the light fluence distribution. Different isotropic detectors with different scattering tip diameters have been compared for their angular dependence, transmission loss, wavelength dependence, and correction factors for different medium. We have also performed measurements to determine the accumulated light fluence dependence and the nonlinearity of the detector sensitivity for various photodiodes over a wide range of fluence (0 – 1200 mW/cm^2). The light dosimetry system can be used to measure light fluence distribution in 3D heterogeneous optical phantoms for comparison with theoretical calculations.

Compared with existing dosimetry system, this one has larger dynamic range for AD converter (16 bit vs. 12 bit), has more channels (16 vs. 12), and is portable.

This dosimetry system has been clinically tested over the last 2 years to be reliable and works well with the motorized probe for accurate in-vivo light fluence dosimetry in real-time. In-vivo comparison between measurement and calculation is discussed below.

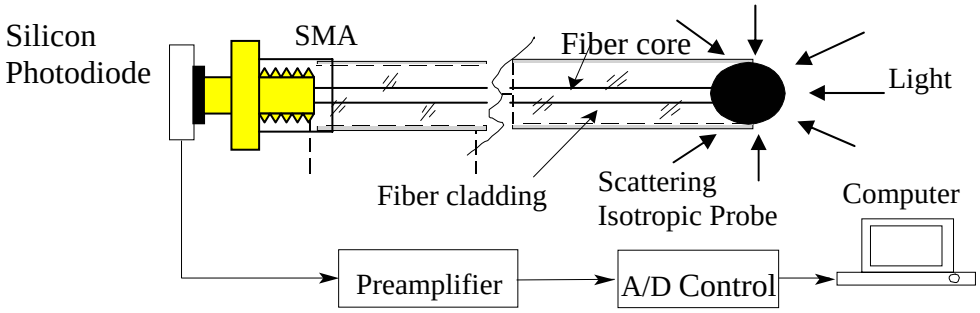

Figure 3: Schematics of the PENN light dosimetry system using a scattering isotropic probe. The fiber detector has a 0.5-mm diameter spherical scattering tip that detects light from all directions. The detector is connected to a silicon photodiode via a SMA connector. The photodiode is connected to a preamplifier that amplifies photocurrent and converts to a voltage to be inputted to an Analog-to-Digital board. A Windows-based PC is used to control the data acquisition and display.

Figure 4: Photograph of the 16-channel dosimetry system. The unit connects to a PC via USB.

3. Development of light dose calculation and optimization and accumulate clinical data

We have developed a kernel model, which allows predict light fluence rates in human prostates during PDT. We have examined the model by comparing the calculations with measurements in 14 patients.

A. Kernel model in homogeneous medium

A kernel model for light fluence rate calculation is developed for each linear light source used in a treatment, which is based on the solution of the diffusion equation for a point source.

$$\phi = \sum_{i=1} \frac{s \cdot \Delta x_i \cdot \mu_{eff}^2 \cdot e^{-\mu_{eff} \cdot r_i}}{4\pi \mu_a r_i}, \qquad (1)$$

where s is the source strength of each segment along the linear light source, Δx_i is the division along the direction parallel to the orientation of the linear source, μ_{eff} is the effective attenuation coefficient, μ_a is the absorption coefficient, and r_i is the distance between the source segment and the detector. The

summation in Eq. (1) is over all the segments composing the linear source. The fluence rate at a point in a prostate is the summation of the fluence rates generated by each linear source. In a calculation, ultrasound images of a prostate are imported and the calculated light fluence rate distribution is superimposed on the contours of the prostate.

B. Application and examination of the model

B.1. Application in treatment planning

With the kernel model, we have been able to calculate light fluence rates in a three-dimensional prostate volume. This is applied to light fluence calculation in current PDT treatment planning (see details in section 6).

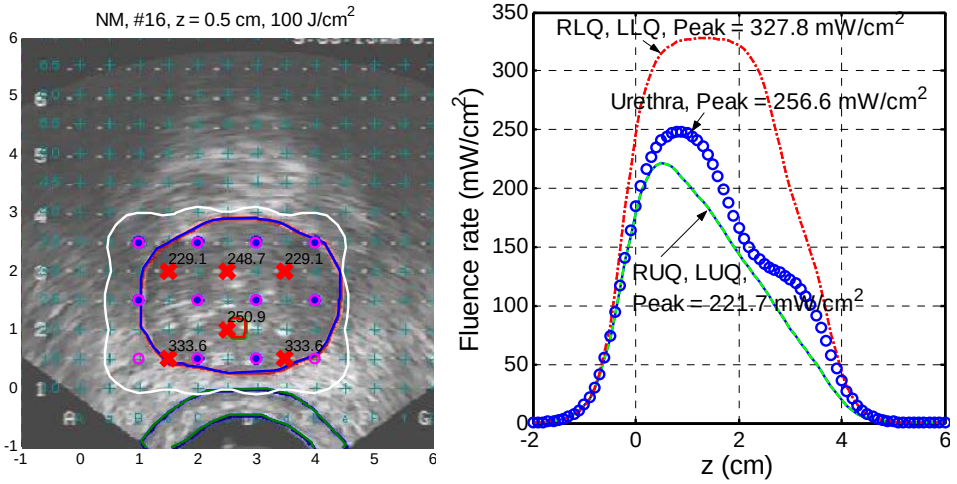

(a) (b)

Figure 5: Calculated light fluence rate distribution superposed on an ultrasound image of prostate cross-section at depth of 0.5 cm, which was used in PDT planning. The outer white line indicates the predicted 100% isodose line and the inner line is the contour of the prostate. The "o" symbols represent the source positions and the predicted light fluence rates at "x" symbol positions are displayed next to the symbols. (b) Light fluence rates along the *z* direction at the detector positions and in the urethra.

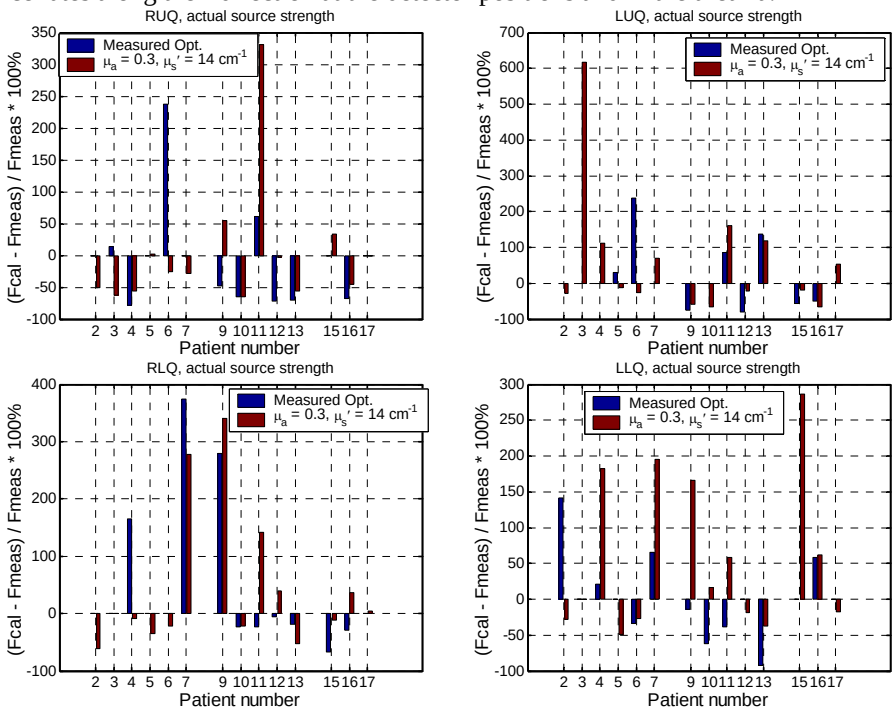

Figure 6: Comparison between light fluence rates calculated using measured optical properties and estimated optical properties with actual source strengths.

Figure 5(a) shows predicted light fluence rate distribution (the outer thin line) superposed on an ultrasound image of a prostate cross-section, which is a calculation result used in a treatment plan. The outer white line shows the isodose line of 100 J/cm^2 and the inner line shows the contour of the prostate. The "o" symbols represent the source positions and the "x" symbols represent the detector positions, next to which the corresponding light fluence rates are displayed. Figure 5(b) shows light fluence rates in the *z* direction at the detector positions and in the urethral as well. We actually can calculate light fluence rates anywhere in the prostate. The treatment time is determined using the predicted light fluence rates. The calculation is fast, taking only a few seconds. The results are summarized in a recent publication (Ref. 4).

B.2. Examination of the model: comparison of calculation and measurement in homogeneous medium

To examine the model and check the accuracy of the calculation, we have made comparisons between the calculations and the measurements in 14 patients. Calculations were done under different conditions, e.g., different source strengths and different optical properties. Overall, the calculations were categorized into two kinds: (1) with assumed parameters, and (2) with actual parameters used in each treatment. The former was like what we have been doing in treatment planning. In that case, we assumed that the optical properties were homogeneous in a prostate and we used the mean optical properties for the whole prostate in the calculation, which was the mean of all the optical properties measured in the patients treated previously, i.e., μ_a = 0.3 cm^{-1} and μ_s' = 14 cm^{-1}. Also, we assumed the source strength to be 150 mW/cm, which was the source strength used in most of the treatments except in the case of bleeding. In the latter case, we used actual source strengths and incorporated heterogeneity of optical properties of a prostate, i.e., we used optical properties measured in different regions in a prostate. We had measured optical properties in most of the patients' prostates.

During each treatment, we measured light fluence rates in four regions in a prostate, which we call quadrants (RUQ, LUQ, RLQ, and LLQ). We compared our calculation results with these measured data in each quadrant. A percentage error is defined as the percentage difference between the calculated and the measured light fluence rates, i.e., *(Calculation-Measurement)/Measurement*. Here we present some of the results. Figure 6 shows comparison between light fluence rates calculated using measured optical properties and the mean optical property, with actual source strengths. The maximum error is over 600% (LUQ, patient 3). This large error may be due to the inaccuracy of the light fluence measurement rather than the calculation, because the measured light fluence rate in this case was unexpectedly low. It is possible that this anomalously low reading was caused by bleeding around the catheter. Since the measurements of optical properties and light fluence rates in patients 11-17 were well controlled, the measurement data in these cases are more reliable.

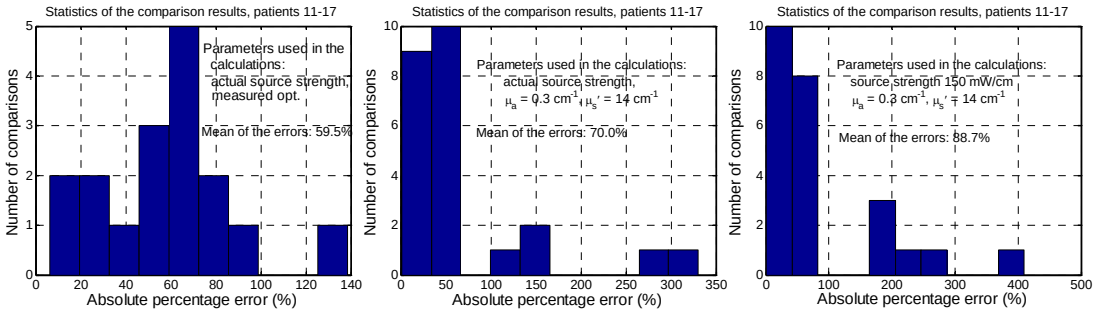

(a) (b) (c)

Figure 7: Histograms of the comparison results in patients 11-17 for calculations using: (a) actual source strengths and measured optical properties; (b) actual source strengths and the mean optical properties (μ_a = 0.3 cm^{-1} and μ_s'= 14 cm^{-1}); and (c) assumed source strength of 150 mW/cm and the mean optical properties.

The histograms of the comparison results for patients 11-17 are shown in Fig. 7, which are the statistics of all the comparisons, i.e., the comparisons of the calculations in all the quadrants for these patients. In the figure, we used the absolute values of the percentage errors. Fig.7a shows the results of the calculations using actual source strengths and measured optical properties. The mean of the absolute percentage errors is 59.5%. Fig. 7b shows the results of the calculations using actual source strengths and the mean optical property, where the mean of the absolute percentage errors is 70.0%, which is larger than that in Fig. 7a. This indicates that accurate optical properties are needed to improve the accuracy of the calculation. Fig. 7c shows the results of the calculations using a source strength of 150 mW/cm and the mean optical properties, analogous to the calculations used in treatment planning. The mean of the errors is 88.7%, not significantly worse than the 59.5% error found when using actual source strengths and measured optical properties.

C. Conclusions

We have developed and applied a kernel model in human prostate PDT treatment. With the model, we are able to calculate light fluence rates inside a human prostate volume. We are applying the calculation in treatment planning and real-time treatment guiding. We have compared the calculations with the measurements in 14 patients. The comparisons with those measurements which had more reliable data show that, the standard uncertainty is 59.5% when actual source strengths and measured optical properties were used in the calculations, and the standard uncertainty is 88.7% when the assumed source strength of 150 mW/cm and the mean optical properties were used in the calculations.

4. Characterization of absorption spectra *in vivo*

The absorption spectroscopy methods described previously (Ref. 5) have been expanded by the use of the multichannel motorized positioning system described above. As before, the diffuse fluence rate spectrum is measured at a number of distances from a white light source of known intensity. The positions of the source and detector are controlled independently by the multichannel motorized positioner. The source position is fixed, and measurements are made at different detector positions. The source is then moved by a predetermined distance, and the process is repeated. By repeating this process multiple times, we can map the distribution of absorption and scattering spectra within the prostate. Each absorption spectrum can then be analyzed using a singular value decomposition (SVD) algorithm to determine the concentrations of oxyhemoglobin (HbO_2), deoxyhemoglobin (Hb), and MLu, as shown in Fig. 8a (Ref. 2).

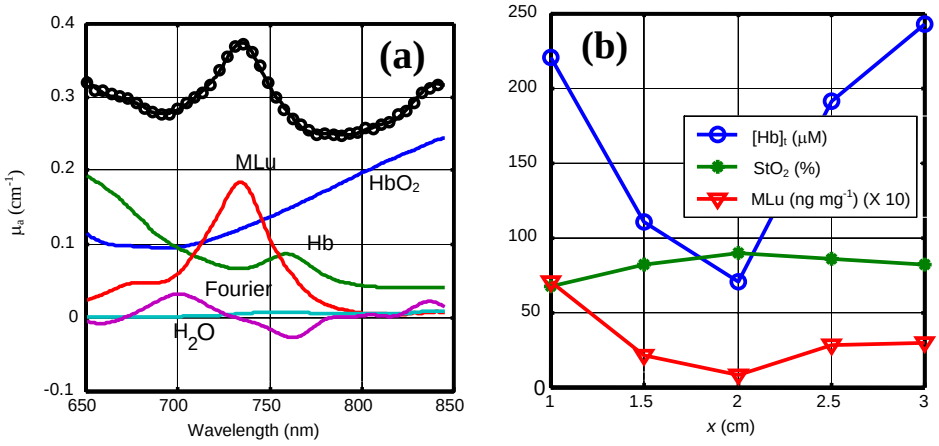

Figure 8: (a) Components of absorption spectra acquired prior to PDT *in vivo*. The measured data are labeled as symbols ('o') and the components are labeled as lines. The components include: MLu, water (H_2O), deoxyhemoglobin (Hb), and hemoglobin (HbO_2). The 'Fourier' component is a Fourier series designed to account for unknown absorbers or fluorophores. (b) The corresponding *in vivo* distribution of (a) StO_2, blood volume, and MLu concentration determined using the absorption spectra.

Combining these measurements allows us to construct a map of the distribution of the sensitizer, the total hemoglobin concentration, and the hemoglobin oxygen saturation (StO_2) (Ref 2). One such distribution, obtained *in vivo* from a human prostate, is shown in figure 8(b). This measurement demonstrates that the heterogeneity in optical properties observed in our single-wavelength measurements is related to the heterogeneity in blood and sensitizer distribution. Recent results indicate that the reliability of this system can be significantly improved by incorporating information obtained from the single-wavelength optical property measurements into the spectrally resolved fitting algorithm. As an example, the left panel of figure 9a shows the fit to the absorption spectrum reconstructed without the use of the single wavelength data. There is a large Fourier (unknown) component and a nonphysically high water concentration assigned by the fitting algorithm. When the single wavelength optical properties data are used to correct errors in detector position (figure 9b), these errors are significantly reduced, and a fit is obtained with minimal contribution from unknown components. A manuscript on this development is in preparation.

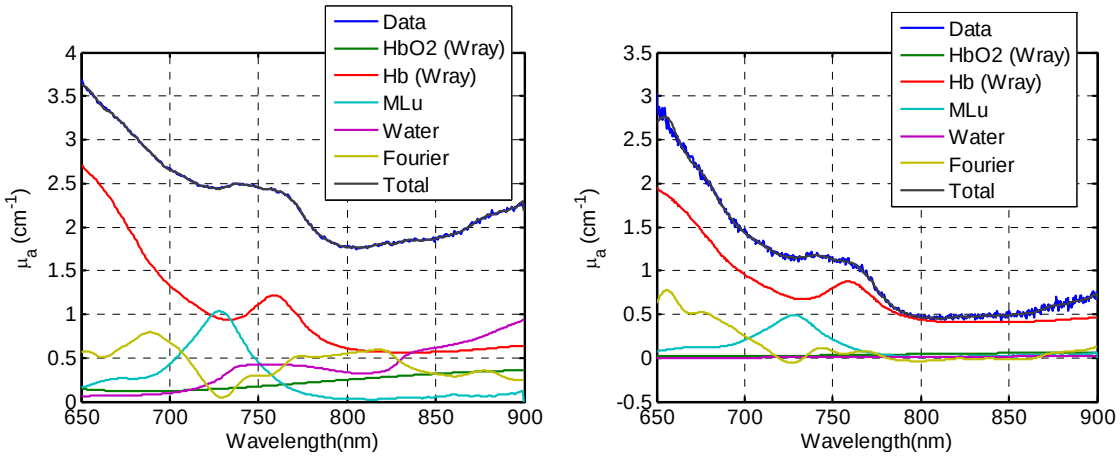

Figure 9: Plots of the fitted concentrations of hemoglobin, MLu, and water obtained from (a) diffuse fluence spectra alone, and (b) spectra with the incorporation of the single-wavelength optical properties data.

5. Fluorescence spectroscopy *in vivo*

The local concentration of sensitizer can also be measured *via* fluorescence spectroscopy (Ref. 6). We have developed a measurement technique to characterize the fluorescence of tissue using a side-firing fiber and the multichannel motorized positioner described above. A schematic of this device is shown in Fig. 10. The fluorescence system consists of an optical fiber terminated in a beveled end that emits and collects light at a right angle to its axis. This sidefiring fiber is connected to a dichroic beamsplitter that delivers 465-nm excitation light provided by a light-emitting diode (LED) to the fiber. The fluorescence excited by this light is then collected by the fiber and, by virtue of its longer wavelength, passes through the dichroic beamsplitter to the spectrograph and CCD.

The spectra captured by the CCD are analyzed using the same SVD algorithm used to analyze the absorption spectra described above. In this case, the basis spectra used are the inherent background fluorescence of the catheter and optical fiber and the fluorescence emission spectrum of MLu. The MLu fluorescence is corrected for variations in lamp intensity by dividing by the inherent background fluorescence and then scaled by an empirically determined value. A typical *in vivo* fluorescence spectrum is shown in figure 11. By moving the sidefiring fiber along its catheter, we can sample the distribution of MLu concentration within the prostate. The distributions in all four quadrants of a typical prostate are shown in figure 12. Profiles acquired before and after irradiation are shown. In general, the shape of the distribution dose not appears to change with irradiation, indicating that there is little redistribution of MLu during treatment.

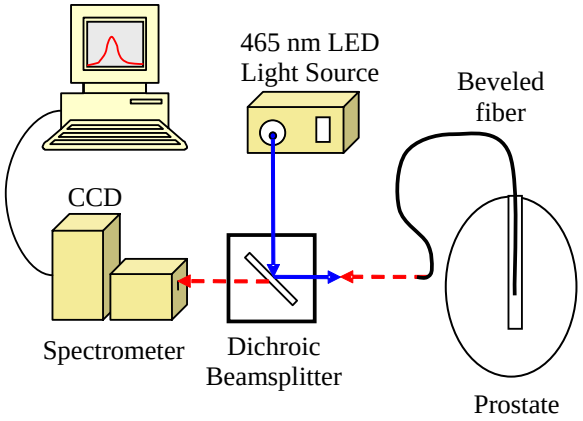

Figure 10: Fluorescence spectroscopy setup. The computer that acquires and stores fluorescence spectra also controls the position of the detection fiber *via* a step-motor positioner (not shown). The dichroic allows a single fiber to deliver excitation light and collect emitted fluorescence.

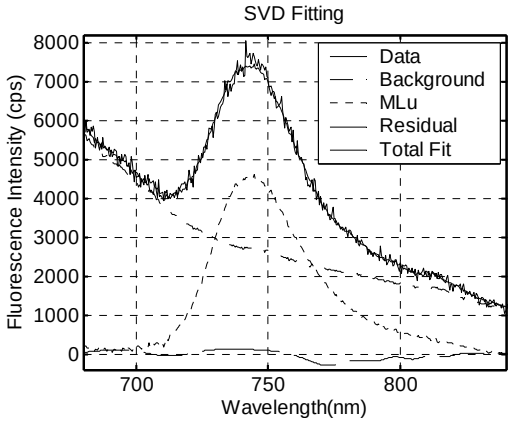

Figure 11: SVD analysis of a typical fluorescence emission spectrum. The spectrum is separated into MLu and background components and a small residual composed of a Fourier series.

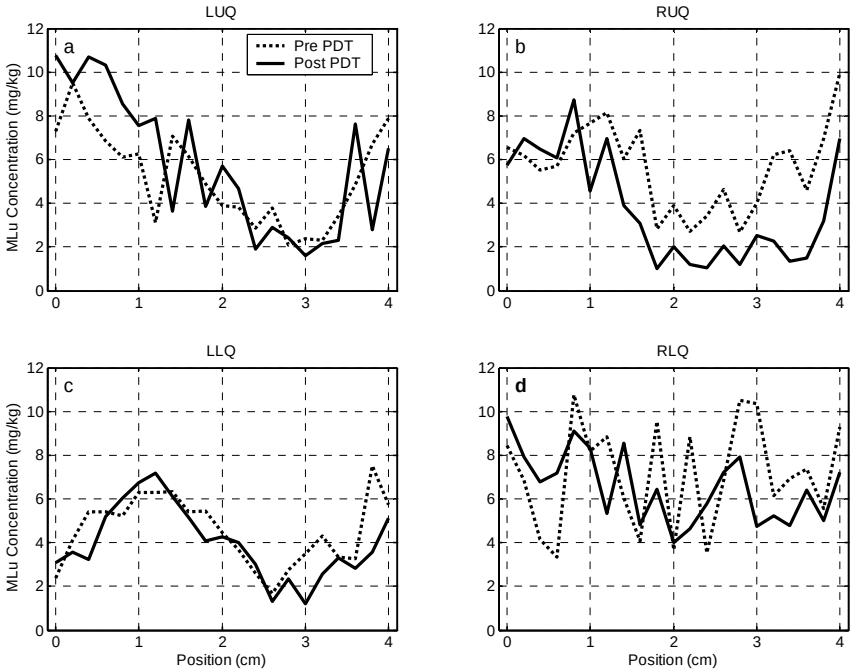

Figure 12: MLu fluorescence profiles acquired in the four quadrants of a single prostate before (dashed lines) and after (solid lines) PDT treatment. Frames a through d depict the results from the right upper, left upper, left lower, and right lower quadrants, respectively, as indicated in the panel titles.

We have described above three independent methods of obtaining MLu profiles *in vivo*, namely fluorescence spectroscopy, absorption spectroscopy, and single-wavelength absorption measurements. In one patient, we have obtained all three measurements in a single quadrant before and after PDT. The distributions obtained from this patient are shown in figure 13. The agreement in shape and amplitude among the three methods confirms that all three are sensitive to the same distribution. The single-wavelength and spectroscopic absorption measurements therefore provide verification of the accuracy of the MLu concentration measured by fluorescence spectroscopy.

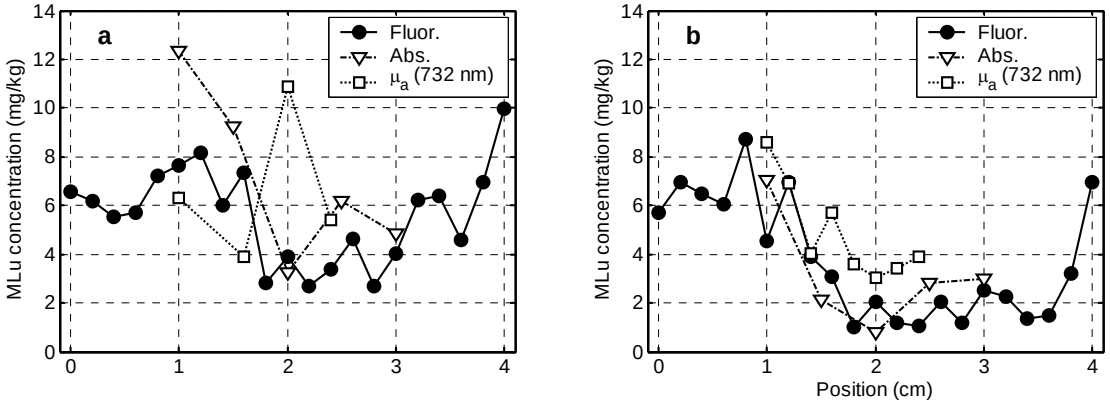

Figure 13: MLu fluorescence (filled circles), absorption spectroscopy (triangles), and 732-nm absorption (squares) profiles as functions of position within the right upper quadrant of patient #13. The profiles measured before (panel a) and after (panel b) PDT treatment are similar in shape, but indicate some photobleaching, especially in the center of the prostate.

Finally, we have, in addition to the three independent optical measurements described above, an independent measurement of tissue MLu concentration based on an *ex vivo* fluorescence analysis of tissue biopsies taken before and after PDT. As these biopsies are taken in only one position in the prostate, we cannot obtain a distribution of MLu from them, however we can compare the *ex vivo* measurement with the means of the values obtained from the three other methods. The results of this comparison for five patients are shown in figure 14. The four measurements agree remarkably well considering the heterogeneity obvious in the distributions shown in figure 13 and the variations among prostates.

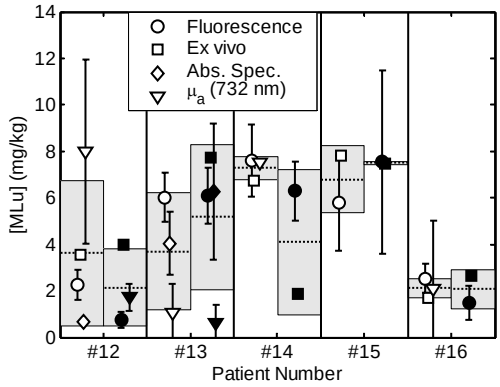

Figure 14: MLu concentration in 5 human prostates measured by fluorescence spectroscopy (circles), *ex vivo* fluoroscopy (squares), absorption spectroscopy (diamonds), and 732 nm absorption (triangles). Both pre-PDT (open symbols) and post-PDT data (filled symbols) are plotted. The dotted lines indicate the mean of all measurements in each patient, and the shaded areas include one standard deviation.

6. Development of treatment planning system for prostate PDT

A treatment planning system has been developed, which is composed of two sub-systems: image acquisition system and light-fluence-rate calculation system. The whole system is built in a personal

computer. Figure 15 shows the diagram of the system structure. Images are acquired from a transrectal ultrasound (TRUS) unit and are input into the computer in real time. The geometrical information of the prostate and the linear light sources is digitized and transferred into the calculation system. Three-dimensional (3D) geometry of the prostate and the light source arrangements are then reconstructed. With optical properties, calculation is carried out in the geometry to predict 3D light fluence rate distribution.

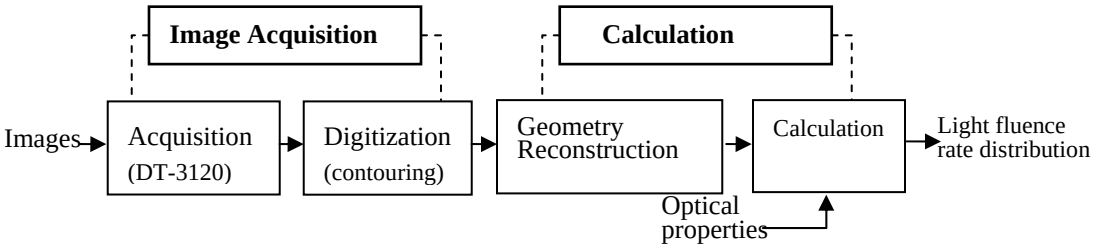

Figure 15: Diagram of treatment planning system.

A. Image acquisition system

An image frame grabber (DT-3120, Data Translation, Inc., MA) is installed in a computer and a Matlab-based software is developed to control the image acquisition. Figure 16(a) shows that ultrasound images of a prostate phantom are acquired into the system, and light source locations and organ contours are being delineated and digitized for planning. Fig. 16(b) shows the measurement of catheter locations (red circles), i.e., source and detector locations, in real time. Once the organ contours and catheter locations are determined, calculation can be carried out to predict the light fluence rate distribution.

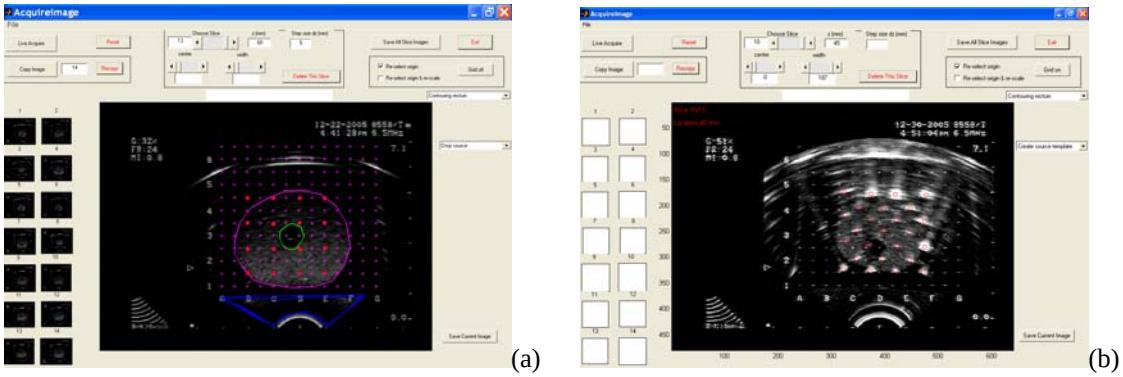

Figure 16: Interface of the image acquisition software. (a) Images of a prostate phantom are acquired and an image is delineated and digitized. (b) Actual catheter locations (red circles) are determined in real time.

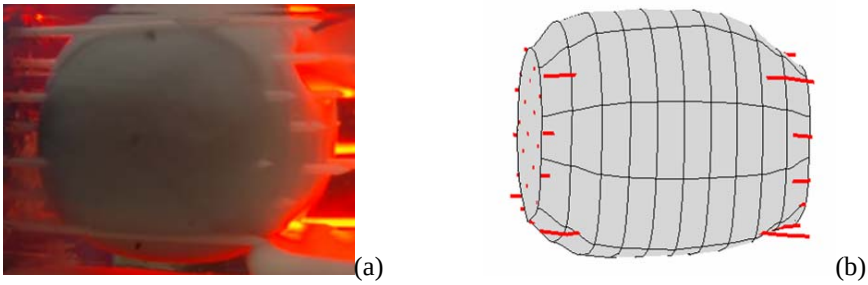

Figure 17: (a) Photograph of a prostate phantom in experiment. (b) Reconstructed geometry with linear light sources.

The system has been tested in phantom experiment and clinical cases. Figure 17(a) is photograph of a prostate phantom with linear light sources. Ultrasound images were acquired and delineated and were

used to reconstruct the phantom geometry. Figure 17(b) shows the reconstructed phantom and light source arrangement.

B. Light dose calculation system with engines dealing with optical heterogeneity

Initially we developed a homogeneous kernel model for light dose calculation in PDT, which can be applied in the situation where optical heterogeneity is not significant. Further we have developed two engines to calculate light dose in an optically heterogeneous prostate. One is finite-element method (FEM) based model and the other is kernel based model.

B1. FEM model in heterogeneous medium

The FEM model is based on the diffusion equation

$$-\nabla \cdot D\nabla\phi + \mu_a\phi = q, \qquad (2)$$

where ϕ is the light fluence rate, D $(=1/(3\mu_s'))$ is the diffusion coefficient (μ_s' is the scattering coefficient), q is the source strength, and μ_a is the absorption coefficient. Cylindrical diffusing fibers used in prostate PDT are modeled as linear sources using weak forms. Meshes are generated in 3D prostate geometry. Different boundary conditions between prostate and outside medium have been studied: Dirichlet boundary ($\phi = 0$), prostate-air boundary, prostate–nonscattering medium boundary, and prostate-tissue (scattering medium) boundary. Our study shows that the prostate-tissue boundary with refractive-index match is a proper boundary condition in prostate PDT. We use the boundary condition in FEM calculation.

The FEM model has been examined with experiments. Figure 18 shows comparison of FEM calculation with measurement in a heterogeneous phantom, which was composed of two media of different optical properties. A detector was scanned through the two media. Calculated fluence rates and measured fluence rates were compared along the scan line. The maximum, minimum, and mean deviations of the calculation results from the measurements are 33%, 1%, and 12%, respectively. Taking into account uncertainty in determining the distance between source and detector, we think the calculation agrees very well with the measurement.

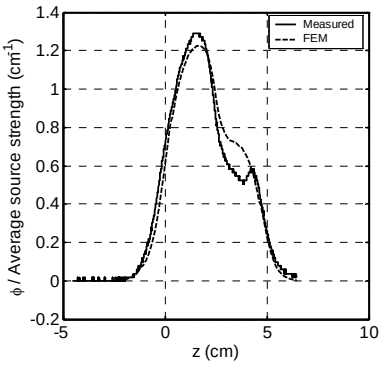

Figure 18. Comparison of FEM calculation with measurement in a heterogeneous phantom.

The FEM model has been applied to calculate light fluence rates in a patient prostate, which has heterogeneous optical properties. Figure 19(a) shows a surface plot of calculated light fluence rates in the prostate. The prostate geometry was reconstructed using transrectal ultrasound images. Figure 19(b) shows the isodose lines calculated using heterogeneous optical properties and homogeneous optical properties (μ_a = 0.3 cm^{-1} and μ_s' = 14 cm^{-1}) in a cross-section slice of the prostate. The calculation using homogeneous optical properties shows similar coverage as the calculation using measured heterogeneous optical properties except for a region in the upper part of the prostate, which has higher absorption. This indicates that the calculation using heterogeneous optical properties gives more accurate result. Figure 19(c) shows comparison of light fluence rates in the longitudinal direction of the prostate, between measurement and FEM calculations using homogeneous and heterogeneous optical properties, respectively. The comparison shows that the calculation using heterogeneous optical properties has better agreement with the measurement.

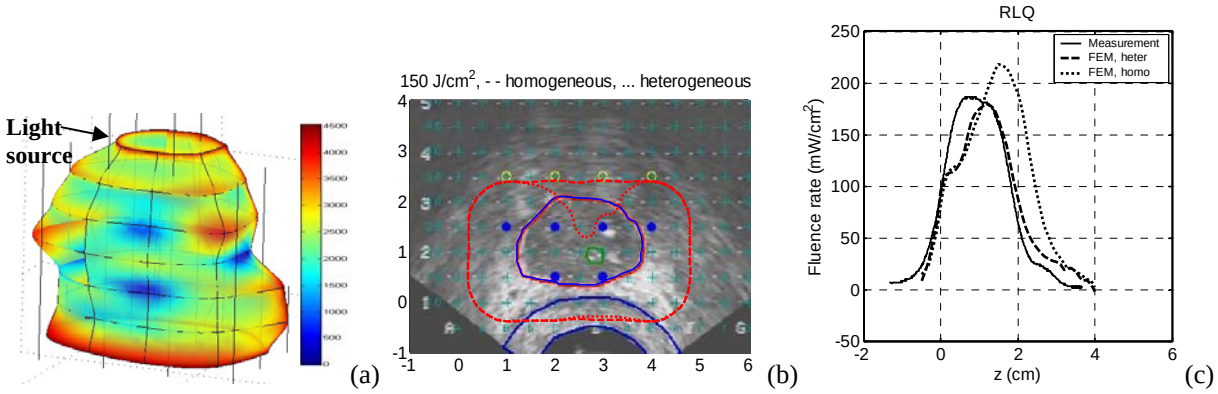

Figure 19: (a) Surface plot of light fluence rate calculated in a prostate. (b) Isodose lines in a slice; blue solid line: prostate contour; red dashed line: isodose line of the calculation using homogeneous optical properties; red dotted line: isodose line of the calculation using heterogeneous optical properties. (c) Comparison of light fluence rates in a quadrant (RLQ) between measurement and FEM calculations using measured heterogeneous optical properties and homogeneous optical properties (μ_a =0.3 cm^{-1} and μ_s' =14 cm^{-1}), respectively.

B2. Kernel model in heterogeneous medium

The kernel model for heterogeneous medium is developed based on a homogeneous kernel model we proposed before. The fluence rate detected at distance *r* from a point source of strength *S* is expressed as

$$\phi = \frac{S \cdot e^{-\int_0^r \mu_{eff}(r')dr'}}{4\pi r \overline{D}}, \qquad (3)$$

where $\overline{D} = \int_0^\infty \mu_a(r) e^{-\int_0^r \mu_{eff}(r')dr'} dr$, and μ_{eff} is the effective attenuation coefficient. Different from the homogeneous model, where $\phi = \frac{3\mu_s'(0) \cdot S \cdot e^{-\mu_{eff}(0) \cdot r}}{4\pi r}$, optical properties are no longer assumed to be homogeneous in this model. Heterogeneously distributed optical properties are taken into account in the calculation by the integral terms. For a linear source, which is considered as composed of multiple (e.g., *N*) segmental sources, the fluence rate is

$$\phi = \sum_{i=1}^{N} \frac{s_i \cdot \Delta x_i \cdot e^{-\int_0^{r_i} \mu_{eff}(r')dr'}}{4\pi r_i \overline{D}}, \qquad (4)$$

where s_i is the source strength of the *i*th segment along the linear light source, Δx_i is the division along the direction parallel to the orientation of the linear source, and r_i is the distance between the source segment and the detector. The summation in the equation is over all the segments composing the linear source.

We have examined kernel calculation by comparing it with FEM calculation, which we take as standard. Figure 20(a) shows comparison of light fluence rates calculated using FEM model and kernel model, respectively, in a quadrant of a patient prostate. Heterogeneous optical properties measured in the patient were used in the calculations. For comparison, the result obtained using a homogeneous kernel model is also presented, which used the mean optical properties of that quadrant. Compared to the result of the homogeneous model, the heterogeneous model gives better result. The histogram of the deviation of the heterogeneous kernel result from the FEM result is shown in Fig. 20(b). The maximum deviation and mean deviation are 27% and 17%, respectively. The results show that the heterogeneous kernel calculation is close to the FEM calculation.

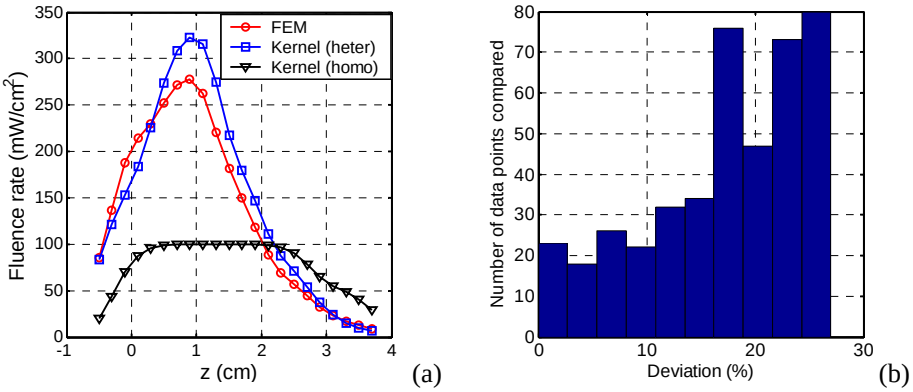

Figure 20: (a) Comparison of light fluence rates calculated using FEM model, heterogeneous kernel model, and homogeneous kernel model. (b) Histogram of the deviation of the fluence rate calculated using the heterogeneous kernel model from the FEM model.

B3. Conclusions

We have developed two models for light dose calculation in heterogeneous prostate. The two models have their particular advantages. The FEM calculation is more accurate and the kernel calculation is faster, for example, seconds *vs* ~hundreds of seconds. The FEM calculation can be applied in situations where boundary effects are significant and can be applied to verify the kernel calculation results. And the kernel calculation can be applied to real-time treatment planning and optimization.

7. Develop optimization methods for weights and placements of the light sources to achieve uniform PDT dose in the prostate gland

To deliver uniform photodynamic therapy (PDT) dose to the prostate gland, it is necessary to develop algorithms that optimize the locations and strengths (power × exposure times, in units of Joule) of the light sources. Since tissue optical properties may change with time, rapid (almost real-time) optimization is desirable. We evaluated the use of the Cimmino feasibility algorithms for this purpose because it is fast, linear, and always converges reliably. PDT for the prostate is performed with cylindrical diffusing fibers (CDF) of various lengths inserted perpendicular to a base plate to obtain longitudinal coverage by a matrix of parallel catheters. The standard plan for the protocol uses equal unit-length source strength and equal spaced (1-cm) loading. We have developed several search procedures to aid the user in choosing the positions, lengths, and intensities of the CDFs. The Cimmino algorithm can be used in these procedures to determine the strengths of the light sources at each step of the iterative selection process. Maximum and minimum bounds for allowed doses to the sample points in four volumes (prostate, urethra, rectum, and background) constrained the solutions for the strengths of the linear light sources. Uniform optical properties were assumed. Compared with the standard plan, our algorithm was shown to quickly produce a plan in real time that covered the planned target volume (PTV) and spared the urethra and rectum.

We have studied three kinds of problems.(Ref. 7) (1) Cimmino 1: Given cylindrical diffusing fibers (CDFs) with every quantity specified, namely, the number of CDFs, the template slots, the source lengths, and the retractions of the CDF into the slot, find the source strengths (emitted power multiplied by duration of illumination [J]) to satisfy the prescribed dose constraints. (2) Cimmino 2 (or 3): Given only the number of CDFs and the allowed set of template slots, find the particular source slots, source parameters, and source strengths that are optimal. (3) Cimmino 4: Given the number and locations of the source slots, find the optimal source parameters (source lengths and retractions) and source strengths. The only difference between Cimmino 2 and 3 is the different constraints for the rectum.

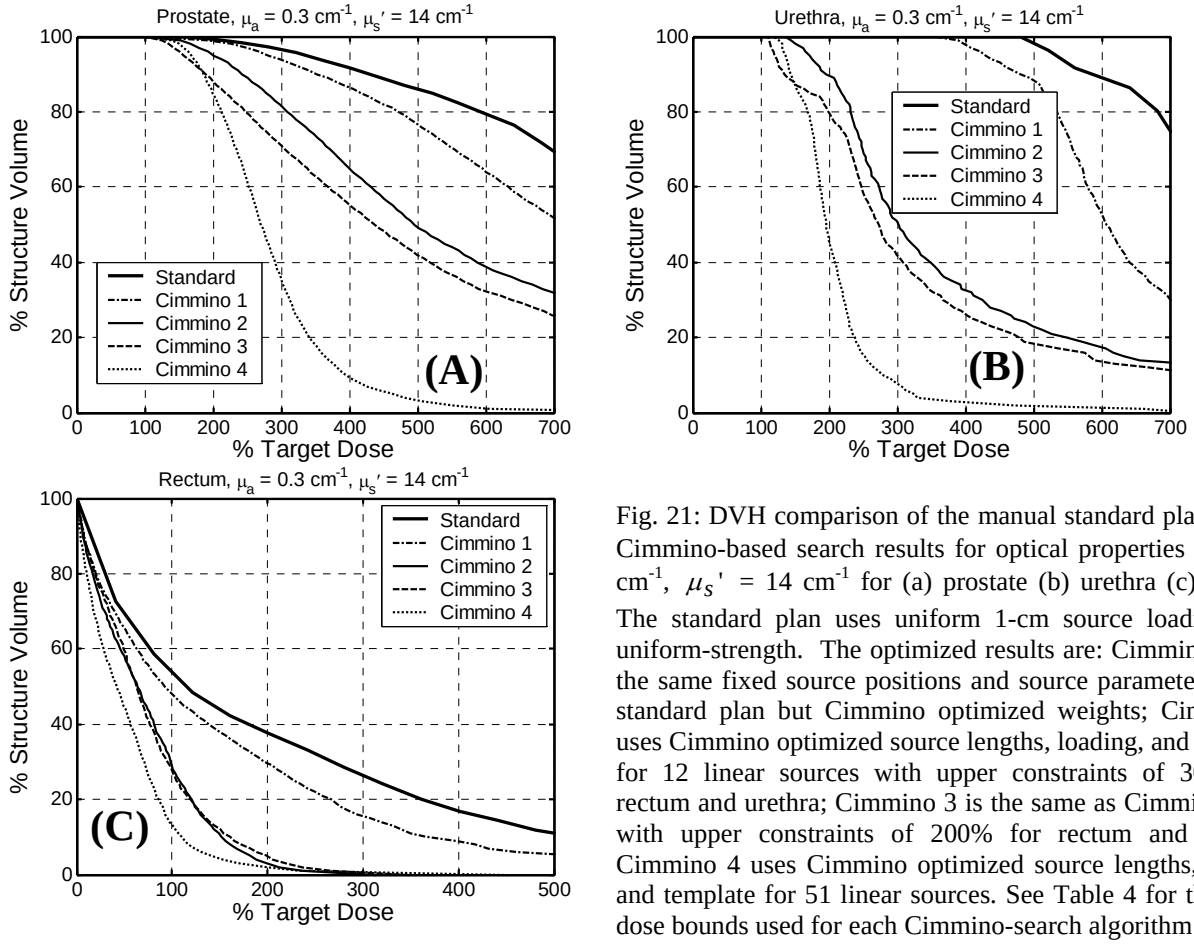

Fig. 21: DVH comparison of the manual standard plan vs. the Cimmino-based search results for optical properties μ_a = 0.3 cm^{-1}, μ_s' = 14 cm^{-1} for (a) prostate (b) urethra (c) rectum. The standard plan uses uniform 1-cm source loading with uniform-strength. The optimized results are: Cimmino 1 uses the same fixed source positions and source parameters as the standard plan but Cimmino optimized weights; Cimmino 2 uses Cimmino optimized source lengths, loading, and template for 12 linear sources with upper constraints of 300% for rectum and urethra; Cimmino 3 is the same as Cimmino 2 but with upper constraints of 200% for rectum and urethra; Cimmino 4 uses Cimmino optimized source lengths, loading and template for 51 linear sources. See Table 4 for the upper dose bounds used for each Cimmino-search algorithm

We have compared the dose-volume histograms (DVHs) obtained in the standard plan, i.e., the case of uniform source strength with all source slots and parameters specified, which is the present practice in the clinic, with those obtained in Cimmino 1, Cimmino 2, Cimmino 3, and Cimmino 4. Figure 10 shows the DVHs for the average optical properties (μ_a = 0.3 cm^{-1} and μ_s' = 14 cm^{-1}), in which dosimetric improvement is observed in the above order. Cimmino 1, which optimizes the source strength only, did not provide significant improvement over the standard plan. Cimmino 4 which had sufficient number (51) of CDFs to cover the entire prostate gave the best DVH, although it is clinically impractical to use so many sources. The DVH for Cimmino 4 represents the best possible mathematical solution. Cimmino 2 and 3, which optimized the source locations, showed substantial improvements over the standard plan, not only for the coverage of the target (prostate) but also for the dose reduction of the urethra and rectum. Cimmino 3, which used 200% upper constraint for rectum, gave better results than Cimmino 2, which used 300% upper constraint for rectum.

Our study has shown that significant sparing of the urethra and rectum could be implemented with the optimization algorithm. The combined selection of positions, lengths, and strengths of interstitial light sources could improve the outcome. Compared with the standard plan, our algorithm has been shown to quickly produce a plan in real time that covered the planned target volume (PTV) and spared the urethra and rectum. The clinical implication of our findings is that changes in the treatment plan may be made in the operating room before and during PDT to optimize light delivery. The calculation time is always less than 300 s (see Table 2 in Appendix 5, Ref. 6).

8. Develop a 12-way beamsplitter system for light delivery

We have developed a 12-channel beamsplitter (shown in Fig. 22). This beamsplitter has an overall efficiency of > 60% and can tolerate at least 15W of incident laser power, thus allowing us to deliver light to 12 channels simultaneously.

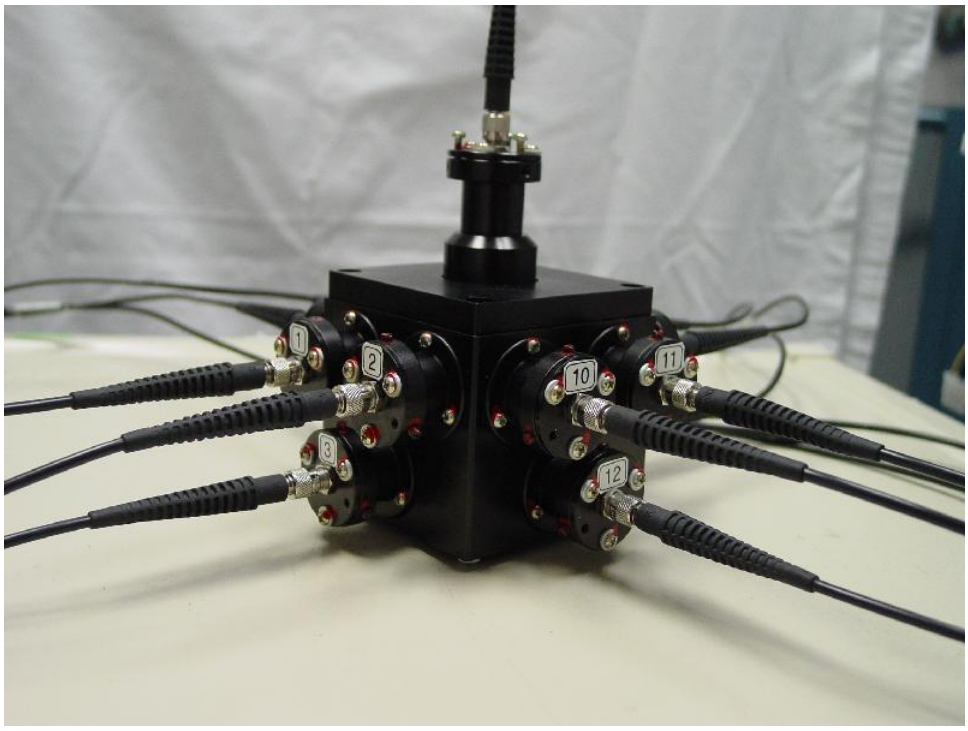

Figure 22: Optical Component of a 12-way beamsplitter system for light delivery

The 12 output channels of the beamsplitter are connected to motorized variable attenuators from OZ Optics. The output of each channel is controlled by PC to preset power levels.

KEY RESEARCH ACCOMPLISHMENTS

1. **Completion of characterization of tissue optical properties in vivo in human prostate.**
2. **Development of instrument for absorption spectra interstitially.**
3. **Completion of the development of a 16-channel in-vivo dosimetry system.**
4. **Completion of comparison between measurement and calculation in prostate in-vivo assuming homogeneous optical properties.**
5. **Development of instrument for fluorescence spectra interstitially.**
6. **Completion of the optimization algorithm for light source weights, locations, and lengths.**
7. **Development of instrument for measuring distribution of optical properties, MLu concentration, and StO_2 *in vivo* and characterization of measurement uncertainty of the instrument.**
8. **Completion of computerized beamsplitter system for linear-source light delivery.**

REPORTABLE OUTCOMES

Peer-reviewed Journals

1. Zhu TC, Dimofte A, Finlay JC, Stripp D, Busch T, Miles J, Whittington R, Malkowicz SB, Tochner Z, Glatstein E, Hahn SM, "Optical properties of Human Prostate at 732nm Measured in vivo during motexafin lutetium-mediated photodynamic therapy," Photochem photobiol. 81: 96-105 (2005).

2. Zhu TC, Finlay JF, Hahn SM, "Determination of the distribution of light, optical properties, drug concentration, and tissue oxygenation in-vivo in human prostate during motexafin lutetium-mediated photodynamic therapy". J. Photochem Photobiol B. 79:231-241 (2005)
3. Dimofte A, Finlay JC, Zhu TC, "A method for determination of the absorption and scattering properties interstitially in turbid media," Phys Med Biol 50 2291-2311 (2005).
4. Altschuler MD, Zhu TC, Jun Li, Hahn SM, "Optimized Interstitial PDT Prostate treatment Planning with the Cimmino Feasibility Algorithm," Med Phys 32: 3524-3536 (2005).
5. Finlay J, Zhu T, Dimofte A, Stripp D, Malkowicz S, Busch T, Hahn S, "Interstitial fluorescence spectroscopy in the human prostate during motexafin lutetium-mediated photodynamic therapy," Photochem photobiol 82: available on line, PMID: 16808592 (2006).
6. Zhu TC and Finlay JC, "Prostate PDT dosimetry," Photodiagnosis and Photodynamic Therapy, 3, (in press, 2006).

Conference Proceedings

1. Finlay JC, Zhu TC, Dimofte A, Stripp D, Malkowicz SB, Whittington R, Miles J, Glatstein E, Hahn SM, "In vivo determination of the absorption and scattering spectra of the human prostate during photodynamic therapy," Proc. SPIE 5315:132-142 (2004).
2. Zhu TC, JC Finlay, Dimofte A, Hahn SM, "Light Dosimetry at Tissue Surfaces for Oblique Incident Circular fields," Proc. SPIE 5315:113-124 (2004).
3. Finlay JC, Zhu TC, Dimofte A, Stripp D, Malkowicz SB, Whittington R, Miles J, Glatstein E, Hahn SM, "*In vivo* measurement of fluorescence emission in the human prostate during photodynamic therapy", Proc SPIE 5689:299-310 (2005)
4. Altschuler MD, Zhu TC, Jun Li, Hahn SM, "Optimization of light sources for prostate photodynamic therapy," Proc. SPIE 5689:186-197 (2005).
5. Zhu TC, Dimofte A, Finlay JC, Glatstein E, Hahn SM, "Detector Calibration factor for interstitial in-vivo light dosimetry using isotropic detectors with scattering tip," Proc. SPIE 5689:174-185 (2005).
6. Zhu TC, Li J, Finlay JC, Dimofte A, Stripp D, Malkowicz BS, Hahn SM, "In-vivo light dosimetry of interstitial PDT of human prostate," Proc. SPIE 6139:61390L 1-11 (2006).
7. Li J, Zhu TC, Finlay JC, "Study of light fluence rate distribution in photodynamic therapy using finite-element method," Proc. SPIE 6139:61390M 1-8 (2006).

Peer-reviewed Abstracts

1. Hahn SM, Zhu TC, Whittington R, Mick R, Tochner Z, Busch TM, Shin D, Smith D, Dimofte A, Miles J, Glatstein E, Malkowicz SB, "A Phase I trial of motexafin lutetium-mediated photodynamic therapy in patients with prostate cancer," IPA 9th World Congress of Photodynamic Medicine, (2003).
2. Zhu TC, Diana S, Dimofte A, Whittington R, Tochner ZA, Malkowicz BS, Glatstein E, Hahn SM, "In vivo optical property of human prostate before and after motexafin lutetium-mediated photodynamic therapy," IPA 9th World Congress of Photodynamic Medicine, (2003).
3. Zhu TC, Altschuler M, Xiao Y, Finlay J, Dimofte A, Hahn SM, "Light Dose calculation and Optimization for Prostate Photodynamic therapy," Med Phys 30:1336 (2003).
4. Finlay J, Dimofte A, and Zhu TC, "A motorized probe for quick determination of tissue optical properties," Med Phys 30:1436 (2003).
5. Dimofte A, Zhu T, Finlay J "A Novel device for determination of the absorption and scattering properties of tissue simulating phantom," Med Phys 31: 1857 (2004).
6. Li J, Altschuler MD, Zhu TC, Hahn SM, "Optimization of treatment plan using Cimmino algorithm in prostate photodynamic therapy," IPA 10th World Congress of Photodynamic Medicine, Munich, Germany (2005).
7. Zhu TC, Finlay JC, Dimofte A, Li J, Altschuler MD, Stripp D, Hahn SM, "An integrated system for interstitial photodynamic therapy (PDT)," IPA 10th World Congress of Photodynamic Medicine, Munich, German (2005).

8. Zhu TC, Finlay JC, Dimofte A, Li J, Hahn SM, "Distribution of optical properties during human prostate photodynamic therapy," IPA 10th World Congress of Photodynamic Medicine, Munich, German (2005).
9. Li J, Zhu TC, Finlay JC, "Prediction of light fluence rate in-vivo for prostate photodynamic therapy," IPA 10th World Congress of Photodynamic Medicine, Munich, German (2005).
10. Finlay JC, Dimofte A, Zhu TC, Stripp D, Hahn SM, "Comparison of absorption and fluorescence spectroscopy of the human prostate in vivo," IPA 10th World Congress of Photodynamic Medicine, Munich, German (2005).
11. Li J and Zhu TC, "A kernel-based Model for light fluence calculation in prostate photodynamic therapy," Med Phys 32:2162 (2005).
12. Li J and Zhu T, "Real-time Treatment Planning System for Prostate Photodynamic Therapy," Med Phys 33: 2133 (2006).
13. Zhou X, Zhu T, Hahn S, and Pogue B, "Reconstruction of Spatially Varying Optical Properties of Human Prostate During Metexafin Lutetium PDT," Med Phys 33: 2273 (2006).
14. Dimofte A, Zhu T, and Finlay J, "Dosimetry for Linear Sources in Heterogeneous Prostate Phantom," Med Phys 33:2094 (2006).

CONCLUSIONS

We have completed all specific aims of the project. **Specific aim 1** is characterization of optical properties in vivo in human prostate at 732nm. We have developed motorized probe and associate software to perform this task. In human prostate, we have shown that the effective attenuation coefficient μ_{eff} varied between 0.91–6.7 cm^{-1} (mean 2.9 ± 0.8 cm^{-1}), corresponding to an optical penetration depth ($\delta = 1/\mu_{eff}$) of 0.2–1.1 cm (mean 0.4 ± 0.1 cm). **Specific aim 2** is light dose calculation and comparison with in-vivo dosimetry. We have made comparison with 14 patients and have shown improved accuracy (within 20%) with several algorithms, e.g., kernel and finite-element methods. **Specific aim 3** is characterization of photosensitizer drug concentration. We have improved the motorized probe and associate software to measure the distribution of optical properties, drug concentration, and StO_2 interstitially. We have developed a fluorescence technique to measure *in-vivo* phototosensitizer distribution interstitially in patients and have verified its accuracy using the absorption spectra. **Specific aim 4** is to develop optimization methods for placement of the light source to achieve uniform PDT dose in the prostate gland. We developed the software to automatically optimize the light source weights, lengths, strengths in near real-time to improve the light fluence rate distribution in prostate and spare dose to critical structures. In addition, we have developed a 12-channel beamsplitter with motorized attenuators for light delivery. Our measurements demonstrate heterogeneity in both the optical properties and the photosensitizer distribution. Thus, we concluded that it is necessary to determine the 3D distribution of optical properties and drug concentration in order to optimize the PDT dose distribution for each individual patient.

REFERENCES

1. Zhu TC, Dimofte A, Finlay JC, Stripp D, Busch T, Miles J, Whittington R, Malkowicz SB, Tochner Z, Glatstein E, Hahn SM, "Optical properties of Human Prostate at 732nm Measured in vivo during motexafin lutetium-mediated photodynamic therapy," Photochem photobiol. 81: 96-105 (2005).

2. Zhu TC, Finlay JF, Hahn SM, "Determination of the distribution of light, optical properties, drug concentration, and tissue oxygenation in-vivo in human prostate during motexafin lutetium-mediated photodynamic therapy". J. Photochem Photobiol B. 79:231-241 (2005)

3. Dimofte A, Finlay JC, Zhu TC, "A method for determination of the absorption and scattering properties interstitially in turbid media," Phys Med Biol 50 2291-2311 (2005).

4. Zhu TC, Li J, Finlay JC, Dimofte A, Stripp D, Malkowicz BS, Hahn SM, “In-vivo light dosimetry of interstitial PDT of human prostate,” Proc. SPIE 6139:61390L 1-11 (2006).
5. Finlay JC, Zhu TC, Dimofte A, Stripp D, Malkowicz SB, Whittington R, Miles J, Glatstein E, Hahn SM, “In vivo determination of the absorption and scattering spectra of the human prostate during photodynamic therapy,” Proc. SPIE 5315: 132-142 (2004).
6. Finlay J, Zhu T, Dimofte A, Stripp D, Malkowicz S, Busch T, Hahn S, “Interstitial fluorescence spectroscopy in the human prostate during motexafin lutetium-mediated photodynamic therapy,” Photochem photobiol 82: available on line, PMID: 16808592 (2006).
7. Altschuler MD, Zhu TC, Jun Li, Hahn SM, “Optimized Interstitial PDT Prostate treatment Planning with the Cimmino Feasibility Algorithm,” Med Phys 32: 3524-3536 (2005).

LIST OF PERSONNEL

1. Timothy C. Zhu, Ph.D., PI, 23%
2. Stephen M. Hahn, MD, Co-PI, 2%
3. Jun Li, PhD., Postdoctoral fellow, 100%

APPENDICES

1. Zhu TC, Dimofte A, Finlay JC, Stripp D, Busch T, Miles J, Whittington R, Malkowicz SB, Tochner Z, Glatstein E, Hahn SM, "Optical properties of Human Prostate at 732nm Measured in vivo during motexafin lutetium-mediated photodynamic therapy," Photochem photobiol. 81: 96-105 (2005).
2. Zhu TC, Finlay JF, Hahn SM, "Determination of the distribution of light, optical properties, drug concentration, and tissue oxygenation in-vivo in human prostate during motexafin lutetium-mediated photodynamic therapy". J. Photochem Photobiol B. 79:231-241 (2005)
3. Dimofte A, Finlay JC, Zhu TC, "A method for determination of the absorption and scattering properties interstitially in turbid media," Phys Med Biol 50 2291-2311 (2005).
4. Finlay J, Zhu T, Dimofte A, Stripp D, Malkowicz S, Busch T, Hahn S, "Interstitial fluorescence spectroscopy in the human prostate during motexafin lutetium-mediated photodynamic therapy," Photochem photobiol 82: available on line, PMID: 16808592 (2006)
5. Altschuler MD, Zhu TC, Jun Li, Hahn SM, "Optimized Interstitial PDT Prostate treatment Planning with the Cimmino Feasibility Algorithm," Med Phys 32: 3524-3536 (2005).

Photochemistry and Photobiology, 2005, 81: 96–105

Optical Properties of Human Prostate at 732 nm Measured *In Vivo* During Motexafin Lutetium–mediated Photodynamic Therapy¶

Timothy C. Zhu*[1], Andreea Dimofte[1], Jarod C. Finlay[1], Diana Stripp[1], Theresa Busch[1], Jeremy Miles[1], Richard Whittington[1], S. Bruce Malkowicz[2], Zelig Tochner[1], Eli Glatstein[1] and Stephen M. Hahn[1]

[1]Department of Radiation Oncology, University of Pennsylvania, Philadelphia, PA
[2]Department of Urology, University of Pennsylvania, Philadelphia, PA

Received 25 June 2004; accepted 8 November 2004

ABSTRACT

Characterization of the tissue light penetration in prostate photodynamic therapy (PDT) is important to plan the arrangement and weighting of light sources so that sufficient light fluence is delivered to the treatment volume. The optical properties (absorption [μ_a], transport scattering [μ_s'] and effective attenuation [μ_{eff}] coefficients) of 13 patients with locally recurrent prostate cancer were measured *in situ* using interstitial isotropic detectors. Measurements were made at 732 nm before and after motexafin lutetium (MLu)–mediated PDT in four quadrants. Optical properties were derived by applying the diffusion theory to the fluence rates measured at several distances (0.5–5 cm) from a point source. μ_a and μ_s' varied between 0.07 and 1.62 cm^{-1} (mean 0.37 ± 0.24 cm^{-1}) and 1.1 and 44 cm^{-1} (mean 14 ± 11 cm^{-1}), respectively. μ_a was proportional to the concentration of MLu measured by an *ex vivo* fluorescence assay. We have observed, on average, a reduction of the MLu concentration after PDT, presumably due to the PDT consumption of MLu. μ_{eff} varied between 0.91 and 6.7 cm^{-1} (mean 2.9 ± 0.7 cm^{-1}), corresponding to an optical penetration depth ($\delta = 1/\mu_{eff}$) of 0.1–1.1 cm (mean 0.4 ± 0.1 cm). The mean penetration depth at 732 nm in human prostate is at least two times smaller than that found in normal canine prostates, which can be explained by a four times increase of the mean value of μ_s' in human prostates. The mean light fluence rate per unit source strength at 0.5 cm from a point source was 1.5 ± 1.1 cm^{-2}, excluding situations when bleeding occurs. The total number of measurements was N = 121 for all mean quantities listed above. This study showed significant inter- and intraprostatic differences in the optical properties, suggesting that a real-time dosimetry measurement and feedback system for monitoring light fluences during treatment should be considered for future PDT studies.

INTRODUCTION

Photodynamic therapy (PDT) is a treatment modality using light of an appropriate wavelength in the presence of oxygen to activate a photosensitizing drug, which then causes localized cell death or tissue necrosis. Using a surface illumination technique, PDT has been used to treat superficial tumors, including those of the skin, lung, esophagus and bladder (1). This technique is, however, inadequate when applied to large bulky tumors or solid organs because of limited light penetration into tissue. Interstitial light delivery, wherein optical fibers are placed directly into bulky tumors or organs, is a more rational approach in these cases.

The prostate gland is an organ that appears to be a good target for interstitial PDT. Tumors of the prostate are often confined to the prostate itself, and brachytherapy techniques used for the placement of radioactive seed implants can be adapted for the placement of interstitial optical fibers (2). Several preclinical studies have evaluated the feasibility of delivering PDT to the prostate via this interstitial approach (3–8). A trial of interstitial prostate PDT in humans has been reported by Nathan *et al*. (9), who treated 14 men with locally recurrent prostate cancer using *meso*-tetrahydroxyphenyl chlorin–mediated interstitial PDT. The light treatment was directed toward regions from which biopsies showed cancer or which were suspicious on imaging studies. Because prostate cancer is a multifocal disease, our PDT protocol is designed to ablate the prostate gland completely. The development of a light delivery technique appropriate to this goal has necessitated an improved understanding of light dosimetry, which is critical in planning the configuration of multiple fibers within the organ or tumor.

Several investigators have attempted to characterize the optical properties of prostate tissue in animals (10–12) and in humans (13–15) to predict light dosimetry more reliably. Using diffusion theory for a point source, the absorption (μ_a) and transport scattering (μ_s') coefficients of a particular tissue can be determined yielding the effective attenuation coefficient (μ_{eff}), which provides a measure of light penetration in that tissue (11). This measurement is a critical factor in planning interstitial light source placement. The optical properties of prostate tissue have been most extensively evaluated at a wavelength of 630 nm because it is used to activate the most widely used photosensitizer, Photofrin. However, it has been suggested that a wavelength of 630 nm is suboptimal in achieving uniform and

¶Posted on the website on 9 November 2004.
*To whom correspondence should be addressed: Department of Radiation Oncology, University of Pennsylvania, 3400 Spruce Street/2 Donner, Philadelphia, PA 19104, USA. Fax: 215-662-4043; e-mail: tzhu@mail.med.upenn.edu

Abbreviations: CDF, cylindrical diffusing fiber; LLQ, left lower quadrant; LUQ, left upper quadrant; MLu, motexafin lutetium; PDT, photodynamic therapy; RLQ, right lower quadrant; RUQ, right upper quadrant; TRUS, transrectal ultrasound; μ_a, absorption coefficient; μ_{eff}, effective attenuation coefficient; μ_s', transport scattering coefficient.

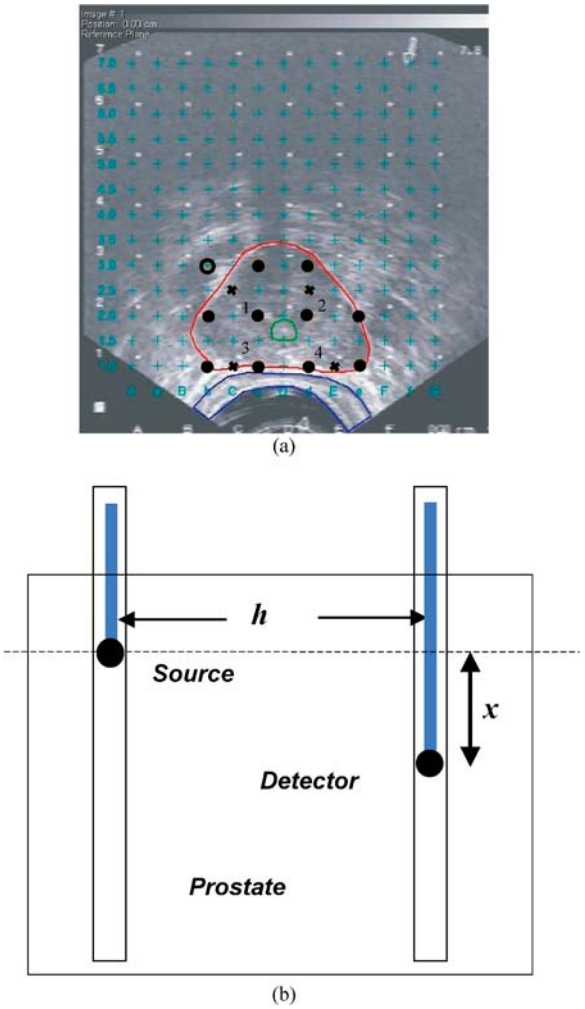

Figure 1. (a) Transrectal ultrasound image of a human prostate, showing the position of source (closed circle) and detector (x) fibers. The source positions labeled 1, 2, 3 and 4 were used for optical properties measurement for the RUQ, LUQ, RLQ and LLQ, respectively, with the detector placed in a separate catheter in each quadrant. The open circle on the right upper quadrant is for a linear source that passed through the position but is too short to have active light component in the cross-section plane. The grid on the template (''+'') is 0.5 cm apart. (b) Schematic of the measurement geometry, illustrating the coordinates used to determine the source–detector distance.

adequate penetration due to the absorption of light by naturally occurring chromophores, such as hemoglobin, melanins, cytochromes and flavoproteins, at that wavelength (10,15). In addition, changing concentrations of hemoglobin (in particular deoxyhemoglobin) during PDT may also alter the optical properties of tissues (11). As a result, Arnfield *et al*. (10) investigated the use of longer wavelengths of light beyond the absorption bands of these naturally occurring molecules. A comparison between 630 and 789 nm light revealed a consistent and substantial increase in light penetration with the 789 nm light.

Based on a feasibility and toxicity study in a canine prostate model (7), we have started a Phase I study of motexafin lutetium (MLu)–mediated PDT for prostate cancer. MLu is a water-soluble, second-generation synthetic photoactive drug that has a Q-band absorption peak at 732 nm (16,17). In this study we evaluated the optical properties of the human prostate by illuminating it with a point source emitting 732 nm light. Differences in optical properties were compared before and after PDT in which the entire prostate was treated. Intraprostatic as well as interprostatic differences were evaluated.

Table 1. Distribution of patients for measurements of optical properties. The number in parentheses is the number of valid measurements that is not affected by bleeding

Patient number	MLu dose (mg/kg)	Drug-treatment interval (h)	Light fluence (J/cm^2)	No. measured before PDT	No. measured after PDT	Optical properties along a catheter?
2	0.5	24	25	4 (1)	4 (1)	No
3	0.5	24	25	4 (1)	1 (1)	No
4	1	24	25	4 (3)	1 (1)	No
5	1	24	25	4 (1)	1 (1)	No
6	1	24	25	3 (2)	3 (2)	No
7	1	6	25	4 (0)	4 (2)	No
8	2	6	25	4 (0)	4 (0)	No
9*	2	6	50	7 (6)	7 (7)	No
10*	2	6	100	8 (6)	7 (5)	No
11*	2	3	25	8 (7)	7 (5)	No
12*	2	3	50	21 (20)	9 (7)	Yes
13*	2	3	100	28 (20)	20 (20)	Yes
14*	2	3	100	29 (2)	29 (0)	Yes

*Measurements made with a motorized probe.

MATERIALS AND METHODS

Patient selection, surgical and PDT procedure. A Phase I clinical trial of MLu-mediated PDT in patients with locally recurrent prostate carcinoma was initiated at the University of Pennsylvania. The protocol was approved by the Institutional Review board of the University of Pennsylvania, the Clinical Trials and Scientific Monitoring Committee of the University of Pennsylvania Cancer Center and the Cancer Therapy Evaluation Program of the National Cancer Institute. A total of 14 patients were treated, of which 13 patients have undergone measurement of optical properties. Each patient who signed the informed consent document underwent an evaluation, which included magnetic resonance imaging of the prostate, bone scan, laboratory studies including prostatic specific antigen and a urological evaluation. Approximately 2 weeks before the scheduled treatment, a transrectal ultrasound (TRUS) was performed for treatment planning. An urologist drew the target volume (the prostate) on each slice of the ultrasound images. These images were spaced 0.5 cm apart and were scanned with the same ultrasound unit used for treatment. A built-in template with a 0.5 cm grid projected the locations of possible light sources relative to the prostate. A treatment plan was then prepared to determine the location and length of light sources. Cylindrical diffusing fibers (CDF) with active lengths of 1, 2, 3, 4 and 5 cm were used as light sources. The sources were spaced 1 cm apart, and the light power per unit length was less than or equal to 150 mW/cm^2 for all optical fibers. The length of the CDF at a particular position within the prostate was selected to cover the full length of the prostate (see Fig. 1a). The final plan often required that the prostate be divided into four quadrants. Four isotropic detectors were used, each placed in the center of one quadrant. A fifth isotropic detector was placed in a urethral catheter to monitor the light fluence in the urethra.

MLu was administered intravenously to patients at various times before light delivery (depending on the dose level). In the initial six patients, MLu was delivered 24 h before light delivery. The drug-treatment interval and dose of MLu were subsequently changed according to a predetermined scheme dictated by the protocol. The drug-treatment interval and the amount of MLu for the latest patients were 3 h and 2 mg/kg, respectively (see Table 1).

The patients were anesthetized in the operating room with general anesthesia to minimize patient movement during the procedure. TRUS-guided biopsies for MLu measurements were obtained before light delivery. The ultrasound unit was used to guide needle placement in the operating room. A template was attached to the ultrasound unit and was matched to the same 5 mm grid used for treatment planning. Four detector catheters (one for each quadrant) were inserted into the prostate. These detectors were kept in place during the entire procedure of PDT treatment. Four additional preplanned treatment catheters for light sources were then inserted 0.5 or

0.7 cm away from the detector catheters. These source catheters were used for light delivery and optical properties measurements. The optical properties of the prostate in each quadrant were then measured before light delivery using these existing detectors and a point source inserted into one source catheter. The time for optical property measurements was approximately 5 min. The PDT treatment was then performed one quadrant at a time by inserting the CDF into the source catheters. A 15 W diode laser, model 730 (Diomed, Ltd., Cambridge, UK) was used as the 732 nm light source. The treatment time for each quadrant was dependent on the detector reading in that quadrant. The light was delivered to ensure that the cumulative fluence reading of all four isotropic detectors reached the same prescription fluence. The total treatment time varied but was always less than 1 h. After light delivery, the optical properties of the prostate in all four quadrants were measured again using a point source (for another 5 min). The light sources and detectors were then removed, and posttreatment biopsies were performed.

Diffusion theory and optimization algorithm. μ_s' and μ_a coefficients characterize the scattering and absorption properties of tissues. With the diffusion approximation, the light fluence rate ϕ at a distance r from a point source of source strength, S, can be expressed as (18)

$$\phi = \frac{S\mu_{eff}^2}{4\pi r\mu_a} e^{-\mu_{eff} r} = \frac{S3\mu_s'}{4\pi r} e^{-\mu_{eff} r} \quad (1)$$

where S is the source strength of the point source, $\phi(r)$ is the fluence rate at position r, $\mu_{eff} = \sqrt{3\mu_a\mu_s'}$ is the μ_{eff} in tissues and is applicable for a wider range of μ_a and μ_s' combinations than the traditional definition of $\mu_{eff} = \sqrt{3\mu_a(\mu_s' + \mu_a)}$ (19), although it is obtained as an approximation of the latter expression. $r = \sqrt{x^2 + h^2}$, where x and h are the parallel and perpendicular distances from the center of the point source (see Fig. 1). The two free parameters (μ_a and μ_s') are inherently separable in that for a point source with a given source strength, the magnitude of the fluence rate near the light source ($x = 0$) is determined by μ_s' only and the slope of the spatial decay of the light fluence rate is determined by μ_{eff} only.

In theory, measurements of ϕ at two different distances r from the point source are sufficient to determine both μ_a and μ_s'. In reality, our measurements contain at least four different distances and up to 800 distances for latter measurements. Measurements at multiple sites allow evaluation of the variation of these optical characteristics within the prostate volume. Because Eq. (1) is a nonlinear equation of two free parameters μ_a and μ_s', we used a differential evolution algorithm developed by Storn and Price (20). This algorithm is simple and robust, and converges faster than adaptive simulated annealing or the annealed Nelder and Mead approach (20). We modified the algorithm to require that all free parameters (μ_a, μ_s' and h) are positive (21). The deviations between measurement and fit are represented by standard deviation, $\sum_{i=1}^{n} \sqrt{((\text{measurement}_i - \text{fit}_i)/\text{fit}_i)^2/(n-1)}$, where n is the number of data points needed in the fit.

Calibration of the isotropic detector and phantom verification. Isotropic detectors described by Marijnissen and Star (22) were used for the study. Each isotropic detector was made of an optical fiber with a spherical tip made of TiO_2 (a scattering material). The isotropic detectors were made by Rare Earth Medical (now CardioFocus, Norton, MA) and have an isotropy of better than ±30% from any direction except for angles within 30° of the optical fiber attachment point. Each detector fiber was connected to a photodiode via an SMA connector. The measured photovoltage (V) from the isotropic detector was converted to light fluence rate using:

$$\phi = a(V - b), \quad (2)$$

where a was the conversion factor and b characterized the leakage of the photodiode. This calibration was performed under collimated 732 nm laser light in air. When the isotropic detector was used to measure fluence rate in tissue (or in a liquid optical phantom), a tissue (or water) correction factor of 2.0 was used. This value was determined by measuring the response of the isotropic detectors in and out of water medium for the same incident irradiance (22). The calibration of the isotropic detectors was checked to be accurate to within 5% using an integrating sphere before each individual measurement.

A homemade, 12-channel light dosimetry system was used for all *in situ* measurements. Five different isotropic detectors were used. The conversion factors were a = 129–161 and a = 63–72 mW/cm^2/V for the four isotropic detectors with 0.5 mm scattering tips and the isotropic detector with 1 mm scattering tip used in the urethra, respectively. b = 0.020 V for all isotropic detectors. The response was found to be linear over the light fluence rate range (0–1200 mW/cm^2) to within ±5%. The minimum resolution of the dosimetry system was better than 0.1 mW/cm^2 after the introduction of an additional software-controllable analog gain to adjust the dynamic range of the light dosimetry system.

To ensure that the optimization technique was robust and to estimate the accuracy of the optimization algorithm to extrapolate optical properties, we measured the optical properties of an optical phantom with known μ_a and μ_s' using the same methods as those used in human patients. The optical phantom was composed of pure scattering medium (liposyn III, 30% Abbott Lab, North Chicago, IL) and pure absorbing medium (green ink). This type of phantom has been described by Flock *et al.* (23). The concentrations of liposyn used were 0.25% and 0.5% by volume in water. Three green ink concentrations were used: 0%, 0.014% and 0.07%. The optical properties (μ_s' and μ_a) of the liquid phantom were independently characterized by analyzing the decay of intensity along the axis of a broad collimated light beam illuminating the phantom from above (12). They were μ_s' = 3.6 and 7.2 cm^{-1} and μ_a = 0.02, 0.1 and 0.5 cm^{-1}. The phantom was placed in a plastic container, which was painted black and was large enough (18.2 × 14.6 × 7.7 cm^3) to protect the detector from boundary effects. A point light source with an outside diameter of 500 μm (Pioneer Optics, Windsor Locks, CT) was used for light delivery, along with a polyurethane template and plastic catheters. Fluence rates were measured at various positions along the length of detector catheters placed at fixed distances (h = 0.5–0.7 cm) from the source catheter.

A second set of phantoms was designed to verify that the μ_a of the phantom varies linearly with MLu concentration. These phantoms were constructed with a lipid content of 0.5%. (Note a different batch of Liposyn was used. As a result, μ_s' = 4 cm^{-1} for 0.5% lipid content.) The measurements and data analysis proceeded as above using 732 nm laser and the same setup.

The transmission of the light from the sources through the transparent catheters was measured in a 6 inch diameter integrating sphere (IS60, LabSphere, Inc., North Sutton, NH) as a ratio of the detector reading with and without the catheter. The result was 1.0 for both point and linear sources. The transmission of the catheter for an isotropic detector in air was between 0.95 and 1 depending on the whether the light source was farther away or very close to the detector. The latter was expected in tissue because the light was coming from all directions and was very close to the detector in the catheter. Based on these results no transmission correction was necessary for the transparent catheters for either the light source or the isotropic detectors.

PDT and in vivo light measurements. A total of 14 patients were treated. MLu (Pharmacyclics, Inc., Sunnyvale, CA) injection was administered intravenously (0.5–2 mg/kg) 3–24 h before light administration (16,24). After the patient was anesthetized, the interstitial CDF were placed in the gland using a template with evenly spaced holes, which was attached to the TRUS unit. A 17-gauge plastic catheter (Flexi-needle, Best Industries, Inc., Springfield, VA) containing a metal trocar was placed through the template and into the prostate. The trocar was removed and replaced with the light diffuser. The light energy delivered was prescribed based on *in situ* measured light fluence. Each patient received a light fluence between 25 and 100 J/cm^2, determined by *in vivo* measurement using isotropic detectors. The maximum unit length source strength in any one fiber was limited to 150 mW/cm. Table 1 summarizes the treatment delivered to all patients.

Measurements were taken at various distances from the light source before and after light treatment in various quadrants of each prostate, measured at 2 cm from the apex of the prostate. For the last two patients, the light sources were moved along the catheter in several locations to also quantify the variation of optical properties in the prostate gland along the catheter.

Ex vivo MLu measurement. In each patient a needle biopsy of prostate tissue from each quadrant was collected before and after light delivery. Biopsies were immediately frozen on dry ice, transported to the laboratory and stored at −80°C until the time of assay. Caution was taken to protect the samples from light. MLu was extracted from the needle biopsies using a procedure based on a previous report (25). Tissue samples were thawed to room temperature, weighed and, depending on the amount of tissue available, two to four of the needle biopsies were combined for analysis. Only biopsies collected at the same time point, *i.e.* either pre- or post-PDT, were combined. A combined tissue weight of ~5–25 mg was sought. Specimens were cut into shorter lengths, placed in a 2 mL capped polypropylene tube and homogenized (Polytron 1200) in 400 μL of phosphate buffer (24 m*M*, pH 7.5). Homogenates were mixed with 400 μL of chloroform, then 400 μL of methanol was added. After centrifugation (3500 rpm, 15 min) the organic layer was collected and 200 μL was transferred to

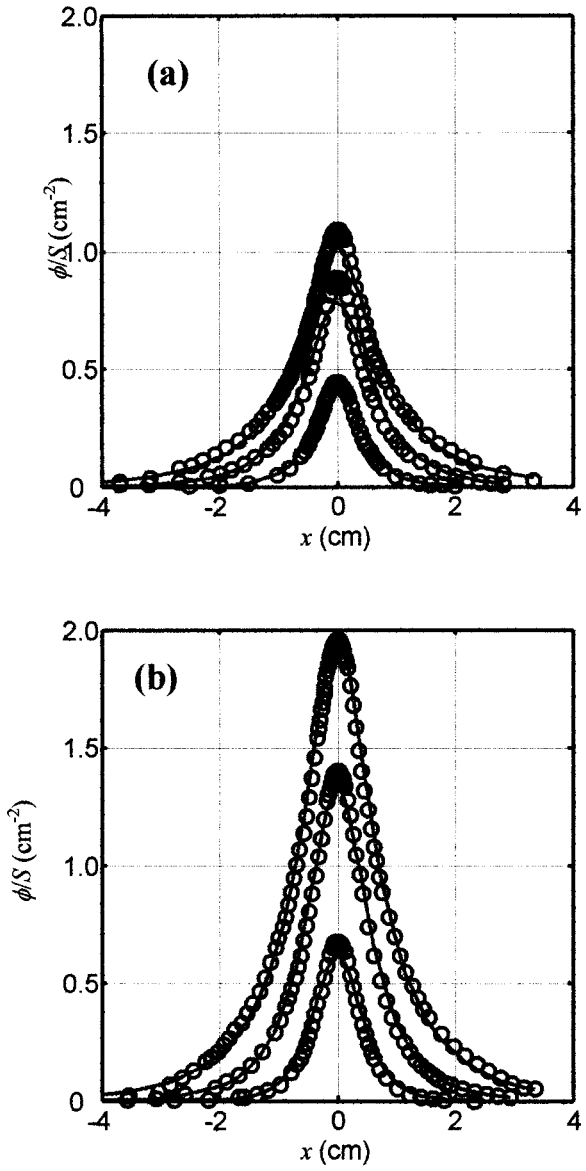

Figure 2. Measurement of light fluence rate (mW/cm^2) at different distances, x, from a point source in liquid optical phantoms: (a) $\mu_s' = 3.6$ cm^{-1} and $\mu_a = 0.02$, 0.1 and 0.5 cm^{-1} and (b) $\mu_s' = 7.2$ cm^{-1}, $\mu_a = 0.02$, 0.08 and 0.40 cm^{-1}. Symbols represent measurements with an isotropic detector. The solid lines are the best fit with the resulting fit optical properties (from top to bottom): (a) $\mu_s' = 3.7$, 3.8 and 3.4 cm^{-1} and $\mu_a = 0.03$, 0.097 and 0.53 cm^{-1} and (b) $\mu_s' = 7.5$, 7.1 and 7.3 cm^{-1}, $\mu_a = 0.022$, 0.074 and 0.38 cm^{-1}, respectively.

a cuvette. The fluorescence of the homogenized sample was measured by a spectrofluorometer (FluoroMax-3, Jobin Yvon, Inc., Edison, NJ) with λ_{ex} of 474 nm and λ_{em} of 740 nm (emission scan range from 650 to 850 nm). MLu concentration in the tissue was calculated on the basis of the increase in fluorescence resulting from the addition of a known amount of MLu to each sample after its initial reading. Data are presented as nanograms of MLu per milligram of tissue.

Correlation between μ_a and MLu concentration. To correlate the relationship between μ_a measured *in vivo* with the MLu measured from *ex vivo* biopsy, we plot out the subset of μ_a data (24 points) that had corresponding *ex vivo* biopsies. Notice that although the *ex vivo* biopsies were taken from the same prostate, they are not necessarily at the same location as that used for μ_a measurement because the prostate template was not used for the biopsy. Once the parameters for a linear relationship between μ_a and MLu concentration are established, all measured μ_a data (121 points) were used to examine the variation of MLu concentration intra- and interprostate.

RESULTS

Figure 2 compares the fit and measurement of light fluence rate at different distances from a point source in two optical phantoms made of different concentrations of liposyn and green ink mixtures. The solid lines are the result of nonlinear fitting using the differential evolution algorithm. The resulting optical properties are shown. The extrapolated μ_s' agreed with the true values to within $\pm 6\%$; the extrapolated μ_a agreed with the true values to within $\pm 11\%$.

Figure 3 shows the variation of measured light fluence rate distribution (solid lines) and associated fit (symbols) for (1) different locations in the same prostate gland and (2) the same location in a prostate before and after light delivery. In Fig. 3a, an example of the light fluence rate radial distribution for the right lower (RLQ), right upper (RUQ) and left upper (LUQ) quadrants of one prostate is shown. In this particular patient, the extrapolated optical properties were very different between RLQ ($\mu_a = 0.23$ cm^{-1}, $\mu_s' = 7.3$ cm^{-1}) and RUQ ($\mu_a = 0.44$ cm^{-1}, $\mu_s' = 12$ cm^{-1}). A large variation was also observed among different patients (see Fig. 5). When evaluated across all patients, the extrapolated attenuation coefficients varied between 0.9 and 6.7 cm^{-1}, whereas the extrapolated μ_s' varied between 1.1 and 44 cm^{-1}. As a result of the heterogeneity of optical properties, the light fluence rates per unit source strength at 0.5 cm from the point source varied between 0.2 and 4.1 cm^{-2} among the patients. However, no significant change of optical properties was observed before and after PDT treatment in the same site for most but not all patients (Fig. 3b).

Figure 4 shows the temporal dependence of the light fluence rate at the center of the four treatment quadrants. The large variation of light fluence rate was due to the movement of the isotropic detector. Notice that we did not observe any significant light fluence rate in urethra in all patients treated so far.

The overall variation of optical properties (μ_a, μ_s' and μ_{eff}) and the optical penetration depth ($\delta = 1/\mu_{eff}$) before (first bar) and after (second bar) PDT for each patient studied is shown in Fig. 5. The error bars represent the standard deviation among the four different quadrants in the same patient. No error bar is present in cases where only one measurement is available. These results are also summarized in Table 2.

The interprostatic heterogeneity of light fluence rate at 0.5 cm from the point source per unit source strength is shown in Fig. 6. The x axis identifies each patient measured. The first bar of the pair was measured before PDT, and the second bar of the pair was measured after PDT. The error bars represent the standard deviation among the four different quadrants in the same patient. The solid line is an average with the range (dashed lines) corresponding to standard deviation. The mean fluence rate per unit source strength at 0.5 cm for all sites (excluding bleeding) was 1.5 ± 1.1 cm^{-2} (sample size 121).

The relationship between the measured μ_a, and the tissue concentration of MLu, measured *ex vivo* after drug extraction from biopsy specimens is shown in Fig. 7a. μ_a were measured *in situ* and biopsies were collected before (○) and after (*) PDT. For comparison, we have also plotted the measured μ_a of MLu *vs* MLu concentration (+) in a pure liposyn phantom. Figure 7b shows the relationship between MLu concentration measured from tissue biopsies (bars) and extrapolated from μ_a (symbols) *vs* the injected

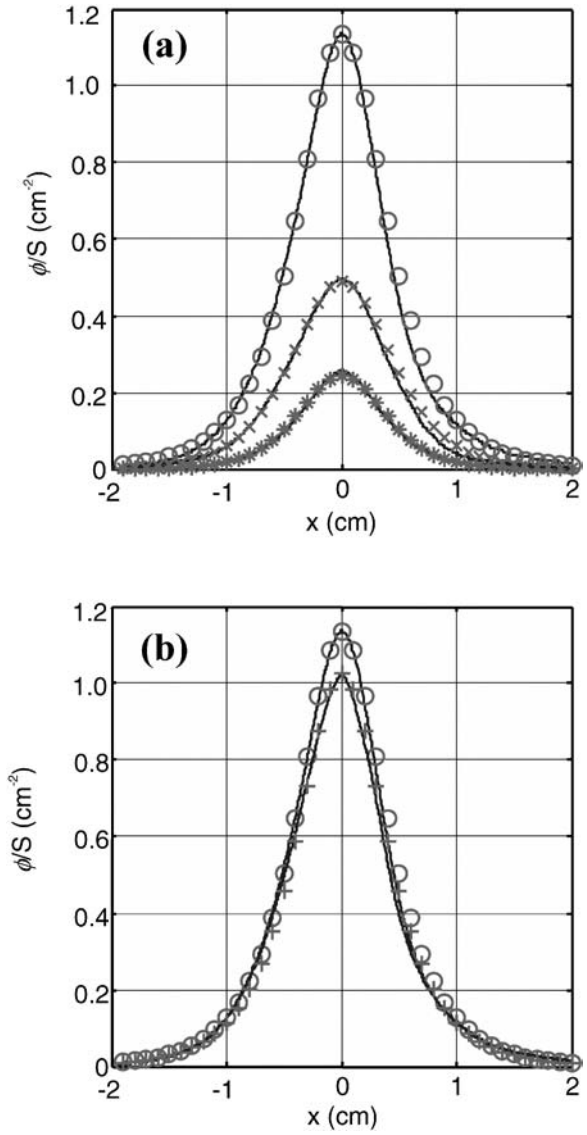

Figure 3. Measured light fluence rate per unit source strength (ϕ/S) at distances along the catheter, x, from the point source measured *in vivo* in human prostate gland for Patient 13. Lines are measured data and symbols are fits. (There are too many measured points to express the measured data clearly as symbols.) (a) Light fluence rates in the right lower quadrant (○), right upper quadrant (x) and left upper quadrant (*) of the same prostate before PDT. (b) Light fluence rates before (○) and after (+) light treatment in the right lower quadrant of the prostate gland. The optical properties are ○—$\mu_a = 0.23$ cm^{-1}, $\mu_s' = 7.3$ cm^{-1}, $\phi(0.5)/S = 1.1$ cm^{-2} and $h = 0.5$; x—$\mu_a = 0.44$ cm^{-1}, $\mu_s' = 12.0$ cm^{-1}, $\phi(0.5)/S = 0.78$ cm^{-2} and $h = 0.7$; *—$\mu_a = 0.25$ cm^{-1}, $\mu_s' = 11.6$ cm^{-1}, $\phi(0.5)/S = 1.3$ cm^{-2} and $h = 0.7$; +—$\mu_a = 0.25$ cm^{-1}, $\mu_s' = 6.6$ cm^{-1}, $\phi(0.5)/S = 1.0$ cm^{-2} and $h = 0.5$ cm.

MLu dosage to patients. Drug concentration was calculated from μ_a using the linear relationship determined in Fig. 7a: c (ng/mg) = (μ_a (cm^{-1}) − 0.227)/0.0658. Error bars represent the standard deviation among measurements in different locations within a prostate or different prostates. The correlation coefficient (R^2 = 0.63) of the linear relationship between μ_a and tissue concentration of MLu suggests good association, although the exact numerical values for the linear equation may contain error due to the spread of the data.

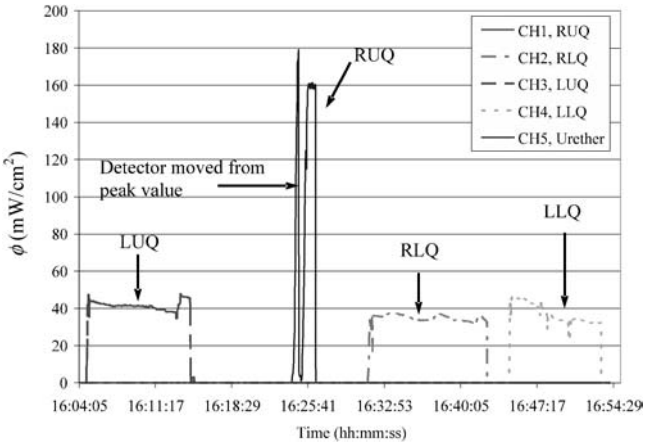

Figure 4. Light fluence rate *vs* time measured by the *in vivo* dosimetry system for the four quadrants for Patient 7 at 732 nm wavelength. Large disturbances of light fluence rate were caused by movement of detector positions, per observation by the operators.

DISCUSSION

The main objective of this study was to evaluate the optical properties of prostate tissue in the human prostate using 732 nm light. Comparisons were made before, during and after MLu-mediated PDT. Differences within and among patients were also studied.

Intrapatient heterogeneity of optical properties was observed. Figure 3 is a representative example of this heterogeneity at 732 nm. There was a difference in the μ_a (0.23–0.4 cm^{-1}) and μ_s' (6.6–12 cm^{-1}) values at different locations within the same prostate gland (Fig. 3a). As a result, the fluence rate per source strength at 0.5 cm from the point source varied from 0.8 to 1.3 cm^{-2}. In contrast, the optical properties (μ_a and μ_s') did not change substantially before or after PDT light delivery. Thus, the light fluence rate at the same site of the same prostate did not vary much before and after PDT light delivery (Fig. 3b).

In general, we found a lack of change in the optical properties in a particular site within the prostate before and after PDT. This was confirmed by the absence of any time dependence of the fluence rate in the middle of the four quadrants (Fig. 4). The results shown in Fig. 4 are typical of temporal fluence rate measurements among patients in the study. It shows very little variation of optical properties for most sites, except for LUQ where the fluence rate seems to decrease. These measurements were performed in such a way that the same site was used before and after PDT. Our general conclusion is consistent with published results at 630 nm for Photofrin-mediated PDT (11) and at 732 nm for MLu-mediated PDT (12) in the canine prostate model, where little time dependence of light fluence rate was observed. However, because of large heterogeneities, variation in optical property measurements before and after PDT was found (see Fig. 5).

There are several potential reasons why no significant light fluence rate was measured in the urethra (Fig. 4). First of all, it could be due to measurement uncertainty. The light treatment was performed one quadrant at a time rather than all four quadrants together. Because the range of the light penetration in human prostate is relatively short (0.4 cm), only those CDF (usually in the RUQ and the LUQ) near the urethra will contribute to the urethra. Because the position of the isotropic detector in urethra was

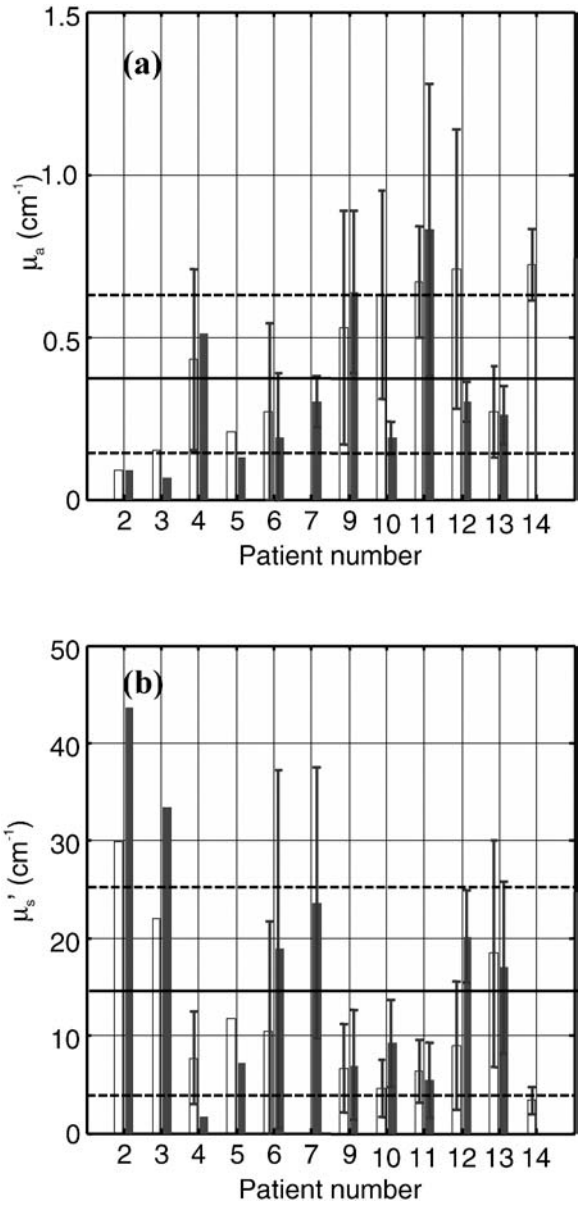

Figure 5. Variation of (a) μ_a, (b) μ_s', (c) μ_{eff} and (d) δ in patients before (open bars) and after (solid bars) PDT. The height of each bar is the mean value measured in each patient. The error bars specify the standard deviation among the four quadrants of a prostate. The solid horizontal line is the average of all measurements, and the dashed lines are the standard deviation of the average.

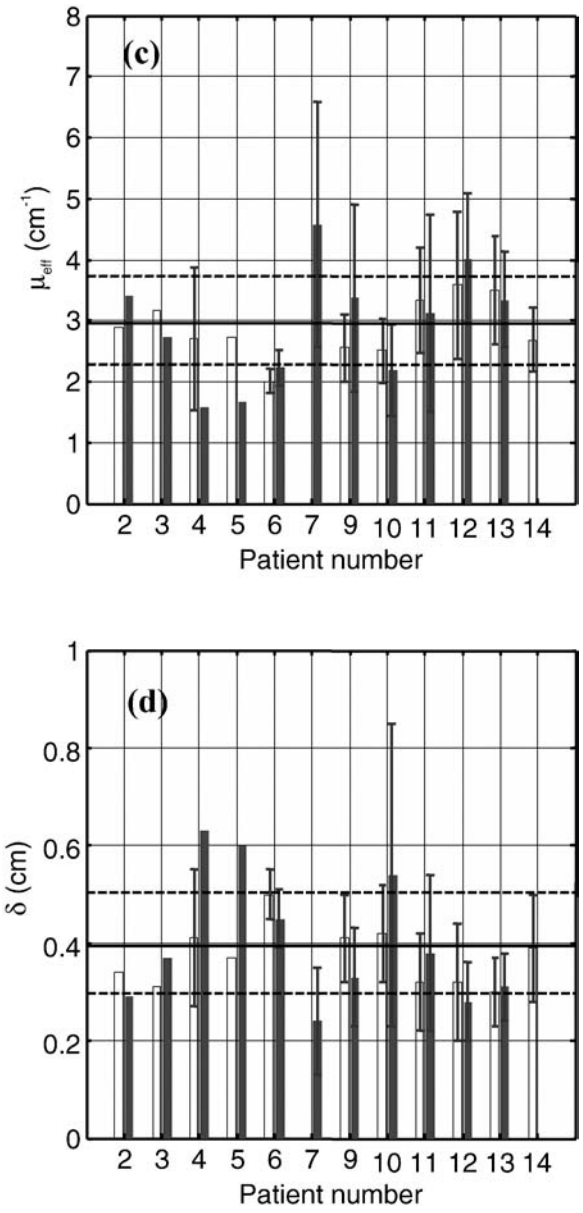

Figure 5. Continued.

optimized only once during the treatment of one quadrant, it is possible that we had not obtained the peak light fluence rate for the entire treatment. (The position of the urethral isotropic detector could not be optimized multiple times because one can only move the position of the urethra isotropic detector in one direction.) Second, the light fluence could actually be lower in the urethra. Besides the fact that we have avoided placing light sources through the urethra, we have noticed increased absorption in the urethra due to high concentrations of MLu in urine, which will reduce the light fluence rate reaching the isotropic detector and thus, the urethra itself. No serious urethral toxicity has been observed in all the patients treated so far.

The accuracy of the method used to determine optical properties from measurements around a point source was dominated by the uncertainty of the distance between the light source and detector catheters (h, see Fig. 1b). This is because the inserted catheters are not exactly parallel to each other and an error of 1–2 mm is possible, despite the use of ultrasound guidance to position the catheters correctly. A detailed error analysis is included in the Appendix. To reduce the positioning error, the later measurements (starting with Patient 9) were made using a motorized probe, with a positioning accuracy of at worst 0.2 mm. The use of the motorized probe also increased the number of measurement points from typically four points per measurement to approximately 800 points per measurement. We then allowed the distance h to be one of the free parameters of the fit (μ_a, μ_s' and h), and h was allowed to be different from the known separation based on the template by 1–2 mm. Using this method our phantom studies confirmed that one

Table 2. Summary of optical properties before and after PDT in human prostates. The values in the parentheses are the standard deviation of the mean values measured from different locations of the same prostate. No standard deviation is listed if only one data point is available

	Before PDT				After PDT			
Patient number	μ_a (cm^{-1})	μ_s' (cm^{-1})	δ (cm)	ϕ/S (cm^{-2})	μ_a (cm^{-1})	μ_s' (cm^{-1})	δ (cm)	ϕ/S (cm^{-2})
2	0.09	29.8	0.34	3.34	0.09	43.7	0.29	3.78
3	0.15	22.0	0.31	2.15	0.07	33.4	0.37	4.07
4	0.43 (0.28)	7.69 (4.76)	0.41 (0.14)	0.97 (0.81)	0.51	1.67	0.63	0.36
5	0.21	11.8	0.37	1.44	0.13	7.18	0.60	1.48
6	0.27 (0.27)	10.5 (11.2)	0.50 (0.05)	1.74 (1.78)	0.19 (0.20)	18.9 (18.4)	0.45 (0.06)	3.18 (3.32)
7	—	—	—	—	0.30 (0.08)	23.7 (13.9)	0.24 (0.11)	1.09 (0.40)
9	0.53 (0.36)	6.61 (4.51)	0.41 (0.09)	0.77 (0.42)	0.64 (0.25)	7.00 (5.59)	0.33 (0.10)	0.54 (0.23)
10	0.63 (0.32)	4.62 (2.87)	0.42 (0.10)	0.56 (0.29)	0.19 (0.05)	9.27 (4.47)	0.54 (0.31)	1.33 (0.64)
11	0.67 (0.17)	6.39 (3.18)	0.32 (0.10)	0.51 (0.18)	0.83 (0.45)	5.45 (3.89)	0.38 (0.16)	0.47 (0.30)
12	0.71 (0.43)	8.99 (6.51)	0.32 (0.12)	0.61 (0.35)	0.30 (0.06)	20.2 (4.8)	0.28 (0.08)	0.98 (0.05)
13	0.27 (0.14)	18.5 (11.6)	0.30 (0.07)	1.46 (0.72)	0.26 (0.09)	17.0 (8.8)	0.31 (0.07)	1.42 (0.56)
14	0.72 (0.11)	3.37 (1.37)	0.39 (0.11)	0.40 (0.01)	—	—	—	—

can determine $\phi(0.5)$ and μ_a to within $\pm 20\%$ for most cases. The error for μ_{eff}, is much smaller ($\pm 5\%$) and is insensitive to the positioning error in h (see Appendix).

Some of the measurements cannot be used to extrapolate optical properties because of bleeding. This happens when blood surrounding one of the catheters (either source catheter or the detector catheter) blocks the light from reaching the detector. We used a standard of $\phi/S > 0.1$ cm^{-2} to determine if there was sufficient signal to analyze the data. The average success rate for the first seven patients was very poor (approximately 35%). This was increased to 64% for later patients using a motorized probe, primarily because more measurements can be made in a shorter period of time.

The overall variation of optical properties (μ_a, μ_s', μ_{eff} and $\delta = 1/\mu_{eff}$) before and after PDT for different patients is shown in Fig. 5 to demonstrate interpatient heterogeneity. The heterogeneity in optical properties was the major reason that the light fluence rate a fixed distance away from the CDF varied from patient to patient. However, the heterogeneity of optical properties in human prostate is somewhat smaller than that observed in canine prostate at 732 nm (12). Overall μ_a varied between 0.07 and 1.62 cm^{-1}, and μ_s' varied between 1.1 and 44 cm^{-1}. μ_{eff} varied between 0.91 and 6.7 cm^{-1}, corresponding to an optical penetration depth ($\delta = 1/\mu_{eff}$) of 0.2–1.1 cm. The mean values of μ_{eff} and δ were 2.9 ± 0.7 cm^{-1} and 0.4 ± 0.1 cm, respectively. This penetration depth is substantially larger than that of 0.1–0.25 cm predicted for 630 nm (11) but is smaller than 0.5–3 cm observed in normal canine prostate at 732 nm (12). The most probably explanation is that canine prostate has different grandular/structure content than that of human prostate. Whereas the mean reduced scattering coefficient in canine prostate was 3.6 ± 4.8 cm^{-1} (12), it was 14 ± 11 cm^{-1} in human prostrate at the same wavelength (732 nm). The increased reduced scattering coefficient resulted in increased μ_{eff}, or a reduction of optical penetration depth, assuming that the μ_a remains the same. In addition, the increase in μ_as in human prostates compared with that in canine prostates contributed to the reduction of the penetration depth in humans compared with that in canines. Human prostates measured in this study had cancer present and had been subjected to previous radiation therapy. The canine prostate is a normal tissue model. Hypoxia has been described in patients with prostate cancer (26), whereas one would expect normal oxygen levels in normal canine prostate tissue. As a result, there may be more deoxyhemoglobin in these prostates than in normal prostates, resulting in higher μ_as and shorter penetration depths at the wavelength range 630–800 nm.

The interprostatic difference in fluence rate per unit source strength at 0.5 cm from the point source was shown in Fig. 6. We chose 0.5 cm because this is the middle point for 1 cm spaced interstitial loading. The mean value was 1.5 ± 1.1 cm^{-2} for all prostates studied (sample size 121). We observed interpatient fluence rate heterogeneity as a result of heterogeneity of optical properties.

The tissue concentration of MLu and the μ_a in the human prostate at 732 nm as shown in Fig. 7a demonstrates a linear relationship with measured MLu concentration (correlation coefficient $R^2 = 0.63$). This relationship is described by the equation $\mu_a = 0.066c + 0.23$. The relatively large spread of the data can be explained by the large heterogeneity of MLu distribution in

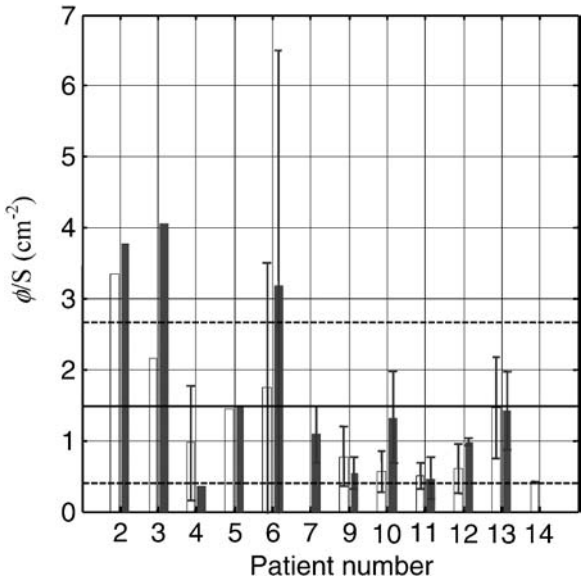

Figure 6. Measured mean fluence rate per power, ϕ/S, at 0.5 cm from the point source at 732 nm in different patients before (open bars) and after (solid bars) PDT. The error bars reflect intraprostate variation of ϕ/S. The solid horizontal line is the average of all measurements, and the dashed lines are the standard deviation of average: 1.5 ± 1.1 cm^{-2}.

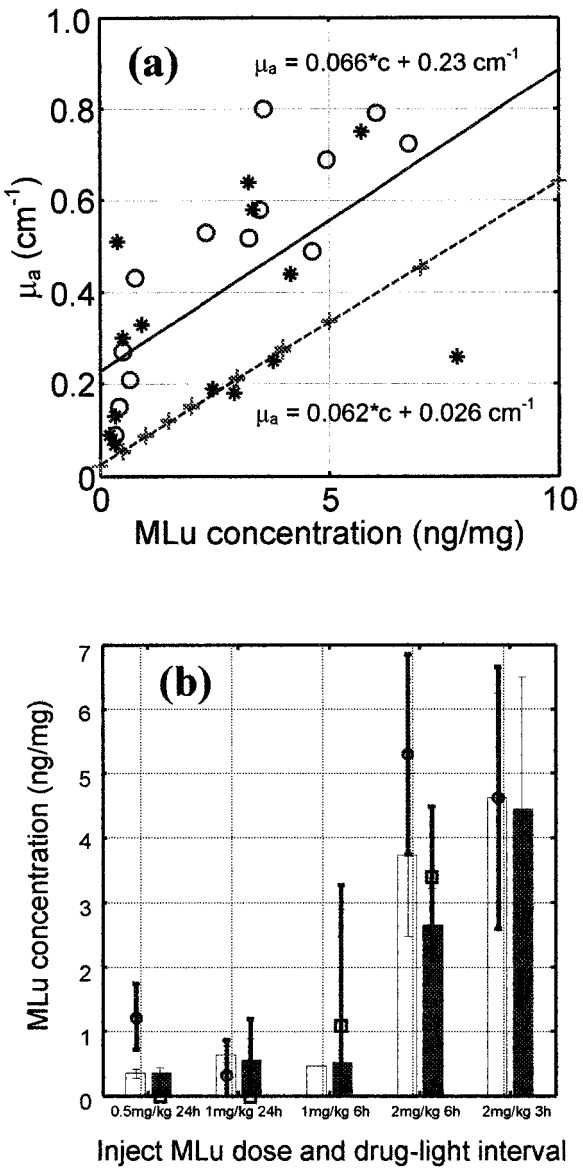

Figure 7. (a) *In vivo* absorption coefficient (μ_a) at 732 nm as a function of measured *ex vivo* MLu concentration (in ng/mg) from the same human prostate. The symbols are measured points *in vivo*: ○—before PDT, *—after PDT. The solid line is a linear fit to the measured *in vivo* data. The symbol "+" represents the measured μ_a of MLu *vs* MLu concentration in a pure liposyn phantom. The dashed line is a linear fit to the phantom data with $\mu_s' = 4$ cm^{-1}. (b) Extrapolated MLu concentration from *ex vivo* fluorescence (bars) and from μ_a (symbols) as a function of injected MLu concentration: open bars (○)—before PDT, solid bar (□)—after PDT. Drug concentration calculated from μ_a uses the linear relationship determined in (a): c (ng/mg) = (μ_a (cm^{-1}) − 0.227)/0.0658. The thin and thick error bars correspond to the standard deviation of the *ex vivo* biopsy and *in vivo* absorption measurements, respectively. Notice that (b) used all measured μ_a data (121 points), whereas (a) used a subset of μ_a data (24 points) that had corresponding *ex vivo* biopsies. (Insufficient data existed to extrapolate tissue concentration from *in vivo* absorption measurement for 1 mg/kg MLu injection at 6 h drug-treatment time interval before PDT due to bleeding.)

different locations of a human prostate (27). Because the location of the *in situ* optical measurements and the tissue biopsies were not exactly the same, some discrepancy between the drug levels measured by the two techniques is expected. Absorption by many naturally occurring chromophores, such as melanins, cytochromes, flavoproteins, and in particular, hemoglobin and deoxyhemoglobin, is small (around 732 nm) (10–13); as such, it is not surprising that the μ_a at 732 nm varies approximately linearly with the MLu concentration. Given the heterogeneity in the patient data, we used a liposyn phantom to examine the relationship between MLu concentration and the μ_a and to confirm the slope of our clinical observations. Data based on this phantom are shown in Fig. 7a by the "+" symbols. The absence of other absorbers in the phantom decreases μ_a. The slope of the best fit line (0.062 cm^{-1}/(ng/mg)) is consistent with that observed *in vivo*. The linear relationship between MLu drug concentration and the μ_a at 732 nm is consistent with that observed in canine prostate at 732 nm, but a larger intersect (μ_a = 0.23 cm^{-1}) is found in humans than in dogs (μ_a = 0.08 cm^{-1}) (12). This may be caused by differences in the oxygenation of cancerous prostate tissue (humans) and normal prostate tissue (dogs) because the attenuation coefficient of oxyhemoglobin at 732 nm is substantially less than that of deoxyhemoglobin. If the tissue is less oxygenated, the attenuation coefficient will increase. The conclusion that more deoxyhemoglobin existed in human prostate is confirmed by *in vivo* diffuse absorption spectroscopy in the same prostate patient population (28). For the two patients studied, the contribution to the μ_a from oxyhemoglobin and deoxyhemoglobin varied between 0.1 and 0.2 cm^{-1} at 732 nm.

The effect of injected drug dose and drug-light interval on tissue concentration of MLu is shown in Fig. 7b. It shows significant intra- and interpatient variation of drug concentration. The extrapolated mean tissue concentration from *in vivo* absorption (symbols) generally agrees with that from *ex vivo* biopsy. Figure 7b was drawn using all 121 absorption measurements available as opposed to Fig. 7a, which used a subset of data (24 points) that had corresponding *ex vivo* biopsies. The large discrepancy between drug concentration measured *in vivo* and *ex vivo* in the two patients receiving 0.5 mg/kg with a 24 h drug-treatment interval is likely a consequence of measurement uncertainties for *in vivo* absorption in this early group of patients. The detector positions for these patients were determined manually using a ruler, which introduced larger errors in the final determination of μ_a. In addition, because μ_a for the earlier patients were small (less MLu), the relative uncertainty in μ_a increased. The large discrepancy in drug concentration measured *in vivo* and *ex vivo* in the group receiving 1 mg/kg with a 6 h drug-treatment interval can be explained by the small number of samples, *i.e.* patients, in this group (n = 1). However, some preliminary conclusions can be made from these data. It appears that a reduction in drug concentration is observed after PDT, which may be consistent with photobleaching. The patients who received higher injected MLu doses generally had higher local drug concentrations in the prostate. If one estimates the MLu concentration for 2 mg/kg at 24 h *in vivo* as twice the MLu concentration for 1 mg/kg at 24 h, then the drug concentration seems to decrease systematically with incubation time, *i.e.* drug-treatment interval, by examining the data for 2 mg/kg at 24 h, 2 mg/kg at 6 h and 2 mg/kg at 3 h in Fig. 7b. The heterogeneity in MLu concentration is sufficiently large to potentially require *in situ* monitoring of MLu distribution for future PDT treatments of the human prostate.

When one examines the variation of drug concentration in a single patient, it is clear that the drug concentration can easily change by three times when measured from different locations of the same prostate (data presented in reference [27]). This strong variation suggests that the mean intraprostatic variation is usually

larger than the mean interprostatic variation, as shown in Fig. 7b, where the difference between bars (*e.g.* before PDT) for different groups is smaller than the range of the error bar, representing the standard deviation of intraprostatic variation in the same group; most of this variation is caused by intraprostatic variation.

CONCLUSIONS

We have measured the optical properties and MLu concentration of human prostates for 732 nm light. Substantial inter- and intra-patient heterogeneity was observed. The mean light penetration depth in the human prostates is about 0.4 cm, at least two times smaller than those found in the normal canine prostates. The μ_a *in vivo* at 732 nm has been found to be proportional to the tissue concentration of MLu, determined from *ex vivo* biopsies. A real-time dosimetry measurement and feedback system for monitoring light fluences during treatment should be considered for such future PDT studies to account for this heterogeneity.

Acknowledgements—This work is supported by grants from National Institute of Health (NIH), R21 CA88064-01 and P01 CA87971-01, and Department of Defense (DOD), DAMD1703-1-0132. We thank the referees for their helpful critiques and constructive suggestions for the manuscript.

APPENDIX

Error analysis of the optimization technique to extrapolate optical properties

There are several uncertainties in determining the optical properties besides uncertainty in measuring the light fluence rate, which accounts for approximately ±5%. One is the uncertainty in the position (x) of the detector, which can be 1–2 mm. Another uncertainty is the uncertainty in the distance (h) between the source catheter and the isotropic detector catheter, which could be different from the distances specified on the template by 1–2 mm as well. Both errors introduce an uncertainty in distance (Fig. 1b), $r = \sqrt{x^2 + h^2}$, which can be 1–2 mm. From the phantom measurements, one can estimate the relative uncertainty introduced by the positioning errors by the ratio of the slope of the fluence rate to fluence rate $d\phi/dr/\phi dr$. Because the fluence rate at distance r from a point source is proportional to $e^{-\mu_{eff}r}/r$, this value decreases with increasing distance r and follows $(\mu_{eff} + 1/r)dr$. Using this relationship one gets a relative uncertainty in fluence rate of 50% for $r = 5$ mm and 39% for $r = 7$ mm assuming that $dr = 2$ mm and $\mu_{eff} < 0.5$ cm^{-1}. To separate the two sources of errors that contribute to an error in r, one writes $dr = x/rdx + h/rdh$. The first error, x, is a random error and approaches $dr = 0$ for $x = 0$ for any dx because $dr = xdx/r$. Thus, the overall error caused by uncertainty of x for determining μ_a and μ_s' should be small. This is also because it is unlikely that all points are off in the same direction thereby introducing a systematic error. We have minimized this error by using a computerized step motor so that the error in x was less than 0.2 mm. In this case, the error in ϕ should be less than 2% even for $x = r$. The second source of error can be large but it is a systematic error.

Table A shows a numerical simulation of the errors in μ_a and μ_s' caused by the errors in h for two conditions of μ_a and μ_s'. The standard deviation of the fit is calculated by $\sum_{i=1}^{n} \sqrt{((\text{measurement}_i - \text{fit}_i)/\text{fit}_i)^2/(n-1)}$. One can use the minimum error to determine the correct h value to within 0.05 cm. In Table A, this corresponds to the fit for $h = 0.55$ cm. The physical separation is $h = 0.6$ cm. We do not understand why the optimal h, which gives the best μ_a and μ_s', is about 0.05 cm shorter than the physical separation of $h = 0.6$ cm. But we have demonstrated that one can extract h to within 0.05 cm. Using this additional constraint and allowing h to deviate from the nominal value will reduce the final uncertainty to less than ±6% for μ_a and less than ±11% for μ_s'. Assuming that the h can still deviate from the true h (0.55 cm) by ±0.05 cm, we estimated that one can determine μ_a to an uncertainty of less than ±20% and μ_s' to an uncertainty of less than ±40%, provided that the optimal h is within 0.5 mm of the true value of h. Clearly, if one allows up to 2 mm uncertainty in h, then one can introduce an unacceptable error for μ_a and μ_s' (see Table A) with up to ±215% and ±450% errors, respectively. The error in μ_{eff} is much smaller (±30%) over the same range of h. To reduce this error further, we have used the value of the standard deviation of the fit as a guide to determine the optimal separation h.

Table A. Error analysis of deviations in μ_a, μ_s', μ_{eff} and ϕ/S(0.5 cm) caused by the uncertainty of h (nominal $h = 0.6$ cm)

h (cm)	μ_a (cm^{-1})	μ_s' (cm^{-1})	μ_{eff} (cm^{-1})	ϕ/S (0.5 cm)	Standard deviation of fit (%)
$\mu_a = 0.5$ cm^{-1}, $\mu_s' = 3.6$ cm^{-1}, $\mu_{eff} = 2.3$ cm^{-1}					
0.40	1.07	1.17	1.93	0.28	27.6
0.45	0.81	1.76	2.07	0.35	17.2
0.50	0.65	2.48	2.20	0.43	11.9
0.55	0.53	3.37	2.32	0.53	10.9
0.60	0.44	4.57	2.45	0.66	12.7
0.65	0.37	5.99	2.57	0.81	15.2
0.70	0.30	7.98	2.69	1.00	17.8
0.75	0.25	10.65	2.81	1.26	20.3
0.80	0.20	14.30	2.93	1.58	22.4
$\mu_a = 0.4$ cm^{-1}, $\mu_s' = 7.2$ cm^{-1}, $\mu_{eff} = 2.9$ cm^{-1}					
0.40	0.70	2.75	2.41	0.43	15.2
0.45	0.56	3.91	2.57	0.54	8.7
0.50	0.46	5.41	2.73	0.68	5.1
0.55	0.38	7.34	2.90	0.83	4.8
0.60	0.30	10.33	3.04	1.09	7.0
0.65	0.24	14.31	3.19	1.39	9.6
0.70	0.19	19.96	3.34	1.80	12.1
0.75	0.14	28.09	3.49	2.35	14.3
0.80	0.11	39.95	3.64	3.10	16.3

REFERENCES

1. Hsi, R. A., D. I. Rosenthal and E. Glatstein (1999) Photodynamic therapy in the treatment of cancer: current state of the art. *Drugs* **57**, 725–734.
2. D'Amico, A. V. (1996) Role of interstitial radiotherapy in the management of clinically organ-confined prostate cancer: the jury is still out. *J. Clin. Oncol.* **14**, 304–315.
3. Chang, S. C., G. Buonaccorsi, A. MacRobert and S. G. Bown (1996) Interstitial photodynamic therapy of the canine prostate using meso-tetra-(m-hydroxyphenyl) chlorine. *Int. J. Cancer* **67**, 555–562.
4. Selman, S. H., R. W. Keck and J. A. Hampton (1996) Transperineal photodynamic ablation of the canine prostate. *J. Urol.* **156**, 258–260.
5. Chang, S. C., G. Buonaccorsi, A. MacRobert and S. G. Bown (1997) Interstitial photodynamic therapy of the canine prostate with disulfonated aluminum phthalocyanine and 5-aminolevulinic acid-induced protoporphyrin IX. *Prostate* **32**, 89–98.
6. Lee, L. K., C. Whitehurst, Q. Chen, M. L. Pantelides, F. W. Hetzel and J. V. Moore (1997) Interstitial photodynamic therapy in the canine prostate. *Br. J. Urol.* **80**, 898–902.

7. Hsi, R. A., A. Kapatkin, J. Strandberg, T. Zhu, T. Vulcan, M. Solonenko, C. Rodriguez, J. Chang, M. Saunders, N. Mason and S. Hahn (2001) Photodynamic therapy in the canine prostate using motexafin lutetium. *Clin. Cancer Res.* **7**, 651–660.
8. Chen, Q., Z. Huang, D. Luck, J. Beckers, P. H. Brun, B. C. Wilson, A. Scherz, Y. Salomon and F. W. Hetzel (2001) Preclinical studies in normal canine prostate of a novel palladium-bacteriopheophorbide (WST09) photosensitizer for photodynamic therapy of prostate cancers. *Photochem. Photobiol.* **76**, 438–445.
9. Nathan, T. R., D. E. Whitelaw, S. C. Chang, W. R. Lees, P. M. Ripley, H. Payne, L. Jones, M. C. Parkinson, M. Emberton, A. R. Gillams, A. R. Mundy and S. G. Bowen (2002) Photodynamic therapy for prostate cancer recurrence after radiotherapy: a phase I study. *J. Urol.* **168**, 1427–1432.
10. Arnfield, M. R., J. D. Chapman, J. Tulip, M. C. Fenning and M. S. McPhee (1993) Optical properties of experimental prostate tumors in vivo. *Photochem. Photobiol.* **57**, 306–311.
11. Chen, Q., B. C. Wilson, S. D. Shetty, M. S. Patterson, J. C. Cerny and F. W. Hetzel (1997) Changes in vivo optical properties and light distributions in normal canine prostate during photodynamic therapy. *Radiat. Res.* **147**, 86–91.
12. Zhu, T. C., S. M. Hahn, A. S. Kapatkin, A. Dimofte, C. E. Rodriguez, T. G. Vulcan, E. Glatstein and R. A. Hsi (2003) In vivo optical properties of normal canine prostate at 732 nm using motexafin lutetium-mediated photodynamic therapy. *Photochem. Photobiol.* **77**, 81–88.
13. Pantilides, M. L., C. Whitehurst, J. V. Moore, T. A. King and N. J. Blacklock (1990) Photodynamic therapy for localized prostatic cancer: light penetration in the human prostate gland. *J. Urol.* **143**, 398–401.
14. Whitehurst, C., M. L. Pantelides, J. V. Moore, P. J. C. Brooman and N. J. Blacklock (1994) In vivo laser light distribution in human prostatic carcinoma. *J. Urol.* **151**, 1411–1415.
15. Lee, L. K., C. Whitehurst, M. L. Pantelides and J. V. Moore (1995) In situ comparison of 665 nm and 633 nm wavelength light penetration in the human prostate gland. *Photochem. Photobiol.* **62**, 882–886.
16. Young, S. W., K. W. Woodburn, M. Wright, T. D. Mody, Q. Fan, J. L. Sessler, W. C. Dow and R. A. Miller (1996) Lutetium texaphyrin (PCI-0123): a near-infrared, water-soluble photosensitizer. *Photochem. Photobiol.* **63**, 892–897.
17. Mody, T. D., L. Fu and J. L. Sessler (2001) Texaphyrins synthesis and development of a novel class of therapeutic agents. In *Progress in Inorganic Chemistry* (Edited by K. D. Karlin), pp. 551–598. John Wiley & Sons, Ltd., Chichester, UK.
18. Jacques, S. L. (1998) Light distributions from point, line and plane sources for photochemical reactions and fluorescence in turbid biological tissues. *Photochem. Photobiol.* **67**, 23–32.
19. Nakai, T., G. Nishimura, K. Yamamoto and M. Tamura (1997) Expression of optical diffusion coefficient in high-absorption turbid media. *Phys. Med. Biol.* **42**, 2541–2549.
20. Storn, R. and K. Price (1997) Differential evolution—a simple and efficient heuristic for global optimization over continuous spaces. *J. Global Optim.* **11**, 341–359.
21. Zhu, T. C., B. E. Bjarngard, X. Ying and C. J. Yang (2001) Modeling the output ratio in air for megavoltage photon beams. *Med. Phys.* **28**, 925–937.
22. Marijnissen, J. P. A. and W. M. Star (1996) Calibration of isotropic light dosimetry probes based on scattering bulbs in clear media. *Phys. Med. Biol.* **41**, 1191–1208.
23. Flock, S. T., S. L. Jacques, B. C. Wilson, W. M. Star and M. J. C. van Gemert (1992) Optical properties of intralipid: a phantom medium for light propagation studies. *Lasers Surg. Med.* **12**, 510–519.
24. Woodburn, K. W., Q. Fan, D. R. Miles, D. Kessel, Y. Luo and S. W. Young (1997) Localization and efficacy analysis of the photo-therapeutic lutetium texaphyrin (PCI-0123) in the murine EMT6 sarcoma model. *Photochem. Photobiol.* **65**, 410–415.
25. Woodburn, K. W., Q. Fan, D. Kessel, Y. Luo and S. W. Young (1998) Photodynamic therapy of B16F10 murine melanoma with lutetium texaphyrin. *J. Invest. Dermatol.* **110**, 746–751.
26. Movsas, B., J. D. Chapman, A. L. Hanlon, E. M. Horwitz, W. H. Pinover, R. E. Greenberg, C. Stobbe and G. E. Hanks (2001) Hypoxia in human prostate carcinoma: an Eppendorf PO2 study. *Am. J. Clin. Oncol.* **24**, 458–461.
27. Zhu, T. C., J. C. Finlay and S. M. Hahn (2005) Determination of the distribution of light, optical properties, drug concentration, and tissue oxygenation in vivo in human prostate during motexafin lutetium-mediated photodynamic therapy. *J. Photochem. Photobiol. B*, DOI: 10.1016/j.photobiol.2004.09.013.
28. Finlay, J. C., T. C. Zhu, A. Dimofte, D. Stripp, S. B. Malkowicz, R. Whittington, J. Miles, E. Glatstein and S. M. Hahn (2004) In vivo determination of the absorption and scattering spectra of the human prostate during photodynamic therapy. *Proc. SPIE* **5315**, 132–142.

Available online at www.sciencedirect.com
SCIENCE DIRECT®
Journal of Photochemistry and Photobiology B: Biology 79 (2005) 231–241
Journal of Photochemistry and Photobiology B:Biology
www.elsevier.com/locate/jphotobiol

Determination of the distribution of light, optical properties, drug concentration, and tissue oxygenation in-vivo in human prostate during motexafin lutetium-mediated photodynamic therapy

Timothy C. Zhu, Jarod C. Finlay, Stephen M. Hahn *

Department of Radiation Oncology, Hospital of the University of Pennsylvania, 3400 Spruce Street, Philadelphia, PA 19104-4283, USA

Received 21 June 2004; received in revised form 5 September 2004; accepted 10 September 2004
Available online 2 December 2004

Abstract

It is desirable to quantify the distribution of the light fluence rate, the optical properties, the drug concentration, and the tissue oxygenation for photodynamic therapy (PDT) of prostate cancer. We have developed an integrated system to determine these quantities before and after PDT treatment using motorized probes. The optical properties (absorption (μ_a), transport scattering (μ_s'), and effective attenuation (μ_{eff}) coefficients) of cancerous human prostate were measured in-vivo using interstitial isotropic detectors. Measurements were made at 732 nm before and after motexafin lutetium (MLu) mediated PDT at different locations along each catheter. The light fluence rate distribution was also measured along the catheters during PDT. Diffuse absorption spectroscopy measurement using a white light source allows extrapolation of the distribution of oxygen saturation (StO_2), total blood volume ($[Hb]_t$), and MLu concentration. The distribution of drug concentration was also studied using fluorescence from a single optical fiber, and was found to be in good agreement with the values determined by absorption spectroscopy. This study shows significant inter- and intra-prostatic variations in the tissue optical properties and MLu drug distribution, suggesting that a real-time dosimetry measurement and feedback system for monitoring these values during treatment should be considered in future PDT studies.

Keywords: PDT; In-vivo; Optical properties; Prostate; MLu; Motexafin lutetium

1. Introduction

Prostate adenocarcinoma is the most common malignancy in men. In 2003, it was estimated that 220,900 cases of prostate adenocarcinoma were diagnosed in the United States [1]. Although the availability of serum prostate-specific antigen (PSA) measurement as a screening tool has resulted in earlier detection of the disease [2], prostate cancer still accounted for 28,900 deaths in 2003 [1].

Photodynamic therapy (PDT) is an emerging treatment modality based on the interaction of light, a photosensitizing drug, and oxygen [3]. PDT has been a proposed treatment for a variety of malignancies and premalignant conditions. PDT has been approved by the US Food and Drug Administration for the treatment of microinvasive lung cancer, obstructing lung cancer, and obstructing esophageal cancer. The prostate gland is an organ that appears to be a good target for interstitial PDT. Tumors of the prostate are often confined to the prostate itself and brachytherapy techniques used for the placement of radioactive seed implants can be adapted for the placement of interstitial optical fibers [4]. Several preclinical studies have evaluated the feasibility of delivering PDT to the prostate via this interstitial approach [5–10]. A trial of interstitial prostate PDT in humans has been reported [11]. Nathan et al. treated

* Corresponding author. Tel.: +1 215 662 7296; fax: +1 215 349 5445.
E-mail address: hahn@xrt.upenn.edu (S.M. Hahn).

1011-1344/$ - see front matter © 2004 Elsevier B.V. All rights reserved.
doi:10.1016/j.jphotobiol.2004.09.013

14 men with locally recurrent prostate cancer using meso-tetrahydroxyphenyl chlorin (mTHPC)-mediated interstitial PDT. The light treatment was directed against regions from which biopsies showed cancer or which were suspicious on imaging studies.

Motexafin lutetium (MLu) is a water-soluble second generation synthetic photoactive drug that has a Q-band absorption peak at 732 nm [12,13]. Based on a feasibility and toxicity study in a canine prostate model [9], we have started a phase I study of MLu-mediated PDT for prostate cancer [14]. In the canine study, comprehensive treatment of the prostate gland was achieved with MLu-mediated PDT using an interstitial approach. The development of this light delivery technique has necessitated an improved understanding of PDT dosimetry, critical for determining the efficacy of the PDT treatment.

Explicit PDT dosimetry includes quantifying the light and tissue optical properties, the drug concentration, and the tissue oxygenation. The light fluence (expressed in J/cm^2) is a measure of light energy imparted to tissue. The total fluence in tissues is a function not only of the incident light delivered by the laser but also of scattered light. Often clinical PDT treatments are prescribed in terms of the incident light delivered from the laser rather than the total fluence of light the tissues receive which is a combination of scattered and incident light. Dosimetry systems using isotropic light detectors have been developed to measure both incident and scattered light [15,16]. These systems allow us to measure and therefore prescribe a consistent total fluence to the tissues.

Several investigators have attempted to characterize the optical properties of prostate tissue in animals [17–19] and in humans [20–22] to more reliably predict the in vivo light distribution. Using diffusion theory for a point source, the absorption and transport scattering coefficients of a particular tissue can be determined, yielding the effective attenuation coefficient, which provides a measure of light penetration in that tissue [18]. This measurement is a critical factor in planning interstitial light source placement. To include the drug concentration in the evaluation of PDT efficacy, in situ measurements of photosensitizer fluorescence emission are made in the prostate using a single optical fiber, originally developed for surface application by Diamond et al. [23]. We have modified their technique by replacing the flat cut fiber with a side fire fiber to introduce light interstitially to the target tissue more efficiently. It has also been shown that one can determine MLu concentration using diffuse absorption spectra [24]. The MLu concentration in prostate tissue can be determined using a slightly modified technique via an interstitial approach [25]. The MLu tissue concentrations determined from absorption spectra can be compared to those obtained using fluorescence spectra. Using the same diffuse absorption spectra, it is also possible to determine the concentrations of deoxyhemoglobin ([Hb]) and oxyhemoglobin ([HbO_2]) [24–27]. To determine the tissue oxygenation, the oxygen saturation ratio $StO_2 = [HbO_2]/([Hb] + [HbO_2])$ and total hemoglobin concentration $[Hb]_t = [Hb] + [HbO_2]$ can be calculated.

In this study, we review our preliminary observations measuring the interstitial distribution of light fluence rate, optical properties, tissue MLu concentration, and tissue oxygenation in two patients with prostate cancer. Measurements were made before and after PDT treatment in which the entire prostate was treated. Intraprostatic as well as interprostatic differences were evaluated.

2. Materials and methods

2.1. Patient selection, surgical and PDT procedure

A Phase I clinical trial of PDT with MLu in patients with locally recurrent prostate carcinoma was initiated at the University of Pennsylvania in 1999. The protocol was approved by the Institutional Review board of the University of Pennsylvania, the Clinical Trials and Scientific Monitoring Committee (CTSRMC) of the University of Pennsylvania Cancer Center, and the Cancer Therapy Evaluation Program (CTEP) of the National Cancer Institute. Each patient who signed the informed consent document underwent an evaluation, which included an MRI of the prostate, bone scan, laboratory studies including PSA, and a urological evaluation. Approximately two weeks prior to the scheduled treatment a transrectal ultrasound (TRUS) was performed for treatment planning. A urologist drew the target volume (the prostate) on each slice of the ultrasound images. These images were spaced 0.5 cm apart and were scanned with the same ultrasound unit used for treatment. A built-in template with a 0.5-cm grid projected the locations of possible light sources relative to the prostate. A treatment plan was then prepared to determine the location and length of light sources. Cylindrical diffusing fibers (CDF's) with active lengths 1, 2, 3, 4, and 5 cm were used. The sources were spaced one centimeter apart and the light power per unit length was the same for all CDF's. The length of a light source at a particular position was selected to cover the full length of the prostate. In the final plan, the prostate was divided into four quadrants. Four isotropic detectors were used, each placed in the center of one quadrant. A fifth isotropic detector was placed in a urethral catheter to monitor the light fluence in the urethra.

The patients were anesthetized in the operating room with general anesthesia to minimize patient movement during the procedure. Transrectal ultrasound-guided biopsies for MLu measurements were obtained prior to light delivery. The same ultrasound unit used to perform the pretreatment TRUS was used to guide needle

placement in the operating room. A template was attached to the ultrasound unit and was matched to the 0.5-cm grid used for treatment planning. Four detector catheters (one for each quadrant) were inserted into the prostate. These detectors were kept in place during the entire light delivery period. The pre-planned treatment catheters for light sources were then inserted 0.5 or 0.7 cm away from the detector catheters. These source catheters were used for light delivery as well as optical properties and absorption spectra measurements. The optical properties and absorption spectra of the prostate in each quadrant were then measured before light delivery using these existing detectors. A point light source was inserted into one source catheter. Fluorescence measurements were made through the detector catheter in each quadrant using a single optical fiber acting as both a light source and a detector. The fiber introduced 460 nm light and collected fluorescence light above 700 nm at right angles from the optical axis of the beveled fiber tip. The distribution measurements of optical properties, absorption spectra and fluorescence were completed in approximately 10 min. Light delivery was then performed one quadrant at a time by inserting the CDFs into the source catheters. The treatment time for each quadrant was dependent on the detector reading in that quadrant. The light fluence rate distributions were measured during PDT along the catheters. Cumulative fluences of 50 and 100 J/cm^2 were delivered to patients 12 and 13, respectively. After light delivery, the optical properties and absorption and fluorescence of the prostate in all four quadrants were measured again. The light sources and detectors were then removed and post-treatment biopsies were performed.

2.2. Computer controlled step motors

Two step motors were used to control the movement of the light source and the isotropic detector during optical property measurements (see Fig. 1(a)). Each step motor and translational stage had a maximum range of 20 cm and a maximum speed of 12.5 mm/s. The step motor produced 400 pulses per rotation, which translated to a resolution of 0.0025 mm. Control software was developed to integrate the movement of the step motor with data acquisition of isotropic detectors as well as the spectrometer for fluorescence and absorption spectra measurements. For the integrated system, the positioning accuracy was 0.1 mm. The data acquisition system was programmed to acquire data every 0.05 mm of detector movement.

To determine the relative position between the light source and the isotropic detector for optical properties or absorption spectra measurements, software was developed to automatically reset the position of the peak fluence rate as the zero position. This point corresponded to the point with the shortest distance between the line defined by the detector catheter and the point source. A similar scan was used for a white light source to determine the relative distances between the light source and the locations where the diffuse absorption spectra were taken, typically at $x = -0.4$, -0.2, 0, 0.2, 0.4, 0.6, 0.8, 1.0, 1.2, 1.4, and 1.6 cm. The position of the light source was defined as the distance of the source from the tip of catheter, intended to be placed at the apex of the prostate under ultrasound guidance.

2.3. Measurement of optical properties at the treatment wavelength

The transport scattering (μ_s') and absorption (μ_a) coefficients characterize the scattering and absorption properties of tissue. Within the diffusion approximation, the light fluence rate ϕ at a distance r from a point source of source strength, S, can be expressed as [28]

$$\phi = \frac{S \cdot \mu_{\text{eff}}^2}{4\pi r \cdot \mu_a} e^{-\mu_{\text{eff}} \cdot r} = \frac{S \cdot 3\mu_s'}{4\pi r} e^{-\mu_{\text{eff}} \cdot r}, \quad (1)$$

where S is the strength of the point source; $\phi(r)$ is the fluence rate at position r; $\mu_{\text{eff}} = \sqrt{3 \cdot \mu_a \cdot \mu_s'}$ is the effective attenuation coefficient in tissues and is applicable for a wider range of μ_a and μ_s' combinations than the traditional definition of $\mu_{\text{eff}} = \sqrt{3 \cdot \mu_a \cdot (\mu_s' + \mu_a)}$ [29]. $r = \sqrt{x^2 + h^2}$, where x and h are the parallel and perpendicular distance from the center of the point source (see Fig. 1(b)). The two free parameters (μ_a and μ_s') are inherently separable in that for a point source with a given source strength, the magnitude of the fluence rate near the light source ($x = 0$) is determined by μ_s' only and the slope of the spatial decay of the light fluence rate is determined by μ_{eff} only.

In theory, measurements of ϕ at two different distances r from the point source with source strength S are sufficient to determine both μ_a and μ_s'. Measurements at multiple sites allow evaluating the variation of these optical characteristics within the prostate volume. Since Eq. (1) is a non-linear equation of two free parameters μ_a and μ_s', we used the differential evolution algorithm developed by Storn et al. [30]. This algorithm is simple, and converges faster and is more robust than adaptive simulated annealing or the annealed Nelder and Mead approach [30]. We modified the algorithm to require that all free parameters (μ_a and μ_s' in this case) are positive [31]. The deviations between measurement and fit are represented by standard deviation, $\sum_{i=1}^{n} \sqrt{(\text{fit}_i - \text{meas}_i)^2/(n-1)}$, where n is the number of data points involved in the fit.

2.4. Calibration of the isotropic detector

Isotropic detectors described by Marijnissen and Star [32] were used as detectors in this study. Each isotropic

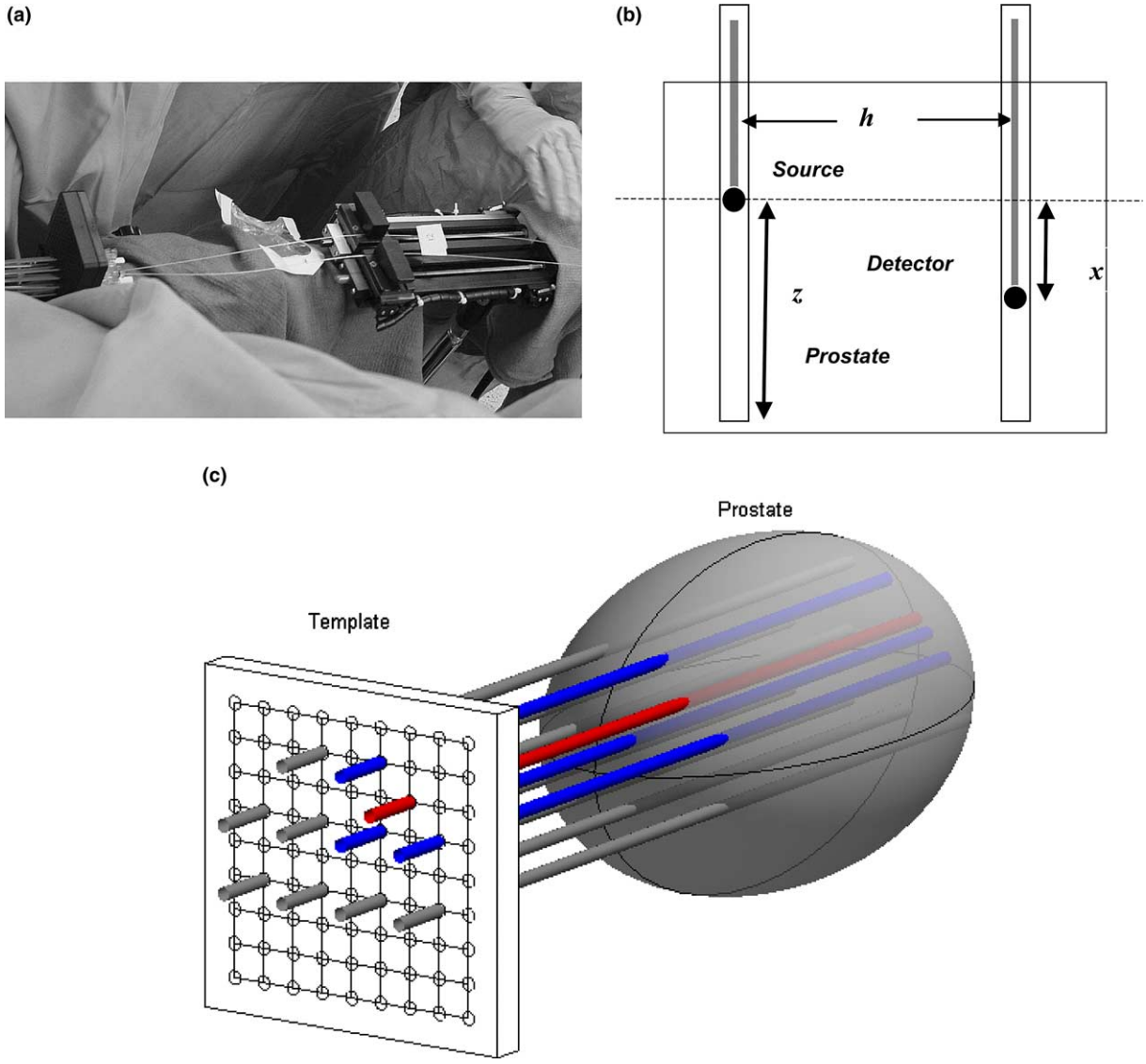

Fig. 1. (a) Photograph and (b) Schematic of the measurement geometry, illustrating the setup for measurement of distribution of light fluence rate, optical properties, and diffuse absorption spectra. Two step motors are used, one for the light source and the other for the detector. The distribution of light fluence rate was determined by moving the detector in a catheter during initial PDT treatment. The experimental setup for the optical properties and absorption spectra measurement is identical except a different light source (732 nm vs. white light) was used. The distribution of optical properties and absorption spectra was determined by moving both a point source (by z from the end of catheter) and a detector (by x from the point source location) before and after PDT treatment. The fluorescence distribution is achieved using a single side firing fiber used as both a light source and light detector. (c) 3D graph of the arrangement of catheters in a typical prostate treatment. The left upper quadrant's treatment (blue) and detector (red) catheters are shown in color for emphasis. The remaining catheters are for treatment of the other quadrants. The detector catheters for these quadrants are not shown.

detector was made of an optical fiber with a spherical tip made of TiO_2 (a scattering material). The isotropic detectors were made by Rare Earth Medical (now CardioFocus, Norton, MA) and had an isotropy of better than ±30% from any direction except for angles within 30° of the optical fiber attachment point. Each detector fiber was connected to a photodiode via a SMA connector. The measured photovoltage (V) from the isotropic detector was converted to light fluence rate using:

$$\phi = a(V - b), \quad (2)$$

where a is the conversion factor and b characterizes the leakage of the photodiode. This calibration was performed under collimated 732-nm laser light in air. When the isotropic detector was used to measure fluence rate in tissue (or in a liquid optical phantom), a tissue (or water) correction factor of 2.0 was used [32]. In our case, the 1 mm inner diameter catheter is filled with air, but the detector tissue correction factor is still 2.0 as if the air is replaced by the outer most medium (tissue). The calibration of the isotropic detectors was checked to

be accurate to within 5% using an integrating sphere before each individual measurement.

A 12-channel light dosimetry system developed in the Department of Radiation Oncology at the University of Pennsylvania was used for all in situ dosimetry measurements. Five different isotropic detectors were used and the conversion factors were $a = 129–161$ and $a = 63–72$ mW/cm^2/V for the four isotropic detectors with 0.5 mm scattering tips and the isotropic detector with 1 mm scattering tip used in the urethra, respectively. For all isotropic detectors, b was found to be 0.020 V. The response was found to be linear over the light fluence rate range (0–1200 mW/cm^2) to within 5%.

2.5. Absorption and fluorescence spectroscopy measurements

To obtain absorption spectra, a method similar to the optical property measurement described above was used. In this case, the laser and photodiode detector were replaced with a white light source and a spectrograph, respectively. To calibrate the detector, the detection fiber and source fiber were both placed in the integrating sphere, and a reference spectrum was obtained by the CCD. The fluence rate measured at each wavelength was related to the source power at that wavelength by a constant factor determined by the geometry of the integrating sphere. This factor was calculated based on independent measurements at three wavelengths using a calibrated detector. With this calibration, the detector measures the ratio of fluence rate to source power. The fluence rate spectra between 650 and 800 nm were fit using a nonlinear fitting algorithm under the assumption that the reduced scattering spectrum had the form $\mu_s' = A\lambda^{-b}$, where λ is expressed in nm. The free parameters in the fit were A, b, and the absorption coefficients at 8 selected wavelengths. Once A and b were determined by this fit, the absorption coefficients at the remaining wavelengths were determined by a second fit in which the value of μ_s' was fixed at its predetermined value for each wavelength [25]. The measurement uncertainty of the absorption spectra has been examined in optical phantoms made of intralipid, MLu, and black ink, each with known absorption spectra. A comparison between the absorption spectra obtained by our measurement and analysis method and the absorption spectrum reconstructed from individual spectra of the phantom components shows that our algorithm can reconstruct μ_a with an uncertainty of approximately 5% for the wavelength range where absorption is appreciable, in the phantom case between 650–800 nm (data not shown).

Fluorescence spectra were acquired using an optical fiber with a beveled tip, which emits and collects light at right angles to its optical axis. Excitation light was provided by a 460-nm light-emitting diode (LED), and passed through a dichroic beamsplitter, which directed the fluorescence collected by the same fiber back into the spectrograph.

Both the absorption and fluorescence spectra were analyzed using the singular value decomposition fitting algorithm developed by Finlay et al. [33] to determine the contributions to the spectra of known absorbers or fluorophores. In addition to the spectra of known components, the basis set included a 61-term, exponentially weighted Fourier series designed to account for the presence of unknown absorbers or fluorophores [33]. In the case of absorption spectra, the known spectra were those of oxy- and deoxyhemoglobin, MLu and water. Because the absorption coefficient at each wavelength is determined absolutely, the absolute concentrations of the various absorbers can be determined quantitatively from their contributions to the complete absorption spectrum.

In the fluorescence case the basis spectra were the fluorescence of MLu and the background fluorescence originating in the catheter. The fitting algorithm allows the separation of these two components, allowing us to determine an MLu contribution free from background contamination. The MLu fluorescence was normalized by dividing by the catheter background to account for variations in lamp output. A single conversion factor of 12.9 mg/kg between normalized fluorescence signal at the peak wavelength (unitless) and MLu concentration (mg/kg) was established by comparing the signal obtained in one prostate in vivo to the MLu concentration at the same position determined by absorption spectroscopy. Once this factor was determined, the fluorescence could be analyzed independent of absorption measurements in each quadrant.

2.6. Photodynamic therapy and in-vivo light measurements

MLu (Pharmacyclics, Inc., Sunnyvale, CA) was administered at a dose of 2 mg/kg intravenously 3 h prior to light administration [12,13]. This drug-light interval was chosen because preclinical studies in other model systems demonstrated the greatest antitumor efficacy with this timing [12,34]. A 15-W diode laser, model 730 (Diomed, Ltd., Cambridge, United Kingdom) was used as the 732 nm light source.

Interstitial CDFs were placed in the gland using a template with evenly spaced holes, which was attached to the TRUS unit. For each light source, a 17-gauge plastic catheter (Flexi-needle from Best Industries, Inc., Springfield, VA) containing a metal trocar was placed through the template and into the prostate. The trocar was removed and replaced with the light diffuser.

The light energy delivered was prescribed based on in situ measured light fluence. Each patient received a light fluence between 50–100 J/cm^2. The maximum unit

length source strength in any one fiber was limited to 150 mW/cm. Measurements were taken at the above mentioned distances from the light source before and after light treatment in the four quadrants of each prostate. The light sources were moved along the catheter in several locations to quantify the variation of optical properties in the prostate gland along the catheter.

3. Results

Table 1 summarizes the treatment parameters and the measurements done for the two patients. We have made four types of measurements: (1) Distribution of light fluence rate; (2) Distribution of optical properties at treatment wavelength; (3) Distribution of absorption spectra; (4) Distribution of fluorescence spectra. Tissue oxygenation and MLu concentration can be extracted from absorption spectra in vivo. MLu concentration in vivo is also extracted from the fluorescence spectra.

3.1. Distribution of fluence rate

Fig. 2 shows the light fluence rate measured in three quadrants during PDT treatment of patient 13. Three curves are shown. The first, labeled 'RUQ' was taken by a detector in the right upper quadrant of the prostate during interstitial illumination of that quadrant. The light fluence rate for RUQ (solid line) between 1.5 and 2.5 cm was about 5 times as high as the rest of region (e.g., between 3 and 4.5 cm). This was caused by the loading pattern of the light sources, in which two 1-cm CDF's were placed at the apex of the prostate. The second curve, labeled 'LLQ' shows the light fluence rate that was measured in the left lower quadrant during illumination of the left upper quadrant, and demonstrates the possible extent of light spread between quadrants. The third curve labeled 'RLQ' shows light fluence rate that was taken in the right lower quadrant during treatment of that quadrant. The symbols correspond to the predicted light fluence rate from a point source with source strength of 35 mW based on the optical properties measured along the detector catheter. (The use of a cylindrical theoretical model is not feasible due to the varying optical properties along the catheters, thus point sources are used.) The corresponding loading patterns of CDF's ('o') and the locations of the detector ('x') are shown in the insert. The number next to each source channel indicates the length in cm of the corresponding CDF. All linear light sources started from the apex of the prostate ($z = 0$ cm).

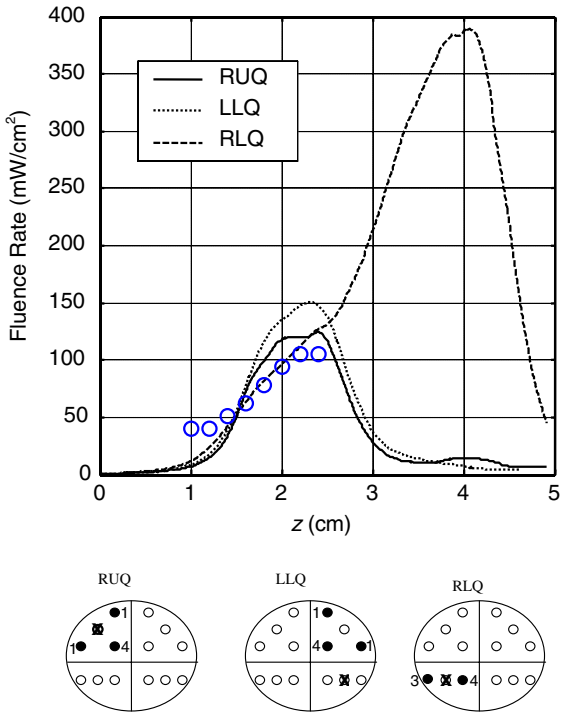

Fig. 2. Distribution of light fluence rate for 732 nm light in-vivo during PDT. The profile measured in the LLQ was acquired during illumination of the LUQ and indicates the spread of light between adjacent quadrants. The open circles indicate the fluence rate at 0.5 cm from the source predicted by the diffusion theory using the optical properties measured at various points in the RLQ. The geometry of each measurement is shown in the diagrams below the figure. In each case, an end-view of the prostate is shown. The measurement channel in each case is marked by an 'x', and the filled circles indicate the channels delivering illumination. The length in cm of the cylindrical diffuser in each channel is indicated in the diagram.

We did not measure significant light fluence rate in urethra for the 12 patients treated so far.

Table 1
Variation of tissue optical properties, tissue concentration of MLu, and tissue oxygenation among the two patients before and after PDT

Patient number	Light fluence (J/cm^2)	Measurement conditions	μ_a (cm^{-1})	μ_s' (cm^{-1})	μ_{eff} (cm^{-1})	MLu[a] (ng/mg)	[Hb]$_t$ (μM)	StO_2 (%)
12	50	Before PDT	0.3–1.6	1.2–18	1.9–5.4	2.5–5.0	–	–
		After PDT	0.25–0.5	5.9–39	2.5–5.0	0.4–1.7	–	–
13	100	Before PDT	0.11–0.9	7.5–40	2.2–6.3	1.4–9.2	51–310	79–88
		After PDT	0.13–0.6	5.5–34	2.2–5.2	1.1–8.1	55–370	67–89

The range specifies the minimum and maximum values of the measured quantities at different locations. Both patients received 2 mg/kg MLu intravenously at a drug-treatment interval of 3 h.

[a] For patient #12, the MLu concentration is determined from the fluorescence measurement.

3.2. Optical properties at treatment wavelength

A typical profile scan from a point source is shown in Fig. 3. The data were fitted using Eq. (1) to obtain the optical properties. The optical properties derived from both patients are shown in Fig. 4. These data show the variation of measured absorption coefficients and effective absorption coefficient vs. positions along the catheters in the prostate gland of patient #12 (a and b) and patient #13 (c and d). Due to time constraints we did not measure LUQ after PDT for patient #12. We did not get any results (before and after PDT) for LLQ of patient #12 and #13 due to bleeding. The effective attenuation coefficients varied between 1.9 and 6.3 cm^{-1} while the absorption coefficients varied between 0.1 and 1.6 cm^{-1}. As a result of the heterogeneity of optical properties, the light fluence rates per unit source strength at 0.5 cm from the point source varied between 0.2 and 0.6 cm^{-2} between the two patients.

3.3. Absorption spectra

A typical absorption spectrum acquired in vivo is shown in Fig. 5(a), along with the components of the spectrum as determined by linear fitting. The dominant absorbers in the wavelength region of our measurement are hemoglobin in its oxygenated and deoxygenated forms, MLu, and, to a lesser extent, water. In the cases presented here, the contribution of the Fourier synthesis was smaller than the contributions of known absorbers, indicating that the majority of absorption in tissue was accurately accounted for by our basis set. From the contributions of oxy- and deoxyhemoglobin to the measured absorption spectrum, we determined the total hemoglobin concentration $[Hb]_t$, the sensitizer concentration [MLu], and the hemoglobin oxygen saturation StO_2, given by

$$StO_2 = [HbO_2]/([Hb] + [HbO_2]). \quad (3)$$

The values of these three parameters as functions of position within a typical prostate quadrant (RUQ, patient 13), are plotted in Fig. 6(a). The concentration of MLu is given in ng mg^{-1} and has been scaled by a factor of 10 for comparison with the hemoglobin concentration and saturation.

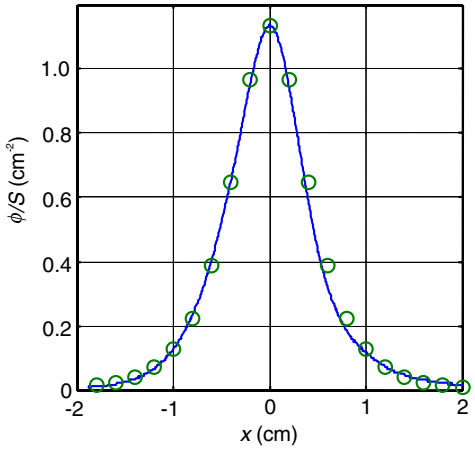

Fig. 3. Measured light fluence rate per unit source strength (ϕ/S) at 732 nm versus distances along the catheter, x, from the point source measured in-vivo in human prostate gland for patient #13. Line is measured data and symbols are fits. The optical properties are: o – $\mu_a = 0.23$ cm^{-1}, $\mu_s' = 7.3$ cm^{-1}, $\phi(0.5)/S = 1.1$ cm^{-2}, $h = 0.5$. Similar measurements were made for different wavelengths for the absorption spectra, although the measurements are now made at only 11 points between −0.4 and 1.6 cm with 0.2 cm steps.

3.4. Fluorescence spectra

The concentration of MLu via its intrinsic fluorescence emission was also measured around 750 nm. A typical fluorescence spectrum is shown in Fig. 5(b). The singular value decomposition fitting algorithm is able to separate the component arising from the background fluorescence of the catheter and fiber assembly (labeled 'Bkgnd') from the MLu component. The small amplitude of the Fourier component indicates that the fluorescence is dominated by these two contributions. The background fluorescence provides a measure of the lamp intensity, and is used to normalize the MLu fluorescence. The MLu distribution determined by fluorescence spectroscopy is overlaid on the corresponding distribution determined by absorption spectroscopy in Fig. 6(b). The spatial distribution of MLu determined by the two methods is similar.

4. Discussion

The main objective of this work was to demonstrate the feasibility of measuring the distribution of important dosimetric parameters for PDT in vivo, namely the tissue optical properties, tissue concentration of drug, and tissue oxygenation. Measurements were made before, during and after PDT. Differences within and between patients were also evaluated.

4.1. Distribution of light fluence rate in vivo

Our data show that there is heterogeneity of light fluence in different regions of the prostate (Fig. 2). The data also show that light delivery to one quadrant of the prostate may lead to the delivery of measurable light fluence to other regions of the prostate. For the region of high fluence rate, there were three CDFs contributing to light fluence rate, due to the contributions from the two 1-cm long CDFs and the one 4-cm long CDF. For the region of low fluence rate, only the 4-cm long linear fiber was contributing to the light fluence rate. A similar explanation can also be used for the fluence

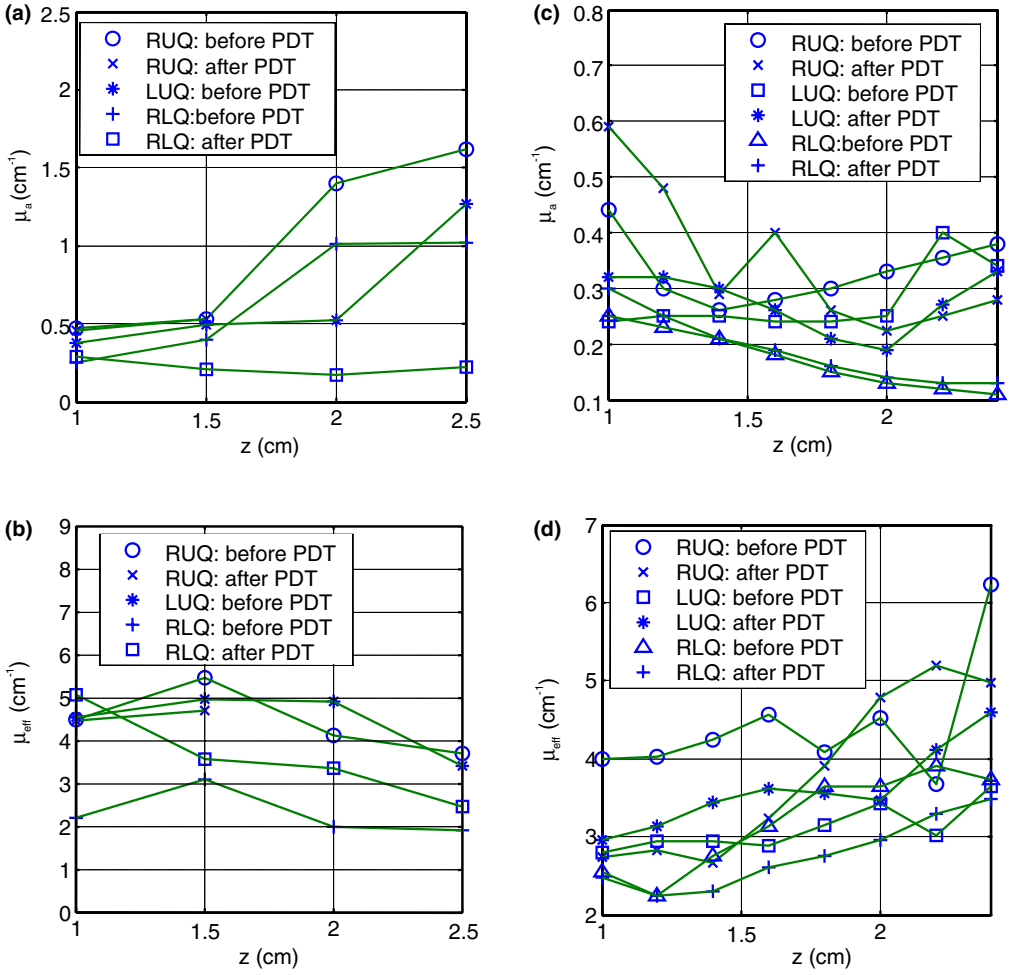

Fig. 4. In-vivo distribution of (a) absorption and (b) effective attenuation coefficients at 732 nm in the human prostate for patient #12. (c) absorption and (d) effective attenuation coefficients at 732 nm in the human prostate for patient #13.

rate distribution in the LLQ. The light fluence rate for the RLQ was much larger than that for the RUQ, which can be explained by differences in optical properties. In the RLQ, two similar length CDF's were used (3 and 4 cm). If the tissue optical properties were uniform along the catheter, the profile would have been uniform. However, the profile of light fluence rate is not uniform because the optical properties change along the catheter. The predicted light fluence rate for a 35 mW source based on measured optical properties (μ_a and μ_{eff}) is indicated by symbols. The similarity in shape between the measured and the predicted light fluence rate indicates the variation of light fluence rate was due to the variation of optical properties.

4.2. Distribution of optical properties at treatment wavelength

Fig. 3 shows a typical example of measured fluence rate per source strength from a point source. The measured profile usually contains 800 data points at 0.05 mm steps. The fitting assumes that the distance h between the source and detector catheter is also a free variable, which is allowed to vary up to 0.2 cm from the known separation determined from the template positions. We used the same method to obtain the absorption spectra from a white light source using a somewhat longer step size (0.2 cm) in the range of −0.4 to 1.6 cm relative to the point source.

The intra-prostatic tissue heterogeneity of the optical properties at 732 nm is demonstrated in Fig. 4. For the same patient, the effective attenuation coefficient, μ_{eff}, varied by up to 3 times between different quadrants of the same prostate (Fig. 4(d)). This large variation of optical properties resulted in a large difference in light fluence rate between the right upper quadrant (RUQ) and the right lower quadrant (RLQ) (see Fig. 2). Within the same quadrant of a prostate, μ_{eff} can change substantially as well. Since each CDF has uniform light strength along the catheter, the variation of optical properties can result in large variation of light fluence rate along the catheter, as demonstrated by the case of

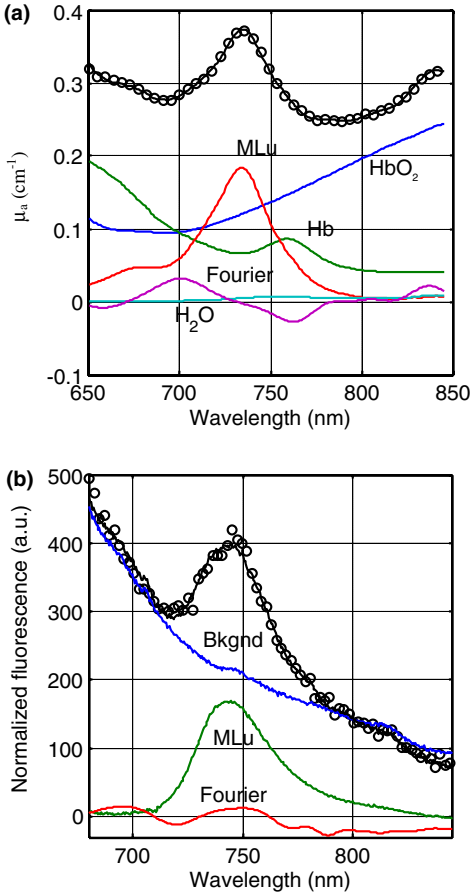

Fig. 5. Components of (a) absorption spectra and (b) fluorescence spectra acquired prior to PDT from the LUQ of patient #13. In each case, the measured data are labeled as symbols ('o') and the components are labeled as lines. The components include: MLu, water (H_2O), deoxyhemoglobin (Hb), and hemoglobin (HbO_2). The 'Fourier' component is a Fourier series designed to account for unknown absorbers or fluorophores.

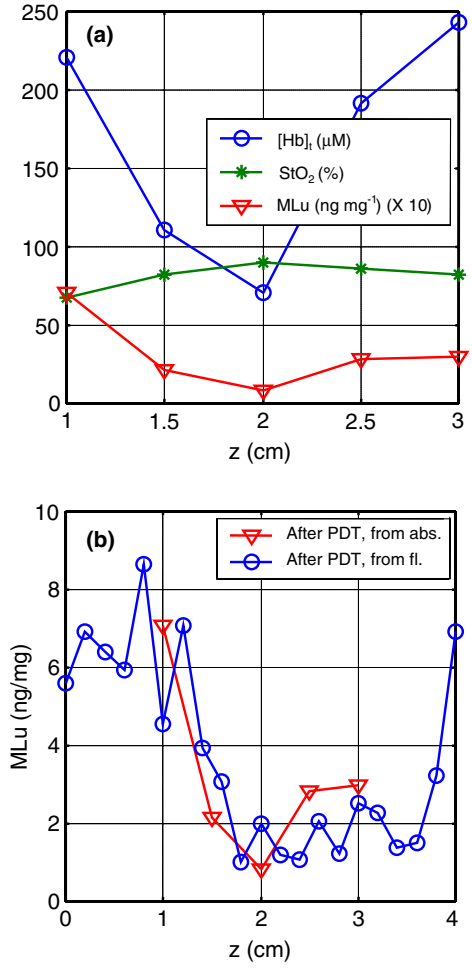

Fig. 6. In vivo distribution of (a) StO_2, blood volume (μM), and MLu concentration determined using the absorption spectra and (b) MLu concentration as determined by absorption spectra (triangles) and fluorescence (circles) measurements for RUQ in patient 13.

the RLQ. Since our model assumes the optical properties of the medium to be homogeneous, the measured optical properties has limitation in that it should be an average of tissue optical properties within the maximum distance between the source and the detector, typically 2 cm (see Fig. 3).

The measurement standard deviation of μ_a, μ_s' and μ_{eff} is 7%, 20%, and 5%, respectively, when h is optimized in the fitting [35]. Details of the error analysis are included in [35].

Since our model assumes infinite medium, we make sure that the measurement points are at least 1 cm away from the boundaries of prostate to minimize the boundary effect. The starting position of the point source is moved 1 cm from the end of the catheter before optical properties measurement. The reduction of the light fluence rate at the tissue boundary has been characterized in a solid prostate phantom to be less than 2% at 1 cm from the boundary at 732 nm for the range of optical properties used in the study [36].

We have demonstrated in canine prostate that the absorption coefficient at 732 nm is approximately proportional to the tissue concentration of MLu [19]. This linear relationship is assumed to hold for human prostate as well. Since μ_a varied by up to 2.5 times along some catheters (Fig. 4(c), RUQ, after PDT), the tissue concentration of MLu should vary by the same magnitude along the catheter. This is consistent with the distribution of MLu concentration measured by absorption spectra and fluorescence in the same location (see Fig. 6(b)).

4.3. Distribution of absorption and fluorescence spectrum

Fig. 5(a) illustrates how one can extract the concentrations of oxyhemoglobin (HbO_2), deoxyhemoglobin (Hb), and MLu from the measured absorption spectrum. Because the absorption spectrum is determined by fitting data using Eq. (1) at each wavelength

independently without the knowledge of the known spectral components [25], and because the sum of known components accurately fits the extracted spectrum with little absorption accounted for by the Fourier components, we are very confident of extracted MLu, HbO_2 and Hb concentrations. Since the average optical penetration depth ($\delta = 1/\mu_{eff}$) at 732 nm is about 0.4 cm in human prostate and the separation between the detector and the light source (0.5–1.5 cm) is generally larger than δ, the extracted quantities reflect a macroscopic average in a tissue dimension of 0.5–1.5 cm, depending on the separation between the detector and the light source. Fig. 5(b) shows the corresponding analysis of a typical fluorescence spectrum. The MLu concentration obtained from each spectrum is normalized to the background signal and therefore the measured MLu concentration is insensitive to variations in lamp intensity and fiber coupling efficiency. The inherent absorption by tissue is much greater at the excitation wavelength (460 nm) than the wavelengths over which we measure absorption spectra. The generation of fluorescence is therefore confined to a smaller region of tissue than that sampled by the absorption spectra measurement.

Fig. 6 illustrates the variation in total hemoglobin concentration, hemoglobin saturation, and MLu concentration within one quadrant of a typical prostate. The variation in measured $[Hb]_t$ and [MLu] likely result from variations in vascular density or perfusion, limiting the supply of drug and blood to some regions of the tissue. The agreement in the shape of the distributions of MLu determined by absorption and fluorescence spectroscopy demonstrates the ability of both methods to give quantitative information concerning the distribution of drug in vivo. While the two methods give similar information, each has its advantages. The absorption spectra measurement gives not only the drug distribution but hemodynamic information as well. The fluorescence measurement, on the other hand, samples a much smaller volume of tissue than the absorption spectra measurement, and samples many more points than is practical for absorption spectra measurements, allowing a higher-resolution map of the spatial drug distribution.

Table 1 shows the variation of optical properties before and after PDT. For patient 12, we have observed substantial reduction of MLu tissue concentration after PDT treatment, presumably due to photobleaching. A smaller reduction of MLu tissue concentration was observed for patient 13. The absorption coefficient, which has been shown to be approximately linear to MLu tissue concentration, also decreased after PDT treatment, more for patient 12 than for patient 13. The effective attenuation coefficient also varied after PDT, although the magnitude of the change was generally much smaller.

5. Conclusions

We have demonstrated inter- and intra-prostate variation of optical properties and MLu tissue concentration. The variation of optical properties can be used to explain the observed variation of light fluence rate. We observed that the optical penetration depth varied between 0.15–0.5 cm for 732 nm light within one prostate. The tissue concentration of MLu varied between 1.1 and 8 ng/mg within one prostate. These studies confirm substantial inter-organ and intra-organ variations in optical properties and drug concentration in the prostates. Given this heterogeneity, a real-time dosimetry measurement and feedback system for monitoring light fluences during treatment should be considered for interstitial prostate PDT studies.

Acknowledgement

This work is supported by a grant from National Institute of Health (NIH), R21 CA88064-01 and P01 CA87971-01, and Department of Defense (DOD), DAMD1703-1-0132.

References

[1] A. Jemal, T. Murray, A. Samuels, A. Ghafoor, E. Ward, M.J. Thun, Cancer statistics, 2003, CA – A Cancer Journal for Clinicians 53 (2003) 5–26.
[2] W.J. Catalona, Screening for early detection, Lancet 347 (1996) 883–884.
[3] T.J. Dougherty, D.J. Gomer, B.W. Henderson, et al., Photodynamic therapy, J. Natl. Cancer. Inst. 90 (1998) 889–905.
[4] A.V. D'Amico, Role of interstitial radiotherapy in the management of clinically organ-confined prostate cancer: the jury is still out, J. Clin. Oncol. 14 (1996) 304–315.
[5] L.K. Lee, C. Whitehurst, Q. Chen, M.L. Pantelides, F.W. Hetzel, J.V. Moore, Interstitial photodynamic therapy in the canine prostate, Br. J. Urol. 80 (1997) 898–902.
[6] S.C. Chang, G. Buonaccorsi, A. MacRobert, S.G. Bown, Interstitial photodynamic therapy of the canine prostate using meso-tetra- (m-hydroxyphenyl) chlorin, Int. J. Cancer 67 (1996) 555–562.
[7] S.C. Chang, G. Buonaccorsi, A. MacRobert, S.G. Bown, Interstitial photodynamic therapy of the canine prostate with disulfonated aluminum phthalocyanine and 5-aminolevulinic acid-induced protoporphyrin IX, Prostate 32 (1997) 89–98.
[8] S.H. Selman, R.W. Keck, J.A. Hampton, Transperineal photodynamic ablation of the canine prostate, J. Urol. 156 (1996) 258–260.
[9] R.A. Hsi, A. Kapatkin, J. Strandberg, T. Zhu, T. Vulcan, M. Solonenko, C. Rodriguez, J. Chang, M. Saunders, N. Mason, S. Hahn, Photodynamic therapy in the canine prostate using motexafin lutetium, Clin. Cancer Res. 7 (2001) 651–660.
[10] Q. Chen, Z. Huang, D. Luck, J. Beckers, P.H. Brun, B.C. Wilson, A. Scherz, Y. Salomon, F.W. Hetzel, Preclinical studies in normal canine prostate of a novel palladium-bacteriopheophorbide (WST09) photosensitizer for photodynamic therapy of prostate cancers, Photochem. Photobiol. 76 (4) (2002) 438–445.

[11] T.R. Nathan, D.E. Whitelaw, S.C. Chang, W.R. Lees, P.M. Ripley, H. Payne, L. Jones, M.C. Parkinson, M. Emberton, A.R. Gillams, A.R. Mundy, S.G. Bowen, Photodynamic therapy for Prostate cancer recurrence after radiotherapy: a phase I study, J. Urol. 168 (2002) 1427–1432.
[12] S.W. Young, K.W. Woodburn, M. Wright, T.D. Mody, Q. Fan, J.L. Sessler, W.C. Dow, R.A. Miller, Lutetium texaphyrin (PCI-0123): a near-infrared, water-soluble photosensitizer, Photochem. Photobiol. 63 (1996) 892–897.
[13] T.D. Mody, L. Fu, J.L. Sessler, Texaphyrins: synthesis and development of a novel class of therapeutic agents, in: K.D. Mody Karlin (Ed.), Progress in Inorg. Chem., John Wiley and Sons Ltd, Chichester, 2001, pp. 551–598.
[14] D.C. Stripp, R. Mick, T.C. Zhu, R. Whittington, D. Smith, A. Dimofte, J.C. Finlay, J. Miles, T.M. Busch, D. Shin, A. Kachur, Z.A. Tochner, S.B. Malkowicz, E. Glatstein, S.M. Hahn, Phase I trial of motexafin-lutetium-mediated interstitial photodynamic therapy in patients with locally recurrent prostate cancer, Proc. SPIE 5315 (2004) 88–99.
[15] P. Baas, L. Murrer, F.A.N. Zoetmulder, et al., Photodynamic therapy as adjuvant therapy in surgically treated pleural malignancies, Br. J. Cancer 76 (1997) 819–826.
[16] M. Solonenko, T.C. Zhu, T. Vulcan, Commissioning of the isotropic light dosimetry system for photodynamic therapy, Med. Phys. 26 (1999) 1124.
[17] M.R. Arnfield, J.D. Chapman, J. Tulip, M.C. Fenning, M.S. McPhee, Optical properties of experimental prostate tumors in vivo, Photochem. Photobiol. 57 (1993) 306–311.
[18] Q. Chen, B.C. Wilson, S.D. Shetty, M.S. Patterson, J.C. Cerny, F.W. Hetzel, Changes in vivo optical properties and light distributions in normal canine prostate during photodynamic therapy, Radiat. Res. 147 (1997) 86–91.
[19] T.C. Zhu, S.M. Hahn, A.S. Kapatkin, A. Dimofte, C.E. Rodriguez, T.G. Vulcan, E. Glatstein, R.A. Hsi, In vivo optical properties of normal canine prostate at 732 nm using motexafin lutetium-mediated photodynamic therapy, Photochem. Photobiol. 77 (2003) 81–88.
[20] M.L. Pantelides, C. Whitehurst, J.V. Moore, T.A. King, N.J. Blacklock, Photodynamic therapy for localized prostatic cancer: light penetration in the human prostate gland, J. Urol. 143 (1990) 398–401.
[21] C. Whitehurst, M.L. Pantelides, J.V. Moore, P.J.C. Brooman, N.J. Blacklock, In vivo laser light distribution in human prostatic carcinoma, J. Urol. 151 (1994) 1411–1415.
[22] L.K. Lee, C. Whitehurst, M.L. Pantelides, J.V. Moore, In situ comparison of 665 nm and 633 nm wavelength light penetration in the human prostate gland, Photochem. Photobiol. 62 (1995) 882–886.
[23] K.R. Diamond, M.S. Patterson, T.J. Farrell, Quantification of fluorophore concentration in tissue-simulating media by fluorescence measurements with a single optical fiber, Appl. Opt. 42 (2003) 2436–2442.
[24] M. Solonenko, R. Cheung, T.M. Busch, A. Kachur, G.M. Griffin, T. Vulcan, T.C. Zhu, H.W. Wang, S. Hahn, A.G. Yodh, In-vivo reflectance measurement of motexafin lutetium uptake, optical properties, and oxygenation of canine large bowels, kidneys, and prostates, Phys. Med. Biol. 47 (2002) 857–873.
[25] J.C. Finlay, T.C. Zhu, A. Dimofte, D. Stripp, S.B. Malkowicz, R. Whittington, J. Miles, E. Glatstein, S.M. Hahn, In vivo determination of the absorption and scattering spectra of the human prostate during photodynamic therapy, Proc. SPIE 5315 (2004) 132–142.
[26] R.M.P. Doornbos, R. Lang, M.C. Aalders, F.W. Cross, H.J.C.M. Sterenborg, The determination of in vivo human tissue optical properties and absolute chromophore concentrations using spatially resolved steady-state diffuse reflectance spectroscopy, Phys. Med. Biol. 44 (1999) 967–981.
[27] A. Kienle, L. Lilge, M.S. Patterson, R. Hibst, R. Steiner, B. Wilson, Spatially resolved absolute diffuse reflectance measurements for noninvasive determination of the optical scattering and absorptions of biological tissue, Appl. Opt. 35 (1996) 2304–2313.
[28] S.L. Jacques, Light Distributions from point, line and plane sources for photochemical reactions and fluorescence in turbid biological tissues, Photochem. Photobiol. 67 (1998) 23–32.
[29] T. Nakai, G. Nishimura, K. Yamamoto, M. Tamura, Expression of optical diffusion coefficient in high-absorption turbid media, Phys. Med. Biol. 42 (1997) 2541–2549.
[30] R. Storn, K. Price, Differential Evolution – a simple and efficient heuristic for global optimization over continuous spacesJ. Global Optimiz., vol. 11, Kluwer Academic Publishers, 1997, pp. 341–359.
[31] T.C. Zhu, B.E. Bjarngard, X. Ying, C.J. Yang, Modeling the output ratio in air for megavoltage photon beams, Med. Phys. 28 (2001) 925–937.
[32] J.P.A. Marijnissen, W.M. Star, Calibration of isotropic light dosimetry probes based on scattering bulbs in clear media, Phys. Med. Biol. 41 (1996) 1191–1208.
[33] J.C. Finlay, D.L. Conover, E.L. Hull, T.H. Foster, Porphyrin bleaching and PDT-induced spectral changes are irradiance dependent in ALA-sensitized normal rat skin in vivo, Photochem. Photobiol. 73 (2001) 54–63.
[34] K.W. Woodburn, Q. Fan, D.R. Miles, D. Kessel, Y. Luo, S.W. Young, Localization and efficacy analysis of the phototherapeutic Lutetium texaphyrin (PCI-0123) in the murine EMT6 sarcoma model, Photochem. Photobiol. 65 (1997) 410–415.
[35] T.C. Zhu, A. Dimofte, J.C. Finlay, D. Stripp, T. Busch, J. Miles, R. Whittington, S.B. Malkowicz, Z. Tochner, E. Glatstein, S.M. Hahn, Optical properties of human prostate at 732 nm measured in vivo during motexafin lutetium-mediated photodynamic therapy, Photochem. Photobiol. (2004) in press.
[36] A. Dimofte, T.C. Zhu, R.-G. Choe, S. Hahn, Interstitial light distribution at 730 nm prostate photodynamic therapy, Med. Phys. 28 (2001) 1186.

INSTITUTE OF PHYSICS PUBLISHING PHYSICS IN MEDICINE AND BIOLOGY

Phys. Med. Biol. **50** (2005) 2291–2311 doi:10.1088/0031-9155/50/10/008

A method for determination of the absorption and scattering properties interstitially in turbid media

Andreea Dimofte, Jarod C Finlay and Timothy C Zhu

Department of Radiation Oncology, University of Pennsylvania, Philadelphia, PA, USA

E-mail: tzhu@mail.med.upenn.edu

Received 10 February 2005, in final form 17 March 2005
Published 5 May 2005
Online at stacks.iop.org/PMB/50/2291

Abstract

We have developed a method to quickly determine tissue optical properties (absorption coefficient μ_a and transport scattering coefficient μ_s') by measuring the ratio of light fluence rate to source power along a linear channel at a fixed distance (5 mm) from an isotropic point source. Diffuse light is collected by an isotropic detector whose position is determined by a computer-controlled step motor, with a positioning accuracy of better than 0.1 mm. The system automatically records and plots the light fluence rate per unit source power as a function of position. The result is fitted with a diffusion equation to determine μ_a and μ_s'. We use an integrating sphere to calibrate each source–detector pair, thus reducing uncertainty of individual calibrations. To test the ability of this algorithm to accurately recover the optical properties of the tissue, we made measurements in tissue simulating phantoms consisting of Liposyn at concentrations of 0.23, 0.53 and 1.14% ($\mu_s' = 1.7$–9.1 cm^{-1}) in the presence of Higgins black India ink at concentrations of 0.002, 0.012 and 0.023% ($\mu_a = 0.1$–1 cm^{-1}). For comparison, the optical properties of each phantom are determined independently using broad-beam illumination. We find that μ_a and μ_s' can be determined by this method with a standard (maximum) deviation of 8% (15%) and 18% (32%) for μ_a and μ_s', respectively. The current method is effective for samples whose optical properties satisfy the requirement of the diffusion approximation. The error caused by the air cavity introduced by the catheter is small, except when μ_a is large ($\mu_a > 1$ cm^{-1}). We presented *in vivo* data measured in human prostate using this method.

(Some figures in this article are in colour only in the electronic version)

1. Introduction

The *in vivo* determination of tissue optical properties has been an area of extensive research. The optical properties include determination of tissue absorption coefficient (μ_a), scattering

coefficient (μ_s) and scattering anisotropy (g). The optical absorption and scattering properties of tissue can be used to calculate the fluence distribution of light during light-based treatments such as photodynamic therapy. In addition, the optical absorption of tissue can be used to monitor changes in the volume and oxygenation of blood and the perfusion of tissues (Liu *et al* 1995, Kienle *et al* 1996, Hull *et al* 1999, Rolfe 2000) and the distribution of exogenous absorbers (Doornbos *et al* 1999, Solonenko *et al* 2002). The scattering coefficient can be used to extract information about cellular structure of tissue (Mourant *et al* 1998, Gurjar *et al* 2001). In the near-infrared region ($\lambda = 600$–800 nm) where tissue scattering far exceeds tissue absorption, the diffusion approximation can be used (Star 1997). Under this approximation, only the linear term of the anisotropy in radiance is considered. A reduced scattering coefficient ($\mu_s' = \mu_s(1 - g)$) is, therefore, sufficient to describe all the tissue scattering properties.

Many techniques (e.g. relative fluence rate versus depth under uniform light illumination) can determine the effective attenuation coefficient, but cannot separate the effects of tissue scattering and absorption. μ_a and μ_s' can be determined separately using *ex vivo* measurements of the absorbing and scattering components of the sample; however, these methods are not practical for determining the optical properties *in vivo*. Existing *in vivo* methods of determining the optical properties of tissue rely on measurement of the diffuse reflectance on tissue surface. For CW reflectance measurements (Farrell and Patterson 1992, Nichols *et al* 1997, Hull *et al* 1998, Solonenko *et al* 2002, Doornbos *et al* 1999, Swartling *et al* 2003), the tissue is illuminated by a pencil-beam CW light source and the diffuse reflectance is recorded at different radial distances from the source. Time-resolved measurements use subnanosecond pulses from a laser (Patterson *et al* 1989, Pogue and Patterson 1994, Kienle and Patterson 1997a, 1997b, Coquoz *et al* 2001, Torricelli *et al* 2001). After a pulse passes through tissue, its time dispersion can be measured. In frequency domain methods, the source is sinusoidally modulated and modulation amplitude and phase shift of the detected signal are measured to obtain information about optical properties.

The diffuse reflectance techniques outlined above, which can determine μ_a and μ_s' simultaneously *in vivo,* cannot be used interstitially. Our goal is to develop an interstitial method that can be used *in vivo* to quickly determine both the absorption and the reduced scattering coefficients of tissue using a spatial CW method. For this, we have developed a device to quickly determine tissue optical properties by measuring the ratio of light fluence rate to the source power along a linear channel at a fixed distance (5 mm) from an isotropic point source. Diffuse light is collected by an isotropic detector whose position is determined by a computer-controlled step motor, with a positioning accuracy of better than 0.1 mm. The result is fitted with a diffusion equation, using a nonlinear optimization algorithm, to determine μ_a and μ_s'. This method has been applied to *in vivo* optical property measurements in human prostate.

2. Broad beam set-up

2.1. Description of the broad beam set-up

We determined the optical properties (μ_a and μ_s') of each optical phantom by measuring the fluence rate as a function of depth under broad beam illumination. We used an isotropic detector manufactured by CardioFocus, Inc (West Yarmouth, MA) that consists of an optical fibre with a 1-mm-diameter spherical scattering bulb at the tip to measure the fluence rate at different depths. The light collected by this detection fibre was measured and digitized by an *in vivo* dosimetry system (to be described later). The detector position was controlled by a computerized positioning system (Velmex, Inc, East Bloomfield, NY). The measurement

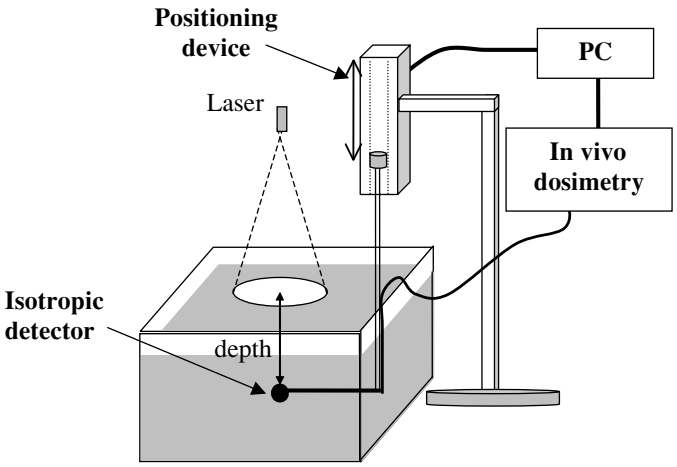

Figure 1. Experimental set-up for broad beam measurements. The optical properties of the Liposyn and ink used for the optical phantom were characterized independently using a broad parallel beam incident on the phantom. We used a 1 mm scattering tip isotropic detector to measure the fluence rate at different depths in the phantom using a step motor that has an accuracy of 0.1 mm. The measurements were made under five different conditions: one for Liposyn solution, three for Liposyn solution plus three ink concentrations with known optical properties, and one for pure water. The ratio between Liposyn (or Liposyn with ink) and water was fit to an exponential function: $\phi = k\exp(-\mu_{\rm eff}d)$, where $\mu_{\rm eff}$ is the effective attenuation coefficient. This ratio eliminates the effect of inverse-square law and the detector sensitivity variation between water and air for the isotropic detector.

set-up is shown in figure 1. For each optical phantom (Liposyn and ink) two scans were made, under the same broad beam illumination, one in the optical phantom, the other in pure water. The ratio of the two scans was used to correct for the detector response difference between air and water. The simultaneous measurements were made for nine different conditions: three Liposyn concentrations for each of the three ink concentrations. In addition, optical properties for a Liposyn phantom without ink were measured.

Analysis of the depth dependence of fluence rate in phantoms illuminated from above by a broad beam requires a one-dimensional solution to the diffusion equation. In this case, the ratio between fluence rates measured in Liposyn with ink and that measured in water was fit to an exponential function:

$$\phi = k\,\mathrm{e}^{-\mu_{\rm eff}d} \tag{1}$$

where $\mu_{\rm eff}$ is the effective attenuation coefficient. $\mu_{\rm s}'$ for the Liposyn and $\mu_{\rm a}$ for water were determined from $\mu_{\rm eff}$ and the $\mu_{\rm a}$ of ink deduced from the known ink concentration. Since $\mu_{\rm s}'$ should be independent of ink concentration for a particular Liposyn concentration, we took the average of the three extrapolated values of $\mu_{\rm s}'$ (one for each ink concentration) as the $\mu_{\rm s}'$ of each Liposyn phantom. The $\mu_{\rm a}$ for different ink concentrations was then determined from the best fit value of $\mu_{\rm eff}$ and the mean value of $\mu_{\rm s}'$ using the relation $\mu_{\rm eff} = \sqrt{3\mu_{\rm a}\mu_{\rm s}'}$. Although $\mu_{\rm eff} = \sqrt{3\mu_{\rm a}\mu_{\rm s}'}$ is an approximation of the expression $\mu_{\rm eff} = \sqrt{3\mu_{\rm a}(\mu_{\rm s}' + \mu_{\rm a})}$, Nakai *et al* (1997) have shown that this expression is valid over a wider range of optical properties, especially in cases of high absorption. The values of $\mu_{\rm a}$ determined by this method and those expected based on the known ink concentrations agreed to within 8%. The uncertainty in $\mu_{\rm eff}$, as determined by propagation of uncertainty based on the 1.5% uncertainty in our fluence measurements, is less than 0.1%. The true uncertainty of this measurement is, therefore, likely

Table 1. A summary of μ_a and μ_s' as a function of percentage concentration for scattering and absorbing materials used in the liquid optical phantom. c% is the percentage concentration of the scattering (or absorption) material in volume dissolved in water (in volume).

Brand	Wavelength (nm)	μ_s' (cm^{-1})	μ_a (cm^{-1})	Source
10% Intralipid	633	$\mu_s' = (11.2 \pm 0.11) \times$ c%	–	Moes *et al* (1989)
Nutralipid	630	$\mu_s' = 17.9 \times$ c% + 0.56	0.0026	Driver *et al* (1989)
10% Intralipid	400–1100	$\mu_s' = 11(\lambda/730)^{-2.4} \times$ c%	–	van Staveren *et al* (1997)
10% Intralipid	460–890	$\mu_s' = 4.4(\lambda/730)^{-2.33} \times$ c%	0.001–0.015	Flock *et al* (1992)
10% Intralipid	700	$\mu_s' = 7.33 \times$ c%	–	Mourant *et al* (1997)
30% Liposyn	730	$\mu_s' = 8.1 \times$ c%	0.020	This study
Higgins Ink	594	–	$\mu_a = 123 \times$ c%	Madsen *et al* (1992)
Higgins Ink	730	–	$\mu_a = 42.99 \times$ c%	This study

limited by the uncertainty in measuring the volumes of phantom components. To minimize this error, we used a pipettor which has an accuracy of 0.01 ml to accurately determine ink and Liposyn volumes of 2000 ml.

2.2. Liquid tissue-simulating phantom

The tissue simulating phantoms are made of separate scattering and absorbing components. The phantoms were placed in a plastic container that was painted in black and was large enough ($18.2 \times 14.6 \times 7.7$ cm^3) to avoid scattering from the boundary. This type of phantom has been described in the literature (Madsen *et al* 1992). The scattering media used are phospholipid emulsions (Liposyn III, 30% Abbott Lab, North Chicago, IL). The scattering coefficient and concentration of Liposyn are related by the expression,

$$\mu_s' = 8.1 \times (\text{c\%IL})\ \text{cm}^{-1} \tag{2}$$

where (c%IL) is the lipid concentration used. This formula was obtained for the specific batch of Liposyn used in the experiments reported here using the broad beam measurement described above.

We used Higgins black India ink #4418 (Higgins, Bellwood, IL) as the absorbing medium. The absorption coefficient dependence on ink concentration is given by:

$$\mu_a = 42.99 \times (\text{c\%ink})\ \text{cm}^{-1} \tag{3}$$

where (c%ink) is the ink concentration in per cent volume. This formula was obtained from transmission measurement of pure ink diluted in water.

Figure 2 shows the results of all experiments using the broad beam method for nine tissue simulating phantoms with Liposyn concentrations of: (A) 0.23%, (B) 0.53% and (C) 1.14% and ink concentrations of: 0.002%, 0.012% and 0.023%. The best fit scattering coefficients were: 1.73 cm^{-1} (with absorption coefficients of 0.10, 0.48 and 1.00 cm^{-1}); 4.19 cm^{-1} (with absorption coefficients of 0.10, 0.49 and 0.99 cm^{-1}) and 9.14 cm^{-1} (with absorption coefficients of 0.10, 0.50 and 0.99 cm^{-1}).

The optical properties of liquid tissue-simulating phantoms composed of Intralipid and ink have been extensively studied for different wavelengths by several investigators. A summary of the measured scattering and absorption coefficients measured by other people (Moes *et al* 1989, Driver *et al* 1989, Flock *et al* 1992, van Staveren *et al* 1997, Mourant *et al* 1997, Madsen *et al* 1992) and the results of this study are given in table 1.

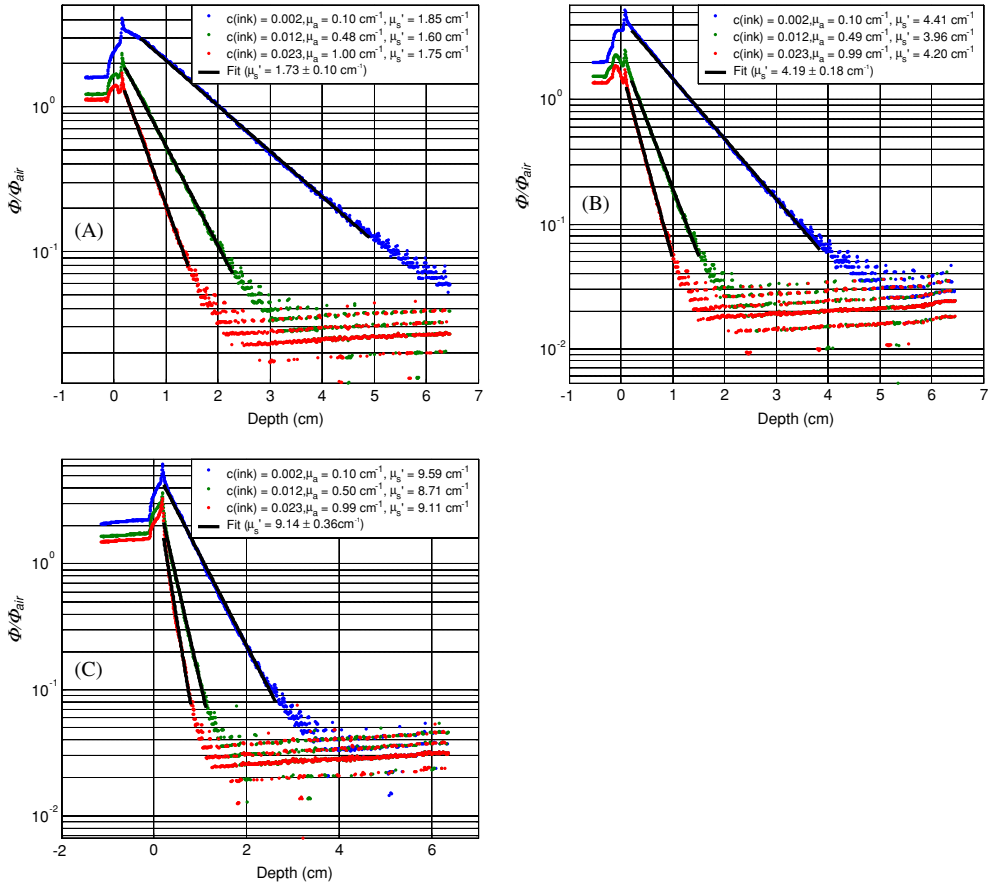

Figure 2. Optical properties characterization using broad beam method. Results are shown for three tissue simulating phantoms with Liposyn concentrations of: (A) 0.23%, (B) 0.53% and (C) 1.14%. For each Liposyn concentration phantom, we added three different concentrations of black ink: 0.002%, 0.012% and 0.023%. Symbols represent measurements with an isotropic detector. Solid lines are the best fit. The resulting optical properties were: (A) $\mu_s' = 1.78\ \mathrm{cm}^{-1}$ and $\mu_a = 0.10, 0.49$ and $1.01\ \mathrm{cm}^{-1}$, (B) $\mu_s' = 4.36\ \mathrm{cm}^{-1}$ and $\mu_a = 0.10, 0.50$ and $0.99\ \mathrm{cm}^{-1}$, (C) $\mu_s' = 9.06\ \mathrm{cm}^{-1}$ and $\mu_a = 0.10, 0.50$ and $1.00\ \mathrm{cm}^{-1}$. See text for details.

3. Interstitial set-up

3.1. Description of the interstitial set-up for phantom measurement

The experimental set-up for the parallel-catheter measurement system is shown in figure 3. We constructed a device consisting of 3 parallel catheters positioned at 3 distances (3, 5 and 7 mm) from a central catheter. Only one separation is required to determine μ_a and μ_s', but we examined the accuracy of the extrapolation for the three separations independently to find the most suitable separation. An isotropic point source was placed in the middle catheter and connected to a 730 nm diode laser (Diomed 730, Cambridge, UK). An isotropic detector was placed in one of the parallel detector channels. This detection fibre was connected to a light dosimetry system (described below). The detector's position was controlled by computer-controlled step motors (Velmex, Inc East Bloomfield, NY), allowing the detector to be moved

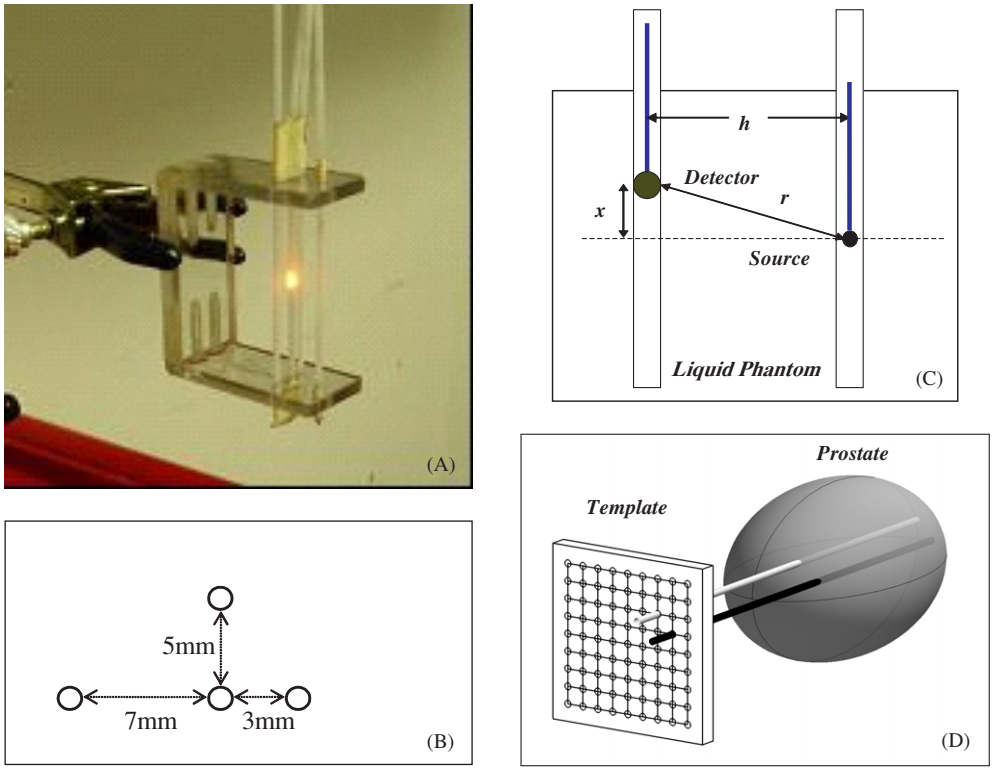

Figure 3. (A) Picture of the optical property device consisting of 4 parallel catheters positioned at 3 different distances (3, 5 and 7 mm) from the central catheter. The light source is placed in the centre catheter, while the detector is moved along each catheter, positioned at different distances from the light source. (B) Top view of the optical property device pictured in (A). (C) Schematics of the light source and detector placement. The distance between the light source and the detector is h. The light source is placed at a distance x from the surface of the phantom, while the detector is moved along the catheter. The distance from the centre of the detector to the point source is given by $r = \sqrt{x^2 + h^2}$. (D) Diagram of cathteter positioning during prostate PDT. The cathteters are placed at fixed distatnces (h) through a template and into the prostate. The light source is placed in one of the cathteters and the isotropic detector is placed in the other catheter.

to different distances from the light source. Each data set was obtained by scanning the detector along its catheter while the source remained fixed and acquiring fluence rate measurements at 0.05 mm intervals along its movement. The data acquisition time for a scan of 10 cm distance with 2000 data points is about 8 s since the speed of the step motor is 12.5 mm s^{-1}. The data acquisition board has a maximum data transfer speed of 300 kilosample/s, which can be adjusted to match the data acquisition rate of 250 samples/s in the application.

Using the diffusion approximation, the light fluence rate ϕ per source power S at a distance r from a point source can be expressed (Jacques 1998):

$$\frac{\phi}{S} = \frac{\mu_{\mathrm{eff}}^2}{4\pi r \mu_{\mathrm{a}}} \mathrm{e}^{-\mu_{\mathrm{eff}} r} = \frac{3\mu_{\mathrm{s}}'}{4\pi r} \mathrm{e}^{-\mu_{\mathrm{eff}} r} \tag{4}$$

where S is the source power of the point source (in mW), $\phi(r)$ is the fluence rate in mW cm^{-2} at r. $r = \sqrt{x^2 + h^2}$, where x and h are parallel and perpendicular distances from the centre of the point source (figure 3(C)).

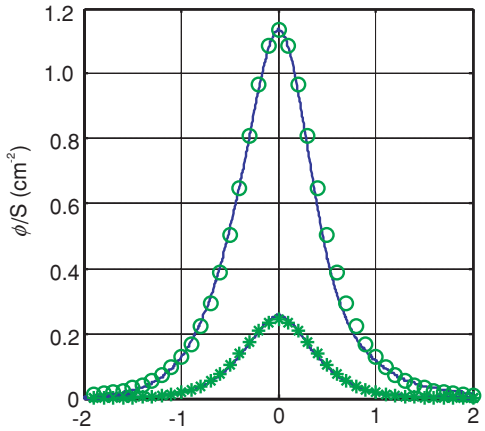

Figure 4. Measured light fluence rate per unit source strength at distances along the catheter, x, from the point source measured *in vivo* in human prostate gland. Lines are measured data and symbols are the fits.

3.2. Description of the interstitial set-up for in vivo patient measurement

Optical properties (μ_a, μ_s' and $\delta = 1/\mu_{eff}$) were also measured in 11 patients with locally recurrent prostate carcinoma using the interstitial set-up. A template with evenly spaced holes 5 mm apart was used for positioning of the catheters inside the prostate gland under ultrasound guidance. One point source and one detector were introduced in two parallel catheters (figure 3(D)). Detectors were placed at 5 or 7 mm (h) away from the light sources. The uncertainty of distance between the light source catheter and the detector catheter (h), which can be off 1–2 mm from the position determined by the template, can introduce errors in determining the optical properties of the phantom. Because of this, the optimization algorithm is designed to include the separation h, as a separate fitting parameter. Optical properties of the prostate were determined applying the diffusion theory (equation (4)) to the fluence rates measured at several distances (5–50 mm) from the light source. The isotropic detectors were calibrated under collimated 732 nm laser light in air as described in section 3.3.

Figure 4 shows the variation of the measured light fluence rate distribution (solid lines) in different quadrants of the prostate and symbols are the fits. There are 800 measured points for each scan with a resolution of 0.05 mm in the range of $(-2, 2)$ cm. The measured optical properties in this particular case varied from 0.23 to 0.4 cm^{-1} for the absorption coefficient and from 6.6 to 12 cm^{-1} for the scattering coefficient for different locations in prostate.

Table 2 summarizes the measured optical properties in human prostate for 11 patients (Zhu *et al* 2005a). Five patients were measured using a few points with manual positioning and six were measured using a motorized probe ($*$ indicates motorized probe measurements). The first column lists the absorption coefficients, the second column lists the scattering coefficients and the last column lists the optical penetration depth, for each patient. The values in the parenthesis are the standard deviations of the mean values measured from different locations in the same prostate gland. Whenever no standard deviation is listed, only one data point was available.

3.3. Calibration of detectors

We used an isotropic detector made of an optical fibre with a 0.5-mm-diameter scattering tip (CardioFocus West Yarmouth, MA) to measure the fluence rate. The fibre is connected to one

Table 2. Summary of optical properties measured in human prostate. The values in parentheses are the standard deviation of the mean values measured from different locations in the same prostate. No standard deviation is listed if only one data point is available. (∗ represents the measurements done with the motorized probe.)

Patient number	μ_a (cm^{-1})	μ_s' (cm^{-1})	δ (cm)
1	0.09	29.8	0.34
2	0.15	22.0	0.31
3	0.43 (0.28)	7.69 (4.76)	0.41 (0.14)
4	0.21	11.8	0.37
5	0.27 (0.27)	10.5 (11.2)	0.50 (0.05)
6 ∗	0.53 (0.36)	6.61 (4.51)	0.41 (0.09)
7 ∗	0.63 (0.32)	4.62 (2.87)	0.42 (0.10)
8 ∗	0.67 (0.17)	6.39 (3.18)	0.32 (0.10)
9 ∗	0.71 (0.43)	8.99 (6.51)	0.32 (0.12)
10 ∗	0.27 (0.14)	18.5 (11.6)	0.30 (0.07)
11 ∗	0.72 (0.11)	3.37 (1.37)	0.39 (0.11)

port of a light dosimetry system, which consists of an array of independent photodiodes, each connected to an SMA-style fibre optic connector. The photovoltage generated by these diodes is amplified and recorded by an analog-to-digital (AD) data acquisition board (DataTranslation, Marlboro, MA). The isotropic detector was calibrated in a 15.2 cm diameter integrating sphere using 730 nm light. The measured photovoltage (V) from the isotropic detector was converted to light fluence rate using the expression,

$$\Phi = A(V - B), \tag{5}$$

where A (mW cm^{-2} V^{-1}) is the conversion factor for fluence rate and B (V) characterizes the leakage of the photodiode. Since the calibration is performed in air, when the isotropic detector is used in tissue a correction factor of $\alpha = 1.9$ was used. This value was measured using the response of the isotropic detector in and out of water medium for the same incident fluence rate (Vulcan *et al* 2000, Marijnissen and Star 2002, Zhu *et al* 2005a, 2005b).

It is possible to determine the light fluence rate per unit power, ϕ/S, without independent calibrations of the isotropic detector (for ϕ) and the light source power (S). An integrating sphere with a built-in detector port and two input ports (one for the light source and the other for the isotropic detector) was used. A custom-made baffle blocked the direct light from the light source to either the built-in detector or the isotropic detector. The integrating sphere was calibrated for the light fluence rate and the light source power (figure 5) as follows. The fluence rate in air ϕ_0 is plotted against the power reading I recorded by the built-in power meter and then fitted to obtain the constant a (figure 5(A)), such that $\phi_0 = aI$. The calibration constant b is then obtained from the fit of the power reading from the integrating sphere as a function of the actual power (figure 5(B)) such that $S = bI$. The fluence rate and the uncalibrated detector signal (F) are related by $\phi_0 = gF_0$ in air and $\phi = \alpha gF$ in tissue, where α is the tissue correction factor and g is a constant that converts the light fluence rate from the detector signal (with leakage correction). One can determine the ratio ϕ/S from a simultaneous measurement of the point source with the power S and the same isotropic detector in the integrating sphere using:

$$\frac{\phi}{S} = \alpha\beta\frac{F}{F_0} \tag{6}$$

where F_0 is the isotropic detector reading in the integrating sphere in air for the same point source with power S, β is the ratio of the integrating sphere calibration coefficients a/b, α is

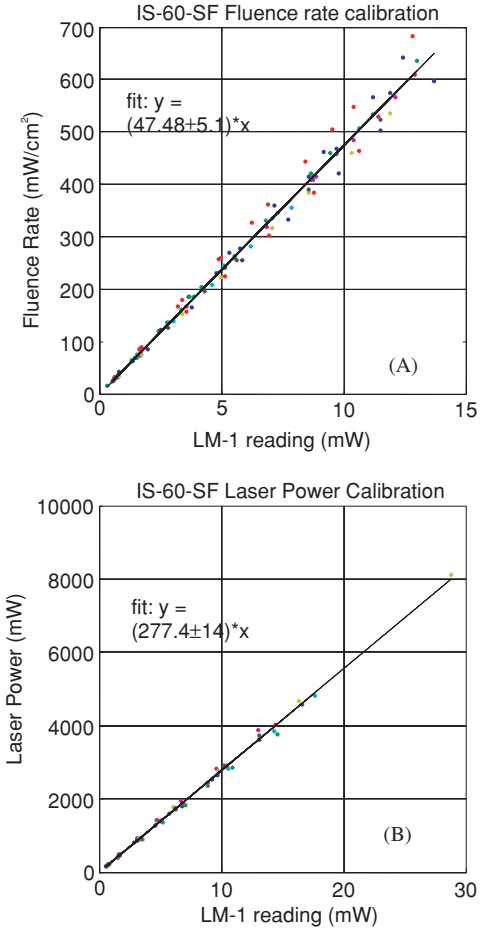

Figure 5. (A) Fluence rate calibration. The constant a is determined from the fit of the fluence rate in air to that of the power meter reading. (B) The power calibration determines the constant b, from the fit of the power reading from the integrating sphere to that of the power meter.

the tissue calibration factor and F is the detector signal in the phantom measurement. $\alpha = 1.9$ for our isotropic detectors, calibrated in air and used in water. $\beta = 0.172$ cm^{-2} for our integrating sphere (see figure 5).

3.4. Fitting algorithm

A Matlab-based program[1] using a graphical user interface (GUI) was developed to analyse the measured data. First, the data are read into the program from the selected files. Each profile is adjusted to account for the difference in sensitivity between in-air and in-water measurements and divided by the source power according to equation (6). The program displays the measured profile and its reflection in the y-axis on a common plot along with the difference between the two. The user has the option of applying an offset to the positions recorded by the motorized

[1] The program is available for download at www.xrt.upenn.edu/radiation_physics/research/index.html.

positioner to place the peak of the profile at $x = 0$. When this is achieved, the profile and its reflection match, and the difference between them is minimized.

Each profile is fit using two independent optimization algorithms. Both algorithms attempt to minimize the reduced χ^2, defined as

$$\chi^2 = \frac{\sum_{i=1}^{N} \left(\frac{(\varphi_{m_i} - \varphi_{t_i})^2}{\sigma_i^2} \right)}{(N - N_p)} \tag{7}$$

where the subscripts m and t denote the measured and theoretical values, respectively. The sum is over the N measured data points. The difference between N and N_p, the number of fitting parameters, gives the number of degrees of freedom of the fit. The uncertainty σ at each data point is estimated based on the measured relationship between noise and signal in our photodiode detectors, which is approximately linear with a coefficient of 0.015 (figure 7). To determine the relationship between the uncertainty in the signal recorded by our dosimetry system and the signal itself, we have performed eight in-air measurements of the same point source and same parallel catheters with $h = 5$ mm. Figure 7 is a plot of the standard deviation in fluence rate as a function of fluence rate. The symbols indicate the measured standard deviation, and the solid line is a linear fit. The measured data for $\phi > 600$ mW cm^{-2} was excluded from the fit. To account for the round-off error associated with conversion from analog to digital signal, we add additional uncertainty to each point equal to the value of the least significant bit of the 12 bit digital signal. In practice, this additional uncertainty is significant only for weak signals.

The GUI of the fitting program for the determination of optical properties is shown in figure 6. The add/delete data button enables one to choose/delete the data one needs to plot/remove. The user can enter the power, the distance between the two catheters *h,* calibration ratio β, the detector tissue correction factor α, as well as the fitting range for x. One has the choice of (1) using a fixed h or (2) using the 'optimize h' to allow the program to find the optimal value of h. In the text, we denoted h as being the physical separation between the catheters and italic h as being the optimized separation. The overlay solution box lets one overlay a plot of the diffusion theory solution for a given set of absorption and scattering coefficients and separation h. Results are summarized in the middle lower portion showing the current file name, source power (in mW), distance h between the catheters, values of absorption, scattering, effective attenuation coefficients, error and time for fitting (in ms).

In the first fitting, equation (4) is linearized by multiplying by r and taking the natural log. A corresponding transformation is performed on the measured data, which is then subjected to a linear fit to determine μ_{eff} and μ_{s}', from which μ_{a} can be determined. To explicitly take into account uncertainty in the measured data, we have adopted the singular value decomposition algorithm of Press *et al* (1992). Because the linear fitting uses $\ln(\Phi r)$ as its independent variable, we must calculate the uncertainty in $\ln(\Phi r)$, given by:

$$\sigma_{\ln(\Phi r)} = \frac{\partial(\ln(\Phi r))}{\partial \Phi} \sigma_{\Phi} = \frac{1}{\Phi} \sigma_{\Phi}. \tag{8}$$

The second fit uses the differential evolution routine adapted by Zhu *et al* (2001) from the work of Storn and Price (1997) with μ_{a} and μ_{s}' as free parameters. This nonlinear algorithm minimizes χ^2 directly.

The results of both fits are displayed as they are calculated, allowing the user to identify regions of the profile that contribute to poor fitting and exclude them from the fit. After the fitting is complete, the diffusion theory expression is evaluated with r equal to 0.5 cm to determine the fluence rate per unit power, and the value of χ^2 of each fit is calculated.

The measurement system described here is intended for use in the measurement of intact human tissues, in which case it is rarely possible to verify the distance between individual

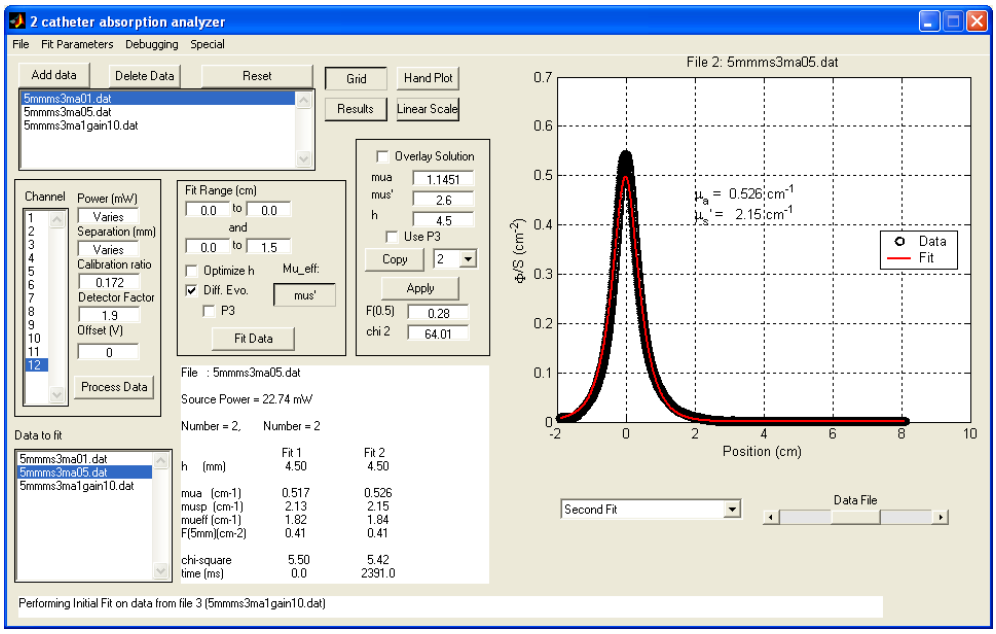

Figure 6. The GUI of the fitting program for the determination of optical properties. The user can enter the power, the distance h calibration ratio, and the detector water correction factor, as well as the fitting range for x. One has the choice of (1) using a fixed h or (2) using the 'optimize h' for the program to find the optimal value of h. The overlay solution box lets one overlay a fit for a set absorption and scattering coefficient, using a constant h. Results summarized in the middle lower portion showing the current file name, source power (in mW), distance h between the catheters, values of absorption, scattering, effective coefficients, error and time for fitting (in ms). The program is available for download. (see text for details).

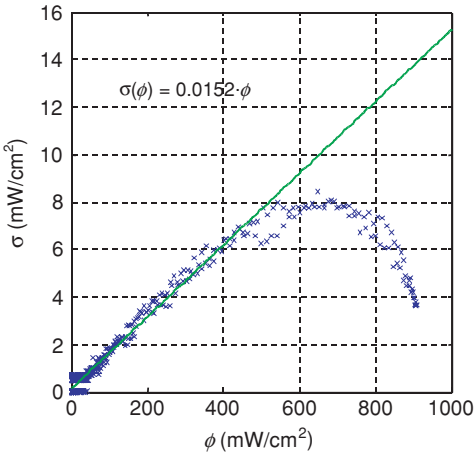

Figure 7. Standard deviation of fluence rate as a function of fluence rate. The symbols were measured data obtained from eight measurements of the same point source. The solid line is a linear fit. The measured data for $\phi > 600$ mW cm^{-2} were excluded from the fit.

catheters. To account to variations in catheter distance, we have implemented a variable-distance version of each of the algorithms described above. In the case of linear fitting, the

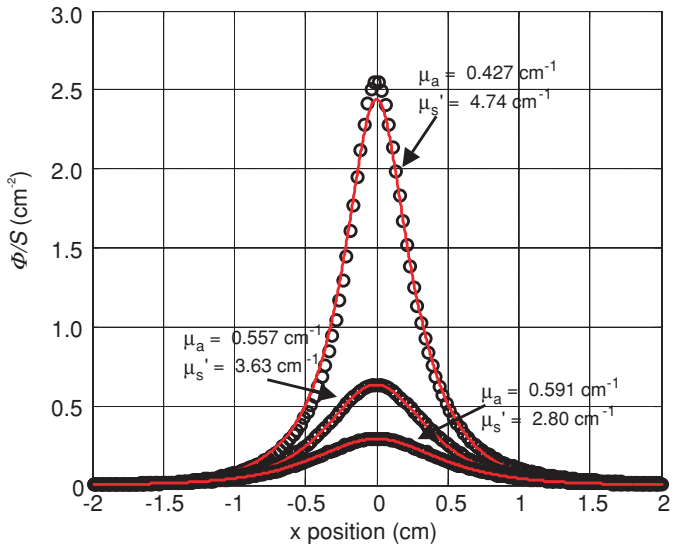

Figure 8. Fluence rate per unit power measured in one phantom (0.53% Liposyn and 0.012% black ink) at source–detector distances of 3, 5 and 7 mm. Fitting parameters are listed in table 3 (B).

fitting described above is repeated inside a nonlinear fitting algorithm native to the Matlab environment, which uses h, the distance between catheters, as part of free parameters (μ_a, μ_s', h). The determination of optical properties is still performed by the linear algorithm. The differential evolution algorithm is modified only slightly, by allowing one additional free parameter (h). In this case, the algorithm optimizes all three parameters simultaneously.

3.5. Results

Table 3 summarizes the optical properties (μ_a, μ_s', μ_{eff}) obtained using the parallel catheter measurements and those obtained from broad-beam measurements in the same phantoms. Results are presented for three optical phantoms with Liposyn concentration of (A) 0.23%, (B) 0.53%, (C) 1.14% and ink concentrations of 0.002%, 0.012%, and 0.023% for three different physical separations (h) between the two catheters. The first column specifies the distance between the light source catheter and the detector catheter. The second column shows the optimized distance (h) between the catheters that gives the best agreement between the optical properties determined by parallel-catheter and broad-beam measurements. The values of the absorption, scattering and effective attenuation coefficients determined by parallel catheter measurement are shown in columns 3–5. These values are then compared to the values measured independently in a broad-beam geometry. The per cent differences between the two are listed in the last three rows.

Figure 8 shows the results for the measurements done in an optical phantom ($\mu_s' = 4.19$ and $\mu_a = 0.5$ cm^{-1}) but at different distances from the light source. From top to bottom, h = 3, 5, and 7 mm, respectively.

Figure 9 plots the error in the optical properties determined by parallel-catheter measurements for all optical phantoms used in the study for physical separation of 5 mm. The Liposyn concentrations are 0.23%, 0.53% and 1.14%, and ink concentrations are 0.002%, 0.012% and 0.023%. We listed fittings using h of: 4, 4.5, 5 and 5.5 mm.

Table 3. A comparison between optical properties (μ_a, μ_s', μ_{eff}) determined by broad-beam and parallel-catheter methods for three optical phantoms with Liposyn concentrations: (A) 0.23%, (B) 0.53%, (C) 1.14% and ink concentrations (0.002%, 0.012% and 0.023%) for three different separations (h) between the catheters.

		Parallel catheters			Broad beam			Difference (%)		
Separation	h	μ_a	μ_s'	μ_{eff}	μ_a	μ_s'	μ_{eff}	μ_a	μ_s'	μ_{eff}
					(A)					
h = 3 mm	2.5	0.10	2.04	0.77	0.10	1.73	0.72	2.0	14.0	6.9
		0.47	2.11	1.72	0.48	1.73	1.58	5.1	17.9	7.5
		0.93	2.49	2.64	1.00	1.73	2.28	8.6	39.1	15.8
h = 5 mm	4.5	0.11	2.04	0.82	0.10	1.73	0.72	8.0	17.9	13.9
		0.53	2.21	1.87	0.48	1.73	1.58	9.4	27.7	18.4
		1.10	2.29	2.75	1.00	1.73	2.28	9.9	32.4	20.6
h = 7 mm	6	0.11	1.93	0.79	0.10	1.73	0.72	9.0	7.8	9.7
		0.55	1.91	1.78	0.48	1.73	1.58	12.7	6.7	11.3
		1.18	1.49	2.29	1.00	1.73	2.28	15.2	16.8	0.4
					(B)					
h = 3 mm	2.5	0.10	4.35	1.15	0.10	4.19	1.11	1.0	3.8	3.6
		0.43	4.74	2.47	0.49	4.19	2.49	12.9	13.1	0.8
		0.89	4.30	3.38	0.99	4.19	3.53	10.3	2.6	4.2
h = 5 mm	4.5	0.09	3.92	1.05	0.10	4.19	1.11	7.0	6.4	5.4
		0.56	3.63	2.46	0.49	4.19	2.49	13.5	13.4	1.2
		1.14	3.53	3.47	0.99	4.19	3.53	15.1	15.8	1.7
h = 7 mm	6	0.08	3.35	0.92	0.10	4.19	1.11	16.0	20.0	17.1
		0.59	2.80	2.23	0.49	4.19	2.49	20.6	33.2	10.4
		1.35	2.57	3.23	0.99	4.19	3.53	36.5	38.7	8.5
					(C)					
h = 3 mm	2.5	0.09	6.97	1.35	0.1	9.14	1.64	13.0	23.7	17.7
		0.46	5.05	2.63	0.5	9.14	3.7	8.8	44.7	28.9
		0.81	5.03	3.49	0.99	9.14	5.2	18.4	45.0	32.9
h = 5 mm	4.5	0.1	8.76	1.62	0.1	9.14	1.64	0	4.2	1.2
		0.51	7.40	3.38	0.5	9.14	3.7	2.0	19.0	8.6
		0.92	8.02	4.70	0.99	9.14	5.2	7.3	12.3	9.6
h = 7 mm	6	0.10	5.92	1.32	0.1	9.14	1.64	2.0	35.2	19.5
		0.78	3.97	3.04	0.5	9.14	3.7	55.6	56.6	17.8
		1.85	3.27	4.26	0.99	9.14	5.2	86.9	64.2	18.1

Figure 10 shows the results of the optical properties for three different scattering coefficients (A) 1.73, (B) 4.19 and (C) 9.14 cm^{-1} and ink concentration of 0.002, 0.012 and 0.023%, giving an absorption coefficient μ_a of 0.1, 0.5 and 1.0 cm^{-1}. The distance between the light source and the detector was kept constant, at 5 mm. The scan for the phantom with optical penetration depth of $\delta = 1/\mu_{eff} = 1.39$ cm (figure 10(A)) has a significant boundary effect since the point source was placed at 1.5 cm from the boundary. For that reason, we only fit the right side of the data further away from the boundary. When the optical penetration depth is shorter than the distance to the boundary, this effect becomes negligible. We have also plotted in figure 10(A), the value of Φ/S calculated using the optical properties determined

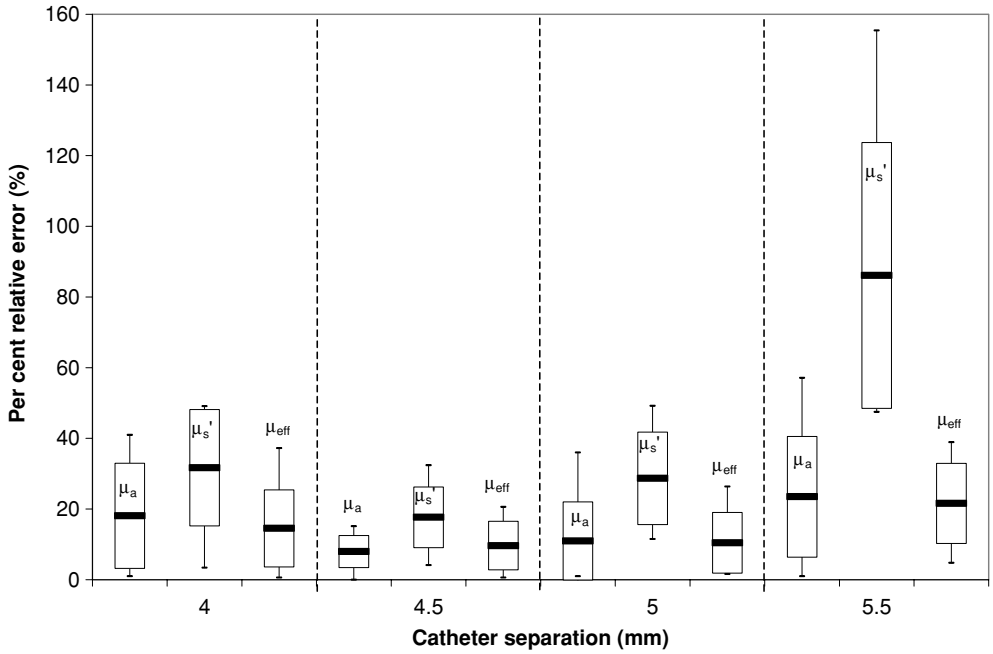

Figure 9. Error in the optical properties determined by parallel-catheter measurements for all optical phantoms used in the study for physical separation of 5 mm. The Liposyn concentrations are 0.23%, 0.53% and 1.14%. Catheter separations h of 4 mm, 4.5 mm, 5 mm and 5.5 mm were plotted.

by the diffusion theory fit, but calculated using the higher-order P3 approximation (Hull and Foster 2001) (dotted lines) since the transport albedo ($a' = \mu_s'/(\mu_a + \mu_s')$) can be significantly smaller than 0.9.

4. Interstitial set-up: advanced

4.1. Validation of the diffusion approximation

For cases where the transport albedo of the turbid medium is small ($a' < 0.8$), the diffusion approximation is known to fail (Star 1997). An example corresponding to the worst case of albedo ($a' = 0.64$) in our study is shown in figure 11, which plots the product of fluence rate and radial distance as a function of radial distance for a Monte Carlo simulation (solid line) of a point source in an optical phantom with $\mu_a = 1.0\ \text{cm}^{-1}$ and $\mu_s' = 1.79\ \text{cm}^{-1}$ ($\mu_{\text{eff}} = 2.32\ \text{cm}^{-1}$). The corresponding solution of the diffusion equation is shown by the dashed line. Our Monte Carlo algorithm was implemented in Matlab using the implicit capture variance reduction technique described by Prahl *et al* (1989) and implemented in the commonly used MCML code by Wang *et al* (1995). The MC solution tends to deviate more from the diffusion solution at shorter distances ($r \leqslant 0.3$ cm). The slopes of the two solutions are slightly different for larger distances. As a result, the best fit to this data using diffusion theory, which is indistinguishable from the data itself on the scale shown, gives an artificially higher value for μ_a ($1.18\ \text{cm}^{-1}$), μ_s' ($2.14\ \text{cm}^{-1}$) and μ_{eff} ($2.7\ \text{cm}^{-1}$), respectively. For comparison, we have also plotted the results of a Monte Carlo simulation that includes the effects of a cylindrical catheter surrounding the isotropic source. A catheter diameter of 1.1 mm and an index of

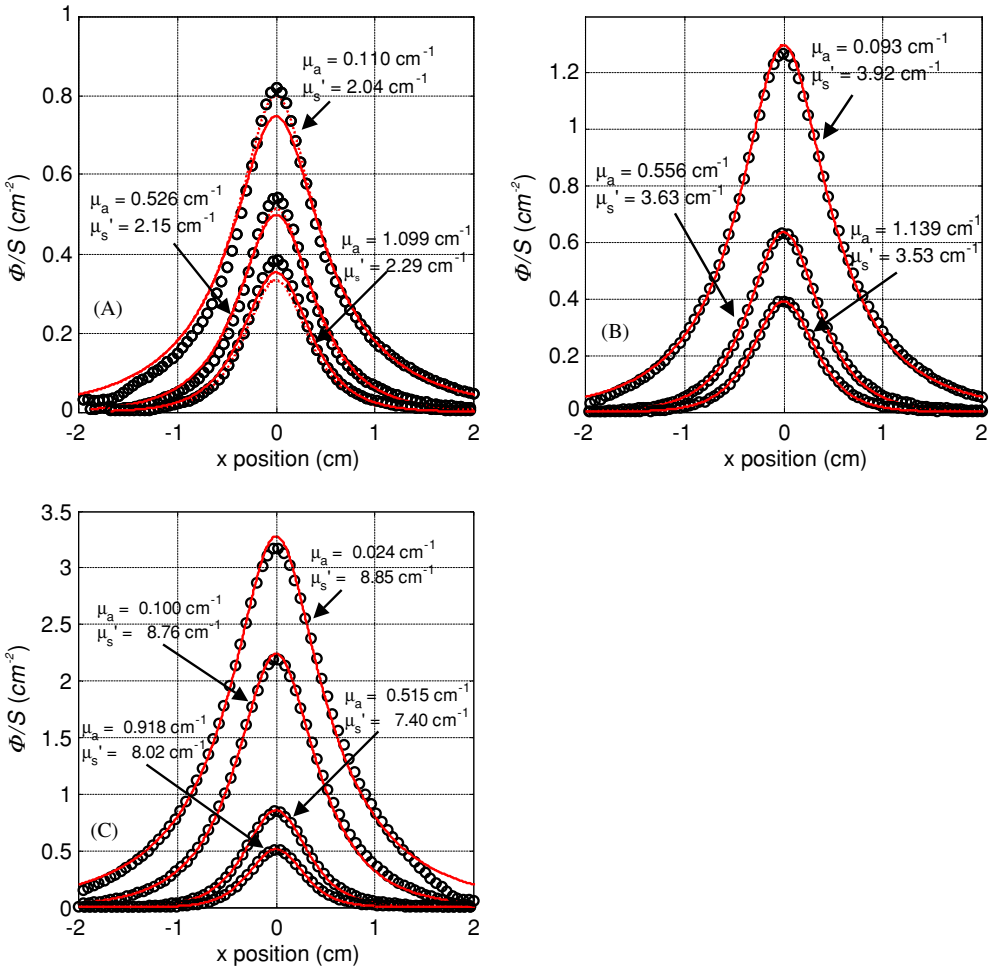

Figure 10. Measured fluence rate per unit source power for different scattering media using 0.23, 0.53 and 1.14% Liposyn concentrations and 0.002, 0.012 and 0.023% ink concentrations at light-detector distance of 0.5 cm. (A) $\mu_s' = 1.73\ \mathrm{cm}^{-1}$, (B) $\mu_s' = 4.19\ \mathrm{cm}^{-1}$, (C) $\mu_s' = 9.14\ \mathrm{cm}^{-1}$. The solid lines are the fit using diffusion theory. The optical properties determined using the diffusion theory are shown next to each fit. The dotted lines represent the fluence rate predicted by the P3 theory for these optical properties.

refraction mismatch between the catheter (air) and tissue of 1.4 were assumed. In this case, the presence of the air cavity makes less difference to the final result than the breakdown of the diffusion approximation. This is expected because μ_{eff} in this case is relatively small. However, even in cases such as this, where the diffusion theory is clearly beginning to fail, the optical properties (μ_a and μ_s') determined by the two-catheter method are still within 20% of the true values. The limitation of the diffusion approximation can be addressed by the use of higher-order approximations (e.g. P3 theory) than the diffusion theory. In figure 10(A), we have shown that the use of P3 approximation (dotted line) does improve the agreement between the measurement and theory in most cases. The apparent disagreement between measurement and P3 calculation for the lowest curve results from the fact that the P3 calculation used the optical properties determined using the diffusion theory ($\mu_a = 1.1\ \mathrm{cm}^{-1}$ and $\mu_s' = 2.29\ \mathrm{cm}^{-1}$), which

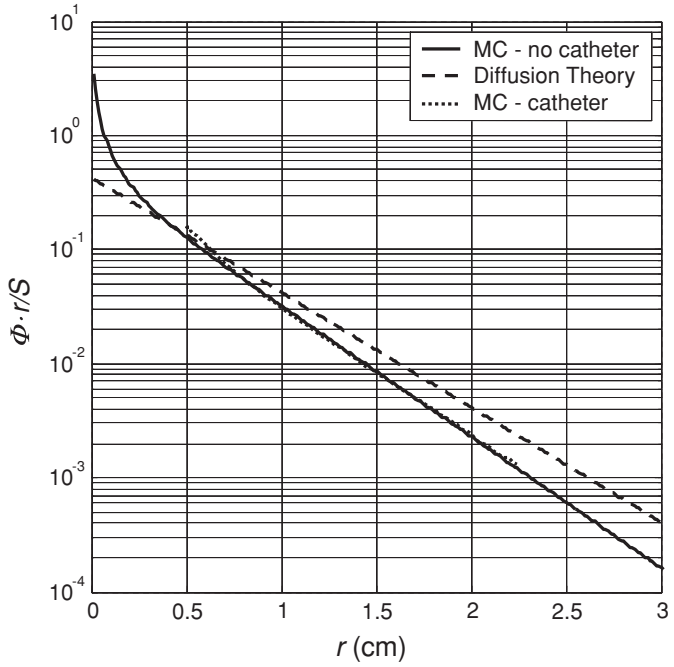

Figure 11. Effect of small transport albedo on diffusion theory-based fitting. The Monte Carlo simulated data set for an isotropic emitter in an infinite medium with μ_a of 1.0 cm^{-1} and μ_s' of 1.79 cm^{-1}, measured by a detector at h = 5 mm, is indicated by the solid line. The diffusion theory solution for these optical properties is shown by the dashed line. The best fit of the diffusion theory to the simulated data is indistinguishable from the data, but gives μ_a of 1.18 and μ_s' of 2.14 cm^{-1}. For comparison, the dotted line indicates the Monte Carlo simulation for the same optical properties with the source embedded in a 1.1 mm diameter catheter.

deviate significantly from the true optical properties ($\mu_a = 1.0$ cm^{-1} and $\mu_s' = 1.73$ cm^{-1}). As the albedo of this phantom was only 0.63, it is not surprising that the diffusion theory failed to recover its optical properties accurately.

4.2. Monte Carlo simulation of the air gap effect

As shown in figure 3(C), the experimental set-up introduces two air cavity columns, one surrounding the detector and one surrounding the light source. These catheters have an outer diameter of 1.1 mm and an inner diameter of 1.0 mm. The light source and the isotropic detector each have an outer diameter of 0.5 mm. To evaluate the effect of these air cavities, we have performed Monte Carlo simulations. The optical properties used were $n = 1.4$, $g = 0.9$, $(\mu_a, \mu_s) = (0.10, 91.3)$, $(1.00, 17.9)$ and $(1.01, 91.3)$ cm^{-1}, respectively. The Monte Carlo simulations were performed in cylindrical coordinates. The simulated volume was divided into annular bins of thickness 0.025 cm and height 0.025 cm. We have simplified the catheter as an air cavity of 1.1 mm diameter in the tissue phantom, with a light source at its centre. Photons launched from the isotropic source were propagated without absorption or scattering to the edge of the source catheter. Refraction at the boundary was accounted for both for the escaping photons and for any photons that re-entered the cavity. To maintain the cylindrical symmetry of the system, we have ignored the air cavity surrounding the detector.

The air cavity's main effect is reducing the distance light must travel in the scattering medium between the source and detector. In cases with small μ_a, the fluence rate changes

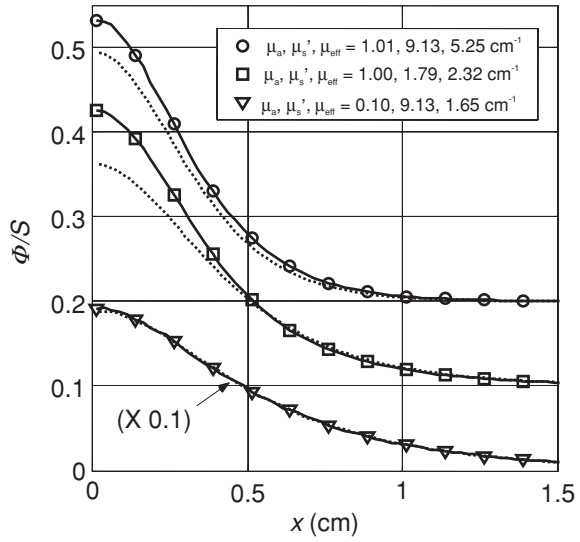

Figure 12. Effect of the air gap introduced by the source catheter on fitting results. For each of three sets of optical properties (indicated in the legend), we plot the Monte Carlo simulated fluence rate measured by a detector at h = 5 mm from a source embedded in a 1.1 mm diameter catheter (solid line) and that in an infinite medium along a line separated by h = 5 mm from the source (dotted line).

slowly with radial distance, so the air cavity has little effect. In contrast, when μ_a is large, the air cavity effect is much more pronounced. In figure 12, we plot the fluence rates predicted by Monte Carlo simulations with (solid line) and without (dashed line) an air cavity for various sets of optical properties. In the cases where μ_a is small ($\mu_a = 0.1$ cm^{-1}), the air cavity effect is negligible. When μ_a is large, however, the effect becomes more significant, and it changes the shape of the curve. The air cavity can be partially accounted for by reducing the value of h. For $\mu_{eff} \leqslant 4$ cm^{-1} and h = 5 mm, the best average value of h is 4.5 mm for the range of optical properties studied.

5. Discussion and conclusion

The main objective of this study was to create a device that can assess the optical properties (scattering and absorption coefficients) *in vivo* by interstitial measurements. We tested this device in tissue-simulating phantoms with different optical properties. During *in vivo* measurement, the scanning distance is typically 5 cm, so each measurement of optical properties takes 4 s. This is the time required to obtain a useful data set. Extensive commissioning of the device has been performed to ensure the accuracy of the measurement at this speed. We compared the results of our measurements with optical properties determined by an *ex vivo* method.

Our characterization of scattering properties for Liposyn 30% yields 8.1 × (c%IL), which is consistent with the literature, considering the variations among brands and batches of lipid solutions. An extensive study was made by Madsen *et al* (1992) for several brands of India ink. The ink concentrations used were 0.01–1% and the total attenuation coefficient was determined as a function of ink concentration with a value of 123 cm^{-1}/% for Higgins ink at 594 nm. This is larger than our value (42.99 cm^{-1}/%) for Higgins ink at 730 nm, but

can easily be attributed to difference among batches. We can determine μ_a and μ_s' of the phantom medium to an uncertainty of better than 5%. This error is determined in part by comparing extrapolated results from broad beam measurements against known ink and Liposyn concentrations. Our independent method of determining the optical properties is shown in figure 2. The optical properties (μ_a and μ_s') were determined for each optical phantom under broad beam illumination. The black curve is the fit to the data that excludes the air–phantom interface and the background. The uncertainty in μ_{eff} can be estimated from the uncertainty in our measured data (see figure 7), giving a relative uncertainty of less than 0.1%, much smaller than the uncertainty in the measurement of the volumes of the ink and Liposyn components of the phantom. The accuracy of determining μ_s' using the broad beam technique is within 8% for the lowest Intralipid concentration of 0.23% and 5% for the 0.53 and 1.14% Liposyn. The relative error of determining μ_s' is less then 5% with a maximum of 8%.

Comparing the uncertainties of optical properties obtained with different source–detector separations (in table 3), it is clear that the best result is obtained using h = 5 mm. For the small separation (h = 3 mm) the uncertainty is larger because when the source-to-detector distance is small, the effect of air cavity introduced by the catheters is increased due to the reduction of the amount of scattering material between the catheters. In addition, diffusion theory breaks down when the detector is near the source ($r \leqslant l_{tr}$, where l_{tr} is the transport mean free path given by $1/(\mu_s')$). For the large separation (h = 7 mm), the uncertainty for phantoms with large μ_{eff} starts to increase greatly because of decrease of the light fluence rate, resulting in larger uncertainty in extrapolating optical properties (see figure 8). Figure 8 shows the fitting results for an optical phantom with $\mu_a = 0.49\ cm^{-1}$ and $\mu_s' = 4.19\ cm^{-1}$. Detailed fitting results are shown in the figure as well as in table 3, (B). While one gets reasonable results of optical properties at h = 3 mm, the fit deviates from measured data near the source. The fits are good for h = 5 and 7 mm. However, some of the resulting optical properties at h = 7 mm deviate from the true value by more than 30% (table 3).

There are several causes that give rise to uncertainties in determining the optical properties of a phantom: (1) measurement uncertainties of light fluence rate, (2) uncertainty in detector positioning (x) and distance between source catheter and detector catheter (h), (3) air cavity introduced by the catheter, and (4) limitations of the diffusion theory.

The first source of error is the uncertainty of light fluence rate measurement. We compared the data from eight identical measurements of the same point source and plotted the standard deviation as a function of fluence rate. The linear fit (shown in figure 7) gives the standard deviation $\sigma(\phi) = 0.015\phi$ as a linear function of fluence rate ϕ. This indicates that the random error of our system corresponds to a relative uncertainty of 1.5%, which is not the limiting factor in our determination of optical properties.

By analysing the measured data using different distances h, we determined the optimal value of h, i.e. that which gives the best agreement with the known optical properties of the sample. Often, this optimal h is smaller than the measured centre-to-centre distance between channels. The major cause of error in determining the optical properties was the uncertainty in the distance between the detector and the light source (see figure 9), where a 0.5 mm error in catheter positioning could change dramatically the uncertainty of the fit. In figure 9, it can be seen that the best fit for the intended 5 mm separation is given by $h = 4.5$ mm for physical separation of 5 mm. Here, we used the standard deviation of the optical properties in all the phantoms as an indication of the separation to be used. As shown in figure 9, the 4 mm separation gave an average error of 21% with a maximum error of 49%, the 5 mm separation gave an average error of 17% with a maximum error of 49% and the 5.5 mm separation gave an average error of 44% with a maximum error of 155%. As can be clearly seen from figure 8, the 4.5 mm separation gives the lowest uncertainty with an average error of 17% and

maximum error of 19%. Reducing the physical separation between the detector and the light source to 4.5 mm from 5 mm partially accounts for the effect of air cavity introduced by the catheter. Another cause of error was the positioning of the detector along the catheter. This error was minimized by using the motorized probe, giving a positioning accuracy of at worst 0.1 mm. The motorized probe is able to take approximately 800 points per measurement, further reducing the error measurement by increasing the number of measurement points.

The range of validity of the parallel-catheter method is limited to cases where $\mu_{\text{eff}} \leqslant 4\ \text{cm}^{-1}$. Cases with $\mu_{\text{eff}} > 4\ \text{cm}^{-1}$ produce large errors in μ_a and μ_s' if h is different from the optimal h by 0.5 mm.

The optical properties (absorption (μ_a), transport scattering (μ_s'), and effective attenuation (μ_{eff}) coefficients) of eleven patients with locally recurrent prostate cancer were measured *in situ* using interstitial isotropic detectors (see table 3). Measurements were made at 732 nm before motexafin lutetium (MLu)-mediated PDT in four quadrants. μ_a and μ_s' varied between 0.07 and 1.62 cm^{-1} (mean $0.37 \pm 0.24\ \text{cm}^{-1}$) and 1.1–44 cm^{-1} (mean $14 \pm 11\ \text{cm}^{-1}$), respectively. μ_a was proportional to the concentration of MLu measured by an *ex vivo* fluorescence assay. μ_{eff} varied between 0.91 and 6.7 cm^{-1} (mean $2.9 \pm 0.7\ \text{cm}^{-1}$), corresponding to an optical penetration depth ($\delta = 1/\mu_{\text{eff}}$) of 0.1–1.1 cm (mean 0.4 ± 0.1 cm). These results are in the range of optical properties used in phantom measurement.

Pathologically, one can attribute the difference in μ_s' to difference in cell and tissue structure caused by, among many possibilities, differences in cell type, the presence of scar tissue or local inflammation. Judging from the difference between the mean value of μ_s' at 732 nm between human ($14 \pm 11\ \text{cm}^{-1}$) and dog prostate ($3.6 \pm 4.8\ \text{cm}^{-1}$) (Zhu *et al* 2005a, 2003), our measurement is sensitive enough to show the glandular structure difference between human and canine prostates. Since our measurement was made in cancerous prostates with prior radiation therapy, it is very possible that there are cancerous cells and normal cells, necrotic cells due to prior radiation therapy, and local inflammation due to the PDT procedure, all of which can contribute to the heterogeneity in μ_s'. We find that in only 14% of cases was the measured μ_s' larger than 20 cm^{-1}. These exceptional values of μ_s' may well indicate the presence of abnormal cells, although more data will be required to determine a correlation between large μ_s' and specific changes in cellular structure. There is also the possibility of errors in estimating μ_s' that contribute to the spread of μ_s'. However, our current paper gives the upper limit of error in estimating μ_s', which in the worst case presented in the paper, is about 155% (see figure 9 for the case for $\mu_a = 0.99\ \text{cm}^{-1}$, $\mu_s' = 9.14\ \text{cm}^{-1}$ and $\text{h} = 5.5$ cm).

Quick and accurate determination of the optical properties of tissue is very important in a variety of diagnostic and therapeutic procedures. We developed a method to quickly determine the optical properties in tissue simulating liquid phantom for μ_a between 0.1 and 1.0 cm^{-1} and μ_s' between 1.8 and 9.0 cm^{-1}. Our device determines the optical properties μ_a and μ_s' with a standard and maximum deviation of 8% (15%) and 18% (32%), respectively. The high uncertainty in determining the scattering coefficient comes from the fact that the diffusion theory only works for high transport albedo ($a' > 0.9$). These errors are due mainly to uncertainty of the distance between the detector catheter and light source catheter, and the effect of the air cavity introduced by the catheter.

Acknowledgments

This work is supported by grants from the Department of Defense (DOD), DAMD1703-1-0132 and National Institute of Health (NIH), PO1 CA87971-01.

References

Coquoz O, Svaasand L O and Tromberg B J 2001 Optical property measurements of turbid media in a small-volume cuvette with frequency-domain photon migration *Appl. Opt.* **40** 6281–91

Doornbos R M P, Lang R, Aalders M C, Cross F W and Sterenborg H J C M 1999 The determination of *in vivo* human tissue optical properties and absolute chromophore concentrations using spatially resolved steady-state diffuse reflectance spectroscopy *Phys. Med. Biol.* **44** 967–81

Driver I, Feather J W, King P R and Dawson J B 1989 The optical properties of aqueous suspensions of Liposyn, a fat emulsion *Phys. Med. Biol.* **34** 1927–30

Farrell T J and Patterson M S 1992 A diffusion theory model of spatially resolved, steady-state diffuse reflectance for the noninvasive determination of tissue optical properties *in vivo Med. Phys.* **19** 879–88

Flock S T, Jacques S L, Wilson B C, Star W M and van Gemert M J C 1992 Optical properties of Liposyn: a phantom medium for light propagation studies *Lasers Surg. Med.* **12** 510–9

Gurjar R S, Backman V, Perelman L T, Georgakoudi I, Badizadegan K, Itzkan I, Dasari R R and Feld M S 2001 Imaging human epithelial properties with polarized light-scattering spectroscopy *Nature Med.* **7** 1245–8

Hull E L, Conover D L and Foster T H 1999 Carbogen-induced changes in rat mammary tumor oxygenation reported by near infrared spectroscopy *Br. J. Cancer* **79** 1709–16

Hull E L and Foster T H 2001 Steady-state reflectance spectroscopy in the P_3 approximation *JOSA* A **18** 584–99

Hull E L, Nichols M G and Foster T H 1998 Quantitative broadband near-infrared spectroscopy of tissue-simulating phantoms containing erythrocytes *Phys. Med. Biol.* **43** 3381–404

Jacques S L 1998 Light distribution from point, line and plane sources for photochemical reactions and fluorescence in turbid biological tissues *Photochem. Photobiol.* **67** 23–32

Kienle A, Lilge L, Patterson M S, Hibst R, Steiner R and Wilson B 1996 Spatially resolved absolute diffuse reflectance measurements for noninvasive determination of the optical scattering and absorptions of biological tissue *Appl. Opt.* **35** 2304–13

Kienle A and Patterson M S 1997a Determination of the optical properties of semi-infinite turbid media from frequency-domain reflectance close to the source *Phys. Med. Biol.* **42** 1801–19

Kienle A and Patterson M S 1997b Improved solutions of the steady-state and the time-resolved diffusion equations for reflectance from a semi-infinite turbid medium *J. Opt. Soc. Am.* A **14** 246–54

Liu H, Boas D A, Zhang Y, Yodh A G and Chance B 1995 Determination of optical properties and blood oxygenation in tissue using continuous nearinfrared light *Phys. Med. Biol.* **40** 1983–93

Madsen S J, Patterson M S and Wilson B C 1992 The use of India ink as an optical absorber in tissue-simulating phantoms *Phys. Med. Biol.* **37** 985–93

Marijnissen J P A and Star W M 2002 Performance of isotropic light dosimetry probes based on scattering bulbs in turbid media *Phys. Med. Biol.* **47** 2049–58

Moes C J M, van Gemert M J C, Star W M, Marijnissen J P A and Prahl S A 1989 Measurements and calculations of the energy fluence rate in a scattering and absorbing phantom at 633 nm *Appl. Opt.* **28** 2292–6

Mourant J R, Freyer J P, Hielscher A H, Eick A A, Shen D and Johnson T M 1998 Mechanisms of light scattering from biological cells relevant to noninvasive optical-tissue diagnosis *Appl. Opt.* **37** 3586–93

Mourant J R, Fuselier T, Boyer J, Johnson T M and Bigio I J 1997 Predictions and measurements of scattering and absorption over broad wavelength ranges in tissue phantoms *Appl. Opt.* **36** 949–57

Nakai T, Nishimura G, Yamamoto K and Tamura M 1997 Expression of optical diffusion coefficient in high-absorption turbid media *Phys. Med. Biol.* **42** 2541–9

Nichols M G, Hull E L and Foster T H 1997 Design and testing of a white-light, steady-state diffuse reflectance spectrometer for determination of optical properties of highly scattering systems *Appl. Opt.* **36** 93–104

Patterson M S, Chance B and Wilson B C 1989 Time resolved reflectance and transmittance for the non-invasive measurement of tissue optical properties *Appl. Opt.* **28** 2331–6

Pogue B W and Patterson M S 1994 Frequency-domain optical absorption spectroscopy of finite tissue volumes using diffusion theory *Phys. Med. Biol.* **39** 1157–80

Prahl S A, Keijzer M, Jacques S L and Welch A J 1989 A Monte Carlo model of light propagation in tissue *SPIE Inst. Ser.* **5** 102–11

Press W H, Teukolsky S A, Vetterling W T and Flannery B P 1992 *Numerical Recipes in C: The Art of Scientific Computing* (New York: Cambridge University Press)

Rolfe P 2000 *In vivo* near-infrared spectroscopy *Ann. Biomed. Eng.* **02** 715–54

Solonenko M, Cheung R, Busch T M, Kachur A, Griffin G M, Vulcan T, Zhu T, Wang H-W, Hahn S M and Yodh A G 2002 *In vivo* reflectance measurements of optical properties, blood oxygenation and motexafin lutetium uptake in canine large bowels, kidneys and prostates *Phys. Med. Biol.* **47** 857–73

Star W M 1997 Light dosimetry *in vivo Phys. Med. Biol.* **42** 763–87

van Staveren H J, Moes C J M, van Marle J, Prahl S A and van Gemert M J C 1997 Light scattering in Intralipid-10% in the wavelength range of 400–1100 nm *Appl. Opt.* **30** 4507–14

Storn R and Price K 1997 Differential evolution—a simple and efficient heuristic for global optimization over continuous spaces *J. Global Optimization* **11** 341–59

Swartling J, Dam J S and Anderson-Engels S 2003 Comparison of spatially and temporally resolved diffuse-reflectance measurement systems for determination of biomedical optical properties *Appl. Opt.* **42** 4612–20

Torricelli A, Pifferi A, Taroni P, Giambattiselli E and Cubeddu R 2001 *In vivo* optical characterization of human tissues from 610 to 1010 nm by time-resolved reflectance spectroscopy *Phys. Med. Biol.* **46** 2227–37

Vulcan T G, Zhu T C, Rodriguez C E, Hsi R A, Fraker D L, Baas P, Murrer L H, Star W M, Glatstein E, Yodh A G and Hahn S M 2000 Comparison between isotropic and nonisotropic dosimetry systems during intraperitoneal photodynamic therapy *Lasers Surg. Med.* 292–301

Wang L I, Jacques S T L and Zheng L 1995 MCML—Monte Carlo modeling of light transport in multi-layered tissues *Comput. Methods Programs Biomed.* **47** 131–46

Zhu T C, Bjarngard B E, Ying X and Yang C J 2001 Modeling the output ratio in air for megavoltage photon beams *Med. Phys.* **28** 925–37

Zhu T C, Dimofte A, Finlay F C, Stripp D, Bush T, Miles J, Whittington R, Malkowicz S B, Tochner Z, Glatstein E and Hahn S M 2005a Optical properties of human prostate at 732 nm measured *in vivo* during Motexafin Lutetium-mediated photodynamic therapy *Potochem. Photobiol.* **81** 96–105

Zhu T C, Dimofte A, Finlay J C, Glatstein E and Hahn S M 2005b Detector calibration factor for interstitial *in vivo* light dosimetry using isotropic detectors with scattering tip *Proc. SPIE* **5689** 174–85

Zhu T C, Hahn S M, Kapatkin A S, Dimofte A, Rodriguez C E, Vulcan T G, Glatstein E and Hsi R A 2003 *In vivo* optical properties of normal canine prostate at 732 nm using motexafin lutetium mediated photodynamic therapy *Photochem. Photobiol.* **77** 81–8

Interstitial fluorescence spectroscopy in the human prostate during motexafin lutetium-mediated photodynamic therapy ‡

Jarod C. Finlay*[1], Timothy C. Zhu[1], Andreea Dimofte[1], Diana Stripp[1], S. Bruce Malkowicz[2], Theresa M. Busch[1], and Stephen M. Hahn[1]

[1] Department of Radiation Oncology, University of Pennsylvania, Philadelphia, PA

[2] Department of Urology, University of Pennsylvania, Philadelphia, PA

3400 Spruce Street / 2 Donner Building

Philadelphia, PA, 19104

Phone: (215) 615-3795

Fax: (215) 349-5978

e-mail: finlay@mail.med.upenn.edu

Keywords: photodynamic therapy, prostate, motexafin lutetium, MLu, fluorescence spectroscopy, interstitial

‡ Published in the journal website (www.ASPjournal.com) on xx-xxx-xxx.

ABSTRACT

The *in vivo* fluorescence emission from human prostates was measured before and after motexafin lutetium (MLu)-mediated photodynamic therapy (PDT). A single side-firing optical fiber was used for both the delivery of 465-nm LED excitation light and the collection of emitted fluorescence. It was placed interstitially within the prostate *via* a closed transparent plastic catheter. Fitting of the collected fluorescence emission spectra using the known fluorescence spectrum of 1 mg/kg MLu in an intralipid phantom yields a quantitative measure of the local MLu concentration. We found that an additional correction factor is needed to account for the reduction of the MLu fluorescence intensity measured *in vivo* due to strong optical absorption in the prostate. We have adopted an empirical correction formula given by $C = (3.1\ cm^{-1}/\mu_s') \exp(\mu_{eff} \cdot 0.97\ cm)$, which ranges from approximately 3 to 16, with a mean of 9.3 ± 4.8. Using a computer-controlled step motor to move the probe incrementally along parallel tracks within the prostate, we can determine one-dimensional profiles of the MLu concentration. The absolute MLu concentration and the shape of its distribution are confirmed by *ex vivo* assay and by diffuse absorption measurements, respectively. We find significant heterogeneity in photosensitizer concentration within and among five patients. These variations occur over large enough spatial scales compared to the sampling volume of the fluorescence emission that mapping the distribution in three dimensions is possible.

INTRODUCTION

The development of photodynamic therapy (PDT) as a modality for the treatment of bulky tumors and solid organs has motivated a parallel development in quantitative photodynamic dosimetry. Many of these efforts have been aimed at light dosimetry (1-4). However, it has also been appreciated that the distribution of photosensitizer and its degradation during PDT treatment may significantly effect the outcome of PDT (5-9). Zhou *et al.* (10) have found significant differences in sensitizer uptake among animal tumors, as measured by fluorescence, and in treatment outcome. However when the PDT light fluence was adjusted such that the product of drug fluorescence and light fluence was constant among animals, the animal-to-animal variation in treatment response was reduced. This confirms that fluorescence measurements can be used to guide the delivery of a uniform drug-light product among different patients and among tumor sites or regions within a single patient, a strategy referred to as 'explicit dosimetry' by Wilson (5)

In conjunction with an ongoing Phase I trial of PDT in the human prostate using the investigational agent motexafin lutetium (MLu), we have developed a set of measurements capable of assessing the heterogeneity in light fluence rate, optical properties, and sensitizer concentration during PDT (11). As part of that effort, this paper reports the results of an investigation of the ability of *in vivo* fluorescence spectroscopy to quantify the concentration and spatial heterogeneity of MLu photosensitizer concentration within and among patients. The motivation for this work is the eventual incorporation of the fluorescence-based sensitizer distribution measurements into a spatially-resolved dose calculation system.

The measurement of fluorescence emission *in vivo* is complicated by the absorption and scattering

of light within the sample being measured. Variations in optical properties may be mistaken for variations in fluorophore concentration. Several researchers have developed methods for reducing the effects of background optical properties on the measured fluorescence, either through specially designed optical probes (12,13) or by using independent measurements of optical properties to apply a correction to the measured fluorescence signal (14-19). In the current paper, we use a single optical fiber as the source and detector. This reduces the effects of background optical properties by allowing us to primarily collect light that has traveled a short distance in the tissue. (12) We have developed an empirical correction method to account for variations due to optical properties based on forward-adjoint fluorescence theory (17,20). The parameters in this model are determined by comparing the spatially resolved drug concentrations obtained from fluorescence spectroscopy with those obtained from spectrally-resolved and single-wavelength optical properties measurements. This method provides an approximate correction factor for position in the prostate at which fluorescence is measured. We provide an assessment of the uncertainty in photosensitizer concentration induced by variations in optical properties.

MATERIALS AND METHODS

Patient preparation and treatment. The *in vivo* results presented here were acquired as part of an ongoing Phase I trial of PDT using the investigational agent motexafin lutetium (MLu, Pharmacyclics, Inc., Sunnyvale, CA) for the treatment of recurrent prostate cancer after radiation therapy at the University of Pennsylvania (21). The protocol was approved by the Institutional Review board of the University of Pennsylvania, the Clinical Trials and Scientific Monitoring Committee of the University of Pennsylvania Cancer Center and the Cancer Therapy Evaluation

Program of the National Cancer Institute. The photosensitizer used in this protocol, MLu, is a second-generation, water-soluble photosensitizer with an absorption maximum around 732 nm (22,23). The design of our protocol involves escalating the administered drug dose and the total light fluence delivered to the prostate, and varying the time between the administration of the photosensitizer and the beginning of irradiation. The values of each of these parameters for each of the five patients reported here are listed in table 1. The numbering of patients correlates with that of Zhu *et al.* (4).

Under our protocol, clear brachytherapy catheters are placed in the prostate using a template consisting of holes spaced 0.5 cm apart. Irradiation of the prostate is accomplished by placing cylindrical diffusing fibers (CDF's) of various lengths into the catheters. The range of MLu concentrations investigated and the light source loading pattern used in human patients are based on a previously reported study in a canine model (24). Several weeks before the planned treatment, patients, having given informed consent, are examined by transrectal ultrasound (TRUS) to determine the size and position of the prostate. For planning purposes, the prostate is divided into four quadrants. The positions of the catheters are chosen to provide uniform illumination of the prostate by maintaining a spacing of 1 cm between them. The length of the CDF in each catheter is chosen to cover the entire length of the prostate.

To monitor the local fluence rate during treatment, one additional catheter is inserted in each quadrant. This catheter holds an isotropic, fiber optic-based detector connected to a calibrated photodiode-based dosimetry system that continuously measures and records the fluence rate at the detector position (3,4). This detection catheter is also used for fluorescence measurements before and after PDT treatment, as described below, as well as to measure tissue optical properties at the treatment wavelength of 732 nm (4) and to quantify the absorption and scattering spectra of the

tissue (11,25). Biopsy samples are acquired before and after treatment. The absolute MLu concentration of these samples is determined by an *ex vivo* fluorescence assay based on that of Woodburn, *et al*. (26). Unlike the optical measurements described below, the biopsies are taken manually, and are not guided by ultrasound. It is therefore impossible to quantitatively relate the biopsy site to the positions of the optical measurements.

Fluorescence spectroscopy setup. A schematic of the fluorescence spectroscopy measurement system is shown in figure 1(a). Fluorescence excitation light from a 465-nm light emitting diode (LED) is collected by an optical fiber, collimated, and directed onto a dichroic beamsplitter (Chroma Technology, Rockingham, VT) with a cutoff wavelength of 600 nm. The reflected beam is then refocused onto the proximal end of a probe consisting of a single optical fiber with a 600 micron core, terminated in a beveled tip (FiberOptic Systems, Inc. Simi Valley, CA). This fiber emits and collects light at right angles to its axis, allowing it to interrogate tissue adjacent to the catheter in which it is placed. The projected area of the emission/collection region on the outside of the catheter is approximately 1 mm^2. Fluorescence collected by the fiber is again collimated and, by virtue of its longer wavelength, passes through the dichroic beamsplitter. To further discriminate against excitation light, an OG 530 glass filter (Schott Glass Technologies, Duryea, PA) is placed in the beam path, blocking light at wavelengths shorter than 530 nm. The transmitted light is coupled by an optical fiber and a 0.125 m focal length spectrograph (Acton Instruments, Acton, MA) onto a liquid nitrogen-cooled charge-coupled device (CCD) (Princeton Instruments, Princeton, NJ). The spectrograph and CCD collect spectra with a pixel width corresponding to 0.43 nm over the range from 440 nm to 940 nm. The actual resolution of the measurement is limited by the spectrograph resolution to approximately 5 nm.

During *in vivo* measurements, the fluorescence probe is placed in one of the clear catheters previously inserted in the prostate for *in-vivo* light dosimetry. The arrangement of the catheters used for detection in a typical prostate is shown in figure 1(b). Fluorescence spectra are acquired at intervals of 0.2 cm along the distal 4 cm of the detection catheter in each quadrant. The position of the fluorescence probe is controlled by a step motor-driven positioning stage (Unislide, Velmex, Inc., East Bloomfield, NY) controlled by the same computer that triggers the data acquisition (11). To ensure repeatable positioning of the probe within the catheter, the probe is aligned to the closed end of the catheter prior to the initialization of each scan. Acquisition of data is coordinated by the light dosimetry computer as follows: First, the light dosimetry system sends a transistor-transistor logic (TTL) pulse *via* the stepper motor controller to the CCD controller. This triggers the acquisition of the first fluorescence spectrum. When the spectrum has been acquired and saved, the CCD controller sends an answering TTL pulse back to the stepper motor controller. Upon receiving this signal, the stepper motor controller moves the optical fiber 0.2 cm, waits for it to come to a complete stop, and triggers the CCD to acquire the next spectrum. This process repeats until the pre-programmed number of spectra has been acquired. Because the TTL triggering is handled within the CCD and motor controllers, the light dosimetry system is not required to monitor the process. At the completion of the process, the light dosimetry system receives a confirmation signal from the motor controller and records the completion time and measurement details in a log file.

Data analysis. The analysis of data is accomplished using a custom-designed graphical user interface (GUI) written in the Matlab® (Mathworks, Inc, Natick, MA) programming environment. While the essential data analysis and fitting could be accomplished using batch programming, the

GUI offers a significant advantage in that it allows the user to see the fitting results as they are generated, and to identify poor fits or spectra that include artifactual data, and to adjust the fitting range to compensate.

Within the GUI program, the spectra acquired by the CCD are corrected for dark current and the offset inherent in the CCD's digitizer, and converted to Matlab matrix format. The spectra are then analyzed using the singular value decomposition (SVD) fitting algorithm described by Finlay *et al.* (27). This algorithm requires the selection of basis spectra corresponding to the known components of the fluorescence emission spectrum. We have constructed two basis spectra, both taken from a Liposyn phantom. The first spectrum is the fluorescence measured in a phantom consisting only of Liposyn dissolved in water to a lipid concentration of 0.5%. This fluorescence signal arises primarily from the plastic catheter and optical components in the beam path. This component is therefore independent of the sample being measured, and can serve as a measure of excitation light intensity. The second basis spectrum is that of MLu, measured at a concentration of 0.5 mg/kg in the same phantom.

The SVD algorithm we employ also includes a 61-term Fourier series (27) to account for fluorescence of unknown origin. The Fourier components are given much lower weight in the fitting routine than the basis spectra of known fluorophores to restrict their application to components of the spectrum that cannot be fit by combinations of these species. In the cases presented here, the Fourier components constitute only a minor contribution to the total fit, indicating that the known fluorophores adequately account for the fluorescence we observe.

The SVD algorithm reduces the measured spectrum to a set of amplitudes, one for the background component, one for MLu, and 61 for the Fourier series. To compensate for variations in lamp intensity, we divide the MLu amplitude by the background amplitude obtained from the

same spectrum, yielding a normalized MLu amplitude. The scaling of the basis spectra is chosen such that the normalized MLu amplitude obtained from the 0.5 mg/kg MLu phantom is 0.5. Therefore, if the fluorescence is not distorted by sample optical properties (see below), the normalized MLu amplitude is numerically equal to the MLu concentration of the sample in mg/kg.

The normalized MLu amplitude provides a quantitative measure of the local MLu concentration. Because it is determined by fitting to the entire measured spectrum, this value is less sensitive to noise at individual wavelengths and to the presence of unknown fluorophores with spectra distinct from that of MLu than a single wavelength measurement would be. The relationship between the amplitude and the local concentration of MLu, however, is not necessarily the same as that in the phantom in which the basis spectrum is measured. The *in vivo* case differs from the phantom case in the chemical composition of the medium and in its absorption and scattering coefficients at both the excitation and emission wavelengths of MLu. To take these effects into account, we multiply the measured MLu amplitude by an empirically determined correction factor, as described below.

Effect of optical properties on the measured fluorescence signal. The effects of absorption and scattering on measured fluorescence in semi-infinite media can be modeled using the forward-adjoint fluorescence scheme proposed by Crilly *et al* (20). Briefly, this method models the forward propagation of excitation light from the source and the time-reversed, or adjoint, propagation of positional importance from the detector. The positional importance is defined as the probability that a photon emitted at a point is eventually captured by a detector. The volume integral of the product of the excitation fluence rate and the importance is proportional to the measured signal. Finlay and Foster (17) have derived an analytic solution to this model for the case of an isotropic

point source and an isotropic detector in an infinite homogeneous medium, which for the diffusion approximation takes the form:

$$F_{\det} = F_0 \frac{1}{4\pi D_x D_m r_{sd} \left(\mu_{eff(x)}^2 - \mu_{eff(m)}^2\right)} \left(e^{-\mu_{eff(m)} r_{sd}} - e^{-\mu_{eff(x)} r_{sd}}\right), \qquad (1)$$

where r_{sd} is the distance between the source and detector, D is the diffusion constant given by $1/(3\mu_s')$ (28), μ_{eff} is the effective attenuation coefficient equal to $\sqrt{3\mu_a\mu_s'}$ (29), the subscripts x and m denote the excitation and emission wavelengths, respectively, and F_0 is the intrinsic fluorescence of the sample. The diffusion theory fails at small albedos and small source-detector separations. To overcome this, we replace equation 1 with the corresponding higher-order P_3 approximation. This approximation has identical form, but has four terms rather than 1, corresponding to the four combinations of the asymptotic and transient solutions of the P_3 equation at the excitation and emission wavelengths (17). This formula assumes that both the source and detector are point-like. In the measurements reported here, a single fiber serves as both source and detector; however it is finite in extent and non-isotropic.

To approximate the true physical situation, we assume that the light beam exiting or entering our probe is a pencil beam. To account for the finite extent of the probe, we represent the excitation source and the detector as two pencil beams separated by an empirically determined shift. We model each pencil beam by a point source at a distance of 1 transport mean free path in the z direction (30). r_{sd} then becomes the distance between these two virtual sources.

To test the accuracy of this model, we designed a set of experiments in tissue-simulating phantoms containing Liposyn as a scatterer and MLu. In the first, the μ_a of the phantom was varied by varying the MLu concentration from 0 to 10 mg/kg, while μ_s' was held constant. In the second, the μ_a was varied by adding black ink in varying amounts to a phantom with constant μ_s'

and constant MLu concentration of 4 mg/kg. The optical properties of each phantom are listed in table 2. In each case, the fluorescence was analyzed as described above and the resulting MLu signal was divided by the known MLu concentration (in units of mg/kg).

To account for differences in optical properties between our phantom and the *in vivo* case, we have introduced an empirical correction factor that depends on the measured 730-nm optical properties of the sample. Ideally, the measured optical properties at each position at which fluorescence is measured could be used as inputs for the theoretical expression described in equation 1, and the resulting correction factor could be calculated from first principles. However, such a calculation would require accurate knowledge of the optical properties at the excitation wavelength as well as the emission wavelength, which is beyond the capability of our current measurement system. Instead, we have adopted an empirical, multiplicative correction of the form

$$C = C_0 \frac{\exp\left(b\mu_{eff}\right)}{\mu_s'}, \qquad (2)$$

where the optical properties are those measured at 732 nm. Equation 2 is an approximation of the inverse of equation 1, in the case of high albedo and unchanging optical properties at the excitation wavelength.

Absorption measurements. In addition to the fluorescence measurements described above, we have measured the MLu concentration using single-wavelength (4) and spectrally resolved absorption measurements (23). These were acquired by placing an isotropic fiber-based light source illuminated by the 732 nm treatment laser or by a broad-spectrum lamp in a catheter parallel to the detection catheter and measuring the fluence rate or spectrum in the detection catheter with an isotropic detector, as reported previously (11,25). In the case of spectroscopy, the

resulting spectra can be fit using photon diffusion theory to determine the absorption and scattering spectra of the prostate. The absorption spectra can then be fit using the SVD algorithm described above to determine the concentrations of oxy- and deoxy-hemoglobin and MLu. In the single-wavelength case, we assume that the μ_a of the prostate varies linearly with MLu concentration as $\mu_a = ([\text{MLu}]\ 0.066\ (\text{mg/kg})^{-1}\ \text{cm}^{-1} + B)$, as determined previously from a larger set of patient measurements (4), where *B* is a constant that accounts for the MLu-independent background absorption of tissue. In the previous work, the best fit value of *B* was found to be 0.23 cm^{-1}.

To determine the optimal value of *B* for the patients shown here, we have compared the absorption spectroscopy and 732-nm absorption measurements taken in three quadrants for patient #13, as shown in figure 2. A linear fit to the combined data for this patient assuming uniform relative error for all data points yields a *B* value of 0.11 cm^{-1}, as indicated by the solid line. The minimum and maximum values of *B* obtained from individual quadrants were 0.16 cm^{-1} and 0.042 cm^{-1} in the right upper and right lower quadrants, respectively, as indicated by the dashed lines in figure 2. For all the patients shown here, we have adopted a value of 0.11 cm^{-1}. This value ensures that none of the MLu concentrations derived from 732-nm measurements are negative, and assures good agreement with the spectrally-resolved absorption measurements and with the value measured previously in a canine model (31). This relation can then be used to determine the MLu concentration in a particular prostate from that prostate's μ_a.

RESULTS AND DISCUSSION

Phantom verification

The MLu fluorescence measured in the two tissue-simulating phantoms described above is shown in figure 3(a) as function of excitation-wavelength μ_{ax}. The data points from the two phantoms do not overlap because the values of μ_s' and μ_{am} for the two phantoms were different.

We have applied equation 1 to predict the variation in measured fluorescence resulting from the optical properties of these phantoms. The results are shown by the solid lines in 3(a). In applying equation 1, we used a lateral shift between pencil beams representing the source and detector of 0.45 cm. It should be emphasized that this lateral shift was determined empirically, and does not necessarily correspond to any physical dimension of the probe. In figure 3(b), we plot the factor needed to correct each measurement for the distortion introduced by the difference in optical properties relative to the 0.5 mg/kg phantom. The correction is the inverse of the fluorescence amplitude per unit MLu concentration shown in panel (a). The correction factors used in analyzing our *in vivo* data correspond to excitation-wavelength absorption coefficients of approximately 1 to 4 cm^{-1}, as indicated by the shaded area.

There may be significant variations in optical properties among prostates (4) and within a single prostate (11). The agreement between theory and experiment indicates that if the reliability and accuracy of absorption measurements can be improved, these effects can be corrected for each individual prostate from first principles. This correction requires accurate knowledge of the absorption and scattering coefficients of the tissue at both the excitation wavelength (465 nm) and the emission wavelength range (approximately 730 to 780 nm). Our current experimental design allows us to measure the optical properties at 732 nm, and our absorption spectroscopy measurements extend over the entire emission range. We do not currently measure the optical properties at the excitation wavelength. Extrapolating the optical properties at 465 nm based on the absorber concentrations obtained from absorption spectroscopy introduces an uncertainty that

is likely as large as the correction being made. We have therefore adopted the empirical correction-factor based method described in Methods.

In vivo MLu fluorescence

We have measured *in vivo* fluorescence spectra for 5 patients thus far. Spectral analysis of a typical fluorescence spectrum is shown in figure 4. The noisy line indicates the measured fluorescence emission data, and the dotted and dashed lines, the components determined by the SVD algorithm. We consistently observe a shift in the emission maximum of MLu from approximately 738 nm in the phantom to 745 nm *in vivo*, probably due to differences in chemical microenvironment between the two systems. We have accounted for this wavelength shift by digitally shifting our basis spectrum prior to fitting. The sum of the known components is represented by the solid line that closely matches the data. The sum of the contributions of the terms of the Fourier series, labeled 'residual' on the plot, is much smaller in amplitude than the contributions of the background fluorescence and MLu, indicating that these known components accurately model the majority of the measured fluorescence.

Determination of parameters for fluorescence correction: In figure 5 we plot the ratios of MLu concentration determined by 732-nm absorption (open squares) and by absorption spectroscopy (open triangles) to the corresponding normalized fluorescence amplitude as functions of the measured μ_a at 732nm. Each value plotted represents the mean from a single quadrant. A total of 13 single wavelength and 6 spectroscopic measurements from 4 patients are included. Equation 2 was fit to the data points shown in figure 5 with C_0 and b as free parameters, resulting in values of 3.1 cm^{-1} and 0.97 cm, respectively. It is likely that these values are specific to the probe design we employed. The solution of Equation 2 for each data point is indicated by the corresponding

filled circles. The points do not lie on a common curve because the value of μ_s' differs from point to point. The correction factor thus determined was applied to all patients for whom 732 nm optical properties measurements were available. Because the fluorescence spectra were measured at more points than the optical properties, the optical properties were interpolated at intermediate points. When the fluorescence measurements extended beyond the range of the optical properties measurements, the mean optical properties for the quadrant were used. In cases where one quadrant was missing these measurements, the mean optical properties for the patient were substituted. In one case where reliable measurements were not available for any quadrant, a global mean correction factor of 9.3 was adopted. This value was determined by averaging the measured correction factors based on comparison with values obtained from 732 nm absorption for the patients listed in table 3.

Spatial distribution of MLu: In one patient (# 13), we have obtained fluorescence profiles in all four quadrants of the prostate both before and after PDT treatment. These profiles, corrected for the effects of optical properties using the equation 2, are shown in figure 6. The profiles taken before and after treatment show similar shape and concentration, with the exception of the RUQ (panel b), which shows a similar shape but reduced concentration compared to the pre-treatment profile. The measurements in the upper quadrants (LUQ and RUQ) were made 1.5 cm anterior to those in the lower quadrants (LLQ and RLQ, respectively), while those in the right quadrants (RUQ and RLQ) were shifted 2 cm laterally from those in the left quadrants (LUQ and LLQ, respectively), as shown in figure 1(b).

As expected, we see significant variation among the four quadrants. However, the general features, namely a peak in MLu concentration around 0.5 to 1.5 cm and a shallow minimum around 3.0 cm, are reproduced in three out of the four quadrants. This indicates that the variations

in MLu concentration occur on a scale of approximately 1.5 to 2 cm (the spacing of the catheters used to make these measurements) in all three dimensions. We therefore expect a set of measurements with a catheter spacing of 1 cm to be sufficient to characterize the MLu distribution in a typical prostate. The origin of this fluorescence variation is not clear, however the phenomenon of increased fluorescence near the periphery or an organ or tumor has been observed in animal models (32).

We have compared spatial distributions obtained by fluorescence measurements with single-wavelength and spectrally-resolved absorption measurements from 16 scans in 4 patients to determine the relation between the optimal correction factor and the measured μ_a at 732 nm, as described in Methods. The mean calculated correction factor used for each patient is listed in table 3. For comparison, we also list the mean values of ratio of MLu concentrations determined by absorption spectroscopy and 732 nm μ_a to that determined by uncorrected fluorescence spectroscopy. These values are in rough agreement with the calculated values for each patient.

The relatively small variation in the correction factor, given the large variation in tissue optical properties (4,11) is likely explained by a combination of several factors. First, the μ_a of hemoglobin at the excitation wavelength is an order of magnitude greater than in the emission window, and that of MLu is greater by a factor of two or more. The result is that optical properties at the excitation wavelength have a much greater effect on the fluorescence than those at the emission wavelengths. At the excitation wavelength, however, the absorption in tissue is dominated by hemoglobin, so variations in MLu concentration will have relatively little effect.

Second, single-wavelength absorption measurements of a larger set of human prostates performed as part of our clinical protocol indicate that the majority of the inter-patient variation in absorption coefficient at 732 nm arises from variations in MLu concentration. This indicates that

the effect of absorption at 732 nm will be to reduce the measured fluorescence in cases of high MLu concentration, and to increase it in cases of low MLu concentration (4). Our fluorescence measurements may therefore underestimate the heterogeneity in MLu, however the fact that our correction factor is determined empirically ensures that the mean MLu concentration will be recovered accurately.

In figure 7, we plot the concentrations of MLu determined by single-wavelength absorption measurements, absorption spectroscopy and fluorescence spectroscopy measured in the right upper quadrant of patient #13. Because comparisons of the type shown in figure 7 were the basis for the patient-specific factor used to correct the fluorescence, it is expected that the three measurements agree in absolute concentration. The single-wavelength and spectrally resolved absorption measurements, however, are independent and have not been scaled or normalized to match one another.

The agreement in the spatial distributions measured by absorption and fluorescence is good, particularly in the post-PDT case (Fig. 5b), and confirms that the fluorescence and absorption measurements are in fact measuring the same distribution. In the case shown here, the shape of the MLu distribution remains similar before and after PDT, however the MLu concentration as reported by all three methods decreases by nearly a factor of two, especially in the region around 2 to 3 cm, in the center of the prostate. Despite this local photobleaching, the mean MLu concentration in the quadrant as a whole decreased by only 20%, because the concentration outside this region remained unchanged.

Comparison of mean MLu concentration among patients

In figure 8, we plot the mean, standard and maximum deviations of MLu concentration in

each quadrant. The samples are restricted to points within 2.5 cm of the distal end of the prostate to prevent including measurements from other structures. The data are grouped by patient. Within each patient, the quadrants are plotted in order from RUQ to LLQ as indicated. Only for patient #13 did we make measurements before and after treatment in all four quadrants. The mean MLu concentration obtained from fluorescence measured *in vivo* is plotted as a function of the corresponding value measured *ex vivo* from biopsies in figure 9. Both the pre-PDT (open squares) and post-PDT (filled squares) data are plotted. The errorbars indicate the range in MLu concentration measured *in vivo.* The dashed lines connect each pre-PDT measurement with its corresponding post-PDT measurement. For comparison, the solid line has a slope of 1, indicating perfect agreement. Although the biopsy-determined value is within the range of the fluorescence measurements for the majority of cases, the uncertainties in the measurements and the sample size make it impossible to draw any statistically significant conclusions based on this comparison.

In figure 10, we plot the mean concentration of MLu in each prostate measured by *in vivo* fluorescence, the *ex vivo* fluorescence assay, and single-wavelength and spectrally resolved absorption, before (open symbols) and after (filled symbols) irradiation. For patient #16, we have measured 732 nm absorption along four catheters in each quadrant. The mean reported here is the mean of all measurements in the entire prostate. Several anomalous values of μ_a larger than 2.5 cm^{-1} were discarded as outliers. The dotted lines show the mean of the four measurements in each patient, and the shaded region extends one standard deviation on each side of the mean.

The light-induced destruction of photosensitizer, or photobleaching, during PDT has been observed for several sensitizers. *In vivo* measurements of photobleaching of MLu, however, have not been previously reported. In one case (patient #12) we observed significant photobleaching of the sensitizer during treatment. In another (patient # 13), we observe some photobleaching in the

RUQ, but no significant photobleaching in other quadrants. In general, the variation in MLu concentration within a given patient is greater than the change induced by irradiation, making a generalization with respect to the photobleaching behavior *in vivo* impossible in the present study.

While the absorption and fluorescence measurements reported here agree in the MLu concentration, the two measurements are not interchangeable. Absorption measurements, because they allow characterization of fluorescent and non-fluorescent absorbers, can provide information about hemoglobin concentration and oxygen saturation, in addition to drug concentration measurement. Fluorescence measurement requires only a single catheter to measure the drug distribution, while the absorption measurements require two. In our clinical experience, we have often encountered cases where the pooling of blood around one or more catheters renders the absorption spectroscopy data uninterpretable. In many of these cases, fluorescence spectra, which require only one catheter to be blood-free, could still be measured and analyzed.

We anticipate that fluorescence measurements similar to those shown here will be useful for PDT dosimetry. They allow rapid acquisition of drug distribution information at high resolution with far fewer scans that would be required for an absorption spectroscopy measurement of comparable resolution. It is true that the fluorescence measurement requires a corresponding optical property measurement for optical properties correction, which adds to the complexity and acquisition time. Ongoing work in our laboratory aims to develop a method for determining absorption and scattering coefficients from a single scan of a single-wavelength linear light source such as that used for treatment. We anticipate that this will greatly improve the efficiency of data acquisition, and make fluorescence spectroscopy practical as part of a near-real time dosimetry system.

CONCLUSIONS

We have demonstrated the ability of fluorescence spectroscopy, coupled with an empirical, model-based fitting algorithm, to quantitatively measure the concentration and distribution of MLu in the human prostate. The variation in MLu concentration among prostates makes individual measurement necessary. In addition, we observe variations in MLu fluorescence within individual prostates that is equal to or greater than the variation among different patients' prostates. This indicates that to optimize treatment for the entire prostate, it will be necessary to build up a map of the MLu concentration in three dimensions. As a first step to creating a map of MLu distribution, we have acquired fluorescence profiles in all four quadrants of the prostate of one patient (Fig. 4). Our current work indicates that the spatial variation of MLu concentration occurs on a scale of approximately 1.5 – 2 cm in all three dimensions. This can be achieved in our current clinical protocol by using the catheters currently reserved for treatment (at 1 cm spacing), in addition to the four dedicated detector catheters for fluorescence measurement. Work in this area is ongoing.

Acknowledgments-- This work has been supported by Department of Defense grant DAMD17-03-1-0132 and by National Institutes of Health PO1 grant CA87971-01. Figure 4 and portions of the methods and data presented here have been published previously in SPIE conference proceedings (33).

REFERENCES

1. Star, W. M., J. P. A. Marijnissen, and M. J. C. van Gemert (1988) Light dosimetry in optical phantoms and in tissues: I. Multiple flux and transport theory. *Phys. Med. Biol.* **33**, 437-454.
2. Jacques, S. L. (1992) Simple optical theory for light dosimetry during PDT. *Proc. SPIE*. **1645**, 155-165.
3. Dimofte, A., T. C. Zhu, S. M. Hahn, and R. A. Lustig (2002) *In vivo* light dosimetry for motexafin lutetium-mediated PDT of recurrent breast cancer. *Lasers Surg. Med.* **31**, 305-312.
4. Zhu, T. C., A. Dimofte, J. C. Finlay, D. Stripp, T. Busch, J. Miles, R. Whittington, S. B. Malkowicz, Z. Tochner, E. Glatstein, and S. M. Hahn (2005) Optical properties of human prostate at 732 nm measured *in vivo* during Motexafin Lutetium–mediated photodynamic therapy. *Photochem Photobiol*. **81**, 96-105.
5. Wilson, B. C., M. S. Patterson, and L. Lilge (1997) Implicit and explicit dosimetry in photodynamic therapy: A new paradigm. *Lasers Med. Sci.* **12**, 182-199.
6. Potter, W. R., T. S. Mang, and T. J. Dougherty (1987) The theory of photodynamic therapy dosimetry: Consequences of photo-destruction of sensitizer. *Photochem. Photobiol.* **46**, 97-101.
7. Jacques, S. L., R. Joseph, and G. Gofstein (1993) How photobleaching effects dosimetery and fluorescence monitoring of PDT in turbid media. *Proc.SPIE*. **1881**, 168-179.

8. Georgakoudi, I., M. G. Nichols, and T. H. Foster (1997) The mechanism of Photofrin photobleaching and its consequences for photodynamic dosimetry. *Photochem. Photobiol.* **65**, 135-144.

9. Farrell, T. J., R. P. Hawkes, M. S. Patterson, and B. C. Wilson (1998) Modeling of photosensitizer fluorescence emission and photobleaching for photodynamic therapy dosimetry. *Appl. Opt.* **37**, 7168-7183.

10. Zhou, X., B. W. Pogue, B. Chen, E. Demidenko, R. Joshi, J. Hoopes, and T. Hasan (2006 (In press)) Pretreatment photosensitizer dosimetry reduces variation in treatment response. *Int. J. Radiation Oncology Biol. Phys.*

11. Zhu, T. C., J. C. Finlay, and S. M. Hahn (2005) Determination of the distribution of light, optical properties, drug concentration, and tissue oxygenation in-vivo in human prostate during motexafin lutetium-mediated photodynamic therapy. *J Photochem. Photobiol. B: Biol.* **79**, 231-241.

12. Weersink, R. W., M. S. Patterson, K. Diamond, S. Silver, and N. Padgett (2001) Noninvasive measurement of fluorophore concentration in turbid media with a simple fluorescence/reflectance ratio technique. *Appl. Opt.* **40**, 6389-6395.

13. Diamond, K. R., M. S. Patterson, and T. J. Farrell (2003) Quantification of fluorophore concentration in tissue-simulating media by fluorescence measurements with a single optical fiber. *Appl. Opt.* **42**, 2436-2442.

14. Muller, M. G., I. Georgakoudi, Q. Zhang, J. Wu, and M. S. Feld (2001) Intrinsic fluorescence spectroscopy in turbid media: Disentangling effects of scattering and absorption. *Appl. Opt.* **40**, 4633-4646.

15. Wu, J., M. S. Feld, and R. P. Rava (1993) Analytical model for extracting intrinsic fluorescence in turbid media. *Appl. Opt.* **32**, 3583-3595.

16. Gardner, C. M., S. L. Jacques, and A. J. Welch (1996) Fluorescence spectroscopy of tissue: Recovery of intrinsic fluorescence from measured fluorescence. *Appl. Opt.* **35**, 1780-1792.

17. Finlay, J. C. and T. H. Foster (2005) Recovery of hemoglobin oxygen saturation and intrinsic fluorescence using a forward adjoint model of fluorescence. *Appl. Opt.* **44**, 1917-1933.

18. Zhadin, N. N. and R. R. Alfano (1998) Correction of the internal absorption effect in fluorescence emission and excitation spectra from absorbing and highly scattering media: Theory and experiment. *J. Biomed. Opt.* **3**, 171-186.

19. Durkin, A. J., S. Jaikumar, N. Ramanujam, and R. Richards-Kortum (1994) Relation between fluorescence spectra of dilute and turbid samples. *Appl. Opt.* **33**, 414-423.

20. Crilly, R. J., W.-F. Cheong, B. C. Wilson, and J. R. Spears (1997) Forward-adjoint fluorescence model: Monte Carlo integration and experimental validation. *Appl. Opt.* **36**, 6513-6519.

21. Stripp, D., R. Mick, T. C. Zhu, R. Whittington, D. Smith, A. Dimofte, J. C. Finlay, J. Miles, T. M. Busch, D. Shin, A. Kachur, Z. Tochner, S. B. Malkowicz, E. Glatstein, and S. M. Hahn (2004) Phase I trial of Motexfin Lutetium-mediated interstitial photodynamic therapy in patients with locally recurrent prostate cancer. *Proc. SPIE.* **5315**, 88-99.

22. Young, S. W., K. Woodburn, M. Wright, T. D. Mody, W. C. Dow, F. Qing, J. Sessler, and R. A. Miller (1996) Lutetium texaphyrin (PCI-0123): a near-infrared, water-soluble photosensitizer. *Photochem. Photobiol.* **63**, 892-897.

23. Mody, T., L. Fu, and J. Sessler (2001) Texaphyrins: synthesis and development of a novel class of therapeutic agents. *Prog. Inorg. Chem.* **49**, 551-598.

24. Hsi, R. A., A. Kapatkin, J. Strandberg, T. Zhu, T. Vulcan, M. Solonenko, C. Rodriguez, J. Chang, M. Saunders, N. Mason, and S. Hahn (2001) Photodynamic therapy in the canine prostate using motexafin lutetium. *Clin. Cancer Res.* **7**, 651-660.

25. Finlay, J. C., T. C. Zhu, A. Dimofte, D. Stripp, S. B. Malkowicz, R. Whittington, J. Miles, E. Glatstein, and S. M. Hahn (2004) *In vivo* determination of the absorption and scattering spectra of the human prostate during photodynamic therapy. *Proc. SPIE*. **5315**, 132-142.

26. Woodburn, K. W., Q. Fan, D. Kessel, Y. Lou, and S. W. Young (1998) Photodynamic therapy of B16F10 murine melanoma with lutetium texaphyrin. *J. Invest. Dermatol.* **110**, 746-751.

27. Finlay, J. C., D. L. Conover, E. L. Hull, and T. H. Foster (2001) Porphyrin bleaching and PDT-induced spectral changes are irradiance dependent in ALA-sensitized normal rat skin *in vivo*. *Photochem. Photobiol.* **73**, 54-63.

28. Durduran, T., A. G. Yodh, B. Chance, and D. A. Boas (1997) Does the photon-diffusion coefficient depend on absorption? *JOSA A*. **14**, 3358-3365.

29. Nakai, T., G. Nishimura, K. Yamamoto, and M. Tamura (1997) Expression of optical diffusion coefficient in high-absorption turbid media. *Phys. Med. Biol.* **42**, 2541-2549.

30. Farrell, T. J., M. S. Patterson, and B. Wilson (1992) A diffusion theory model of spatially resolved, steady-state diffuse reflectance for the noninvasive determination of tissue optical properties *in vivo*. *Med. Phys.* **19**, 879-888.

31. Zhu, T. C., S. M. Hahn, A. S. Kapatkin, A. Dimofte, C. E. Rodriguez, T. G. Vulcan, E. Glatstein, and R. A. Hsi (2003) In vivo optical properties of normal canine prostate at 732 nm using motexafin lutetium-mediated photodynamic therapy. *Photochem Photobiol*. **77**, 81-88.

32. Pogue, B. W., B. Chen, X. Zhou, and P. J. Hoopes (2005) Analysis of sampling volume and tissue heterogeneity on the *in vivo* detection of fluorescence. *J Biomed Opt*. **10**, 41206.

33. Finlay, J. C., T. C. Zhu, A. Dimofte, D. Stripp, S. B. Malkowicz, R. Whittington, J. Miles, E. Glatstein, and S. M. Hahn (2005) *In vivo* measurement of fluorescence emission in the human prostate during photodynamic therapy. *Proc. SPIE*. **5689**, 299-310.

FIGURE LEGENDS

Figure 1. a) Fluorescence spectroscopy setup. The computer that acquires and stores fluorescence spectra also controls the position of the detection fiber *via* a step-motor positioner (not shown). The dichroic allows a single fiber to deliver excitation light and collect emitted fluorescence. b) Arrangement of the fluorescence detection catheters in a typical human prostate.

Figure 2. Comparison of the 732-nm absorption coefficient with the MLu concentration determined by absorption spectroscopy. The quadrant from which each data point was taken is indicated in the legend. The solid line indicates the best fit used to determine the offset *B*, as described in the text.

Figure 3. a) MLu fluorescence measured in two sets of phantoms, plotted as a function of excitation-wavelength absorption coefficient. See text for details. The solid lines indicate the values predicted by eq. 1, and b) the corresponding correction factor required to recover (F_0) found from eq. 1. The shaded area indicates the range of correction factors determined by comparing *in vivo* scans, and the dashed line indicates the mean *in vivo* correction factor. In both cases, the correction factor was normalized to 1.0 for the case of the 0.5 mg/kg MLu phantom.

Figure 4. SVD analysis of a typical fluorescence emission spectrum. The spectrum is separated into MLu and background components and a small residual composed of a Fourier series.

Figure 5. Correction factor (ratio of fluorescence amplitude to concentration) determined by absorption spectroscopy and by 732-nm absorption coefficient, plotted as a function of absorption coefficient measured at 732 nm.

Figure 6. MLu fluorescence profiles acquired in the four quadrants of the prostate for patient #13 before (dashed lines) and after (solid lines) PDT treatment. Frames (a) through (d) depict the results from the right upper, left upper, left lower, and right lower quadrants, respectively, as indicated in the panel titles. Measurements in all four quadrants were corrected for optical properties using the correction factor appropriate to this patient.

Figure 7. MLu fluorescence (filled circles), absorption spectroscopy (triangles), and 732-nm absorption (squares) profiles as functions of position within the right upper quadrant of patient #13. The profiles measured before (panel a) and after (panel b) PDT treatment are similar in shape, but indicate some photobleaching, especially in the center of the prostate.

Figure 8. Concentration of MLu measured by fluorescence spectroscopy for each patient. Within each patient, the concentration from each quadrant is plotted separately, as indicated. The solid and dashed error bars represent the standard and maximum deviations of measurements within each quadrant, respectively. The concentrations measured before

treatment (open circles) are grouped with the corresponding measurements made after treatment (solid diamonds), and all are corrected using the factors listed in table 3.

Figure 9. Mean MLu concentration determined by *in vivo* fluorescence plotted as a function of the concentration determined by an independent *ex vivo* assay. The dotted and solid errorbars indicate the maximum and standard deviations, respectively, of measurements within each prostate. Dashed lines connect the pre-PDT measurements with their corresponding post-PDT measurements. The solid line indicates exact agreement.

Figure 10. MLu concentration in 5 human prostates measured by fluorescence spectroscopy (circles), *ex vivo* fluoroscopy (squares), absorption spectroscopy (diamonds), and 732 nm absorption (triangles). Both pre-PDT (open symbols) and post-PDT data (filled symbols) are plotted. The dotted lines indicate the mean of all measurements in each patient, and the shaded areas include one standard deviation. The mean fluorescence correction factor for each patient is given in table 3.

Table 1. Treatment parameters for each patient, including MLu dose, interval between drug administration and beginning of irradiation, and total fluence prescribed to the prostate.

Patient Number	MLu dose (mg/kg)	Interval (hours)	Total Fluence (J/cm^2)
12	2	3	50
13	2	3	100
14	2	3	100
15	2	3	100
16	2	3	150

Table 2: Constituents and optical properties of the two sets of phantoms used to investigate the effect of absorption on fluorescence measurements. In each case, the absorption coefficient due to MLu ($\mu_{a\ MLu}$) and the total absorption coefficient ($\mu_{a\ Total}$) are listed separately.

Phantom		1	2
Liposyn (%)		0.5	0.75
MLu (mg/kg)		0 to 10	4
Ink (%)		0	0 to 0.5
465 nm	$\mu_{a\ MLu}$ (cm^{-1})	0 to 1.6	0.63
	$\mu_{a\ Total}$ (cm^{-1})	0 to 1.6	0.63 to 5.0
	μ_s' (cm^{-1})	6.8	10.2
732 nm	$\mu_{a\ MLu}$ (cm^{-1})	0 to 0.63	0.25
	$\mu_{a\ Total}$ (cm^{-1})	0 to 0.63	0.25 to 0.39
	μ_s' (cm^{-1})	4.0	6.0
Symbol in fig. 3		○	■

Table 3: Fluorescence correction factors determined by comparing spatially resolved fluorescence, absorption spectroscopy, and 732-nm absorption measurements in four patients, and the correction factor determined using equation 2

Patient	Abs. Spec./Fluorescence		732 nm/Fluorescence		Calculated C
	No. of scans	Mean	No. of scans	Mean	
12			1	7.3	7.3
13	6	5.8	6	6.4	7.3
15			1	11.4	12.8
16			3	12.1	10.2
Overall	6	5.8	11	9.3 ± 4.8	9.4 ± 2.7

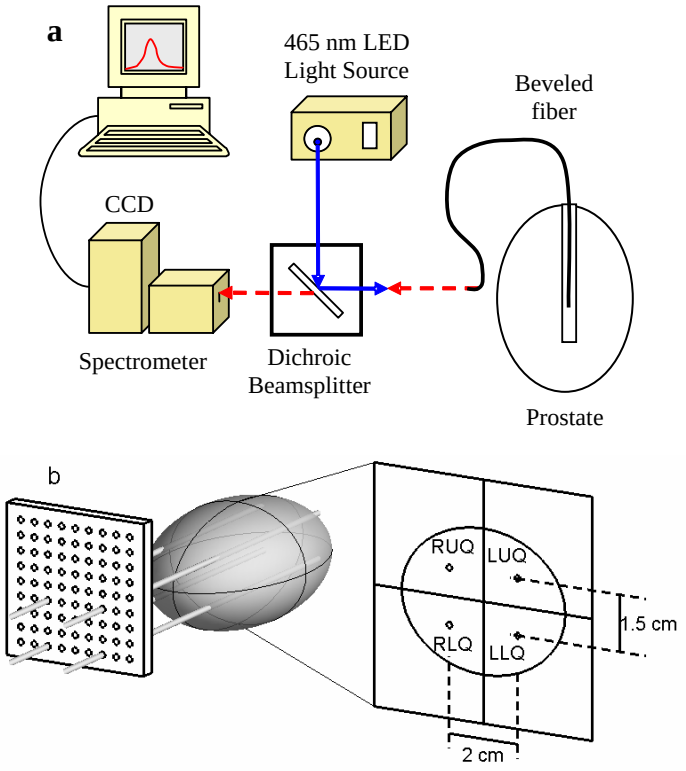
a
465 nm LED
Light Source
Beveled
fiber
CCD
Spectrometer
Dichroic
Beamsplitter
Prostate
b
RUQ
LUQ
RLQ
LLQ
1.5 cm
2 cm

Figure 1

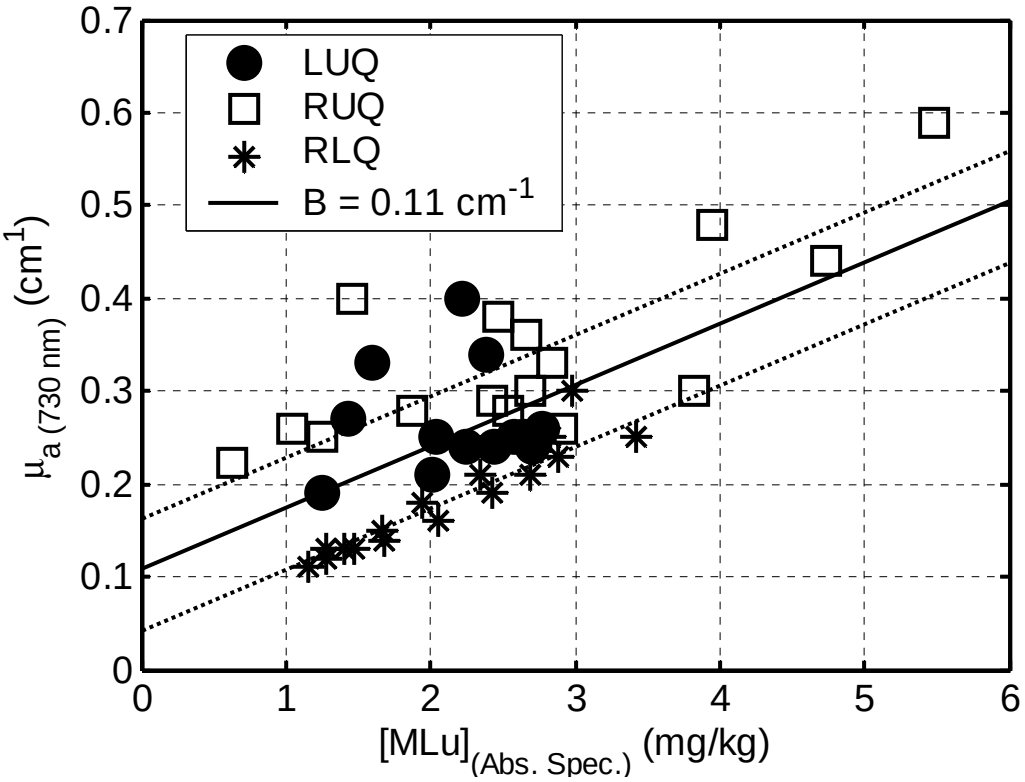
LUQ
RUQ
RLQ
B = 0.11 cm-1
μa (730 nm) (cm-1)
[MLu](Abs. Spec.) (mg/kg)
0
0.1
0.2
0.3
0.4
0.5
0.6
0.7
0
1
2
3
4
5
6

Figure 2

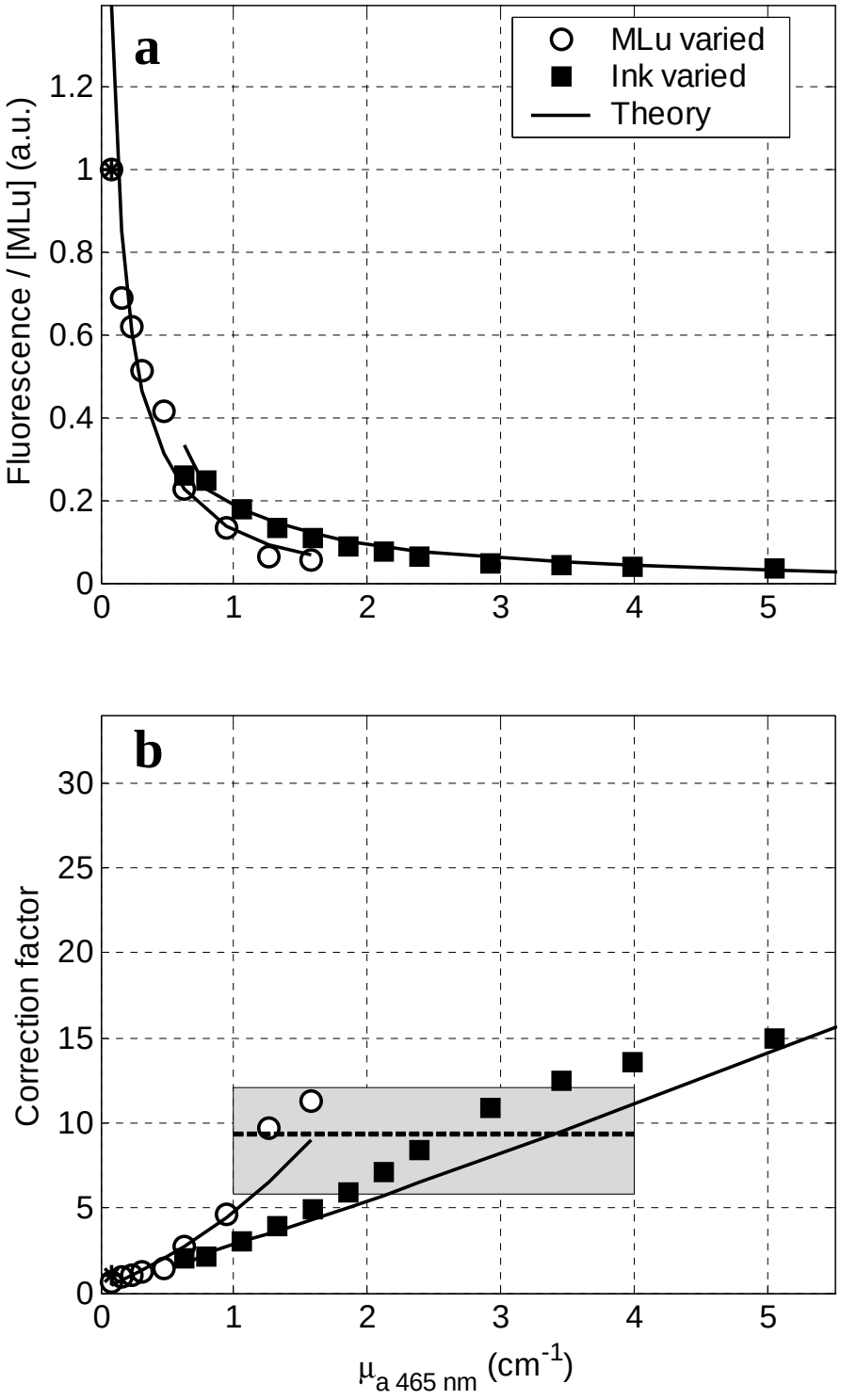
a
MLu varied
Ink varied
Theory
Fluorescence / [MLu] (a.u.)
0
0.2
0.4
0.6
0.8
1
1.2
0
1
2
3
4
5
b
Correction factor
0
5
10
15
20
25
30
0
1
2
3
4
5
μa 465 nm (cm-1)

Figure 3

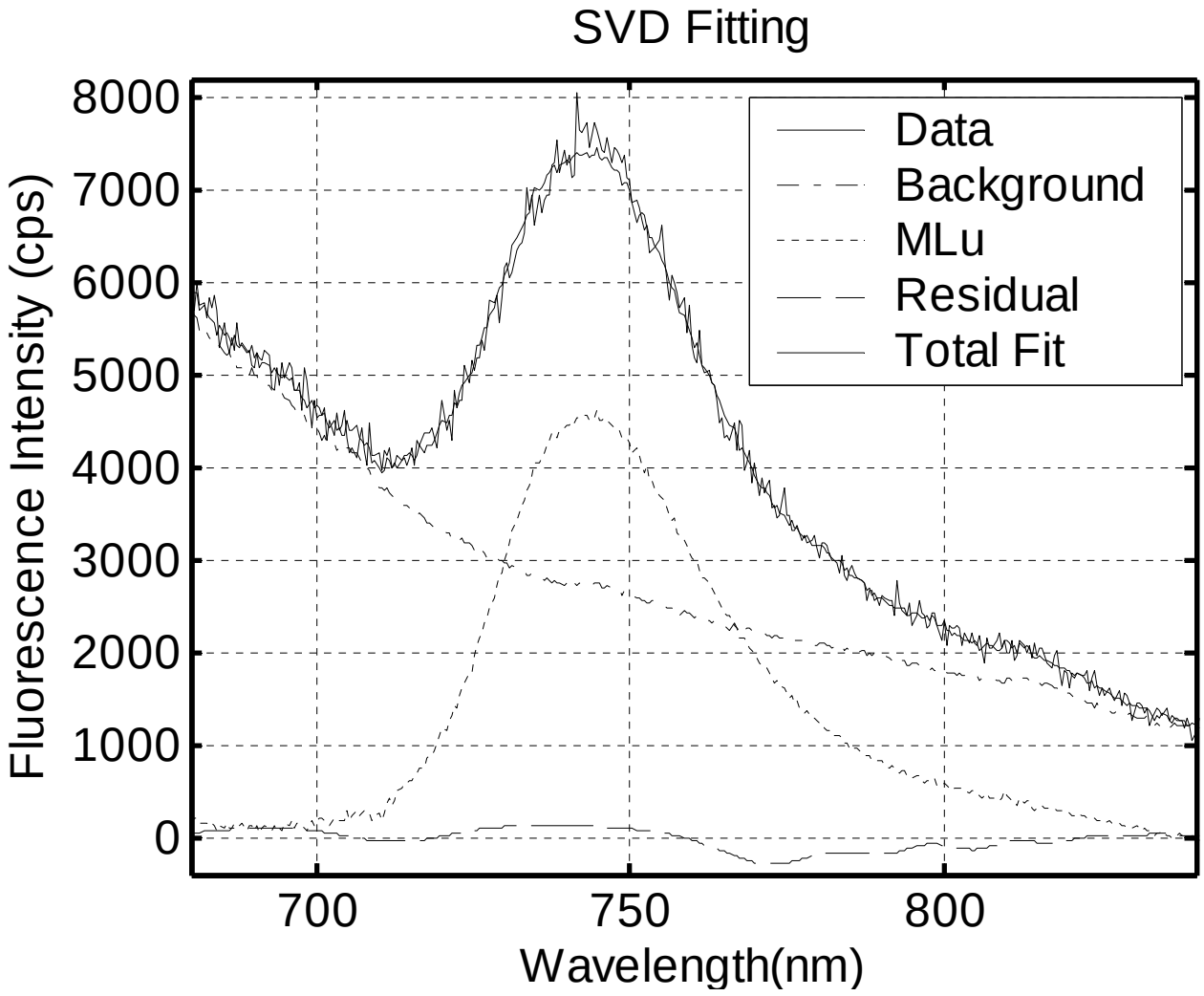
SVD Fitting
Fluorescence Intensity (cps)
8000
7000
6000
5000
4000
3000
2000
1000
0
700
750
800
Wavelength(nm)
Data
Background
MLu
Residual
Total Fit

Figure 4

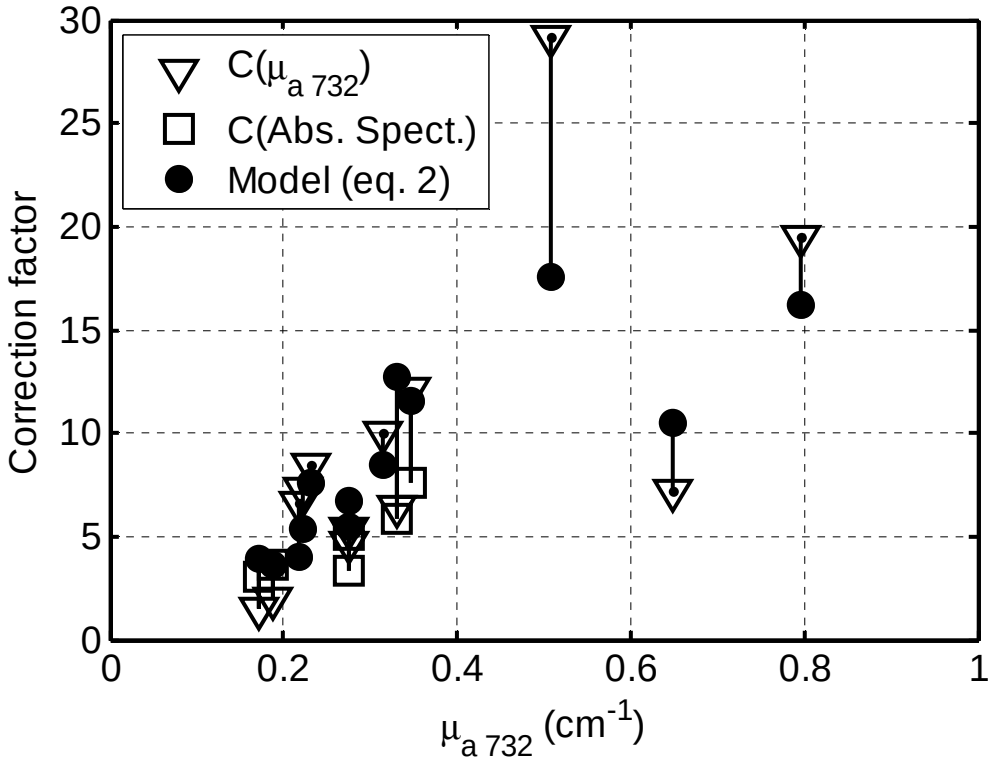
C(μa 732)
C(Abs. Spect.)
Model (eq. 2)
Correction factor
μa 732 (cm-1)
0
5
10
15
20
25
30
0
0.2
0.4
0.6
0.8
1

Figure 5

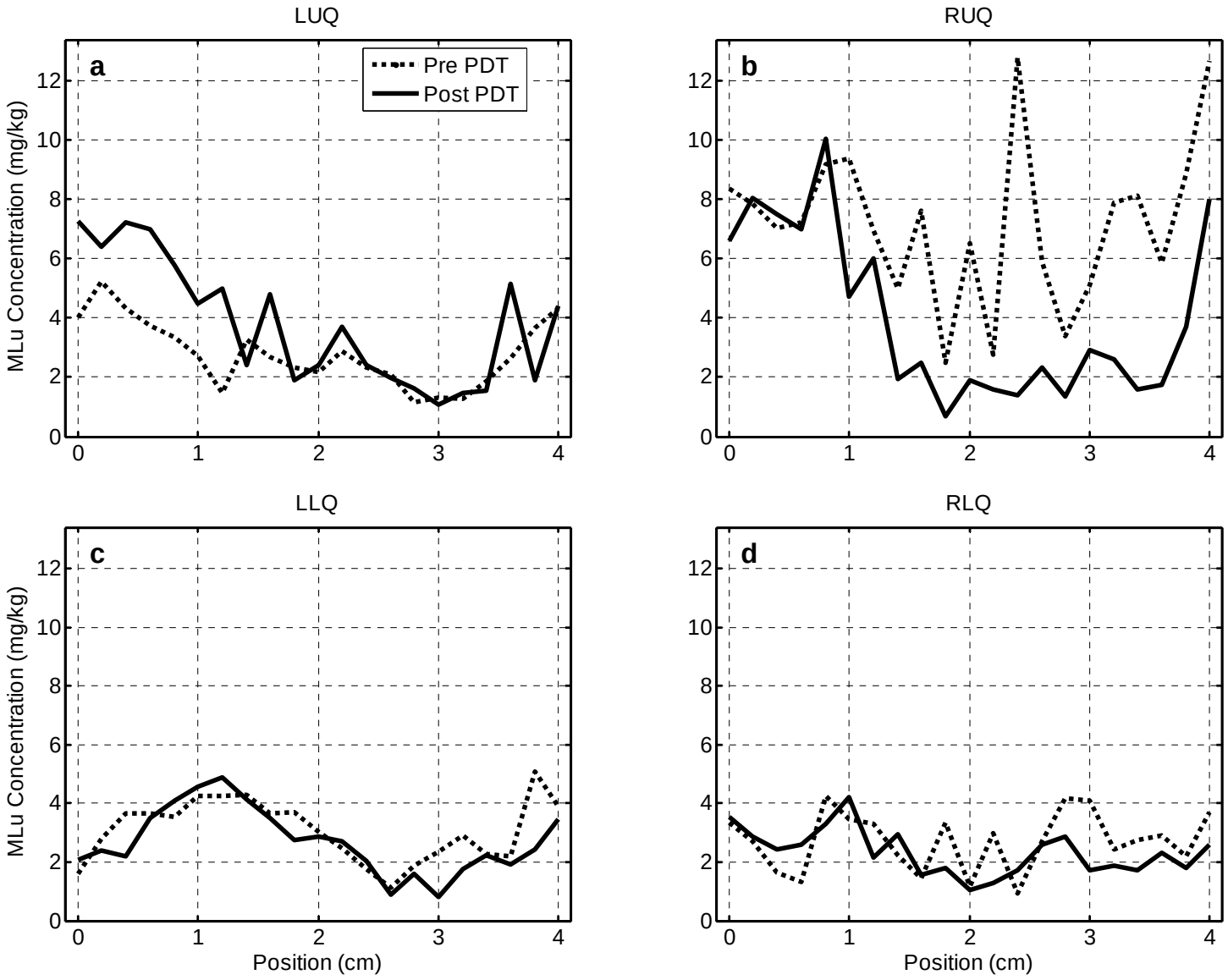
LUQ
RUQ
LLQ
RLQ
a
b
c
d
Pre PDT
Post PDT
MLu Concentration (mg/kg)
Position (cm)
0
1
2
3
4
0
2
4
6
8
10
12

Figure 6

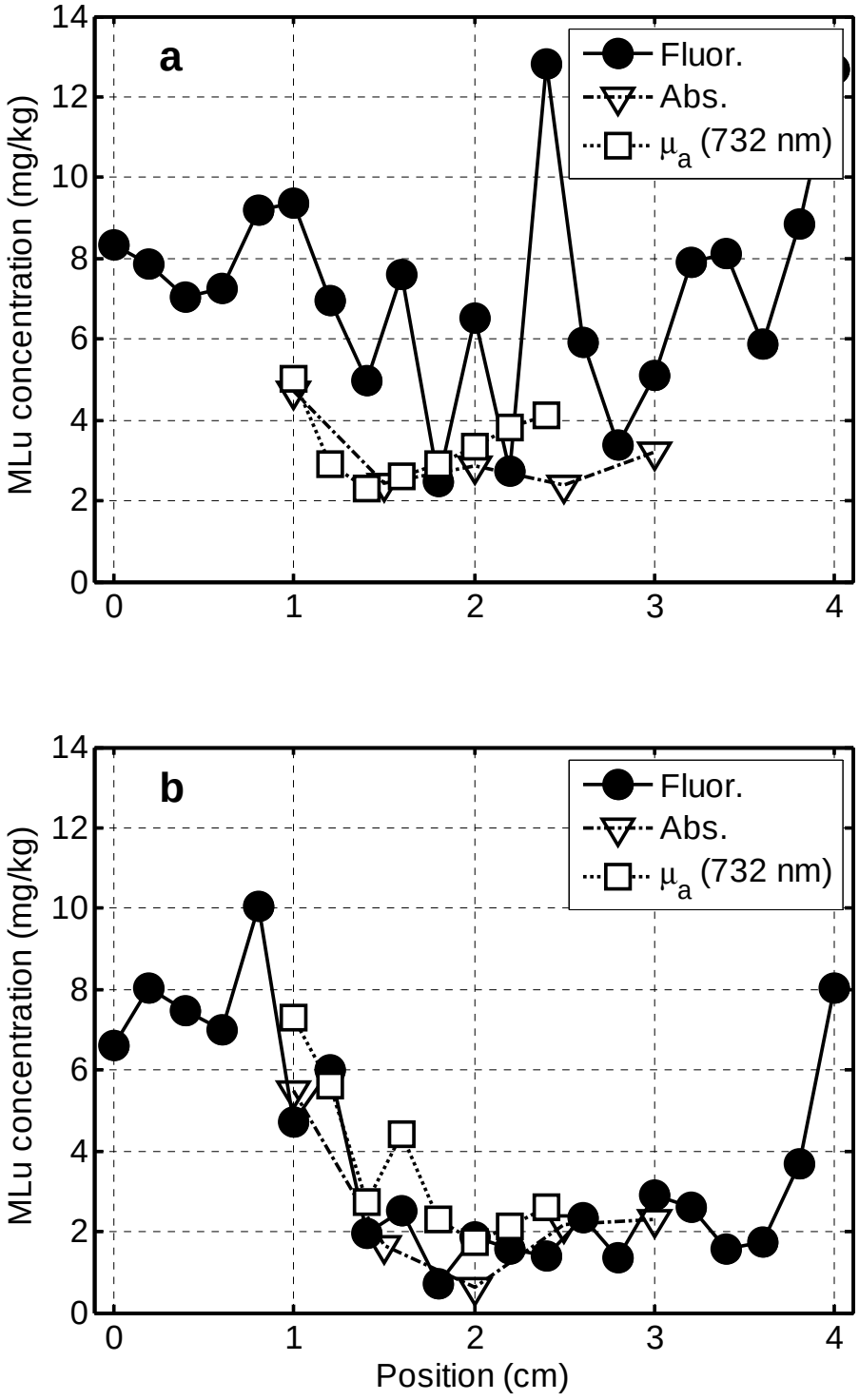
a
b
Fluor.
Abs.
μa (732 nm)
MLu concentration (mg/kg)
Position (cm)
0
2
4
6
8
10
12
14
0
1
2
3
4

Figure 7

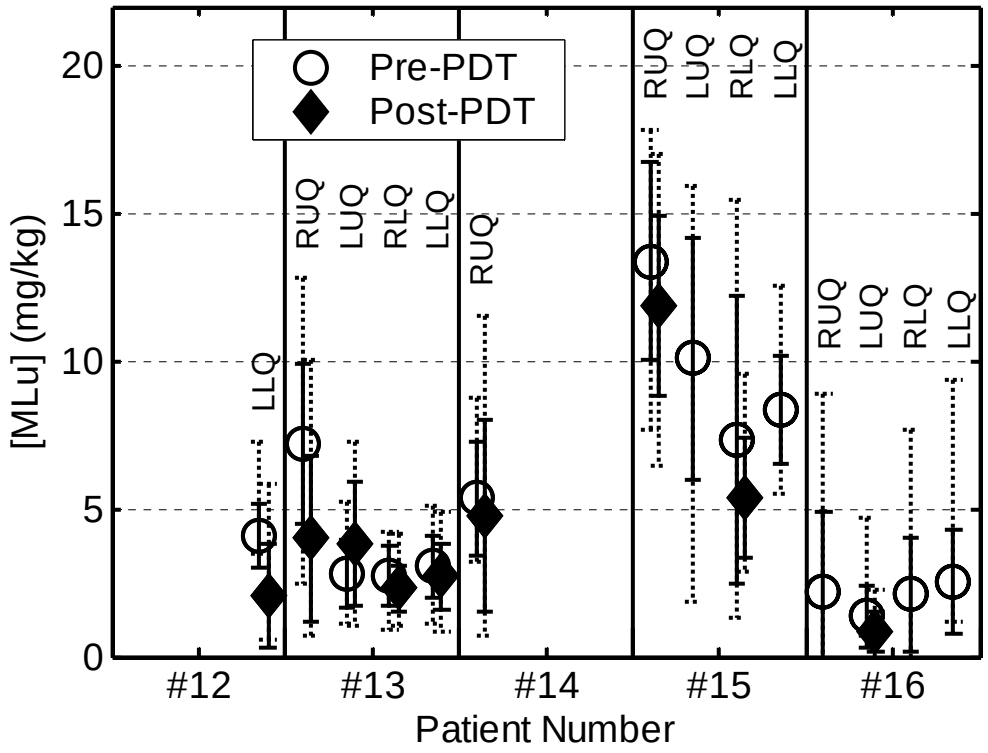
Pre-PDT
Post-PDT
[MLu] (mg/kg)
0
5
10
15
20
LLQ
RUQ
LUQ
RLQ
LLQ
RUQ
RUQ
LUQ
RLQ
LLQ
RUQ
LUQ
RLQ
LLQ
#12
#13
#14
#15
#16
Patient Number

Figure 8

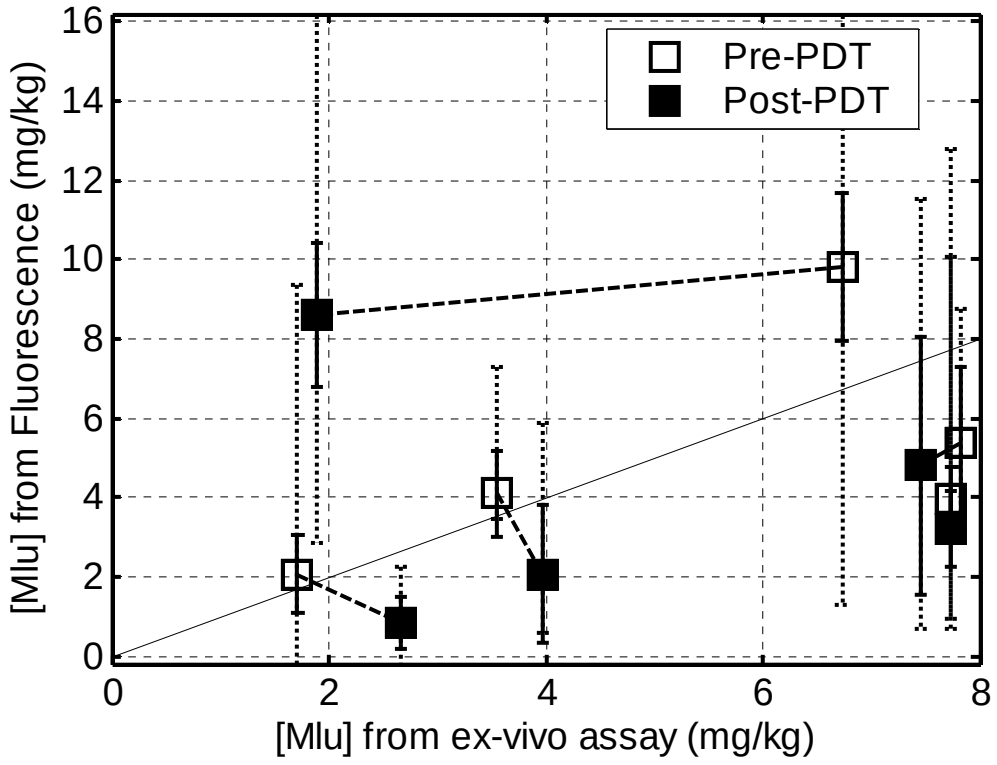
Pre-PDT
Post-PDT
[Mlu] from Fluorescence (mg/kg)
[Mlu] from ex-vivo assay (mg/kg)
0
2
4
6
8
0
2
4
6
8
10
12
14
16

Figure 9

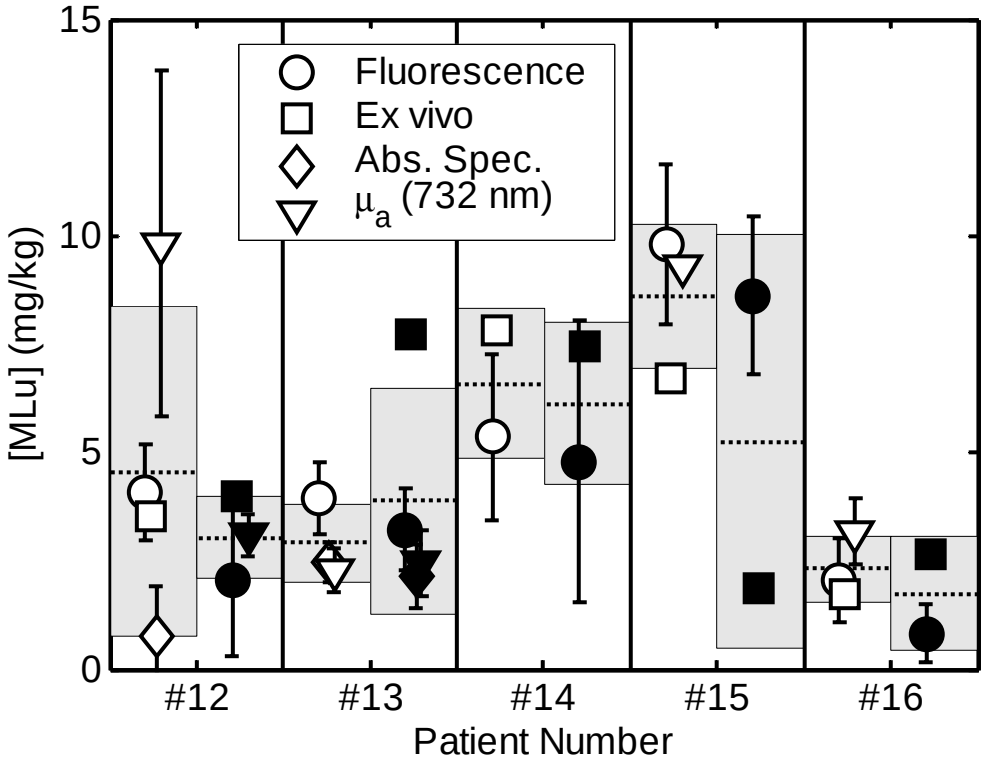
15
10
5
0
[MLu] (mg/kg)
Fluorescence
Ex vivo
Abs. Spec.
μa (732 nm)
#12
#13
#14
#15
#16
Patient Number

Figure 10

Optimized interstitial PDT prostate treatment planning with the Cimmino feasibility algorithm

Martin D. Altschuler, Timothy C. Zhu,[a] Jun Li, and Stephen M. Hahn
Department of Radiation Oncology, University of Pennsylvania, Philadelphia, Pennsylvania 19104

(Received 10 May 2005; revised 6 September 2005; accepted for publication 13 September 2005; published 9 November 2005)

The primary aim of this study was to determine whether optimized photodynamic therapy (PDT) treatment planning (seeking optimized positions, lengths, and strengths of the light sources to satisfy a given dose prescription) can improve dose coverage to the prostate and the sparing of critical organs relative to what can be achieved by the standard PDT plan. The Cimmino algorithm and search procedures based on that algorithm were tested for this purpose. A phase I motexafin lutetium (MLu)-mediated photodynamic therapy protocol is ongoing at the University of Pennsylvania. PDT for the prostate is performed with cylindrical diffusing fibers of various lengths inserted perpendicular to a base plate to obtain longitudinal coverage by a matrix of parallel catheters. The standard plan for the protocol uses sources of equal strength with equal spaced (1-cm) loading. Uniform optical properties were assumed. Our algorithms produce plans that cover the prostate and spare the urethra and rectum with less discrepancy from the dose prescription than the standard plan. The Cimmino feasibility algorithm is fast enough that changes to the treatment plan may be made in the operating room before and during PDT to optimize light delivery. © *2005 American Association of Physicists in Medicine*. [DOI: 10.1118/1.2107047]

Key words: PDT, *in vivo*, optical properties, prostate, Cimmino feasibility algorithm, combinatorial search, optimization

I. INTRODUCTION

Photodynamic therapy (PDT) is a treatment modality employing light of an appropriate wavelength in the presence of oxygen to activate a photosensitizing drug which then causes localized cell death or tissue necrosis. PDT has been used with a surface illumination technique to treat many superficial tumors including skin, lung, esophagus, and bladder.[1] This technique is inadequate for large bulky tumors in solid organs because of limited light penetration into tissue. A more efficient illumination scheme for such tumors is interstitial light delivery whereby optical fibers are placed directly into the bulky tumors or organs.

The prostate gland is an organ that appears to be a good target for interstitial PDT. Tumors of the prostate are often confined to the prostate itself so that brachytherapy techniques used for the placement of radioactive seed implants can be adapted for the placement of interstitial optical fibers.[2] Several preclinical studies have evaluated the feasibility of delivering PDT to the prostate via this interstitial approach.[3–7] The development of an interstitial light delivery technique required improved understanding of light dosimetry, critical in planning the configuration of multiple fibers within the organ or tumor. Based on the results of a preclinical study in canines,[8] we have initiated a protocol for motexafin lutetium (MLu)-mediated PDT of the prostate in patients at the University of Pennsylvania.[9] MLu is a second generation synthetic photoactive drug that has a *Q*-band absorption peak at 732 nm.[10,11]

At present, measurements at more than a few sample points within the patient during the clinical procedure are difficult to make. The state of the art is to obtain measurements before the actual clinical procedure, and to assume that during the procedure all these distributions are uniform throughout the prostate and static in time. We have previously shown that the human prostate has an inhomogeneous light-opacity distribution *in vivo*, which calls into question some of these assumptions.[12,13]

A number of optimization algorithms used in brachytherapy are of interest for prostate photodynamic therapy. The most common ones are simulated annealing algorithms[14–16] and genetic algorithms.[17–19] Gradient algorithms also have been applied.[20] In general, gradient algorithms give reproducible solutions but may be trapped in local minima far from the global minimum.[21] Simulated annealing and genetic algorithms avoid getting trapped in local minima, but are relatively slow because they are stochastic algorithms.

To the best of our knowledge, optimization algorithms for photodynamic therapy have not yet been validated and reported in the literature. In this study, we describe and evaluate a systematic search procedure, based on the Cimmino feasibility algorithm,[22,23] that optimizes the locations, lengths, and strengths of light sources for photodynamic treatment. The Cimmino feasibility algorithm is an iterative linear algorithm which was first applied to radiotherapy inverse problems by Censor *et al.*[23–25] The algorithm is safer than most common optimization algorithms outlined earlier since it always converges and, if the prescribed dose constraints are not all satisfied, it reverts to the least-squares solution.[26]

II. MATERIALS AND METHODS

A. Diffusion theory and determination of optical properties

The transport scattering (μ_s') and absorption (μ_a) coefficients characterize the scattering and absorption properties of tissue. With the diffusion approximation, the light fluence rate ϕ at a distance r from a point source can be expressed as[27]

$$\phi = \frac{S \cdot \mu_{\text{eff}}^2}{4\pi r \cdot \mu_a} \cdot e^{-\mu_{\text{eff}} \cdot r} = \frac{S \cdot 3\mu_s'}{4\pi r} \cdot e^{-\mu_{\text{eff}} \cdot r}, \quad (1)$$

where S is the power of the point source [mW]; $\phi(r)$ is the the fluence rate [mW/cm^2]; the quantity $\mu_{\text{eff}} = \sqrt{3 \cdot \mu_a \cdot \mu_s'}$[27] is the effective attenuation coefficient in tissues, applicable over a wider range of μ_a and μ_s' than the traditional definition $\mu_{\text{eff}} = \sqrt{3 \cdot \mu_a \cdot (\mu_s' + \mu_a)}$.[28] The PDT dose is defined as the product of light fluence and photosensitizer concentration. For simplicity, we use the light fluence (fluence rate $\times$ exposure time, $\phi \cdot t$) for the PDT dose throughout the paper, assuming uniform drug concentration.

For a cylindrical diffusing fiber (CDF) of length l, the light fluence rate at a point can be calculated with Eq. (1) by the discretized superposition:

$$\phi = \sum_{i=1}^{N} \frac{s \cdot \Delta x \cdot \mu_{\text{eff}}^2 \cdot e^{-\mu_{\text{eff}} r_i}}{4\pi \mu_a r_i} = \frac{3sl\mu_s'}{4\pi} \cdot \left(\frac{1}{N-1} \sum_{i=1}^{N} \frac{e^{-\mu_{\text{eff}} \cdot r_i}}{r_i} \right), \quad (2)$$

where s is the light energy released per unit time per unit length [mW/cm], also called the unit-length source strength. The differential $\Delta x = l/(N-1)$ is the length of the elemental (discretized) source segment. The odd integer N is the number of points used in the summation over the source [parentheses in Eq. (2)], with one point always placed in the middle of the CDF. The distance between the ith point of the linear light source and the observing point is $r_i = \sqrt{x_i^2 + h^2}$, where $x_i = (i - 1 - (N-1)/2)\Delta x$ is the cylindrical coordinate along the fiber from the center of the linear source and h is the distance perpendicular to the fiber axis. The numerical value of the summation should be independent of N (or Δx) if N is large enough. We found that accurate results of the summation can be obtained if $\Delta x \leqslant 0.1$ cm. In all our calculations $N = 201$ was used.

In theory, measurements of ϕ at two different distances r from a point source of known power S are sufficient to determine both μ_a and μ_s'. The two free parameters (μ_a and μ_s') are inherently separable because for a CDF of given length the magnitude of the fluence rate near the light source ($h = 0$) is determined by μ_s' only and the slope of the spatial decay of the light fluence rate is determined by μ_{eff} only. Measurements at multiple sites allow evaluating the variation of these optical characteristics within the prostate volume. Since Eq. (1) is a nonlinear equation of two free parameters μ_a and μ_s', we used a differential evolution algorithm developed by Storn *et al.*[29] This algorithm is simple and robust, and converges faster and with more certainty than both the adaptive simulated annealing and the annealed Nelder and Mead approach.[29] We modified the algorithm to require that all parameters (μ_a and μ_s') were positive.[30] The effect of this variation of optical properties on the kernels for a point light source was examined. A summary of the average optical properties in each patient before and after PDT is listed in Table I.

B. Patient selection, surgical, and PDT procedure

A Phase I clinical trial of motexafin lutetium (MLu)-mediated PDT in patients with locally recurrent prostate carcinoma was initiated at the University of Pennsylvania. The protocol was approved by the Institutional Review board of the University of Pennsylvania, the Clinical Trials Scientific Review and Monitoring Committee (CTSRMC) of the University of Pennsylvania Cancer Center, and the Cancer Therapy Evaluation Program (CTEP) of the National Cancer Institute. A total of 15 patients were treated, of which 14 patients have undergone measurement of optical properties (one patient yielded no results due to heavy bleeding). Each patient who signed the informed consent document underwent an evaluation, which included an MRI of the prostate, bone scan, laboratory studies including PSA (prostatic specific antigen), and a urological evaluation. Approximately two weeks prior to the scheduled treatment a transrectal ultrasound was performed for treatment planning. An urologist drew the target volume (the prostate) on each slice of the ultrasound images. These images were spaced 0.5 cm apart and were scanned with the same ultrasound unit used for treatment.

A built-in template with a 0.5-cm grid projected the locations of possible light sources relative to the prostate. A treatment plan was then prepared to determine the locations and lengths of the light sources. Cylindrical diffusing fibers (CDF) with active lengths 1–5 cm were used as light sources. The CDF sources were parallel, spaced 1 cm apart and the light power per unit length was less than or equal to 150 mW/cm for each CDF. The length of the CDF at a particular position within the prostate was selected to cover the full length of the prostate [see Fig. 1(a)]. For practical reasons, clinical application often required that the prostate be divided into four quadrants. Four isotropic detectors were used, each placed in the center of one quadrant. A fifth isotropic detector was placed in an urethral catheter to monitor the light fluence in the urethra [Fig. 1(b)].

The patients were anesthetized in the operating room with general anesthesia to minimize patient movement during the procedure. Transrectal ultrasound-guided biopsies for MLu measurements were obtained prior to light delivery. The ultrasound unit was used to guide needle placement in the operating room. A template was attached to the ultrasound unit and was matched to the same 0.5-cm grid used for treatment planning. Four detector catheters (one for each quadrant) were inserted into the prostate. These detectors were kept in place during the entire procedure of PDT treatment. Four additional preplanned treatment catheters for light sources were then inserted 0.5 or 0.7 cm away from the de-

TABLE I. *In vivo* optical properties measured at 732 nm in human prostate. The values in parentheses are the standard deviation (s.d.) of the average values measured from different locations of the same prostate. No s.d. is listed if only one data point is available.

Patient number	Before PDT			After PDT		
	μ_a (cm^{-1})	μ_s' (cm^{-1})	δ (cm)	μ_a (cm^{-1})	μ_s' (cm^{-1})	δ (cm)
2	0.09	29.8	0.34	0.09	43.7	0.29
3	0.15	22.0	0.31	0.07	33.4	0.37
4	0.43 (0.28)	7.69 (4.76)	0.41 (0.14)	0.51	1.67	0.63
5	0.21	11.8	0.37	0.13	7.18	0.60
6	0.27 (0.27)	10.5 (11.2)	0.50 (0.05)	0.19 (0.20)	18.9 (18.4)	0.45 (0.06)
7	⋯	⋯	⋯	0.30 (0.08)	23.7 (13.9)	0.24 (0.11)
9	0.53 (0.36)	6.61 (4.51)	0.41 (0.09)	0.64 (0.25)	7.00 (5.59)	0.33 (0.10)
10	0.63 (0.32)	4.62 (2.87)	0.42 (0.10)	0.19 (0.05)	9.27 (4.47)	0.54 (0.31)
11	0.67 (0.17)	6.39 (3.18)	0.32 (0.10)	0.83 (0.45)	5.45 (3.89)	0.38 (0.16)
12	0.71 (0.43)	8.99 (6.51)	0.32 (0.12)	0.30 (0.06)	20.2 (4.8)	0.28 (0.08)
13	0.27 (0.14)	18.5 (11.6)	0.30 (0.07)	0.26 (0.09)	17.0 (8.8)	0.31 (0.07)
14	0.72 (0.11)	3.37 (1.37)	0.39 (0.11)	⋯	⋯	⋯
15	⋯	⋯	⋯	⋯	⋯	⋯

tector catheters [Fig. 1(b)]. These source catheters were used for both light delivery and measurement of optical properties. A 15-W diode laser (model 730, Diomed, Ltd., Cambridge, United Kingdom) was used as the 732-nm light source.

C. Searching with the Cimmino feasibility algorithm

The "forward" problem of PDT is to find the dose distribution when the source locations, lengths, and strengths are all known. The "inverse" problem of PDT is the concern of this paper.

The "simple" inverse problem of PDT is to find individual source strengths that collectively deliver a prescribed minimum dose to the (target) prostate without exceeding specified maximum dose values for the target and nontarget regions (urethra, rectum, and unspecified background), when given all the source locations and source lengths. The Cimmino feasibility algorithm[22–26] is used in this paper as the method of choice to determine directly a "best" solution for the simple inverse problem.

The "general" inverse problem is to find not only the source strengths but the source locations and lengths as well, to best satisfy the dose prescription. This problem requires a search over different source positions and source lengths. At each step of the search new source positions and lengths are examined and the Cimmino algorithm is applied to solve the simple inverse problem. If the Cimmino-derived source strengths give a better dose distribution (relative to the dose prescription) than any found for previous source positions and lengths, these source strengths are stored as the new standard along with the new source lengths and positions, and the search is continued. When no significant improvement (with respect to the user chosen dose prescription) is found, the search is ended.

The discretized simple inverse problem can be written

$$b_i^{\min} \leqslant \sum_j A_{ij} x_j \leqslant b_i^{\max} \quad (i = 1, \ldots, I;\ j = 1, \ldots, J) \tag{3a}$$

or in matrix form as

$$\mathbf{b}^{\min} \leqslant \mathbf{A}\mathbf{x} \leqslant \mathbf{b}^{\max} \tag{3b}$$

where I is the number of voxels (or constraint points); $\mathbf{b}^{\max}$ and $\mathbf{b}^{\min}$ are the dose bounds on the voxels; J is the number of light sources; a component of matrix $\mathbf{A}$ denoted A_{ij} gives the dose absorbed at voxel i per unit strength of light source j. A positive lower bound prescribes a minimum dose for a prostate (target) voxel; it is zero for nonprostate voxels. An upper bound on dose is provided for every voxel. The goal is to find the vector $\mathbf{x}$ of source strengths that satisfies the inequality constraints of expression (3b).

The matrix $\mathbf{A}$ is a precalculated two-dimensional table (or kernel) for sources of all allowed lengths. The source lengths are discretized in 0.5-cm steps, corresponding to the length of the smallest possible segment of a light source (the light seed). The dose at a point due to a particular light source is found by specifying the perpendicular distance of the point to the source axis and the longitudinal distance of the point to the source midpoint, and then reading the proper component A_{ij}. The dose at any point is then found by summing the dose contributions of all the sources. The opacities for light absorption and scatter (assumed to be constant in this paper) are built into the kernel.

The operation of the Cimmino feasibility algorithm can be visualized in terms of a J-dimensional space whose coordinate axes correspond to the strengths of the light sources. Any point $\mathbf{x}$ in the positive "2^J-tant" (where $x_j \geqslant 0$ for all j) corresponds to a particular set of non-negative source strengths, and thus to a dose distribution given by $\mathbf{A}\mathbf{x}$. (A 2^J-tant is called a quadrant in 2D, and an octant in 3D.) The upper and lower inequalities of a voxel i form a hyperslab region in the positive 2^J-tant that contains allowable dose to

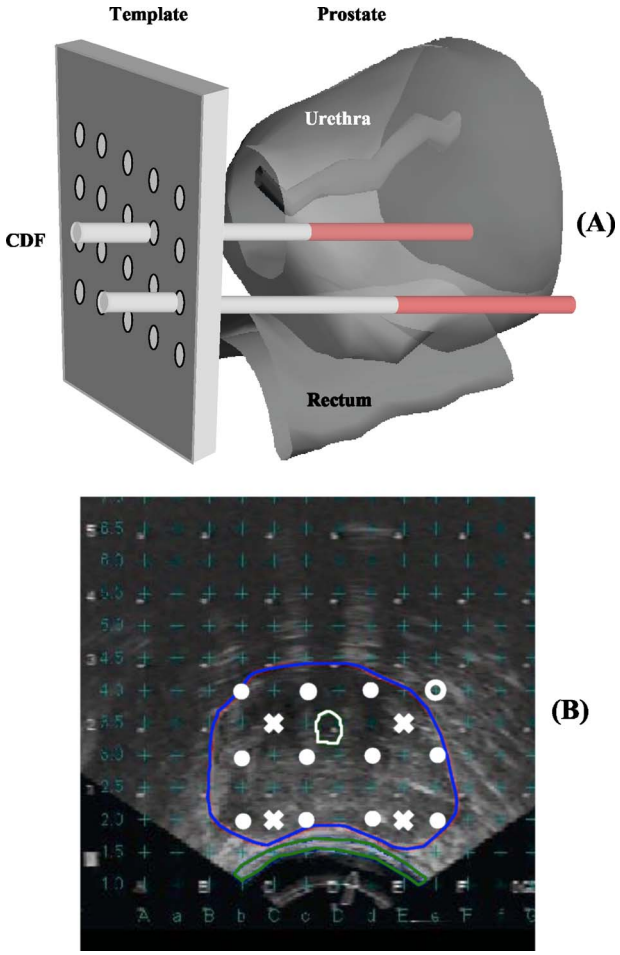

FIG. 1. (a) Experimental setup for measuring the *in vivo* optical properties of human prostate. The prostate template was drilled with a 0.5-cm equal spaced grid. Cylindrical diffusing fibers (CDF) were inserted into the catheters to illuminate the entire prostate gland. (b) Transrectal ultrasound image. Isotropic detectors ("×") were placed in one of the catheters, which is located at a distance between 0.5 and 1.1 cm from the light source ("●"). The detector reading at each location is peaked to ensure that it is at the middle of the CDF.

the voxel. A point in the positive 2^J-tant that lies within the hyperslab of every voxel (that is, satisfies all inequalities), is called a feasible solution.

The Cimmino algorithm can start from an arbitrary point in the positive 2^J-tant, but the work reported here always started from the origin ($\mathbf{x}=\mathbf{0}$).[23] In each iteration, only those constraints are used that are violated by the current estimate $\mathbf{x}$ of the unknown optimal result $\mathbf{x}^{\text{opt}}$. Rays are directed from $\mathbf{x}$ perpendicularly toward each violated hyperplane, and a resultant vector, computed as a linear combination of the rays, shifts $\mathbf{x}$ to a new position in the 2^J-tant. The new estimate $\mathbf{x}$ of $\mathbf{x}^{\text{opt}}$ will always be closer to the specified dose prescription [expression (3)] than the previous estimate.[31]

If there are few constraint points and many sources there is a better chance that every inequality can be satisfied, that is, that a feasible solution for expression (3) exists. If there are more than one feasible solution [that is, several feasible $\mathbf{x}^{\text{opt}}$ exist], the Cimmino algorithm will choose the first feasible solution it finds, determined primarily by the starting point and a relaxation parameter.[23]

For the PDT problem of interest there are significantly more constraints (voxels) than light sources, so that most often there are no feasible solutions. For this case it has been shown[31] that the Cimmino algorithm will always converge to a unique least-squares (compromise) solution.

The least-squares solution can be shifted somewhat by introducing importance weights for the volumes (i.e., for the prostate, urethra, rectum, and background). Each volume is given a non-negative importance weight by the user. (For example, the user chooses weight 100 for the prostate, 50 for both the urethra and rectum, and 10 for the background.) The sum of the importance weights is normalized to unity. (Since the sum of the chosen weights in the example is 210, the normalized organ weights are 0.48, 0.24, 0.24, and 0.04, respectively). The importance weight of each constraint point is set equal to the normalized importance weight of its volume divided by the number of constraint points in that volume. (So if there are 1000 constraint points in the prostate, the weight of each is 0.000 48, and similarly for the voxels in other organs.) Thus the importance weights of all the voxels again sum to unity. (The default is to give equal importance to each organ, thus a normalized weight of 0.25 in the example). These weights are applied within the algorithm.[23,26] Importance weighting of the volumes in the domain of calculation allows relatively more of the error of the compromise solution to fall on the less important volumes. It also allows additional constraint points to augment those of the discretization grid, e.g., extra constraint points to better define the peripheral dose of the prostate. As additional constraint points are added to the prostate, the importance weight of each prostate constraint point decreases in such a way that the normalized importance weight of the entire prostate remains constant.

The Cimmino feasibility algorithm was chosen because it is linear, conceptually simple, relatively fast, easy to constrain to positive source strengths (the positive 2^J-tant), allows importance weighting of the volumes, and converges to a unique least-squares compromise solution when not every constraint can be satisfied.[31] It is well-behaved, and will not create unpleasant surprises. It is ideal for both the simple inverse problem of PDT and as an "optimizing" tool for the general inverse problem. No attempt was made to code other algorithms for the PDT inverse problem.

When dose distributions derived from different sets of constraints (dose bounds) or search strategies are compared, there is the difficulty that the compromise solution may involve both underdosing to the prostate and overdosing to some of the volumes. To simplify comparison, it may be useful to renormalize the dose after the Cimmino calculation is completed. Since the PDT dose from a set of sources is a linear combination of the contributions of the individual sources, the Cimmino-derived source strengths can be increased proportionately until the minimum PDT dose received by every voxel within the prostate equals or exceeds the prescribed lower bound for the prostate PDT dose. With

the minimum PDT dose to the prostate equal to the minimum prescribed PDT dose, the only comparison needed is for the overdoses. The underdosing to the prostate has been translated to an overdosing of the other volumes and the prostate itself. This process is called "renormalization."

At present a medical physicist chooses the number of CDFs, the particular template holes (or "slots") for source insertion, the length of the CDF for each slot, the position of the CDF within each slot (retraction), and a single duration of illumination for the entire set of sources. This is a tedious and time-consuming process that requires contours from ultrasonic tomographic images, visualization of three-dimensional volumes (prostate, urethra, and rectum) and their intersections with linear light sources, estimation of the mean opacity of the prostate, and visualization of the scattered light distribution within the prostate, for different choices of source parameters.

The template currently being used for source insertion is a plate with a square array of $13 \times 13 = 169$ holes (slots for linear light sources) spaced 0.5 cm apart [Fig. 1(b)]. For the particular patient data being used as a benchmark, only 51 slots are situated to allow the light source either to penetrate the prostate or approach within a 0.1-cm margin. In present clinical practice, sources are separated by 1 cm, that is, every other template slot. Thus for the benchmark patient, only 12 of the 169 template slots are used for sources.

The light source is a tube of illumination, 0.1 cm in diameter and at most 5 cm in length from template base to maximum penetration. Creating the illumination within the tube are "light seeds" of 0.5 cm length (thus 0.5 cm between the centers of adjacent light seeds). The algorithms of this study enforce two clinical requirements: (1) the seeds within a light source are contiguous (i.e., no gaps occur between light seeds), and (2) each light source has at least two seeds. Although violation of these restrictions might yield mathematically improved light distributions, the clinical use of short discontinuous light sources requires greater precision and increased time for *in vivo* placement, thus an increased risk to the patient.

There are three mathematical problems. (1) Given CDFs with every quantity specified, namely, the number of CDFs, the template slots, the source lengths, and the retractions of the CDF into the slot, find the source strengths (emitted power multiplied by duration of illumination [J]) to satisfy the prescribed PDT dose constraints. (2) Given the number and locations of the source slots, find the optimal source parameters (source lengths and retractions) and source strengths. (3) Given only the number of CDFs and the allowed set of template slots, find the particular source slots, source parameters, and source strengths that are optimal. These three problems must be solved for two cases: individual source strengths (sources may have different strengths), and uniform source strength (all sources have the same strength). The case of uniform source strength with all source slots and parameters specified is the present practice in the clinic and is our baseline for improvement. These different problems are listed in Table II.

TABLE II. Summaries of optimization problems solved in this paper.

Problems	No. of CDFs	Slots	Lengths	Retractions	Strengths
1	Given	Given	Given	Given	Find
2	Given	Given	Find	Find	Find
3	Given	Find	Find	Find	Find

The first problem, with all quantities specified, requires only a Cimmino feasibility solution for the source strengths. The second and third problems require search procedures over allowed slots, source lengths, and retractions (as appropriate). These problems are "combinatorial," so that exhaustive searches are not possible in very short time. Nonexhaustive searches risk encountering local minima, so that finding the solution for the "absolute-minimum" discrepancy cannot be guaranteed or even recognized. Thus the key to the second and third problems is a good search strategy.

The weighted discrepancy (or objective function) determined after each run of the Cimmino algorithm is the weighted sum of the overdose or underdose at each constraint point with respect to the prescribed PDT dose bounds,

$$\text{Wgtd discrep} = \sum_{i=1} w_i[\dim(d_i^{\min}, d_i) + \dim(d_i, d_i^{\max})] \quad (4a)$$

where

$$\dim(x,y) = \begin{cases} x - y, & x > y \\ 0, & x \leqslant y. \end{cases} \quad (4b)$$

The first term in brackets on the right-hand side of Eq. (4a) gives the underdose and the second term gives the overdose at constraint point i. The underdose is the amount that the minimum PDT dose constraint $d_i^{\min}$ exceeds the calculated PDT dose d_i. The overdose is the amount the calculated PDT dose exceeds the maximum PDT dose constraint $d_i^{\max}$. A constraint point that satisfies both the upper and lower PDT dose constraints contributes no discrepancy. The sum can be over all constraint points (total weighted discrepancy) or over just constraint points of a specific organ (weighted discrepancy of the organ). The factor w_i is the importance weight of the constraint point, which has been normalized by the number of voxels of each organ.

The total weighted discrepancy between the calculated PDT dose and the prescribed PDT dose bounds is sensitive to the number and positioning of the constraint points. Our constraint points are determined by identical fixed grids in each slice of a rectangular prism that circumscribes the prostate plus a 0.1-cm margin. This grid will encompass the entire urethra and part of the rectum. The number of grid points is $13 \times 13 \times$ number of slices distributed within the walls of the encompassing prism. Additional constraint points can be inserted in each slice around the contours of a named volume. In this paper, these additional constraint points are added only for the prostate. Since calculation time to obtain the solution (source strengths and, when appropriate, slot posi-

TABLE III. Source strengths obtained using various Cimmino-based search algorithms with renormalization. Cimmino 1: optimize source strengths only; Cimmino 2: optimize source lengths, strengths, and template slot locations; Cimmino 3: the same as Cimmino 2 with a different constraint for rectum; and Cimmino 4: optimize source lengths, and strengths for 51 CDFs filling the entire prostate. This is shown for the average and the most transparent prostate optical properties: Opt 1: $\mu_a=0.3\ \mathrm{cm}^{-1}$, $\mu_s'=14\ \mathrm{cm}^{-1}$; Opt 2: $\mu_a=0.04\ \mathrm{cm}^{-1}$, $\mu_s'=30\ \mathrm{cm}^{-1}$, respectively. The calculation time is for a Dell PC with 2.8 GHz Pentium IV processor and 1 Gbyte RAM. The source strengths for the standard plan are 410.83 and 24.86, for Opt 1 and Opt 2, respectively. These source strengths (in units of J/cm) give prescribed light fluence of 100 $\mathrm{J/cm}^2$ to cover the prostate.

	Cimmino 1		Cimmino 2		Cimmino 3		Cimmino 4	
Source No.	Opt 1	Opt 2	Opt 1	Opt 2	Opt 1	Opt 2	Opt 1	Opt 2
1	286.22	19.26	267.66	33.36	296.82	33.36	22.76	3.78
2	232.24	19.20	271.56	18.38	292.12	18.38	22.50	3.54
3	264.92	16.04	222.82	14.56	312.78	14.56	18.58	3.46
4	242.40	17.00	213.14	23.52	240.62	23.52	21.92	4.04
5	350.54	21.92	349.38	13.18	344.94	13.18	42.84	6.52
6	293.08	20.38	358.48	29.32	244.36	29.32	21.92	3.36
7	595.94	30.18	219.50	11.30	239.14	11.30	22.80	2.96
8	429.26	26.50	293.76	13.08	159.44	13.08	29.32	3.54
9	306.20	21.82	219.16	27.70	171.24	27.70	30.22	3.76
10	289.82	18.20	351.70	25.58	229.26	25.58	30.96	3.90
11	290.28	17.74	258.80	19.80	241.88	19.80	37.26	5.20
12	391.96	25.96	209.24	19.94	183.74	19.94	21.54	3.24
…							…	…
Calculation time (s)	1	1	272	223	309	224	17	18

tions and source parameters) increases with the number of constraint points, we have limited that number to a few thousand.

To check the solution obtained with the chosen constraint points, a dose volume histogram (DVH) is calculated for a much finer 3D grid after the optimal solution is obtained for any of the three mathematical problems described earlier. The DVH uses a rectangular prism that encompasses every named volume (prostate, urethra, and rectum) plus a 0.1-cm margin, and sample points numbering $101\times101\times$number of slices. The time needed to calculate the DVH is only a second or so because no feasibility or search procedures are involved.

For the second mathematical problem, the template slots are given and the search is for source lengths and positions within the template slots. The source lengths are initialized to maximum length and then geometrically pruned so that no source extends out of the prostate. Then the computer tries to eliminate an end seed of a source (at the proximal or distal source end relative to the template). This attempt is done for each source in turn. If a solution of lower discrepancy is found, it is taken as the new optimum solution. If no seed can be eliminated from any source to give a lower total weighted discrepancy, the computer tries to add an end seed to a source. Iteration (elimination and addition of end seeds) continues if lower discrepancy solutions are found. Failure to improve the solution after an iteration ends the search.

For the third mathematical problem, sources of maximum length are embedded initially in every template slot. All CDFs that never approach within a margin (usually 0.1 cm) of the prostate are immediately eliminated. The remaining sources are geometrically pruned from maximum length so as not to extend out of the prostate. The Cimmino solution at this iteration gives the least possible discrepancy. However, usually the number of sources still exceeds what is clinically feasible. The computer then eliminates the source of least

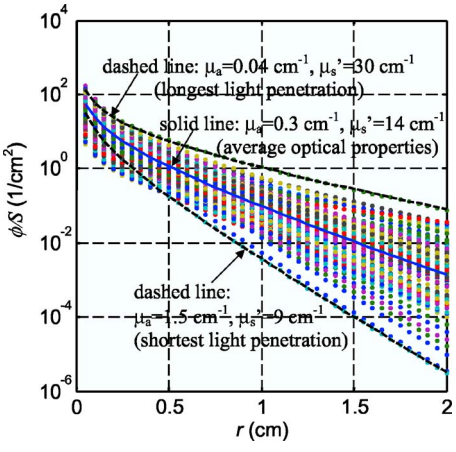

FIG. 2. Light fluence rate per source strength, ϕ/S, for a point source for the optical properties determined from human prostate. The solid line corresponds to ϕ/S for the average optical properties: $\mu_a=0.3\ \mathrm{cm}^{-1}$, $\mu_s'=14\ \mathrm{cm}^{-1}$. The dashed lines correspond to ϕ/S for the longest and shortest light penetrations: $\mu_a=0.04\ \mathrm{cm}^{-1}$, $\mu_s'=30\ \mathrm{cm}^{-1}$ and $\mu_a=1.5\ \mathrm{cm}^{-1}$, $\mu_s'=9\ \mathrm{cm}^{-1}$, respectively.

TABLE IV. Summary of the calculation results with renormalization of source strengths. "Wgtd discrep" means weighted discrepancy and "back" means background. The optimization grid gives the constraint points (a few thousand) used for the Cimmino feasibility algorithm while the DVH grid is finer and gives many sample points (a few tens of thousands) to calculate the DVH after the source parameters and source strengths have been obtained.

	Opt 1 (μ_a=0.3 cm^{-1}, μ_s'=14 cm^{-1}) Wgtd discrep for organs (DVH grid)				Opt 2 (μ_a=0.04 cm^{-1}, μ_s'=30 cm^{-1}) Wgtd discrep for organs (DVH grid)			
Algorithms	Prostate	Urethra	Rectum	Back	Prostate	Urethra	Rectum	Back
Standard	220	138	29.1	20.4	32.5	30.1	1.70	1.41
Cimmino 1	168	89.9	7.77	8.28	18.2	13.1	0.131	0.439
Cimmino 2	102	45.0	0.001 20	4.65	9.46	0.824	0.00	0.291
Cimmino 3	84.5	36.0	0.47	5.47	9.46	0.824	0.00	0.291
Cimmino 4	5.35	5.53	0.005 30	0.159	6.71	6.08	0.008 20	0.0003
	Total wgtd discrep				Total wgtd discrep			
	Optim grid		DVH grid		Optim grid		DVH grid	
Standard	392		408		59.8		65.7	
Cimmino 1	240		274		28.3		31.9	
Cimmino 2	101		152		8.53		10.6	
Cimmino 3	93.2		126		8.53		10.6	
Cimmino 4	5.88		11.0		9.12		12.8	

(calculated) strength and repeats the Cimmino calculation and source elimination until the maximum allowed number of sources is present. Since this elimination process is quick but not perfect, each source in turn is then allowed to shift to any of four neighboring template positions when that slot is vacant. (After a shift, the source length will conform to the prostate geometry at the new position.) If a better Cimmino solution results from the shift, it is kept, otherwise the shifted source is replaced to its previous position, and the search continues. When no further improvement can be obtained from shifting sources, the final template slots are stored and the program reverts to the search described in the previous paragraph for the source lengths and retractions in the given slots.

To check the effect of different optical properties on Cimmino feasibility results, two different sets of uniform optical opacities were chosen: (a) the average opacities measured for all prostate patients, μ_a=0.3 cm^{-1} and μ_s'=14 cm^{-1}; and (b) the opacity values measured for the patient with the greatest penetration depth (see Fig. 2), μ_a=0.04 cm^{-1} and μ_s'=30 cm^{-1}.

We studied three problems. (1) Cimmino 1 optimizes source strengths only (problem 1 of Table II); (2) Cimmino 2 optimizes source strengths, template locations, lengths, and retractions (problem 3 of Table II); Cimmino 3 is the same as Cimmino 2 with a lower constraint for rectum; (3) Cimmino 4 optimizes source lengths and strengths for all possible (51) CDFs that intersect the prostate (problem 2 of Table II).

TABLE V. Optimization parameters used for various Cimmino-based search algorithms in the paper. The lower dose constraints, $d^{\min}$, are kept at 100 for prostate and 0 for all other critical structures (rectum, urethra, and background). The normalized importance weights, w_i, are kept at 100 for all calculations unless explicitly stated otherwise. Opt 1: μ_a=0.3 cm^{-1}, μ_s'=14 cm^{-1}; Opt 2: μ_a=0.04 cm^{-1}, μ_s'=30 cm^{-1}. The numbers in parentheses are for Opt 1 without normalization (dashed lines in Fig. 6).

			The upper dose constraints, $d^{\max}$							
			Opt 1				Opt 2			
Figures	Cimmino names	Problems	Prostate	Urethra	Rectum	Back	Prostate	Urethra	Rectum	Back
4–7	Cimmino 1	1	300 (500)	300	300	300	300	300	300	300
4–8	Cimmino 2	3	300 (500)	300	300	300	300	300	300	300
4–7	Cimmino 3	3	300 (500)	300	200	300	300	300	200	300
4–7	Cimmino 4	2 or 3	300	200	300	300	200	200	200	300
8(a)		3	Vary	300	300	300				
8(b)		3	Vary	300	300	300				

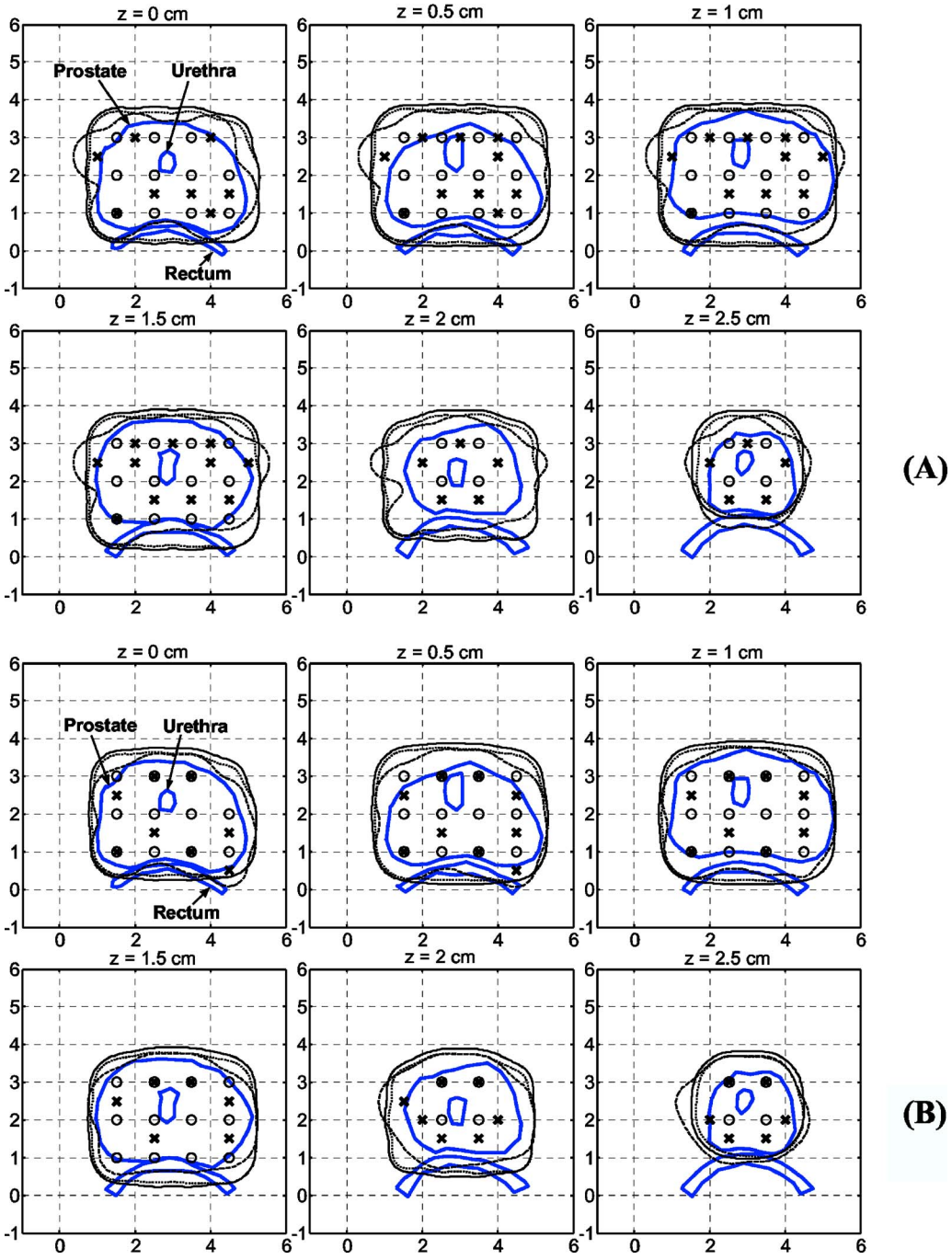

FIG. 3. Comparison of 100% isodose lines for the manual standard plan (solid line) vs Cimmino 1 (dotted line) and Cimmino 3 (dashed line) for two optical properties: (a) μ_a=0.3 cm^{-1}, μ_s'=14 cm^{-1}, and (b) μ_a=0.04, μ_s'=30 cm^{-1}. (○) The source positions in the standard plan or Cimmino 1. (×) The source positions in Cimmino 3. The source strengths are summarized in Table III.

Summaries of source strengths and weighted discrepancies of the Cimmino calculations are shown in Tables III and IV, respectively. The optimization parameters used in the paper for all Cimmino calculations are listed in Table V. Table III shows the resulting source strengths for the CDFs obtained from Cimmino-based search algorithms. For each Cimmino method, there is a tenfold ratio in source strength for the two different optical properties. This shows the critical importance of optical properties in determining the PDT dose coverage of the prostate.

In Table IV, we compared the total weighted discrepancy of the constraint points that were used to find the source strengths with that of the DVH sample points. The total weighted discrepancy of the DVH sample points was larger than that of the constraint points, probably because it included more points, and was thus more representative of reality. The total weighted discrepancy generally decreases for better DVH, except for Cimmino 4 when the optical properties had the largest optical penetration depth. This latter case corresponded to a different upper PDT dose bound for pros-

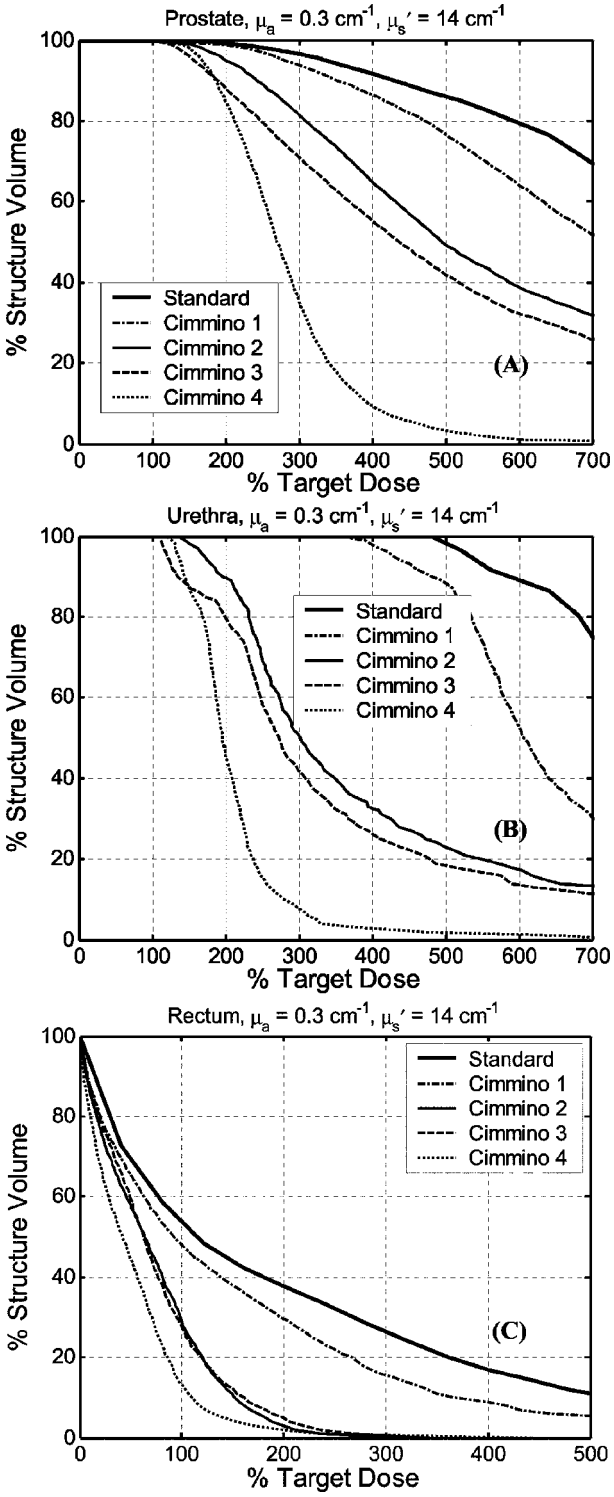

FIG. 4. DVH comparison of the manual standard plan vs the Cimmino-based search results for optical properties μ_a=0.3 cm^{-1}, μ_s'=14 cm^{-1} for (a) prostate, (b) urethra, and (c) rectum. The standard plan uses uniform 1-cm source loading with uniform-strength. The optimized results are: Cimmino 1 uses the same fixed source positions and source parameters as the standard plan but Cimmino optimized weights for each source; Cimmino 2 finds optimized source lengths, loading, and template locations for 12 linear sources with upper constraints of 300% for rectum and urethra; Cimmino 3 is the same as Cimmino 2 but with upper constraints of 200% for rectum and urethra; Cimmino 4 uses Cimmino optimized source lengths, loading and template for all 51 possible CDF sources through the prostate. See Table IV for the upper dose bounds used for each Cimmino-search algorithm.

tate, rectum, and urethra (200%). All other calculations, except for Cimmino 3, use an upper bound of 300% (see Table V).

III. RESULTS AND DISCUSSION

Optical properties measured in 13 patients have been summarized in Table I. The heterogeneity of optical properties in human prostates was somewhat smaller than that observed in canine prostates at 732 nm.[7] Overall μ_a varied between 0.07 and 1.62 cm^{-1} (mean 0.3±0.2 cm^{-1}) and μ_s' varied between 1.1 and 44 cm^{-1} (mean 14±11 cm^{-1}). The effective attenuation coefficient μ_{eff} varied between 0.91 and 6.7 cm^{-1}, corresponding to an optical penetration depth ($\delta = 1/\mu_{\text{eff}}$) of 0.2–1.1 cm. The mean values of μ_{eff} and δ were 2.9±0.8 cm^{-1} and 0.4±0.1 cm, respectively. This penetration depth was substantially larger than that of 0.1–0.25 cm reported for 630 nm[6] but was smaller than the 0.5–3 cm observed in normal canine prostate at 732 nm.[7] The most probable explanation is that canine prostate has a different glandular/structure content than that of the human prostate. While the mean reduced scattering coefficient in canine was 3.6±4.8 cm^{-1},[7] it was 15±11 cm^{-1} in human at the same wavelength (732 nm).[12] The increased reduced scattering coefficient resulted in an increased effective attenuation coefficient, or a reduction of optical penetration depth, assuming the absorption coefficient remains the same.

Figure 2 shows the light fluence rate per power, ϕ/S, as a function of distances from a point source for all the optical properties measured in patients (119 data points, symbols). The average optical properties (μ_a=0.3 cm^{-1}, μ_s'=14 cm^{-1}) produced an optical kernel approximately in the middle of the range of kernel variations (solid line in Fig. 2). As a result, they were used for most analyses in the current study. Since the corresponding optical penetration depth (δ =0.28 cm) was shorter than the spacing between the catheters (0.5 cm), we also examined the extreme case where the optical penetration depth was greatest. This corresponded to μ_a=0.04 cm^{-1}, μ_s'=30 cm^{-1} (δ=0.5 cm, upper dashed line in Fig. 2). We did not show results for the optical properties (μ_a=1.5 cm^{-1}, μ_s'=9 cm^{-1}) with the shortest optical penetration depth (δ=0.16 cm) since it behaved similarly to that of the average optical properties, which had an optical penetration depth shorter than the spacing of the template (0.5 cm).

Figure 3 compares computer runs of optimized 100% isodose distributions of Cimmino 1 and Cimmino 3 with the standard plan. We used our standard plan, based on geometrical coverage, 1-cm spaced loading, and uniform source strength as our default plan to judge the improvement made by the Cimmino feasibility algorithm and the search strategies. There was no substantial difference in the isodose distributions of equal-source-strength and individual-source-strength (Cimmino 1 of Fig. 3). This was true for both the average and most penetrating optical properties found in the human prostate [Figs. 3(a) and 3(b)]. However, substantial sparing of rectum was obtained when the source positions were also optimized (Cimmino 3). This is not surprising since for shorter light penetration depths, the light coverage

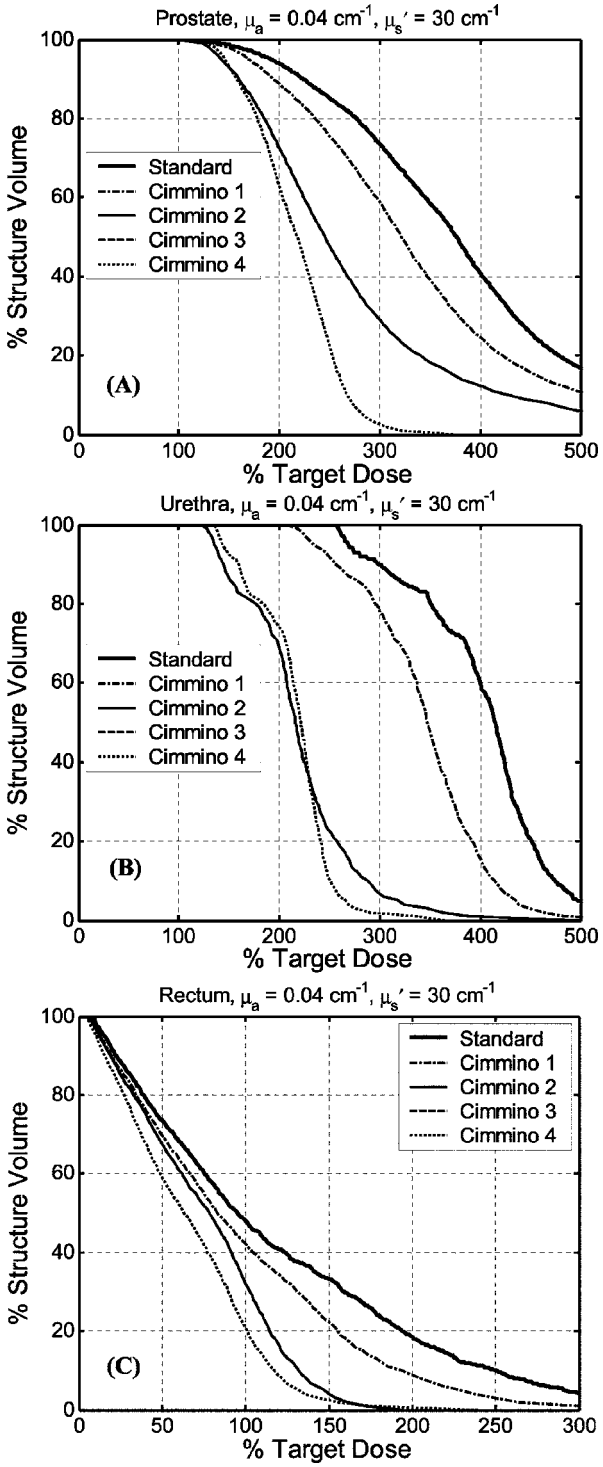

FIG. 5. Comparison of DVH of manual standard plan vs Cimmino-based search results for optical properties μ_a=0.04 cm^{-1}, μ_s'=30 cm^{-1} for (a) prostate, (b) urethra, and (c) rectum. The definition of the standard and Cimmino 1–4 are the same as in Fig. 4. Cimmino 2 and 3 produced identical DVH, i.e., the solid and dashed lines overlapped.

is determined more by the light source location than the source strength, provided all other conditions are the same. The Cimmino feasibility algorithm is fast enough for this problem to obtain clinical near real-time optimization (less than 300 s, see Table III).

The DVHs for prostate, urethra, and rectum are shown in Fig. 4 for average optical properties (μ_a=0.3 cm^{-1}, μ_s' =14 cm^{-1}) and in Fig. 5 for the largest optical penetration (μ_a=0.04 cm^{-1}, μ_s'=30 cm^{-1}). All plans performed so far used source strength renormalization to guarantee prescribed PDT dose coverage over the entire prostate.

When the DVHs were compared, the dosimetry improved going from the standard plan to Cimmino 1, Cimmino 2, Cimmino 3, and Cimmino 4 in that order for the average optical properties, see Fig. 4. Since the optical penetration was less than 0.5 cm, the standard plan used 1-cm spaced loading to uniformly cover the entire prostate with 12 CDFs. Cimmino 1, which optimizes the source strength only, did not provide significant improvement over the standard plan, as discussed before. When one started to optimize the source locations (e.g., for Cimmino 2 and 3), one observed a substantial improvement over the standard plan, not only for the coverage of the target (prostate) but also for the PDT dose reduction of the urethra and rectum. This is expected since the optical range of each source is so short that the geometrical locations of the source determine where the doses are delivered. Cimmino 3, which used 200% upper constraint for rectum, gave better results than Cimmino 2, which used 300% upper constraint for rectum. For comparison, we also examined the case of all possible (51) linear sources through the prostate (Cimmino 4). Not surprisingly, we got the best DVH with this option, although it is clinically impractical to use so many sources. The DVH for this option represents the best possible mathematical solution.

Similar comparison was also made for the longest optical penetration depth, as shown in Fig. 5. DVH results were similar to the case of the average optical properties except that we did not see any difference between Cimmino 2 and 3, probably because the PDT dose was already optimized even with a higher upper PDT dose bound for the rectum. Comparing Figs. 4 and 5, we concluded that the rectum sparing was improved when the optical penetration of the prostate is less than 0.3 cm. Less significant improvement was observed when the optical penetration was longer. The result showed that for low opacities (greater light penetration) the rectal sparing of the 12-source plan was not much worse than that of the 51-source plan (Fig. 5). For the average optical parameters, however, improved rectum sparing can be achieved with more CDFs (Fig. 4).

Solution of the first mathematical problem allows comparison of individual source strengths versus a single uniform strength for all user-chosen sources. Solution of the second problem allows a similar comparison but with source lengths, retractions, and strengths chosen by prostate geometry and minimum PDT dose discrepancy. A solution of the third problem allows the treatment planner to find automatically the best (or almost-best) light sources and source strengths from just the specified PDT dose constraints to the prostate and organs, and the choice for the number of sources. Such a solution would be virtually impossible to find by human visualization and estimation. Automatic source selection and weighting becomes even more impor-

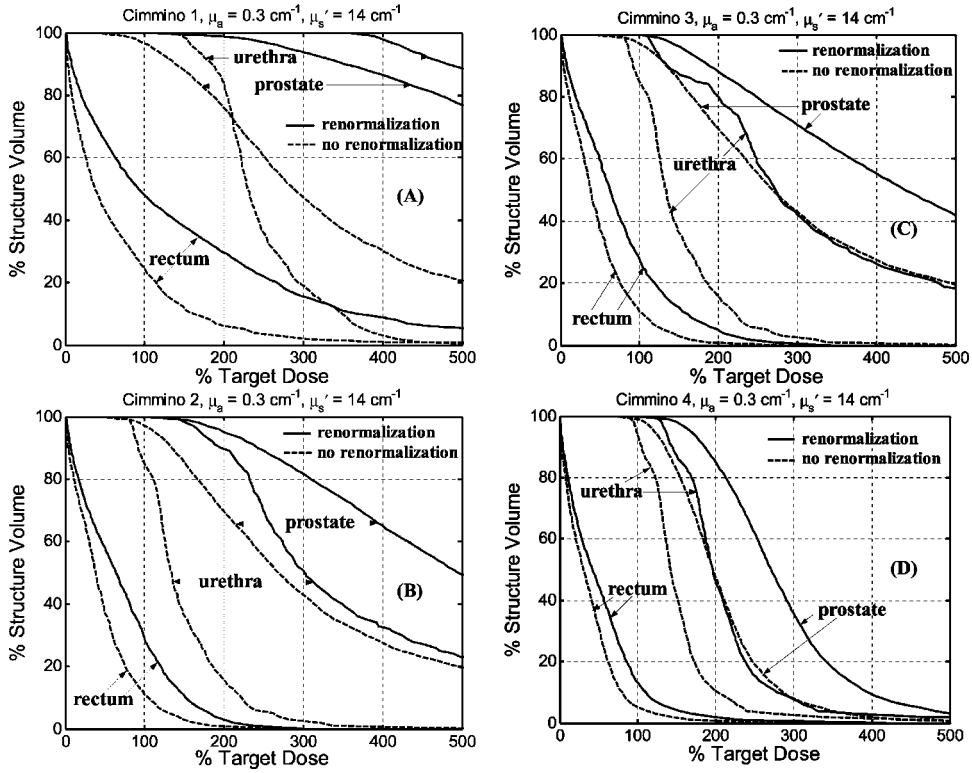

FIG. 6. Comparison of DVH for Cimmino-based search algorithm with (solid lines) and without (dashed lines) renormalization of source strengths for prostate coverage for optical properties μ_a=0.3 cm^{-1}, μ_s'=14 cm^{-1}. The results are: (a) Cimmino 1; (b) Cimmino 2; (c) Cimmino 3; (d) Cimmino 4.

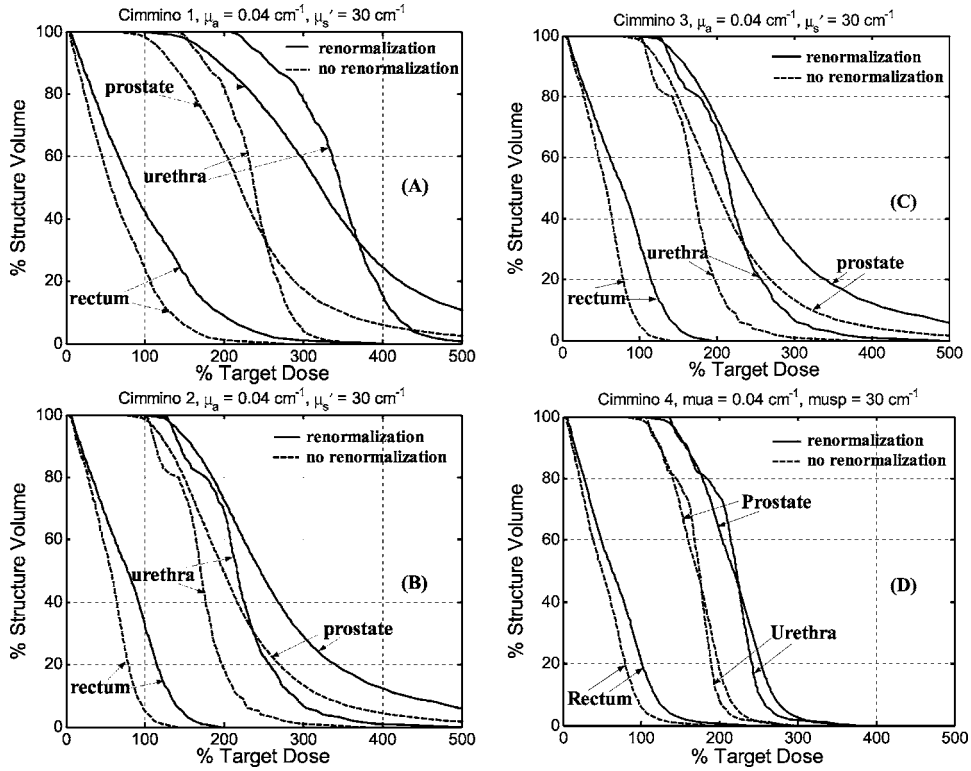

FIG. 7. Comparison of DVH for Cimmino-based search algorithm with (solid lines) and without (dashed lines) renormalization of source strengths for prostate coverage for optical properties μ_a=0.04 cm^{-1}, μ_s'=30 cm^{-1}. The results are: (a) Cimmino 1; (b) Cimmino 2; (c) Cimmino 3; (d) Cimmino 4.

tant if it is necessary to limit PDT dose to the urethra and rectum without compromising treatment effectiveness to the prostate.

The selection of the number of light sources is as much a clinical as a mathematical problem. To find mathematically the best number of linear light sources to insert, one can rerun repeatedly any procedure used to solve problem 3 with different numbers of sources. However changing the number of CDFs differs from rearranging source positions and solving for source strengths; it involves a tradeoff between (a) fewer sources—less homogeneous dose coverage, higher source strengths, but fewer surgical complications, and (b) more sources—better dose coverage, lower source strengths, but more surgical complications). Thus choosing the number of sources requires clinician input based on medical experience and judgment.

Each search procedure allows the number of CDFs to be decreased by one. A new optimization calculation is then performed and the resulting PDT dose distribution compared with the previous. The decrease in the number of CDFs can be continued iteratively. If the number of sources can be decreased without significantly increasing discrepancy between the prescribed and optimized PDT dose distribution, fewer sources need be used, thereby reducing the complication of the procedure and discomfort of the patient.

We also compared DVH between Cimmino feasibility algorithms with and without renormalization. Figure 6 is for average optical properties and Fig. 7 is for optical properties of greatest penetration. For average optical properties and 12 CDFs, only 96% of the volume of the prostate was covered to prescribed PDT dose without renormalization of the source strengths. The upper dose bounds were set to 300% with, and 500% without, renormalization. (A higher upper bound was used without renormalization because coverage of the prostate volume to prescribed dose fell to 93% with the lower dose bound.) For the optical properties of larger penetration, the volume coverage was 97% with 12 CDFs. When more light sources were used (e.g., 51 CDFs for Cimmino 4), the prostate was adequately covered for the range of optical properties without renormalization. This may provide an indication as to when one can be sure sufficient source locations are obtained. For the Cimmino-based search algorithms 1–3, the ratios of the total source strengths with and without renormalization were 1.9–2.5 for the average optical properties, which implies that treatment time can be reduced by factors of 1.9–2.5 if renormalization is not applied. For the optical properties with the largest penetration, the ratios were approximately 1.5 among the Cimmino-based search algorithms 1–3.

We also studied how importance weighting of the named volumes (prostate, urethra, rectum, or background) would affect the Cimmino results. The prostate (target) importance weight was allowed to vary between 100 and 500 relative to an importance weight of 100 for the other volumes. (Before any calculation, importance weights are normalized so that their sum over all volumes is unity.) For both the average optical properties and the optical properties of greatest penetration, the different values of importance weight had negligible effect on the DVH of any of the named volumes. For this reason, the importance weight of every named volume was chosen to be the same.

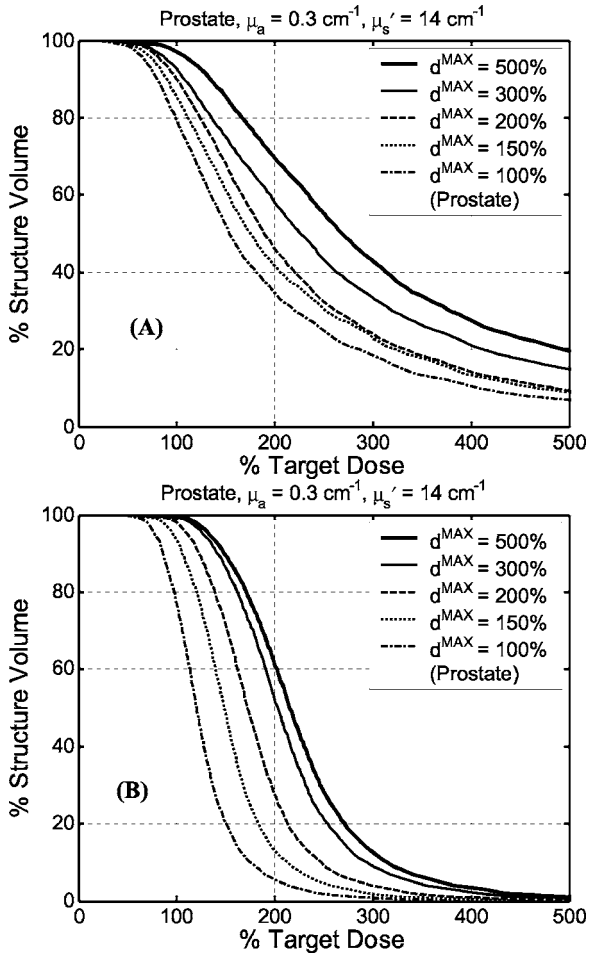

FIG. 8. Comparison of DVH for Cimmino-based search algorithm (problem option 3) with various upper dose bounds (d^{max}) for prostate for (a) 12 CDFs and (b) 51 CDFs for the average optical properties. No renormalization is used.

To examine the effect of upper dose bounds on the Cimmino results, we repeated the Cimmino feasibility algorithm using 12 or 51 CDFs, respectively, for the average optical properties without renormalization, as shown in Figs. 8(a) and 8(b). The best upper dose bound was 500% for 12 CDF and 200% for 51 CDF. Under this condition, 97% volume of prostate was covered by the 100% dose line without renormalization. This conclusion was also valid for the greatest optical penetration depth (data not shown), where the percentage volume of 100% dose coverage was higher than that for the average optical properties. The effect of upper dose bounds on the critical organs (urethra and rectum) was generally negligible (for upper bounds changing from 150% to 500%, data not shown). As a result, we kept upper bounds for the critical organs at 300% for all our optimization algorithms (see Table IV).

The present paper assumes uniform (homogeneous) optical properties. An open question is whether optimized solutions for inhomogeneous media will further improve over the

present uniform-medium calculations. Another open question is the number of control/constraint/sample points required to guarantee the optimized outcome. Further studies are also needed to determine the minimum number of CDFs needed to achieve complete coverage.

IV. CONCLUSIONS

The question addressed is whether any significant advantage may derive from methods that allow different strengths for the CDFs and/or choose the geometry (locations, lengths) of the light sources. Our comparison shows: (1) It is important to measure the optical properties of a patient because it determines the light fluence distribution. This effect is more predominant than optimizing the source position, length, and strength. (2) For the range of optical properties in the human prostate, when CDF positions and strengths are both found by a search based on the Cimmino feasibility algorithm, there is significant improvement over the current standard method of equal-source-strength optimization. (3) Computer optimization saves the user time in setup and reduces human stress. The Cimmino feasibility algorithm is fast enough to be the core of search algorithms to obtain clinical real-time optimization.

ACKNOWLEDGMENTS

This work is supported by Department of Defense (DOD), US Medical Research and Material Command, Grant No. DAMD17-03-1-0132 and National Institute of Health (HIN), R01 CA109456 and R21 CA088064.

[a]Electronic mail: tzhu@mail.med.upenn.edu

[1]R. A. Hsi, D. I. Rosenthal, and E. Glatstein, "Photodynamic therapy in the treatment of cancer: Current state of the art," Drugs **57**, 725–734 (1999).

[2]A. V. D'Amico, "Role of interstitial radiotherapy in the management of clinically organ-confined prostate cancer: The jury is still out," J. Clin. Oncol. **14**, 304–315 (1996).

[3]L. K. Lee, C. Whitehurst, Q. Chen, M. L. Pantelides, F. W. Hetzel, and J. V. Moore, "Interstitial photodynamic therapy in the canine prostate," Br. J. Urol. **80**, 898–902 (1997).

[4]S. C. Chang, G. Buonaccorsi, A. MacRobert, and S. G. Bown, "Interstitial photodynamic therapy of the canine prostate using meso-tetra-(m-hydroxyphenyl) chlorine," Int. J. Cancer **67**, 555–562 (1996).

[5]S. C. Chang, G. Buonaccorsi, A. MacRobert, and S. G. Bown, "Interstitial photodynamic therapy of the canine prostate with disulfonated aluminum phthalocyanine and 5-aminolevulinic acid-induced protoporphyrin IX," Prostate **32**, 89–98 (1997).

[6]Q. Chen, B. C. Wilson, S. D. Shetty, M. S. Patterson, J. C. Cerny, and F. W. Hetzel, "Changes *in vivo* optical properties and light distributions in normal canine prostate during photodynamic therapy," Radiat. Res. **147**, 86–91 (1997).

[7]T. C. Zhu, S. M. Hahn, A. S. Kapatkin, A. Dimofte, C. E. Rodriguez, T. G. Vulcan, E. Glatstein, and R. A. Hsi, "In vivo optical properties of normal canine prostate at 732 nm using motexafin lutetium-mediated photodynamic therapy," Photochem. Photobiol. **77**, 81–88 (2003).

[8]R. A. Hsi, A. Kapatkin, J. Strandberg, T. Zhu, T. Vulcan, M. Solonenko, C. Rodriguez, J. Chang, M. Saunders, N. Mason, and S. Hahn, "Photodynamic therapy in the canine prostate using motexafin lutetium," Clin. Cancer Res. **7**, 651–660 (2001).

[9]D. C. Stripp, R. Mick, T. C. Zhu, R. Whittington, D. Smith, A. Dimofte, J. C. Finlay, J. Miles, T. M. Busch, D. Shin, A. Kachur, Z. A. Tochner, S. B. Malkowicz, E. Glatstein, and S. M. Hahn, "Phase I trial of motexafin-lutetium-mediated interstitial photodynamic therapy in patients with locally recurrent prostate cancer," Proc. SPIE **5315**, 88–99 (2004).

[10]S. W. Young, K. W. Woodburn, M. Wright, T. D. Mody, Q. Fan, J. L. Sessler, W. C. Dow, and R. A. Miller, "Lutetium texaphyrin (PCI-0123): A near-infrared, water-soluble photosensitizer," Photochem. Photobiol. **63**, 892–897 (1996).

[11]T. D. Mody, L. Fu, and J. L. Sessler, "Texaphyrins: Synthesis and development of a novel class of therapeutic agents," in *Progress in Inorganic Chemistry*, edited by K. D. Karlin (Wiley, Chichester, 2001), pp. 551–598.

[12]T. C. Zhu, A. Dimofte, J. C. Finlay, D. Stripp, T. Busch, J. Miles, R. Whittington, S. B. Malkowicz, Z. Tochner, E. Glatstein, and S. M. Hahn, "Optical properties of human prostate at 732 nm measured *in vivo* during motexafin lutetium-mediated photodynamic therapy," Photochem. Photobiol. **81**, 96–105 (2005).

[13]T. C. Zhu, J. C. Finlay, and S. M. Hahn, "Determination of the distribution of light, optical properties, drug concentration, and tissue oxygenation *in vivo* in human prostate during motexafin lutetium-mediated photodynamic therapy," J. Photochem. Photobiol., B **79**, 231–241 (2005).

[14]R. S. Sloboda, "Optimization of brachytherapy dose distributions by simulated annealing," Med. Phys. **19**, 955–964 (1992).

[15]J. Pouliot, D. Tremblay, J. Roy, and S. Filice, "Optimization of permanent ^{125}I prostate implants using fast simulated annealing," Int. J. Radiat. Oncol., Biol., Phys. **36**, 711–720 (1996).

[16]E. Lessard and J. Pouliot, "Inverse planning anatomy-based dose optimization for HDR-brachytherapy of the prostate using fast simulated annealing algorithm and dedicated objective function," Med. Phys. **28**, 773–779 (2001).

[17]Y. Yu and M. C. Schell, "A genetic algorithm for the optimization of prostate implants," Med. Phys. **23**, 2085–2091 (1996).

[18]G. Yang, L. E. Reinstein, S. Pai, Z. Xu, and D. L. Carroll, "A new genetic algorithm technique in optimization of permanent ^{125}I prostate implants," Med. Phys. **25**, 2308–2315 (1998).

[19]M. Lahanas, D. Baltas, and N. Zamboglou, "Anatomy-based three-dimensional dose optimization in brachytherapy using multiobjective genetic algorithms," Med. Phys. **26**, 1904–1918 (1999).

[20]M. Lahanas, D. Baltas, and S. Giannouli, "Global convergence analysis of fast multiobjective gradient-based dose optimization algorithms for high-dose-rate brachytherapy," Phys. Med. Biol. **48**, 599–617 (2003).

[21]X. Zhang, H. Liu, X. Wang, L. Dong, Q. Wu, and R. Mohan, "Speed and convergence properties of gradient algorithms for optimization of IMRT," Med. Phys. **31**, 1141–1152 (2004).

[22]G. Cimmino, "Calcolo approssimato per le soluzioni dei sistemi di equazioni lineari," La Ric. Sci. Roma XVI, Ser. II, Anno IX **1**, 326–333 (1938).

[23]Y. Censor, M. D. Altschuler, and W. Powlis, "On the use of Cimmino's simultaneous projections method for computing a solution of the inverse problem in radiation therapy treatment planning," Inverse Probl. **4**, 607–623 (1988).

[24]M. Benzi, "Gianfranco Cimmino's contributions to numerical mathematics." Atti del Seminario di Analisi Matematica, Dipartimento di Matematica dell 'Universita' di Bologna, Volune speciale: Ciclo di conferenze in ricordo di Gianfranco Cimmino, Marzo-Aprile 2004, pp. 87–109, Tecnoprint, Bologna, 2005.

[25]W. D. Powlis, M. D. Altschuler, Y. Censor, and E. L. Buhle, Jr., "Semi-automated radiotherapy treatment planning with a mathematical model to satisfy treatment goals," Int. J. Radiat. Oncol., Biol., Phys. **16**, 271–276 (1989).

[26]Y. Censor, D. Gordon, and R. Gordon, "Component averaging: An efficient iterative parallel algorithm for large and sparse unstructured problems," Parallel Comput. **27**, 777–808 (2001).

[27]S. L. Jacques, "Light distributions from point, line and plane sources for photochemical reactions and fluorescence in turbid biological tissues," Photochem. Photobiol. **67**, 23–32 (1998).

[28]T. Nakai, G. Nishimura, K. Yamamoto, and M. Tamura, "Expression of optical diffusion coefficient in high-absorption turbid media," Phys. Med. Biol. **42**, 2541–2549 (1997).

[29]R. Storn and K. Price, *Differential Evolution—a Simple and Efficient Heuristic for Global Optimization over Continuous Spaces*, Journal of Global Optimization, Vol. 11 (Kluwer Academic, Dordrecht, 1997), pp. 341–359.

[30]T. C. Zhu, B. E. Bjarngard, X. Ying, and C. J. Yang, "Modeling the output ratio in air for megavoltage photon beams," Med. Phys. **28**, 925–937 (2001).

[31]A. R. De Pierro and A. N. Iusem, "A simultaneous projections method for linear inequalities," Linear Algebr. Appl. **64**, 243–253 (1985).